ASME
SETTING THE STANDARD

Transactions of the ASME, Journal of Fluids Engineering (ISSN 0098-2202) is published monthly by The American Society of Mechanical Engineers, Three Park Avenue, New York, NY 10016. Periodicals postage paid at New York, NY and additional mailing offices.
POSTMASTER: Send address changes to Transactions of the ASME, Journal of Fluids Engineering, c/o THE AMERICAN SOCIETY OF MECHANICAL ENGINEERS, 22 Law Drive, Box 2300, Fairfield, NJ 07007-2300.
CHANGES OF ADDRESS must be received at Society headquarters seven weeks before they are to be effective. Please send old label and new address.
STATEMENT from By-Laws. The Society shall not be responsible for statements or opinions advanced in papers or ... printed in its publications (B7.1, Par. 3).

Journal of Fluids Engineering

Published Monthly by ASME

VOLUME 130 • NUMBER 9 • SEPTEMBER 2008

RESEARCH PAPERS

Flows in Complex Systems

Fundamental Issues and Canonical Flows

Multiphase Flows

Techniques and Procedures

(Contents continued on inside back cover)

This journal is printed on acid-free paper, which exceeds the ANSI Z39.48-1992 specification for permanence of paper and library materials. ♾™
♻ 85% recycled content, including 10% post-consumer fibers.

(**Contents continued**)

Journal of Fluids Engineering **Volume 130, Number 9** **SEPTEMBER 2008**

TECHNICAL BRIEFS

The ASME Journal of Fluids Engineering is abstracted and indexed in the following:

Applied Science & Technology Index, Chemical Abstracts, Chemical Engineering and Biotechnology Abstracts (Electronic equivalent of Process and Chemical Engineering), Civil Engineering Abstracts, Computer & Information Systems Abstracts, Corrosion Abstracts, Current Contents, Ei EncompassLit, Electronics & Communications Abstracts, Engineered Materials Abstracts, Engineering Index, Environmental Engineering Abstracts, Environmental Science and Pollution Management, Excerpta Medica, Fluidex, Index to Scientific Reviews, INSPEC, International Building Services Abstracts, Mechanical & Transportation Engineering Abstracts, Mechanical Engineering Abstracts, METADEX (The electronic equivalent of Metals Abstracts and Alloys Index), Petroleum Abstracts, Process and Chemical Engineering, Referativnyi Zhurnal, Science Citation Index, SciSearch (The electronic equivalent of Science Citation Index), Shock and Vibration Digest, Solid State and Superconductivity Abstracts, Theoretical Chemical Engineering

LES Study of the Influence of a Train-Nose Shape on the Flow Structures Under Cross-Wind Conditions

Hassan Hemida
e-mail: hemida@chalmers.se
e-mail: hassan.hemida@epsilon.nu

Siniša Krajnović

Division of Fluid Dynamics,
Department of Applied Mechanics,
Chalmers University of Technology,
SE-41296 Gothenburg, Sweden

Cross-wind flows around two simplified high-speed trains with different nose shapes are studied using large-eddy simulation (LES) with the standard Smagorinsky model. The Reynolds number is 3×10^5 based on the height of the train and the freestream velocity. The cross section and the length of the two train models are identical while one model has a nose length twice that of the other. The three-dimensional effects of the nose on the flow structures in the wake and on the aerodynamic quantities such as lift and side force coefficients, flow patterns, local pressure coefficient, and wake frequencies are investigated. The short-nose train simulation shows highly unsteady and three-dimensional flow around the nose yielding more vortex structures in the wake. These structures result in a surface flow that differs from that in the long-nose train flow. They also influence the dominating frequencies that arise due to the shear-layer instabilities. Prediction of vortex shedding, flow patterns in the train surface, and time-averaged pressure distribution obtained from the long-nose train simulation are in good agreement with the available experimental data. [DOI: 10.1115/1.2953228]

Keywords: flow structures, cross wind, LES, train aerodynamics, front shape

1 Introduction

High-speed trains experience strong aerodynamic forces and moments when cruising in a strong cross wind. Due to these aerodynamic forces and moments, high-speed trains, which most of them are characterized by light weight, are at high risk of overturning or derailment. These phenomena opened new research territory in recent years that attracted the attention of many researchers trying to investigate the different parameters that influence train instability in a strong cross wind. Prevention of the unwanted influences of a cross wind requires that the flow structures on the train surface and around it are fully understood in both the instantaneous and the time-averaged flow. Unsteady flow past a train in a cross wind has been the object of numerous experimental investigations [1–7]. The primary interest in these investigations was the measurement of some integral parameters such as drag, lift, and side force coefficients together with the measurements of the wind characteristics around the train. Some other researchers have investigated the flow structures numerically to obtain a better understanding of the flow behavior. Reynolds-averaged Navier–Stokes (RANS) equations, time varying RANS (URANS) [8,9], and large-eddy simulation (LES) [10] were used. Since the cross-wind instability is a consequence of the unsteadiness of the flow field around the train, accurate time-dependent solution is necessary. Copley [5] investigated the influence of Reynolds number on the flow field around a train subjected to a cross wind. He found that, for very low Reynolds number, the flow around the train is laminar everywhere and remains attached to the train surface. Increasing the Reynolds number results in a separation on the roof-side streamwise edge and the flow detaches from the face. At the same time, the wake begins to shed vortices in a regular fashion. A further increase in Reynolds number makes the flow fully turbulent in the wake and in the separation region over the roof-side face. At some critical Reynolds number, the flow reattaches to the face, forming a separation bubble. For higher Reynolds number, this separation bubble is suppressed and the flow over the roof-side face is fully attached. However, although the influence of train-nose shape is believed to play an important role in the flow structures and the aerodynamics of high-speed trains, it has not been properly investigated in previous studies.

Numerical and experimental studies of flows around bluff bodies [11–18] show that these flows are highly unsteady and three dimensional. Moreover, when the Reynolds number is high enough to obtain a fully turbulent flow in the shear layers, two main instability modes are present in the flow. The first is the large-scale shedding in the wake, which manifests itself as a progressive wave motion with alternate fluctuations produced by the shear present at the limit between the recirculation zone and the exterior fluid. These fluctuations determine the periodic shedding of the vortices that form behind the bluff body. The second high frequency mode is the so called spiral mode, which is associated with the small-scale shear-layer Kelvin–Helmholtz instability on the periphery of the recirculation and separation regions. This instability is responsible for the distortion of the large vortex structures, shedding of the vortex tubes in a quasicoherent fashion inside the detached shear layers, production of the small scales, and, eventually, transition to turbulence in the wake (for more details, see Ref. [15]). Capturing these structures and investigating the flow features require simulation methods that resolve, rather than model, the main dynamics governing the flow. Numerical solutions using URANS are not able to capture these high frequency modes since the Reynolds stresses representing the turbulence in URANS are modeled with a turbulence model. Thus, the success in finding a true representation of the flow is dependent on the turbulence model used. Moreover, it is difficult to define a model that can accurately represent the Reynolds stresses in the region of separated flow, such as a wake behind a train. In the present work, LES using the standard Smagorinsky subgrid scale (SGS) model with model constant $C_s=0.1$ is used to compute the flow field around the train models. LES with the same SGS model

Contributed by the Fluids Engineering Division of ASME for publication in the JOURNAL OF FLUIDS ENGINEERING. Manuscript received December 20, 2006; final manuscript received April 26, 2008; published online August 12, 2008. Assoc. Editor: Ye Zhou.

was successfully used in previous studies to investigate the flow around road vehicles [16–18] and in a cross-wind flow [10].

The flow over a real train involves many complexities and the complete modeling of these complexities is generally regarded as impossible [3,4]. For this reason, we chose the idealized model of Copley [5] and Chiu [3,4] as the train geometry in our investigations. The model is an ideal since its cross section follows a simple algebraic equation and many of the geometrical details are not included. The model is without intercarriage gaps between the coaches nor underbody blockages. The slenderness ratio of the model is 10. More details about our idealized train model is in Sec. 3 of the present paper.

The main aim of the present work is to investigate the influence of the shape of the nose on the flow structures, aerodynamic coefficients, and flow frequencies around the simplified high-speed train. Two stationary train models are used that have the same length and cross section but different nose lengths. The cross-wind flow is obtained around the simplified models at a 90 deg yaw angle and a Reynolds number of $\mathrm{Re}=3\times10^5$ based on the train height and freestream velocity. At this Reynolds number, the flow is fully turbulent and hence the aerodynamic coefficients are believed to be Reynolds number independent since the drag crisis occurs at lower Reynolds number. The long-nose model together with the flow conditions (i.e., Reynolds number and the setup) are identical to those in the experimental studies of Copley [5] and Chiu [3,4].

This paper is organized as follows. The numerical method and the LES used in the present paper are described in Sec. 2. The geometry of the simplified train bodies and the computational domains as well as the boundary conditions are presented in Sec. 3. Numerical accuracy is discussed in Sec. 4. Comparisons of the time-averaged flow structures, pressure coefficient, and aerodynamic forces obtained from the two nose shapes are made in Sec. 5.1. The influence of the nose shape on the instantaneous flow structures and wake flow frequencies is reported in Sec. 5.2.

2 Numerical Method

Since cross-wind stability is a consequence of the flow unsteadiness, it is crucial to understand the instantaneous flow in order to investigate its impact on the time varying aerodynamic forces. Thus, a time-dependent method, such as LES, should be used in order to gain instantaneous information about the flow. LES has already been proven to be a reliable technique in the prediction of flows around simplified vehicles [10,16–18]. Until recently, it was impossible to numerically predict the time-dependent flow around a train model, even at moderate Reynolds numbers. In recent years, increases in computer capability have made these simulations (at moderate Reynolds numbers) possible with LES.

It is worth mentioning that complicated flow structures develop in the wake region behind trains. These wake structures are dominated by large turbulent structures. Most of these structures are resolved using LES and only the influence of the scales smaller than computational cells is modeled. Although LES is computationally more expensive than URANS, it can provide more accurate time-averaged results and also give information on the instantaneous flow, which is out of the reach of URANS.

In LES, the large eddies are solved directly and the influences of the small-scale eddies on the large-scale eddies are modeled. Thus, the incompressible Navier–Stokes equations and the continuity equation are filtered using an implicit spatial filter. The resulting filtered equations are

$$\frac{\partial \bar{u}_i}{\partial t} + \frac{\partial}{\partial x_j}(\bar{u}_i\bar{u}_j) = -\frac{1}{\rho}\frac{\partial \bar{p}}{\partial x_i} + \nu\frac{\partial^2 \bar{u}_i}{\partial x_j x_j} - \frac{\partial \tau_{ij}}{\partial x_j} \tag{1}$$

and,

$$\frac{\partial \bar{u}_i}{\partial x_i} = 0 \tag{2}$$

Here, $\bar{u}_i$ and $\bar{p}$ are the resolved filtered velocity and pressure, respectively, while $\tau_{ij}=\overline{u_i u_j}-\bar{u}_i\bar{u}_j$ are the SGS stresses. The SGS stresses represent the contribution of the small unresolved scales to the large resolved ones. These are unknown and must be modeled. The Smagorinsky model is used in the present work to model the SGS stresses because of its simplicity and to reduce computational cost. It models the SGS stresses as

$$\tau_{ij} - \tfrac{1}{3}\delta_{ij}\tau_{kk} = -2\nu_{\mathrm{SGS}}\bar{S}_{ij} \tag{3}$$

where $\bar{S}_{ij}$ is the resolved rate of strain defined as

$$\bar{S}_{ij} = \frac{1}{2}\left(\frac{\partial \bar{u}_i}{\partial x_j} + \frac{\partial \bar{u}_j}{\partial x_i}\right) \tag{4}$$

and ν_{SGS} is the SGS viscosity defined as

$$\nu_{\mathrm{SGS}} = (C_s f\Delta)^2|\bar{S}| \tag{5}$$

Here, $|\bar{S}|=(2\bar{S}_{ij}\bar{S}_{ij})^{1/2}$, C_s is the SGS model coefficient, and f is the van Driest damping function that has the form

$$f = 1 - \exp\left(\frac{y^+}{25}\right) \tag{6}$$

The value of the SGS model coefficient, C_s, is 0.1 in the present work. Since the resolved strain-rate tensor, $\bar{S}_{ij}$, does not vanish at the wall, the value of the coefficient, C_s, should be adjusted to take partially into account the effect of the wall. Thus, the damping function, f, is used to damp the turbulence length scale next to the wall. The same model constant has been used in simulations of the flow around simplified road vehicles [16–18]. The filter width, Δ, is taken as the cubic root of the volume of a finite volume cell.

3 Simplified Train Body and Boundary Conditions

It is difficult to experimentally investigate the flow behavior around a full-scale train, especially in the case of a cross wind, simply because it requires a very large wind tunnel for even small yaw angles. Furthermore, the data obtained in experimental studies are limited to a confined region of a line or a plane. It is also impossible to simulate the full-scale train using LES due to the limited computer resources. In addition, real trains are often not used for aerodynamic studies owing to their geometrical complexities. Instead, simplified train models are used in both experimental and numerical studies. Baker et al. [2] carried out a series of experimental studies of a full-scale train consisting of three vehicles at a coastal site at Eskmeals in Cumbria in northwest England during the winters of 2001/2002 and 2002/2003. The aim of their studies was to measure the wind characteristics around the full-scale train and the time-averaged and instantaneous aerodynamic coefficients. They used the results of the full-scale measurements to make comparisons with wind tunnel experiments for a 1/30 scale model. It was discovered that the wind tunnel measurements gave results that agreed reasonably well with the full-scale train measurements except for the vertical component of the aerodynamic forces, the lift force, that results from the local roughness variations in close proximity to the wind tunnel models. These roughness variations caused significant variations in the underbody flow.

In our work, the simplified model of Chiu and Squire [4] was chosen to study the effect of the shape of the nose on the flow structures. The cross-sectional profile of the idealized train model was defined by the following equation:

$$|y|^n + |z|^n = c^n \tag{7}$$

The model consists of two parts, a train body and a nose (see Fig. 1(*a*)). The train body has a cylindrical shape with a height of $D=125$ mm and a total length of $9.36D$. The profile of the cross section follows Eq. (7), in which the value of $c=62.5$ mm$(D/2)$ and $n=5$. The cross section and the length of the body part are

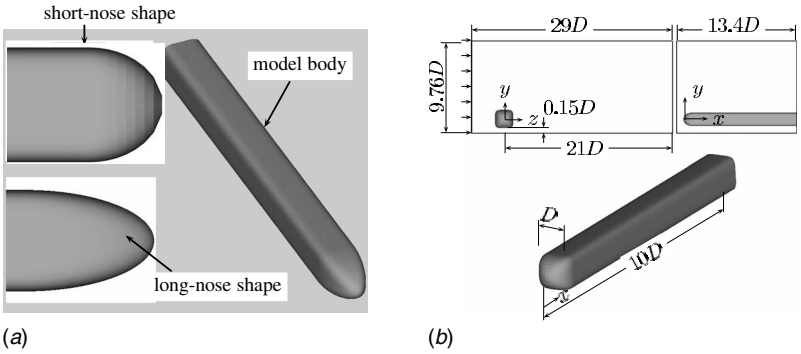

(*a*) (*b*)

Fig. 1 (*a*) The shape of the simplified train models. (*b*) Computational domain.

identical for the two models. The nose cross section is given by the same equation, in which c follows a semielliptical profile with a major diameter of $1.28D$ for the long-nose model and $0.64D$ for the short-nose model, while n reduces uniformly to 2 at the nose tip. In this way, the cross section becomes smaller and more circular toward the nose.

The train model is mounted in a closed channel (wind tunnel), as shown in Fig. 1(*b*). The channel has an extension of $29D$ in the streamwise direction, a height of $9.76D$, and a width of $13.4D$. It has walls at all sides except the inlet and the outlet. Similar to the experimental setup, the train model used in our LES is mounted horizontally on the wind tunnel sidewall. The distance between the model and the ground is chosen to be $0.15D$, which is typical for real trains. The model centerline position is chosen to be $8D$ from the inlet and $21D$ from the outlet of the numerical wind tunnel. These lengths were found sufficient in previous LES of flows around similar bodies [10,11].

In the experiment, a groundboard was used above the tunnel floor to control the boundary layer growth. Four movable flaps were mounted at the downstream end of the rear groundboard to control the flow in a way that the mainstream was parallel to the groundboard when approaching its leading edge. The groundboard boundary condition was modeled in LES by simply placing the bottom of the computational domain at the height of the groundboard.

The flow enters the channel with a uniform velocity profile constant in time. No-slip boundary conditions are used on the train surface and channel floor. Wall functions are used on the channel side walls and ceiling. Details on the implementations of the wall functions can be found in Ref. [18]. A homogeneous Neumann boundary condition is used for the pressure on all the boundaries. A convective outlet boundary condition, $\partial \bar{u}_i/\partial t + U_\infty(\partial \bar{u}_i/\partial z)=0$, where U_∞ is the freestream velocity, is used at the channel outlet.

4 Numerical Accuracy

Two computations on two different computational grids were made for each model to investigate the influence of the mesh resolution on the results and to establish numerical accuracy. The ICEM-CFD commercial grid-generator package was used to create both the model geometries and the meshes around them. The train model was constructed using Eq. (7). Another dummy train with a height equal to $1.15D$ is built around the model. The ICEM-CFD Hexa package was employed to generate a hexahedral mesh around the previously described model. An *O*-type mesh was made in the belt of thickness of $0.075D$ between the model and the dummy train. This allows the generation of a smooth mesh in all directions, see Fig. 2(*a*). Figure 2(*a*) also shows another *O*-type mesh with thicknesses of $0.5D$ (in the coarse mesh) and $0.1D$ (in the fine mesh) that is made around the first *O*-type mesh. The dummy train surface is used as a shared surface between the two *O*-type meshes. Figure 2(*b*) shows the mesh shape around the nose of the train and one block under the train (block *U*), which is enclosed between the second *O*-type mesh and the groundboard. The rest of the blocking structures were made using *H* grids. Hyperbolic stretching is used to make a finer mesh close to the train model and a coarser mesh in the regions away from the train. The total numbers of nodes are 11.5×10^6 and 8×10^6 for the fine mesh and the coarse mesh, respectively.

In the present work, the numerical flow predictions were carried out using an in-house finite volume developed multipurpose package, CALC-PVM, for parallel computations of turbulent flow in complex multiblock domains. LES equations were discretized using a three-dimensional finite volume method in a collocated grid arrangement using the Rie–Chow interpolation. The high frequency modes in the model boundary and shear layers are important in these simulations. Thus, the convective, viscous diffusion plus subgrid fluxes were approximated by a second-order-accurate

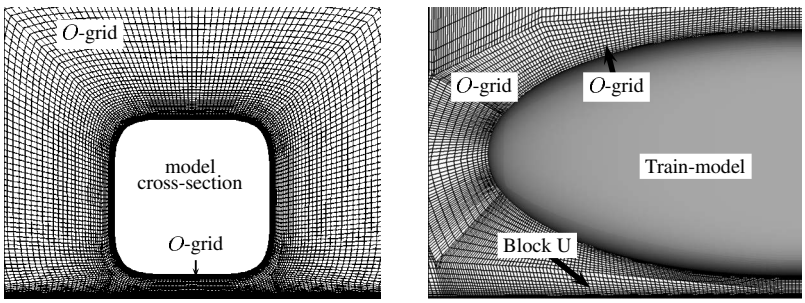

(*a*) (*b*)

Fig. 2 Coarse mesh (*a*) cross section of the mesh shows the first and the second *O*-grids around the train model. (*b*) Mesh shape around the train nose in the symmetric *x*–*y* plane of the train.

Table 1 Maximum spatial resolutions for the fine and coarse mesh simulations over the two train models

Train model	Mesh	$y^+=nu^*/\nu$	$z^+=\Delta su^*/\nu$	$x^+=\Delta lu^*/\nu$
Long nose	Fine	1.5	50	125
	Coarse	2.5	100	400
Short nose	Fine	1.8	60	140
	Coarse	2.6	110	440

central difference scheme. To reduce numerical dissipation, no upwind schemes were used in the simulations. The mesh stretching ratio was kept below 1.1 in the *O*-type meshes around the train models since the central difference scheme is more sensitive to the stretching ratio in the places where large flow variations are expected. The time integration was done using the Crank–Nicolson second-order scheme. The SIMPLEC algorithm was used for the pressure-velocity coupling. Additional details about this code can be found in Ref. [19].

The equations are solved for both the coarse and fine mesh simulations starting from zero air velocity around the train models. A second-order upwind scheme (Van–Leer) for the convective terms was used at the beginning of the simulations. The numerical dissipation resulting from the upwind scheme contributes to better convergence. A fully developed solution is obtained from the coarse mesh after time $t^*=tU_\infty/D=120$, while $t^*=150$ is needed to obtain fully developed turbulent flow in the fine mesh simulations. After the initial run with the upwind scheme, the convective terms were discretized using the second-order-accurate central difference scheme and the time averaging was not started until fully stabilized turbulent flow was obtained. The physical time step is 1.0×10^{-4} ($t^*=0.0008$) in both the coarse and the fine mesh simulations. This value of the time step gives maximum CFL numbers of about 0.8 and 0.75 for the coarse and fine meshes, respectively. The time-averaged flow is obtained using $t^*=80$ counted after the initial run as mentioned before. This time covers at least 15 shedding cycles in the wake, corresponding to the frequency containing most of the energy in the autopower spectra of the aerodynamic force coefficients.

In all the simulations, the governing equations are solved all the way to the model wall to ensure proper variation of the flow quantities in the near-wall region, where much of the flow physics originates. The instantaneous flow shows boundary layer separation on the train surface. Consequently, small separation bubbles appear on the roof-side face of the train. These separation bubbles form shear layers next to the wall. The grid density near the wall was fine enough to resolve the small-scale structures that arise via the shear-layer instabilities. The maximum spatial resolutions of the model surface cells expressed in the wall units for all the simulations are shown in Table 1, where u^* is the friction velocity, n is the distance between the first node and the train surface in the wall normal direction, Δs is the cell width in the streamwise direction, and Δl is the cell width in the spanwise direction.

Table 2 Time-averaged LES force coefficients

	Long-nose model			Short-nose model		
	fine	rms	coarse	fine	rms	coarse
$\langle C_s\rangle_t$	0.63	0.01	0.655	0.65	0.02	1.1
$\langle C_l\rangle_t$	0.82	0.024	0.78	0.83	0.03	0.3

The time-averaged aerodynamic coefficients obtained from the simulations are reported in Table 2, where $\langle C_s\rangle_t$ is the time-averaged side force coefficient, $\langle C_l\rangle_t$ is the time-averaged lift force coefficient, and rms is the root-mean-square values of the aerodynamic coefficients obtained from the fine mesh. The instantaneous values of these coefficients are defined as

$$C_s=\frac{\int p_s dA_z}{\frac{1}{2}\rho U_\infty{}^2 A_z} \tag{8}$$

and

$$C_l=\frac{\int p_s dA_y}{\frac{1}{2}\rho U_\infty{}^2 A_y} \tag{9}$$

where p_s is the surface pressure, ρ is the density of air at the freestream, and A_z and A_y are the projected surface areas in the z and y directions, respectively.

Figure 3(*a*) shows the time-averaged pressure distribution at $x/D=6.5$ on the long-nose model surface obtained from the fine and coarse meshes as well as the time-averaged pressure distribution collected from the experimental model. The experimental data have been measured at the same position as the numerical data. The time-averaged pressure distribution is expressed in terms of the local pressure coefficient, C_p. This coefficient is defined as

$$C_p=\frac{\langle p\rangle_t-p_\infty}{\frac{1}{2}\rho U_\infty{}^2} \tag{10}$$

where $\langle\cdot\rangle_t$ denotes time averaging, U_∞ is the inlet channel velocity, and p_∞ is the reference pressure, which is chosen to be the pressure at a point in the top corner of the channel inlet. The position of the reference pressure is chosen to be at a sufficient distance from the model so that the total inlet pressure is not influenced by the model. The corresponding results are collected on the short-nose model and are shown in Fig. 3(*b*). It is worth mentioning that the experimental data of Chiu [3] have been collected on the long-

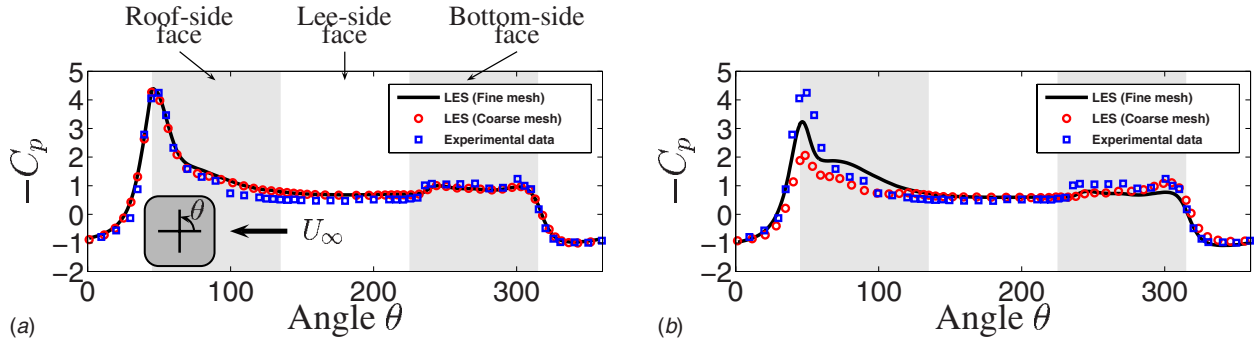

Fig. 3 Time-averaged local surface pressure coefficient, C_p, at $x/D=6.5$. (*a*) Long-nose model; (*b*) short-nose model. The experimental data of Chiu [3] shown in (*a*) and (*b*) have been collected on the long-nose model.

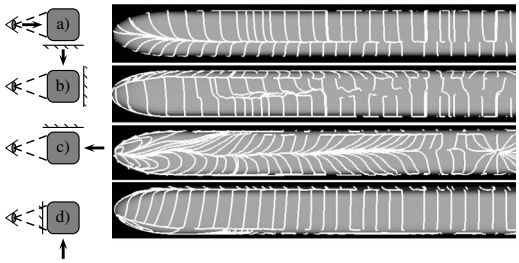

Fig. 4 Long-nose model flow: time-averaged trace lines projected on the train surface

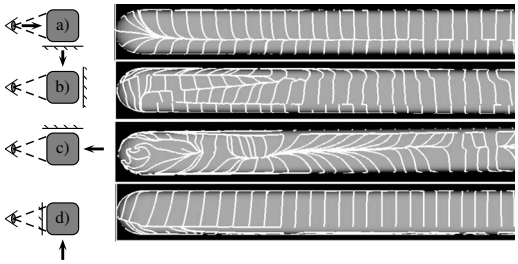

Fig. 5 Short-nose model flow: time-averaged trace lines projected on the train surface

nose model. The good agreement between the LES with the long-nose model and the experimental data in Fig. 3(*a*) indicates that our simulations predict the flow accurately. On the other hand, we cannot judge the performance of the short-nose simulations due to the absence of the experimental data. It is likely that the results from the fine mesh simulation are accurate, however, as the resolution is similar to that in the simulations using model with the long nose. The fine and coarse mesh simulations on the long-nose model produce similar results. The collapse of the LES results from the long-nose simulation with the experimental data means that the mesh is fine enough to give accurate time-averaged pressure distributions. At the same time, the discrepancies between the computed results of the coarse and fine mesh simulations on the short-nose model mean that the coarse mesh resolution is not sufficient to resolve the flow field. It is worth mentioning here that the simulations made on the long-nose model have the same number of nodes and topologies as the simulations made on the short-nose model.

Both the fine and coarse mesh simulations made on the long-nose model are in good agreement with the experiments in terms of the time-averaged surface flow patterns, time-averaged pressure distributions, groundboard flow and surface separations, and reattachment lines. Further comparisons between the LES on the long-nose model and experiments have been reported in Ref. [10].

5 Results

LES are made for the flow around two stationary train models that differ only in the nose shapes, for a 90 deg yaw angle. The Reynolds number is 3×10^5 based on the train height and the freestream velocity. The primary aim of this study is to investigate the influence of a nose shape of a train on the time-averaged and time-dependent flow structures and resulting aerodynamic coefficients. Different visualization techniques are used to visualize flow structures in different parts of the flow. All the results presented in this section are from the fine mesh computations unless otherwise stated.

5.1 Time-Averaged Flow

5.1.1 Surface Flow Patterns. The statistics of the flow are computed using approximately 15 shedding cycles. The time-averaged surface flow patterns are visualized using the trace lines projected on the train surface. Figures 4 and 5 show the surface flow patterns on the long-nose and short-nose models, respectively.

It can be seen in Figs. 4 and 5 that the flow patterns are similar for the two models on the underbody face and streamwise face while a significant difference in the flow patterns is found on the roof and leeward sides. In addition, it can be seen from Figs. 4(*c*) and 5(*c*) that the flow patterns are completely different close to the train nose, where the effect of the three-dimensional nose flow on the flow patterns is strong. For the long-nose train, the flow moves axially from the nose on the leeward side. This agrees well with the experimental observations. At the same time, a reverse axial flow is obtained from the simulation over the short-nose train, where the flow moves axially toward the nose tip (these flow patterns are discussed further in Sec. 5.1.3). Although flow separates on the roof-side face in both cases, different flow patterns are obtained. Figure 4(*b*) shows that the attached flow dominates on the roof-side face of the long-nose model, while Fig. 5(*b*) shows a dominating separated flow on the roof-side face in the case of the short-nose train.

5.1.2 Wake Flow. The vortex sheets shedding from the underside and the roof of the train are rolled up to form two large bubbles that dominate the leeward flow field. A vortex core technique based on the eigenvalues of the velocity gradient tensor is used to detect the vortices in the three-dimensional flow field. Details about vortex core technique can be found in Sujudi and Haimes [20], which is implemented in ENSIGHT (the visualization package used to visualize the flow in this paper). This technique is used here with the assistance of surface streamlines to explore the flow structures around the train and in the wake flow. Figures 6(*a*) and 6(*b*) show the vortex cores in the flow over the short-nose and

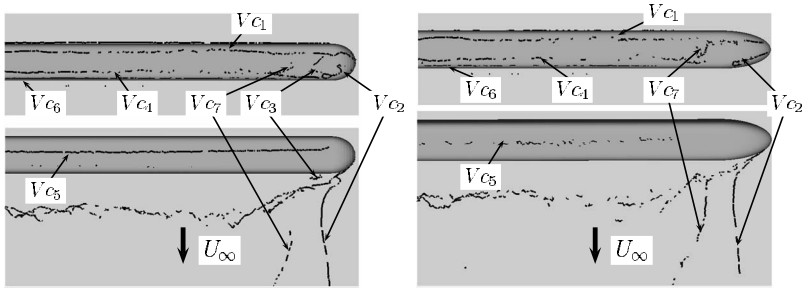

Fig. 6 Vortex cores in the wake flow showing the time-averaged flow structures. (*a*) Short-nose model; (*b*) long-nose model. Upper figures: view from the exit; lower figures: view from the roof.

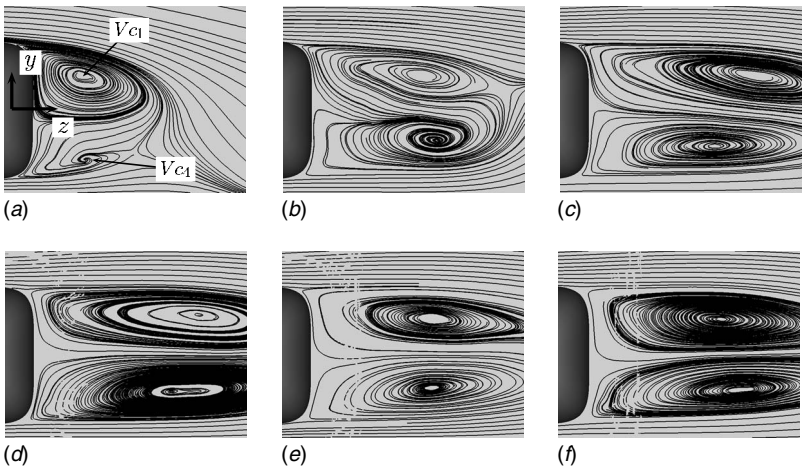

Fig. 7 Long-nose model flow: time-averaged streamlines showing the circulation regions projected onto the *y–z* planes at (*a*) *x/D*=1.5, (*b*) *x/D*=2.5, (*c*) *x/D*=3.5, (*d*) *x/D*=4.5, (*e*) *x/D*=6, and (*f*) *x/D*=8.

the long-nose trains, respectively.

The vortices that appear in the flow field over the short-nose train in Fig. 6(*a*) can be described as follows:

(1) Vortex Vc_1 emerges from a focus on the train nose (roof side). It stretches along the train length in the x-direction.
(2) Vortex Vc_2 originates from a focus very close to the train nose (floor side).
(3) Small vortex Vc_3 is responsible for the nose axial flow on the leeward side.
(4) Vortex Vc_4 onsets in the wake flow with a focus standing in the flow at a position about two train height far from the train nose tip in the direction of the train length.
(5) Vortex Vc_5 appears due to the separation in the roof-side flow. It originates from a focus on the train surface close to the base of the nose of the train.
(6) Small vortex Vc_6 is at the bottom edge of the leeward side.
(7) Vortex Vc_7 starts on the train surface at a distance of about one train height from the tip of the nose. It is convected in the wake flow in a position at which the vortex Vc_4 starts.

The same vortices that appear in the flow over the short-nose train are found in the flow over the long-nose train. The two vortices Vc_1 and Vc_2, that appear in the flow around the short nose train, originate from two foci on the train surface. Once they emerge, they detach from the train wall with axes quite close to the normal of the surface of the nose. However, in the long-nose flow, the two vortices Vc_1 and Vc_2 originate from two foci on the train nose and stretch axially toward the wake with axes in directions closer to the tangent of the surface. The flow between them remains attached to the train surface. Consequently, vortex Vc_3 found in the short-nose train flow does not exist here.

The formation of the circulation regions Vc_1 and Vc_4 in the wake is shown in Figs. 7 and 8 through streamline patterns plotted at different cross sections. These figures demonstrate that the circulation regions in the flow over the two train models have a fixed size in space after $x/D \approx 3.5$ and $x/D \approx 4.5$ for the long-nose and short-nose trains, respectively. Once the size of these regions has stabilized along the train, their centers are approximately one train height downstream the of the models. The width of the vortices in the streamwise direction is about $2D$ and their height is about $0.5D$. However, the recirculation regions structures are different in the developing region, i.e., $x/D < 3.5$ and $x/D < 4.5$ for the long-nose and short-nose models, respectively. Figure 7 demonstrates that the recirculation regions develop smoothly from the nose in the long-nose case, while Fig. 8 shows a different flow situation for the short-nose case as a result of the existence of the vortex

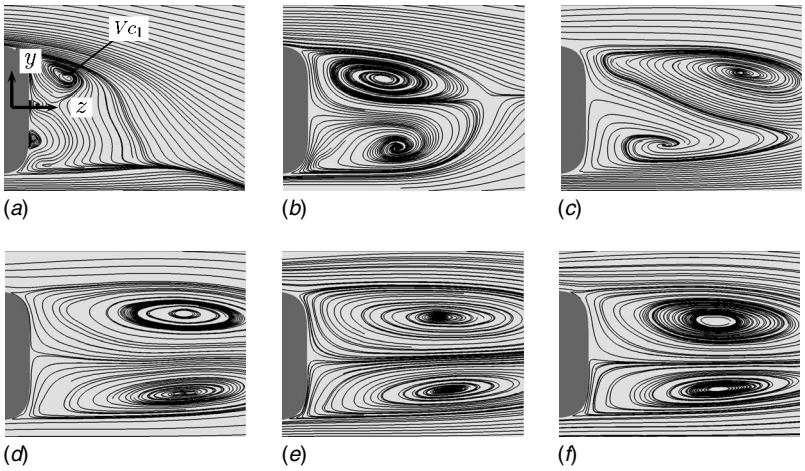

Fig. 8 Short-nose model flow: time-averaged streamlines showing the circulation regions projected onto the *y–z* planes at (*a*) *x/D*=1.5, (*b*) *x/D*=2.5, (*c*) *x/D*=3.5, (*d*) *x/D*=4.5, (*e*) *x/D*=6, and (*f*) *x/D*=8.

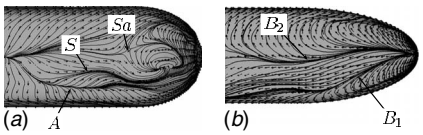

Fig. 9 Time-averaged velocity vectors on the leeward side of the train close to the nose: (*a*) short-nose train; (*b*) long-nose train

V_{c_3}, which affects the formation of the recirculation regions. The influence of this vortex on the surface flow patterns can be seen in Fig. 5(*c*) since the surface flow patterns have stabilized after $x/D \approx 4.5$. On the other side, the flow patterns on the leeward side of the long-nose train have stabilized after $x/D \approx 3.5$, as shown in Fig. 4(*c*).

5.1.3 Surface Axial Flow on the Leeward Side Close to the Nose. The time-averaged flow shows axial surface flow on the leeward sides for both the long- and short-nose trains. In the case of the short-nose train, the flow moves axially toward the tip of the nose, as shown in Fig. 9(*a*). On the other side, the flow moves axially from the tip in the case of the long-nose train, as shown in Fig. 9(*b*).

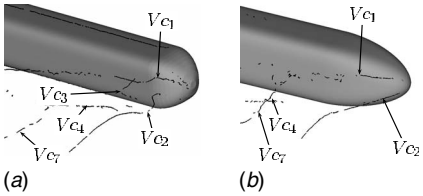

Fig. 10 Vortex cores in the time-averaged wake flow close to the nose: (*a*) short-nose train; (*b*) long-nose train

Figures 10(*a*) and 10(*b*) show vortex cores in the wake flow close to the nose of the short and long-nose trains, respectively. The schematic representation of these vortices is shown in Fig. 11. Line vortex Vc_1 originates from focus F_1 while vortex line Vc_2 originates from focus F_2 on the train nose, as shown in Figs. 11(*a*) and 11(*b*). In the case of the short-nose train, vortex lines Vc_1 and Vc_2 emerge with axes quite close to the normal of the train surface. Vortex Vc_1 circulates with positive vorticity in the z-direction, w_z^+, while vortex Vc_2 circulates with negative vorticity to the z-direction, w_z^-. The flow between these two vortices is forced to move axially out from the nose in the direction of the train base. Part of this flow moves with enough inertia to escape from these two vortices to form a small vortex, Vc_3, as shown in Fig. 11(*a*). The axis of vortex Vc_3 is parallel to the leeward side. It stretches in the lower leg parallel to the train length in the x-direction, forming one separation line, S, and one reattachment line, A, as shown in Fig 9(*a*). It then changes direction to stretch vertically in the y-direction when it encounters the flow in the recirculation regions. This vortex has a negative vorticity in the y-direction, w_y^-. The vertical orientation of vortex Vc_3 forces the flow to move axially toward the nose. The incoming flow toward the nose, from vortex Vc_3, and the incoming flow from the nose, caused by the circulation of the two vortices Vc_1 and Vc_2, meet in the saddle point, Sa, as shown in Fig. 9(*a*).

Figure 12 shows the streamlines and velocity vectors projected on surfaces parallel to the train length on planes $y/D=-0.5$,

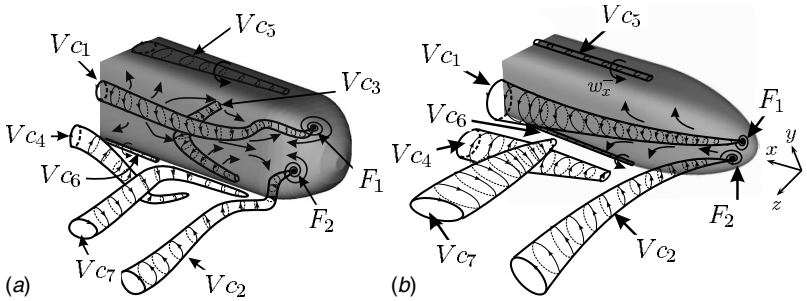

Fig. 11 Schematic representation showing the time-averaged flow structures around the nose: (*a*) short-nose train; (*b*) long-nose train

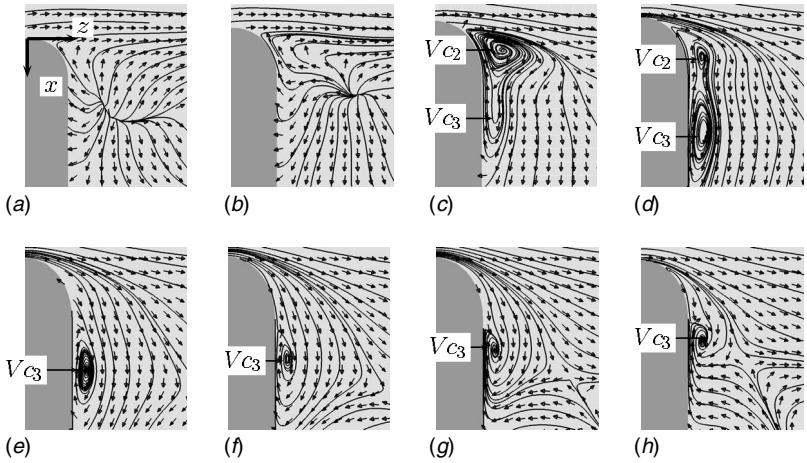

Fig. 12 Short-nose model flow: time-averaged streamlines and velocity vectors projected onto the *x–z* planes parallel to the train length: (*a*) *y/D*=–0.5, (*b*) *y/D*=–0.4, (*c*) *y/D*=–0.3, (*d*) *y/D*=–0.2, (*e*) *y/D*=–0.1, (*f*) *y/D*=0, (*g*) *y/D*=0.1, and (*h*) *y/D*=0.2. View is from the upper side of the train.

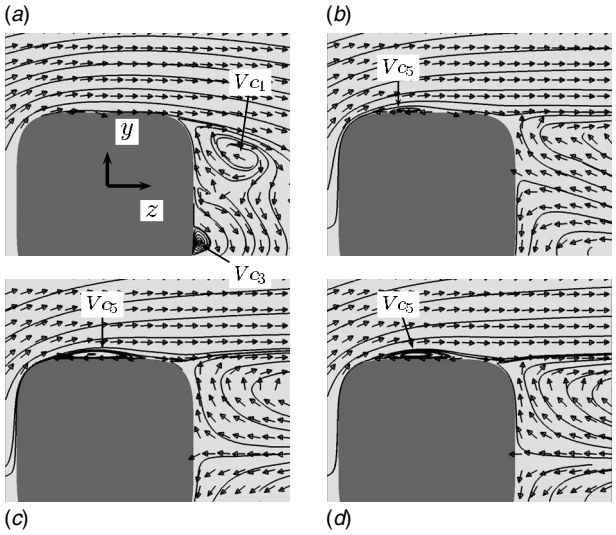

Fig. 13 Short-nose model flow: time-averaged streamlines and velocity vectors showing the separation bubble on the roof-side face, projected onto the *y–z* planes at (*a*) *x/D*=1, (*b*) *x/D*=3, (*c*) *x/D*=5, and (*d*) *x/D*=8.

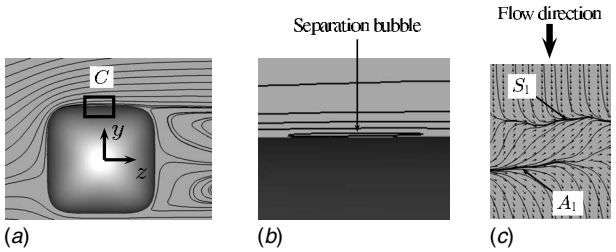

Fig. 14 Long-nose model flow: (*a*) time-averaged streamlines projected onto the *y–z* plane *x/D*=4 showing the separation bubble on the roof-side face, (*b*) zoom of region *C* from Fig. 14(*a*) and (*c*) a zoom of region *R* in Fig. 4(*b*) showing vector plots on the separation region

$-0.4, -0.3, \ldots, 0.2$. Vortices V_{c_2} and V_{c_3} are visible in Fig. 12(*c*) since the plane passes through them. When the plane moves up, vortex V_{c_3} appears clearly while V_{c_2} disappears. The maximum distance of the center of vortex V_{c_3} from the nose tip is found in Fig. 12(*e*) at $y/D \approx -0.1$ and $x/D \approx 1.7$.

In the case of the long-nose train, vortices V_{c_1} and V_{c_2} emerge from foci F_1 and F_2 on the nose of the train and stretch with the direction of their axes quite close to the tangential of the nose surface, as shown in Fig. 11(*b*). The flow between them is forced to move axially from the nose tip. Three different flow patterns close to the nose are found over the long-nose train. The flow on the upper part of the nose turns direction to circulate around focus $F1$, forming the first flow pattern. Similarly, the flow on the lower part of the nose circulates around the focus $F2$ forming the second flow pattern. Part of the circulated flow escapes from the two vortices and continues to move axially toward the train body, forming the third flow pattern. Two bifurcation lines, $B1$ and $B2$, are formed between these three different flow patterns, as shown in Fig. 9(*b*).

5.1.4 Separation on the Roof of the Train. The effect of Reynolds number on the flow separation on the roof-side face was investigated by Copley [5]. He showed a direct relation between the Reynolds number and the size of the separation bubble on the roof-side face. The Reynolds number of the flow over the real train is in the order of 10^7, which is impossible to simulate using LES. Since the Reynolds number chosen in the experimental work is 3×10^5, a separation bubble is expected both in the numerical simulations and experiments. Thus, in the experimental work, a trip wire is attached to the windward edge to obtain an attached turbulent boundary layer on the roof-side face. This is necessary to be able to simulate the same flow patterns as in the case of a real train. Copley [5] stated that there is no significant Reynolds number effect above Reynolds numbers of about 2×10^5 since the integral parameters become Reynolds number independent. The LES Reynolds number is the same as the experimental one but it is rather difficult to simulate the trip wire used in the experiment. Thus, the trip wire was neither modeled nor simulated, and therefore, a separation is expected on the roof-side face in our LES.

Figure 13 shows the short-nose train separation bubble on the roof-side face at different distances from the nose ($x/D = 1, 3, 5, 8$). The separation starts directly after the nose of the train. Figure 13(*a*) shows that the separation bubble starts with a very small size in both the *z*- and *y*-directions. It grows in the direction of the length of the train. Consequently, the region with attached flow on the roof-side face decreases along the train close to the base of the model. At $x/D \approx 4$, the entire roof-side face is dominated by the separation bubble. The size of the separation bubble remains constant after $x/D \approx 4$ with height $\approx 0.045D$, as shown in Figs. 13(*c*) and 13(*d*).

Figure 14 shows long-nose train time-averaged streamlines projected to a plane perpendicular to the length of the train train at distance $x/D=4$ from the tip of the nose. The flow separates at the separation line S_1 to form the separation bubble before it reattaches to the surface at the reattachment line A_1, as shown in Fig. 14(*c*). Figure 14(*b*) demonstrates that the separation bubble is very small and thin in both the *z*- and *y*-directions as compared to the bubble obtained in the short-nose train simulation. Figure 4(*b*) shows that the separation bubble does not grow in the direction of the length of the train. The instantaneous flow corresponding to that in Fig. 14 shows that this separation bubble is unstable, i.e., it appears and disappears with time, making the flow highly unsteady (pictures not shown here).

5.2 Surface Pressure Distribution. The time-averaged pressure distribution is used to calculate the local pressure coefficient, C_p, at different positions of the length of the train. A comparison of C_p values from our LES with the experimental data of Chiu [3] is shown in Fig. 15. Keeping in mind that the experimental data are for the long-nose case, the surface pressure distribution on the long-nose train does not change a great deal along the length of the train except in the small region close to the nose ($x/D < 1.5$). Figure 15 shows that the LES profile changes very little after $x/D \approx 3.5$, in agreement with the experimental data.

The effect of the separation on the roof-side face of the short-nose train is shown as a lower pressure over the face along the length of the train, as shown in Fig. 15. Figure 15 shows that the pressure prediction in our LES is higher than the experimental one on the underbody. Both the short- and long-nose models show this discrepancy. This discrepancy might be due to a difference in the groundboard boundary layer thickness between the LES and the experiments, since no information is available about the experimental boundary layer. In our LES, we have a no-slip boundary condition on the channel floor. This allows the boundary layer to grow, and it approaches the train with a thickness equal to the clearance down the train. In the experimental work, they used a groundboard in the region around the train and the rest of the floor has the open wind tunnel boundary condition. There is no information about the extension of this groundboard.

5.3 Instantaneous Flow. The force coefficients, C_s and C_l, are saved at each time step and their time histories are used to calculate the frequencies of the flow around the train. Instantaneous data covering 260 time steps ($t' = 1.2$) were saved and used

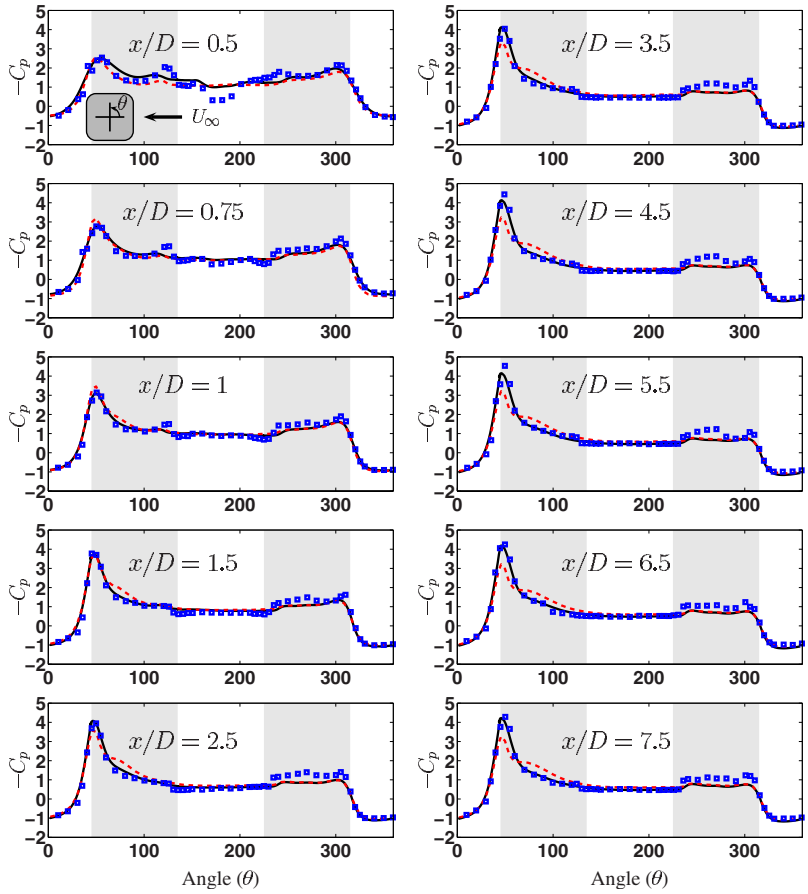

Fig. 15 Comparison of the surface pressure distributions along the train length: (solid line) long-nose LES; (dashed) short-nose LES; (symbols) experiment from Chiu [3]

to study the temporal development of the coherent structures around the body. Below we present the result of this study.

5.3.1 Temporal Evolution of Coherent Structures. The isosurface of the instantaneous second invariant of the velocity gradient, $Q=-1/2\partial u_i/\partial x_j \partial u_j/\partial x_i$, and the isosurface of the instantaneous pressure are used to study the temporal evolution of the coherent structures around the body. The isosurface of the instantaneous second invariant of the velocity gradient technique as it is describe by Jeong and Hussain [21] is the best technique to track the vortices in the instantaneous flow. Figures 16(*a*)–16(*c*) show the isosurface of the instantaneous pressure at three different time steps with a time difference between equal to $t'=0.12$. The value for the gauge pressure used is $p=-0.19$ Pa. On the other side, Figs. 16(a')–c' show the isosurface of the instantaneous second invariant of the velocity gradient at the same three times ($Q=7000$). The structures shown in Fig. 16 are from the long-nose train flow. Similar structures are found around the short-nose train. These structures are not shown here to avoid duplication.

Elongated coherent structures that are extended in the spanwise direction are formed at the windward edge on the roof-side face, as shown in Fig. 16. Many vortices are born in that region and convected downstream. The small convected vortices merge with each other to form slightly larger vortices. Figures 16(*a*) and 16(a') show three different vortices, λ_1, λ_2, and λ_3, at time $t'=0$. After time $t'=0.12$, vortices λ_2 and λ_3 are convected downstream and their middle part is lifted from the surface, as shown in Figs. 16(*b*) and 16(b'). Their legs are still attached to the surface to form hairpinlike vortices. At the same time, vortex λ_1 is destroyed and only a small portion of it continues downstream. After time $t'=0.24$, the three vortices are destroyed and convected downstream while other vortices are formed at the windward edge, as shown in Figs. 16(*c*) and 16(c'). This process of formation, attachment, and detachment of the vortices leaves a disturbance in the surface pressure. This process, in addition to the deformation of the shear layers in the periphery of the circulation regions due to Kelvin–Helmholtz instability, is responsible for the high frequency mode in the aerodynamic forces. Although the time-averaged flow shows a small separation region on the roof-side face of the long-nose train simulation, this separation might be large in a certain time in the instantaneous flow. The pressure fluctuation caused by this process contributes to the time variation in values of the aerodynamic forces around the train.

5.3.2 Aerodynamic Forces. The time histories of the side and lift force coefficients obtained from the long-nose train are shown in Figs. 17(*a*) and 17(*b*). Figures 18(*a*) and 18(*b*) show the same data obtained from the short-nose model. The time-averaged values of these coefficients are given in Table 2. For the long-nose model, the peak value for the side force coefficient is 0.67 while the minimum value is 0.6. The maximum and minimum values of the lift force coefficient are 0.88 and 0.75, respectively. Different extreme values are obtained for the short-nose model: 0.7 and 0.59 for the maximum and minimum cross-force coefficients and 0.9 and 0.73 for the maximum and minimum lift-force coefficients. Although the two models have similar time-averaged aerodynamic coefficients, as reported in Table 2, the short-nose model gives a slightly higher time-varying amplitude for these coefficients. The rms values of C_s and C_l are given in Table 2.

Special attention was paid to the time histories of these coeffi-

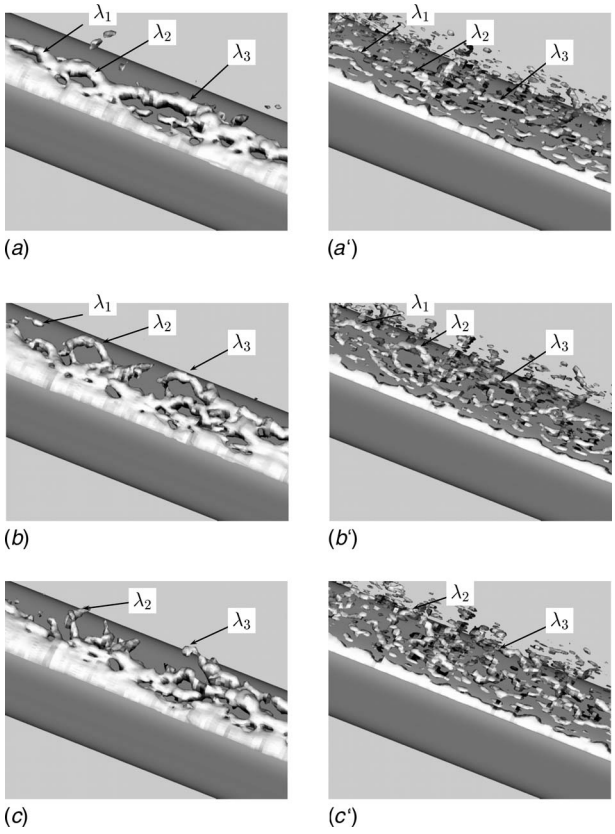

Fig. 16 Long-nose model flow: temporal evolution of the coherent structures in the region between $x/D=3$ and $x/D=6$. (*a*), (*b*), and (*c*) show the isosurface of the instantaneous static pressure, $p=-0.19$ Pa, at three different times. (*a'*), (*b'*), and (*c'*) show the isosurface of the instantaneous second invariant of the velocity gradient $Q=7000$. The time difference between two successive pictures is $t'=0.12$.

cients. Fourier transform is used to resolve their dominating frequencies representing the cross-wind induced force frequencies. Figures 19(*a*) and 19(*b*) show the autopower spectra of the time-varying signals of C_s and C_l, obtained from the long-nose model, respectively. The autopower spectra are drawn against Strouhal number $\mathrm{St}=fD/U_\infty$, where f is the time-varying frequency of C_s and C_l. Figures 20(*a*) and 20(*b*) show the corresponding spectra for the short-nose model. Three dominating peaks are found in the Fourier transform of C_s in Fig. 19(*a*) at St=0.07, 0.2, and 0.3. Some high frequencies in the range of St=0.4–0.9 can also be seen in this figure. The C_l signal produces three low frequencies in the spectrum, corresponding to St=0.1, 0.24, and 0.3, and no high frequency peaks. Four dominating peaks representing the shedding frequencies are seen in Fig. 20(*a*) at St=0.02, 0.08, 0.13, and 0.18. A number of high frequency peaks is found in the range of St=0.2–0.8 in Fig. 20(*a*). For the lift force coefficient, five peaks are found in the range of St=0.02–0.2 and many high frequencies are found in the range of St=0.2–0.8. The lift force high frequencies come from the separation on the roof-side face, while the side force ones correspond to the shear layer instabilities that exist in the wake. It should be mentioned here that the reliability of the low frequencies is weak since the total averaging time is not sufficient to properly resolve them. The total averaging time, $t^*=80$, corresponds to about 2 cycles for St=0.02 while it corresponds to 6 cycles for St=0.07.

6 Conclusion

Although the flows around trains are highly unsteady, the available knowledge about such flows is mainly that concerning the resulting time-averaged flow. The cross-wind stability of high-speed trains is particularly influenced by the transient effect of the flow. Large-eddy simulation is used in the present work to establish both the instantaneous and time-averaged pictures of the flow around the simplified high-speed train under the influence of cross wind. Two different models are used in order to investigate the influence of the shape of the nose of the train on the flow structures. The main objective of this study was comparison of the influence of two different fronts of the train on the surrounding flow. Our LES using the long-nose train (equivalent to the experimental model) provided results in agreement with the experimental data. From the LES results, the general features of the flow on the short-nose model show the following:

1. The three-dimensional effect of the nose on the streamwise, roof-side faces, and underbody streamline patterns is confined to the region very close to the nose. On the other side, its effect on the leeward flow pattern is extended to a region of $x/D \approx 4$ from the nose.

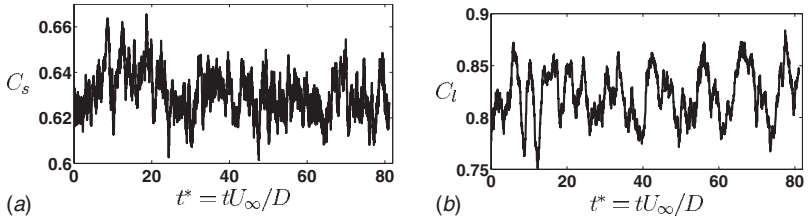

Fig. 17 Long-nose model flow: time history of the force coefficients; (*a*) Side force coefficient; (*b*) lift force coefficient.

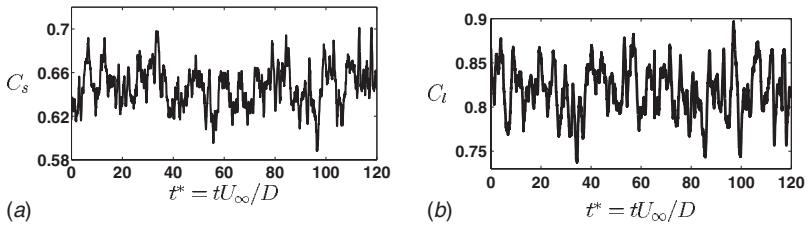

Fig. 18 Short-nose model flow: time history of the force coefficients. (*a*) Side force coefficient; (*b*) lift force coefficient.

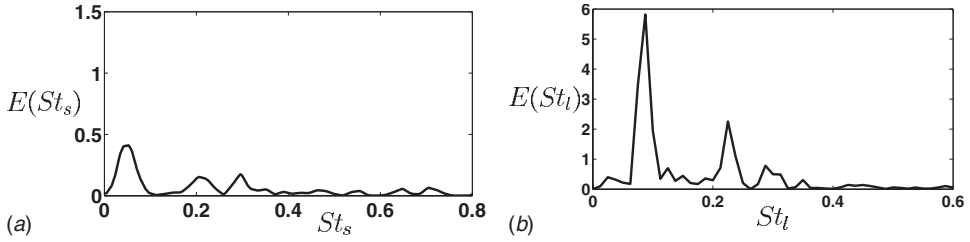

Fig. 19 Long-nose model flow: autopower spectra $E(\mathrm{St}) = F(\mathrm{St})\bar{F}(\mathrm{St})$ of the time-varying force coefficients, where $F(\mathrm{St})$ is the Fourier transform of the time-varying signal and $\bar{F}(\mathrm{St})$ is the complex conjugate of $F(\mathrm{St})$. (*a*) and (*b*) are the autopower spectra of C_s and C_l, respectively, drawn against Strouhal number $\mathrm{St} = fD/U_\infty$, where f is the force's time-varying frequency.

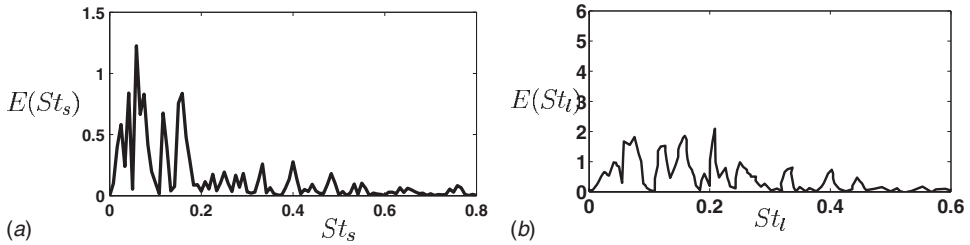

Fig. 20 Short-nose model flow: autopower spectra of the time-varying force coefficients.

2. A separation bubble appeared at the windward corner on the roof-side face at the simulated Reynolds number (3×10^5). To correctly simulate the flow around a real train, either the Reynolds number should be increased or a trip wire should be used in the windward corner.
3. Axial flow is obtained on the leeward side close to the train nose owing to the existence of a small vortex in the wake close to the nose.
4. Two large bubbles are obtained in the wake. They are elongated in the direction of the length of the train. The position of their cores is $1D$ downstream from the model. Their size is constant after $x/D \approx 3.5$ with a height $\approx 0.5D$ and a width $\approx 2D$.
5. The time-dependent flow is used to show very small structures close to the wall. The evolution of the coherent structures is explained and the effect of this evolution on the surface forces is also revealed.
6. The time history of the force coefficients is used to find the dominating frequencies of the flow around the train. Four dominating peaks are found in the Fourier transform of the cross-force coefficient, C_s, at Strouhal numbers $\mathrm{St} = 0.02$, 0.08, 0.13, and 0.18. On the other side, a large number of peaks is found in the Fourier transform of the lift force coefficient, C_l, in the range of $0.01 < \mathrm{St} < 0.4$.
7. High-frequency modes are obtained in both the side and the lift forces. These high frequencies are a result of the separations on the roof-side face and the Kelvin–Helmholtz instability on the shear layers.

LES of the flow over the long-nose model shows similar flow structures as are observed in the short-nose model except in a region on the leeward side close to the nose and on the roof-side face. The small vortex that appears over the short-nose train in the leeward flow close to the nose disappeared here and, as a consequence, the flow was axial from the nose tip toward the train body. As a result, the flow on the roof-side face remained attached along most of the surface. The time-averaged surface pressure distributions agree well with the experiments. Small discrepancies appear in the underbody. These discrepancies might be due to the difference in boundary layer thickness between the LES flow and the experimental flow field. The more attached flow on the roof-side face suppressed the high frequencies in the lift force, while high frequencies still existed in the side force due to the shear layers instabilities. In general, the shape of the nose of the train proved to have a great effect on both the time-averaged and instantaneous flows. The effect of the three-dimensional nose flow on the surface flow patterns extended to about $x/D \approx 3.5$ and $x/D \approx 4.5$ in the case of the long-nose and short-nose models, respectively, but there is a global effect on the flow. The knowledge gained in this work will hopefully help engineers to better understand the flow around similar bodies at higher Reynolds number and prevent the unwanted influences of side winds.

Acknowledgment

This work was supported by the Swedish Agency for Innovation System (VINNOVA), Bombardier Transportation, and Scania. Computer time at SNIC (Swedish National Infrastructure for Computing) resources (High Performance Computing Center North, HPC2N, National Supercomputer Center in Sweden, NSC, and Center for Scientific Computing at Chalmers, C3SE) is gratefully acknowledged.

References

[1] Baker, C. J., 2003, "Some Complex Applications of the Wind Loading Chain," J. Wind. Eng. Ind. Aerodyn., **91**, pp. 1791–1811.
[2] Baker, C. J., Jones, J., Lopez-Calleja, F., and Munday, J., 2004, "Measurements of the Cross Wind Forces on Trains," J. Wind. Eng. Ind. Aerodyn., **92**, pp. 547–563.
[3] Chiu, T. W., 1995, "Prediction of the Aerodynamic Loads on a Railway Train in a Cross-Wind at Large Yaw Angles Using an Integrated Two- and Three-Dimensional Source/Vortex Panel Method," J. Wind. Eng. Ind. Aerodyn., **57**, pp. 19–39.
[4] Chiu, T. W., and Squire, L. C., 1992, "An Experimental Study of the Flow Over a Train in a Crosswind at Large Yaw Angles up to 90°," J. Wind. Eng. Ind. Aerodyn., **45**, pp. 47–74.
[5] Copley, J. M., 1987, "The Three-Dimensional Flow Around Railway Trains," J. Wind. Eng. Ind. Aerodyn., **26**, pp. 21–52.
[6] Suzuki, M., Tanemoto, K., and Maeda, T., 2003, "Aerodynamic Characteristics of Train/Vehicles Under Cross Winds," J. Wind. Eng. Ind. Aerodyn., **91**, pp. 209–218.
[7] Hoppmann, U., Koenig, S., Tielkes, T., and Matschke, G., 2002, "A Short-Term Strong Wind Prediction Model for Railway Application: Design and Verification," J. Wind. Eng. Ind. Aerodyn., **90**, pp. 1127–1134.

[8] Diedrichs, B., 2003, "On Computational Fluid Dynamics Modelling of Cross-wind Effects for High-Speed Rolling Stock," IMechE Conf. Trans., **217**(F), pp. 203–226.
[9] Durst, F., Khier, W., and Breuer, M., 2000, "Flow Structure Around Trains Under Side Wind Conditions: A Numerical Study," Comput. Fluids, **29**, pp. 179–195.
[10] Hemida, H., Krajnović, S., and Davidson, L., 2005, "Large-Eddy Simulations of the Flow Around a Simplified High Speed Train Under the Influence of a Cross-Wind," AIAA Paper No. AIAA-2005-5354.
[11] Krajnović, S., and Davidson, L., 2004, "Large Eddy Simulation of the Flow Around an Ahmed Body," in *2004 ASME Heat Transfer/Fluids Engineering Summer Conference*, Charlotte, NC.
[12] Singh, S., and Mittal, S., 2005, "Flow Past a Cylinder: Shear Layer Instability and Drag Crisis," Int. J. Numer. Methods Fluids, **47**, pp. 75–98.
[13] Kravchenko, G., and Moin, P., 2000, "Numerical Studies of Flow Over a Circular Cylinder at Re=3900," Phys. Fluids, **12**(2), pp. 403–417.
[14] Mittal, R., and Moin, P., 1997, "Stability of Upwind-Biased Finite Difference Schemes for Large-Eddy Simulation of Turbulent Flows," AIAA J., **35**(8), pp. 1415–1417.
[15] Constantinuescu, G. S., and Squires, K. D., 2003, "LES and DES Investigations of Turbulent Flow Over a Sphere at Re=10,000," Flow, Turbul. Combust., **70**, pp. 267–298.
[16] Krajnović, S., and Davidson, L., 2005, "Flow Around a Simplified Car, Part 1: Large-Eddy Simulation," ASME J. Fluids Eng., **127**, pp. 907–918.
[17] Krajnović, S., and Davidson, L., 2005, "Flow Around a Simplified Car, Part 2: Understanding the Flow," ASME J. Fluids Eng., **127**, pp. 919–928.
[18] Krajnović, S., and Davidson, L., 2003, "Numerical Study of the Flow Around the Bus-Shaped Body," ASME J. Fluids Eng., **125**, pp. 500–509.
[19] Nilsson, H., and Davidson, L., 1992, "CALC-PVM: A Parallel Multiblock SIMPLE Multiblock Solver for Turbulent Flow in Complex Domains," Department of Thermo and Fluid Dynamics, Chalmers University of Technology, Technical Report.
[20] Sujudi, D., and Haimes, R., 1995, "Identification of Swirling Flow in 3D Vector Fields," AIAA Paper No. AIAA 95-1715.
[21] Jeong, J., and Hussain, F., 1995, "On the Identification of a Vortex," J. Fluid Mech., **285**, pp. 69–94.

Noise Prediction of a Centrifugal Fan: Numerical Results and Experimental Validation

Rafael Ballesteros-Tajadura
e-mail: rballest@uniovi.es

Sandra Velarde-Suárez
e-mail: sandrav@uniovi.es

Juan Pablo Hurtado-Cruz
e-mail: jhurtado@usach.cl

Área de Mecánica de Fluidos,
Universidad de Oviedo,
Campus de Gijón,
33271 Gijón, Spain

*Centrifugal fans are widely used in several applications, and in some cases, the noise generated by these machines has become a serious problem. The centrifugal fan noise is frequently dominated by tones at the blade passing frequency as a consequence of the strong interaction between the flow discharged from the impeller and the volute tongue. In this study, a previously published aeroacoustic prediction methodology (Cho, Y., and Moon, Y.J., 2003, "Discrete Noise Prediction of Variable Pitch Cross-Flow Fans by Unsteady Navier-Stokes Computations," ASME J. Fluids Eng., **125**, pp. 543–550) has been extended to three-dimensional turbulent flow in order to predict the noise generated by a centrifugal fan. A three-dimensional numerical simulation of the complete unsteady flow on the whole impeller-volute configuration has been carried out using the computational fluid dynamics code FLUENT®. The unsteady forces applied by the fan blades to the fluid are obtained from the data provided by the simulation. The Ffowcs Williams and Hawkings model extension of Lighthill's analogy has been used to predict the aerodynamic noise generated by the centrifugal fan from these unsteady forces. Also, the noise generated by the fan has been measured experimentally, and the experimental results have been compared to the numerical results in order to validate the aerodynamic noise prediction methodology. Reasonable agreement has been found between the numerical and the experimental results.* [DOI: 10.1115/1.2953229]

Keywords: centrifugal fan, noise prediction, aeroacoustic

Introduction

Centrifugal fans are widely used because they achieve high pressure ratios in a short axial distance compared to axial fans. However, the noise generated by these machines can become a serious problem. The aerodynamic noise of the fan can be divided into a discrete tonal noise, induced by the periodic interactions between the rotating blades and the volute tongue, and a broadband noise, mainly due to the turbulent fluctuations. In particular, the blade passing frequency (BPF) tonal noise is known as the most annoying component to the human ear. Neise [1] made a complete review of the fan noise generation mechanisms and the methods of control.

The capability of the existing computers allows the numerical simulation of complex flow features that commonly take place in centrifugal fans: unsteady flow, important three-dimensional effects, and on complex geometries. Presently, some commercial codes exist that have shown their validity and reliability for the description and prediction of the unsteady flow into turbomachinery. Also, the development of powerful computers and more efficient codes has brought the application of the acoustic analogy to predict the noise of turbomachinery not involved in aeronautical applications, as the fans used in air-conditioning, home appliance machines, or industrial ventilation. For the past years, an increasing number of works has applied the acoustic analogy to such fans. Jeon et al. [2] calculate the aeroacoustic pressure generated by a centrifugal fan in a vacuum cleaner by the Ffowcs Williams and Hawkings formulation [3]. Jeon et al. [4] obtain acoustic far-field information from the unsteady force fluctuations on the blade by the Lowson's equation; in this way, the effects of some design parameters on the noise of a centrifugal fan are investigated. Choo and Moon [5] and Moon et al. [6] predict the noise generated by cross flow fans using Ffowcs Williams and Hawkings formulation and Curle's equation, respectively. Ffowcs Williams and Hawkings formulation is also used by Maaloum et al. [7] to predict the tonal noise generated by an axial flow fan used in an automotive air cooling system.

In this study, an aeroacoustic predictive capability has been implemented and tested. First, the unsteady flow solutions of the fan were worked out with a commercial software package, FLUENT®. Second, the sound pressure in the far field around the fan is predicted by the Ffowcs Williams–Hawkings formulation [3], based on unsteady pressure data obtained at the surfaces of the rotating blades and the volute tongue. Finally, experimental measurements of the sound pressure level around the fan are shown and compared to the numerical results provided by the prediction method.

Description of the Fan

The studied machine is a simple aspirating centrifugal fan driven by an ac 9.2 kW motor rotating at 1500 rpm. The shrouded impeller tested has ten backward-curved blades with an outlet diameter of 400 mm. The blades are made of flat sheet metal. The minimum distance between the impeller and the volute tongue is 12.5% of the outlet impeller diameter. The widths of the impeller and volute are, respectively, 130 mm and 248 mm. Figure 1 shows two pictures of the tested fan and Table 1 summarizes the main dimensions of its impeller. The tests for the aerodynamic and acoustic characterization of the fan have been made in a normalized ducted installation (Type B according to ISO 5136 [8]). Figure 2 shows a sketch of this installation. More details about the installation and measurement procedures have been reported in previous works [9,10].

Contributed by the Fluids Engineering Division of ASME for publication in the JOURNAL OF FLUIDS ENGINEERING. Manuscript received March 23, 2007; final manuscript received April 17, 2008; published online August 12, 2008. Assoc. Editor: Chunill Hah. Paper presented at the 2006 ASME Fluids Engineering Division Summer Meeting and Exhibition (FEDSM2006), Miami, FL, July 17–20, 2006.

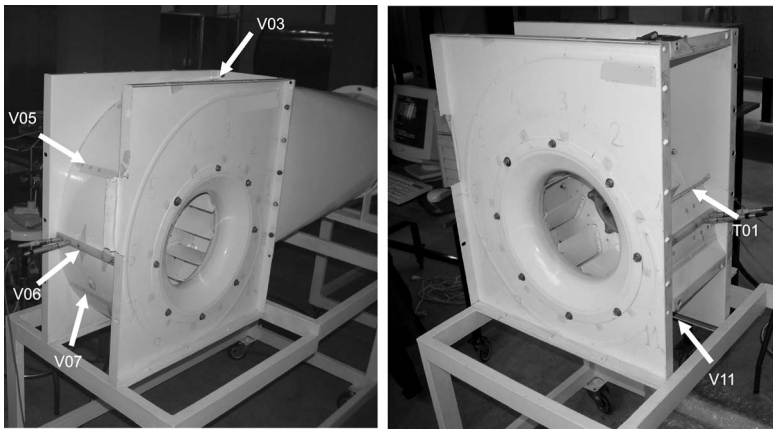

Fig. 1 Tested fan with the location of some measurement points

Numerical Methodology

Unsteady Viscous Flow Computation. A full three-dimensional simulation of the unsteady flow in the centrifugal fan described above was carried out. The calculations have been performed with a commercial software package, FLUENT®. This code uses the finite volume method and the Navier–Stokes equations are solved on an unstructured grid. The unsteady flow is solved applying a sliding mesh technique, which has been successfully applied to turbomachinery flows [11,12].

The basic equations describing the flow in FLUENT® are the conservation of mass and the conservation of momentum. In the general form, the conservation of mass in direction x_i, $i=1,2,3$ ($x_1=x$, $x_2=y$ and $x_3=z$) at time t, is given by

$$\frac{\partial \rho}{\partial t} + \frac{\partial}{\partial x_i}(\rho u_i) = 0 \tag{1}$$

where ρ is the density and u_i is the velocity in direction i. The conservation of momentum is described by

$$\frac{\partial}{\partial t}(\rho u_i) + \frac{\partial}{\partial x_i}(\rho u_i u_j) = -\frac{\partial p}{\partial x_i} + \frac{\partial \tau_{ij}}{\partial x_j} \tag{2}$$

in which p denotes the pressure and τ_{ij} is the stress tensor.

Turbulence is simulated with the standard k-ε model. The standard k-ε model is an eddy-viscosity model consisting of two equations for the turbulent kinetic energy k and its dissipation rate ε. The k-ε model was introduced by Launder and Spalding [13]. The high Reynolds number version is obtained by neglecting all the terms containing the kinematic viscosity. In the proximity of solid walls, viscous effects become important and this assumption no longer holds. Several modifications have been proposed: In the two-layer formulation [14], a simpler model is used close to the wall (usually a one-equation model) and then the eddy viscosity is patched at a certain distance from the wall; FLUENT® offers this option. More precisely, the additional transport equations in direction x_i at time t that are solved for k and ε are given by

$$\frac{\partial}{\partial t}(\rho k) + \frac{\partial}{\partial x_i}(\rho u_i k) = \frac{\partial}{\partial x_i}\left[\left(\frac{\mu_t}{\sigma_k}\frac{\partial k}{\partial x_i}\right)\right] + G_k - \rho\varepsilon \tag{3}$$

$$\frac{\partial}{\partial t}(\rho \varepsilon) + \frac{\partial}{\partial x_i}(\rho u_i \varepsilon) = \frac{\partial}{\partial x_i}\left[\left(\frac{\mu_t}{\sigma_\varepsilon}\frac{\partial \varepsilon}{\partial x_i}\right)\right] + C_{1\varepsilon}\frac{\varepsilon}{k}G_k - C_{2\varepsilon}\rho\frac{\varepsilon^2}{k} \tag{4}$$

Here, ρ and u_i denote the density and the velocity in direction i, respectively. Furthermore, the turbulent viscosity is given by

$$\mu_t = C_\mu \rho \frac{k^2}{\varepsilon} \tag{5}$$

and

$$G_k = \mu_t\left(\frac{\partial u_j}{\partial x_i} + \frac{\partial u_i}{\partial x_j}\right)\frac{\partial u_j}{\partial x_i} \tag{6}$$

represents the rate of production of the turbulent kinetic energy. In these equations, the coefficients $C_{1\varepsilon}$, $C_{2\varepsilon}$, C_μ, σ_k, and σ_ε are parameters of the standard k-ε model, which have the following empirically derived values: $C_{1\varepsilon}=1.44$, $C_{2\varepsilon}=1.92$, $C_\mu=0.09$, $\sigma_k=1.0$, and $\sigma_\varepsilon=1.3$.

The time-dependent term of all the equations is discretized with a second order, implicit scheme. Second order, upwind discretization has been used for convection terms and central difference schemes for diffusion terms.

The momentum equations and the continuity equation are solved sequentially. Once the components of velocity have been

Table 1 Impeller dimensions

Outlet diameter (mm)	400
Inlet diameter (mm)	280
Outlet width (mm)	130
Impeller-tongue distance (mm)	50
Impeller-tongue distance (% of outlet diameter)	12.5%

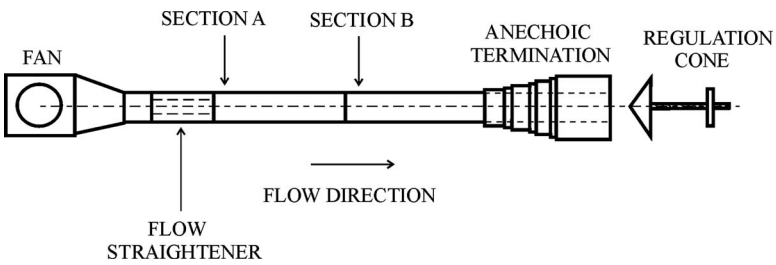

Fig. 2 Sketch of the test installation

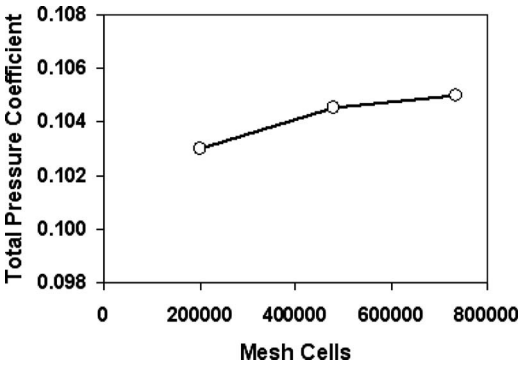

Fig. 3 Influence of mesh size on the fan total pressure coefficient

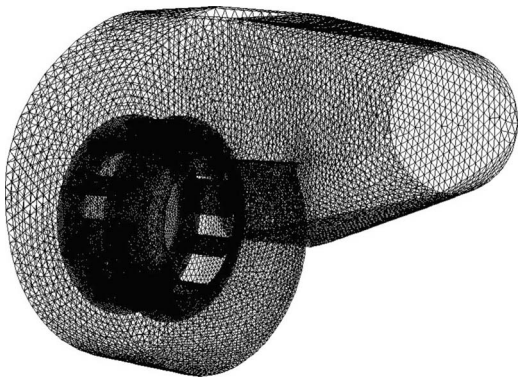

Fig. 4 Sketch of the fan unstructured mesh

calculated for each mesh cell the velocities may not satisfy the continuity equation and then a "Poisson-type" equation for a so-called "pressure correction" is derived from the continuity equation and the linearized momentum equations. This pressure correction equation is then solved to obtain the necessary corrections to the pressure and velocity fields such that continuity is satisfied.

The set of simultaneous algebraic equations is solved by a semi-implicit iterative scheme, which starts from an arbitrary initial solution and converges to the correct solution after several iterations. The SIMPLEC algorithm was used in the present work. A comprehensive description of this algorithm is given by Patankar [15].

First, a steady-state simulation has been performed. Its results are used as an initial value for the unsteady simulation. In this way, the computation time of the unsteady simulation is reduced. During the unsteady simulation, both unsteady and averaged flow quantities are stored. The simulation ends when the obtained solution becomes periodic. The errors in the solution related to the mesh must disappear for an increasingly finer mesh. The total pressure coefficient at the flow rate where the fan exhibits its best efficiency point was used to determine the influence of the mesh size on the solution. The convergence criterion was a maximum residual of 10^{-6}. Figure 3 shows the evolution of the fan total pressure coefficient with the mesh cells. According to this figure, the grids with the highest number of mesh cells were considered to be reliable enough to assure mesh independence.

Unstructured tetrahedral cells are used to define the open inlet zone, the impeller, and the volute (with a total of 733,400 cells). The mesh is refined near the volute tongue and in the impeller domain. The small axial gap (9 mm) between the impeller and the volute rear casing was not modeled. However, the radial gap between the impeller front shroud (5 mm) and the casing was taken into account in the model. Figure 4 shows a general view of the

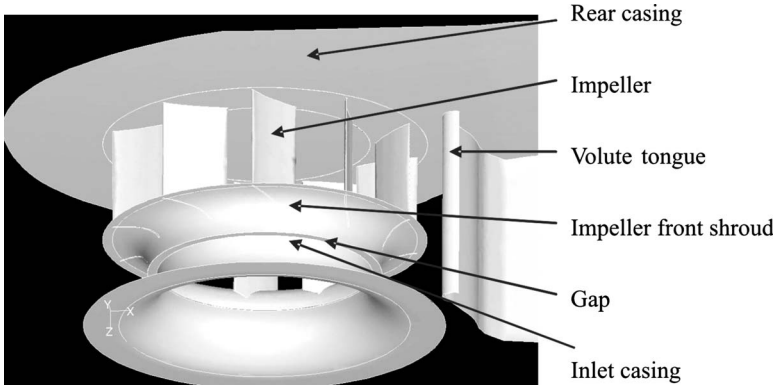

Fig. 5 General view of the geometry of the fan

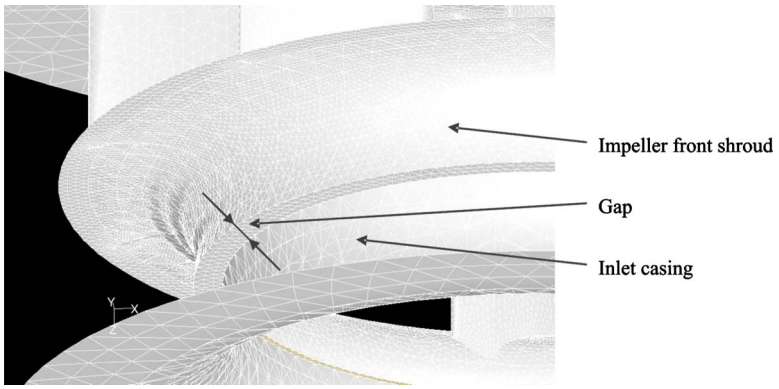

Fig. 6 Mesh details around the radial gap between the impeller front shroud and the casing

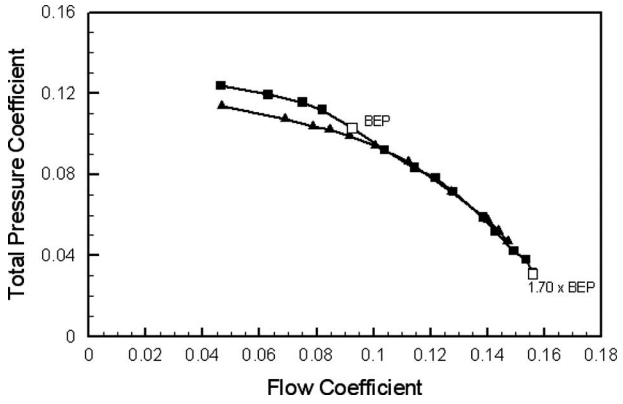

Fig. 7 Fan performance dimensionless curves: experimental (black squares) and numerical (black triangles), with the operating points selected in this study (white squares)

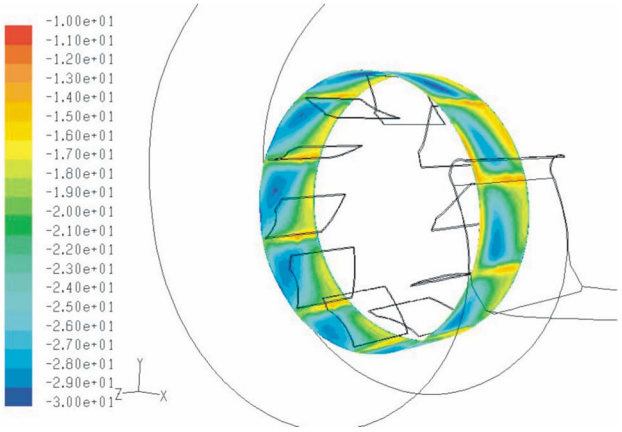

Fig. 8 Contours of the relative tangential component of velocity at the impeller outlet (negative values are clockwise)

unstructured mesh; some details of the geometric features of the model are shown in Fig. 5 and the mesh used in the modeled gap is shown in Fig. 6. The minimum cell volume is 2.21×10^{-11} m^3 and the maximum cell volume is 6.47×10^{-5} m^3.

The modeled boundary conditions are those considered with more physical meaning for turbomachinery flow simulations, that is, total pressure at the domain inlet and a pressure drop proportional to the kinetic energy at the domain outlet. The flow rate is changed by modifying the constant for that pressure drop at the outlet condition, which simulates the closure of a valve.

The walls of the model are stationary with respect to their respective frame of reference, and the nonslip condition is applied.

The code was run in a cluster of 8 Pentium 4 (2.4 GHz) nodes. The time step used in the unsteady calculation has been set to 1.34×10^{-4} s seconds in order to get enough time resolution for the dynamic analysis. The impeller grid movement is related to this time step and the rotational speed imposed ($\omega=157$ rad s^{-1}), so a complete revolution is performed each in 300 steps (i.e., one blade passage each in 30 time steps).

The number of iterations has been adjusted to reduce the residual below an acceptable value in each time step. In particular, the ratio between the sum of the residuals and the sum of the fluxes for a given variable in all the cells is reduced to the value of 10^{-5} (five orders of magnitude). Initializing the unsteady calculation with the steady solution, over 17 impeller revolutions (approximately 5000 time steps) are necessary to achieve the convergence to the periodic unsteady solution.

Flow Field Results. The method described above has been employed to make a comparison for both the numerical and experimental performance curves for the tested fan. The numerical data are obtained after averaging the values of the unsteady calculation. In Fig. 7, the numerical and experimental performance curves for the tested fan are compared. The best efficiency point (BEP) corresponds to a flow rate $Q=0.92$ m^3/s ($\varphi=0.093$), with a total pressure rise $P_T=500$ Pa ($\psi=0.105$).

The experimental and 3D-numerical simulated curves agree for flow rates equal and higher than the BEP. At partial load, the matching between 3D-numerical and experimental results is not so high, probably due to the presence of flow separation in the blade channels, which has not been correctly captured by the numerical procedure.

The three-dimensional effects of the flow are illustrated in Figs. 8 and 9. These figures show the 3D-numerical results of the relative tangential component and of the radial component of velocity over a cylindrical surface around the impeller outlet, with the fan operating at the BEP. Both components of velocity exhibit important gradients in the axial direction. In the tangential component, where the negative values are clockwise, the maximum absolute values correspond to zones into the blade channels located near the impeller shroud whereas the minimum ones appear in the blade wakes and close to the back impeller plate. The case of the radial component is different: Zones with very low values (even negatives, with a recirculation pattern) are present near the impeller shroud, whereas the maximum values are concentrated near the hub. This feature indicates that the main fraction of the flow rate passes through the rear middle part of the impeller.

The numerical model described above has been employed to calculate the time-dependent pressure both in the impeller and in the volute. In this way, the pressure fluctuations in some locations over the volute wall have been obtained. The measurement positions shown in Fig. 10 and detailed in Table 2 have been selected in order to make comparisons between the numerical and experimental results. The z-coordinate has been normalized by the volute width B (248 mm). The impeller shroud corresponds to $z/B=0.54$, while $z/B=0$ is the volute rear casing and $z/B=1$ is the volute front casing. Figures 11 and 12 show the evolution of pressure fluctuations with time obtained both by 3D-numerical model and experimentally, for two different flow rates: the BEP and $1.35\times$BEP. The experimental pressure fluctuations were obtained with B&K 4138 1/8 in. microphones flush mounted on the volute surface. The uncertainty of these two types of microphones has been established by the manufacturer in ±0.2 dB, with a confidence level of 95%. As these microphones are only able to measure pressure fluctuations, only the fluctuating part of the signals is compared.

In Fig. 11, the results obtained at Position P02 (angular position

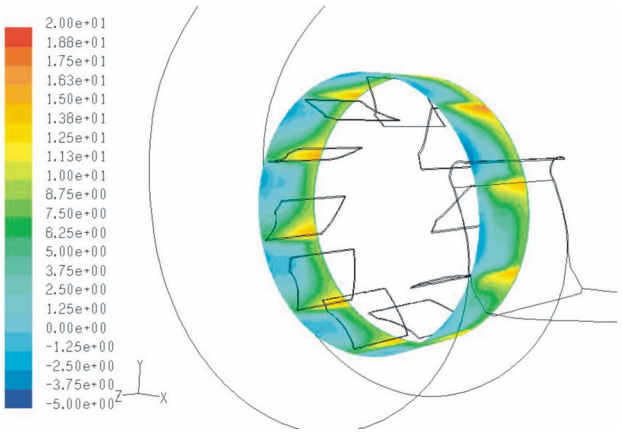

Fig. 9 Contours of the radial component of velocity at the impeller outlet

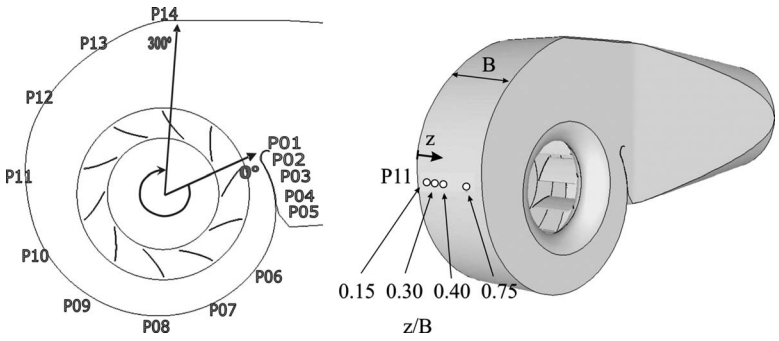

Fig. 10 Sketch of the fan with the measurement points

at 2 deg from the tongue, $z/B=0.30$) have been represented. The passing of the ten blades in front of the selected position is clearly observed. The amplitude of the pressure fluctuation increases with the flow rate in this case. The numerical code has reproduced in a reasonable way both the order of magnitude and the temporal pattern of the pressure fluctuations found experimentally.

In Fig. 12, the results obtained at Position P10 (180 deg from the tongue, $z/B=0.30$) have been represented. The amplitude of the pressure fluctuation at this point diminishes strongly with respect to the precedent case, shown in Fig. 11. The passing of the blades is still clearly observed in the numerical results and the amplitude of the pressure fluctuations is similar to the experimental ones. However, the experimental signals show other sources of pressure fluctuation besides the blade passage, which distorts the clear sinusoidal pattern shown at the tongue. The origin of these distortions will be discussed later on.

In Figs. 13–15, the power spectra of pressure fluctuations at Points P02 (2 deg from the tongue), P06 (60 deg from the tongue), and P10 (180 deg from the tongue) have been represented.

The peak corresponding to the BPF exhibits high amplitude in Position P02 near the volute tongue, both in the numerical and the experimental signals (Fig. 13) basically due to the interaction between the flow leaving the impeller and the tongue. The numerical and experimental amplitudes coincide in the axial position $z/B=0.40$, while in the position $z/B=0.15$ they are slightly different. This disagreement was expected because the position $z/B=0.15$ is very close to the impeller hub and it is not easy to simulate precisely the small axial gap between the impeller and the volute rear casing.

In Position P06 (60 deg from the tongue), the situation is quite different (Fig. 14). First of all, the amplitudes corresponding to the BPF have strongly diminished with respect to the previous case (Fig. 13), although they contribute largely in the spectra, both numerically and experimentally. In this position, the interaction between the impeller and the volute tongue does not appear, besides the radial distance from the impeller to the volute is greater than in the previous case. These two reasons explain the great reduction in the amplitude of the pressure fluctuations with respect to the previous case. Also, the experimental and numerical amplitudes at the BPF in $z/B=0.40$ are similar and slightly different in $z/B=0.15$. Second, great peak and broadband amplitudes at low frequencies appear in the experimental spectra. A peak at 25 Hz stands out, corresponding to the impeller rotational frequency. Also, some peaks at 275 Hz, 300 Hz, and 325 Hz appear besides the BPF at 250 Hz with comparable amplitudes, suggesting the existence of mechanical sources of noise. In order to clarify the origin of the peaks observed at 275 Hz, 300 Hz, and 325 Hz in the experimental spectra, some vibration signals at the volute front casing were obtained with a 4384 B&K piezoelectric accelerometer, connected to a 2635 B&K amplifier. The amplitudes at these frequencies did not vary with the flow rate, thus indicating its mechanical origin. Moreover, an impact test demonstrated that the vibration signal at 300 Hz was due to a casing resonance caused by the excitation of a natural frequency.

In Position P10 (180 deg from the tongue), the amplitude of the pressure fluctuations is lower than in the previous positions mentioned (Fig. 15), as a result of the increase in the radial distance between the impeller and the volute wall. The amplitudes at the BPF are quite similar in the experimental and the numerical spectra. On the other hand, in the experimental spectra important broadband levels at low frequencies appear, especially in the axial position $z/B=0.15$.

In Fig. 16, the amplitudes of volute pressure fluctuations at the BPF have been represented, both 3D numerical and experimental with the fan operating at the BEP ($\varphi=0.093$). In this case (and for other flow rates tested [12]), the maximum values appear concentrated in a small zone very close to the volute tongue, as it was expected. These pressure fluctuations are generated by the interaction between the unsteady flow leaving the impeller and the fixed volute tongue. In the rest of the volute, noticeable amplitudes are also present due to the jet-wake pattern associated with the continuous blade rotation around the volute.

The 3D-numerical model can reproduce in a reasonable way the trend and the order of magnitude of the pressure fluctuations obtained experimentally. The agreement between experimental and numerical results is especially good in the axial position $z/B=0.40$. As the small axial gap between the impeller and the volute rear casing was not modeled, the 3D-numerical and experimental

Table 2 Angular coordinates of the measurement points over the volute

Tongue points	Angular position (deg)	Volute points	Angular position (deg)	Volute points	Angular position (deg)
P01	0	P06	60	P11	210
P02	2	P07	90	P12	240
P03	9	P08	120	P13	270
P04	16	P09	150	P14	300
P05	23	P10	180		

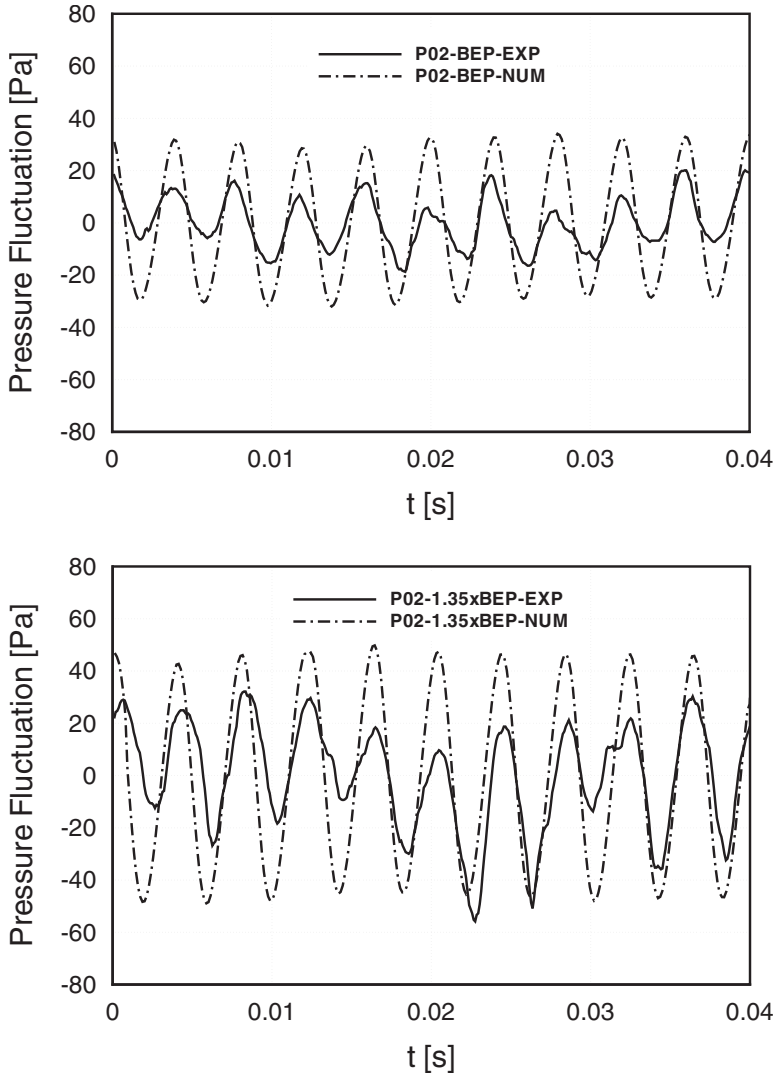

Fig. 11 Evolution of volute pressure fluctuations with time at Point P02 (at the tongue, $z/B=0.30$)

results corresponding to low values of z/B are slightly different, especially near the volute tongue. Some other differences are probably due to the presence of flow separation in the blade channels at partial load, which has not been correctly captured by the numerical procedure.

Another source of discrepancies between the 3D-numerical and the experimental pressure fluctuations can be taken into account: the feasibility that the microphones placed on the volute wall measure noise from distant zones of the flow, i.e., pressure fluctuations of the "acoustic type," which cannot be calculated in the three-dimensional simulation. The computation of pressure fluctuations of the acoustic type by CFD codes, which solve the unsteady compressible Navier–Stokes equations, exceeds by far the current computational capabilities. In any case, the authors acknowledge that these errors in the volute pressure fluctuations could result in errors in the computed far-field noise.

Regardless the exposed constraints, which would be possibly overcome with a greater computational capability, the presented results permit to conclude that the 3D-numerical methodology developed is a useful tool for the unsteady simulation of the three-dimensional flow in a centrifugal fan. The application of this method to other alternative geometries would permit to establish design criteria for the improvement of the aerodynamic performance of these machines. On the other hand, the results obtained in the unsteady flow numerical simulation constitute the basis for a second step in which the sound field will be computed by a numerical solution of an appropriate system of acoustic equations based on the acoustic analogy of Lighthill.

Aeroacoustic Noise Prediction. The sound pressure generated from the impeller blades and the volute tongue is predicted by the Ffowcs Williams–Hawkings equation [3]. The integration surfaces of the Ffowcs Williams–Hawkings calculation are the ten impeller blades and the volute tongue. It is well known that the sound pressure p', i.e., the solution of the inhomogeneous wave equation following Ffowcs–Williams–Hawkings approach, comes for the contribution of three types of sources: the monopole noise related to the blade moving volume (i.e., blade thickness), the dipole noises related to the forces (pressures) exerted on the surface of the blades, and the quadrupole noise associated with flow turbulences. In this work, the later contribution is neglected because the flow Mach number of the fan is low. The present numerical study does not account for the influence of the casing on the noise, and as a result the predicted far-field noise could differ from the experimentally measured noise.

Also, the noise sources are assumed compact, since the compact noise source conditions suggested by Farassat [16] are satisfied. The maximum length of the noise source corresponding to a

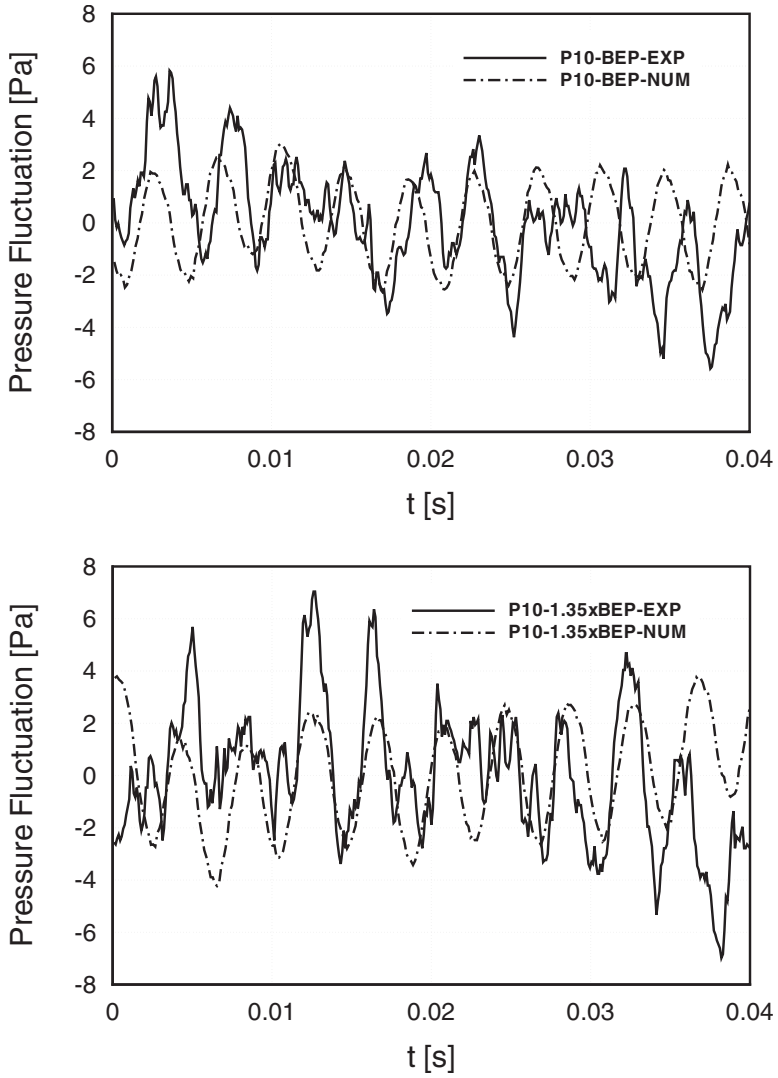

Fig. 12 Evolution of volute pressure fluctuations with time at Point P10 (180 deg from the tongue, $z/B=0.30$)

grid section along the blades and tongue is much smaller than the minimum distance between the noise source and the observer considered and the time step that takes for a sound wave to cross that maximum length is also much smaller than the period of the BPF.

Using the compact noise source formula given by Cho and Moon [5] and the geometric parameters shown in Fig. 17, contributions of n noise sources are added as the following:

$$p'(\mathbf{x},t)=\sum_{i=1}^{n}\left[p'_{\mathrm{th},i}(\mathbf{x},t)+p'_{\mathrm{fn},i}(\mathbf{x},t)+p'_{\mathrm{ff},i}(\mathbf{x},t)\right] \tag{7}$$

where $\mathbf{x}$ is a position vector to the observer and t is the observer time. As it was stated before, the first term represents the monopole noise related to the displacement of fluid due to the motion of the blades. If the rotation speed is low or the blade geometry is thin, monopole sources are expected to be a negligible contribution. The second and third terms are the near-field and far-field dipole noises related to the time varying forces acting on the fluid.

Following Ref. [15], each term is written as

$$p'_{\mathrm{th},i}(\mathbf{x},t)=\frac{\rho_0 V_0}{4\pi}\left[\frac{1}{1-M_r}\frac{\partial}{\partial\tau}\left(\frac{1}{1-M_r}\frac{\partial}{\partial\tau}\left(\frac{1}{r_i|1-M_r|}\right)\right)\right]_{\tau} \tag{8a}$$

$$p'_{\mathrm{fn},i}(\mathbf{x},t)=\frac{1}{4\pi}\left[\frac{1}{r_i^2}\frac{1}{(1-M_r)^2}\left(\mathbf{r}_i\cdot\mathbf{f}_i\frac{1-\mathbf{M}_i\cdot\mathbf{M}_i}{1-M_r}-\mathbf{f}_i\cdot\mathbf{M}_i\right)\right]_{\tau} \tag{8b}$$

$$p'_{\mathrm{fn},i}(\mathbf{x},t)=\frac{1}{4\pi}\left[\frac{1}{r_i}\frac{1}{(1-M_r)^2}\left(\frac{\mathbf{r}_i}{c_0}\cdot\frac{\partial\mathbf{f}_i}{\partial\tau}+\frac{\mathbf{r}_i\cdot\mathbf{f}_i}{1-M_r}\left(\frac{\mathbf{r}_i}{c_0}\cdot\frac{\partial\mathbf{M}_i}{\partial\tau}\right)\right)\right]_{\tau} \tag{8c}$$

The terms in the square brackets of Eqs. (8*a*)–(8*c*) are evaluated at a retarded time τ, which is related to the observer time, t, by means of the expression

$$\tau=t-\frac{r_i(\tau)}{c_0} \tag{9}$$

In Eqs. (8*a*)–(8*c*), ρ_0 is the density of the undisturbed medium, c_0 is the speed of sound, V_0 is the blade volume, $\mathbf{r}_i=(\mathbf{x}-\mathbf{y}_i)/r_i$ is a unit vector from the noise source i to the observer, and $\mathbf{f}_i$ is the force vector acting onto the fluid. The local source Mach number vector and the relative Mach number are also defined as

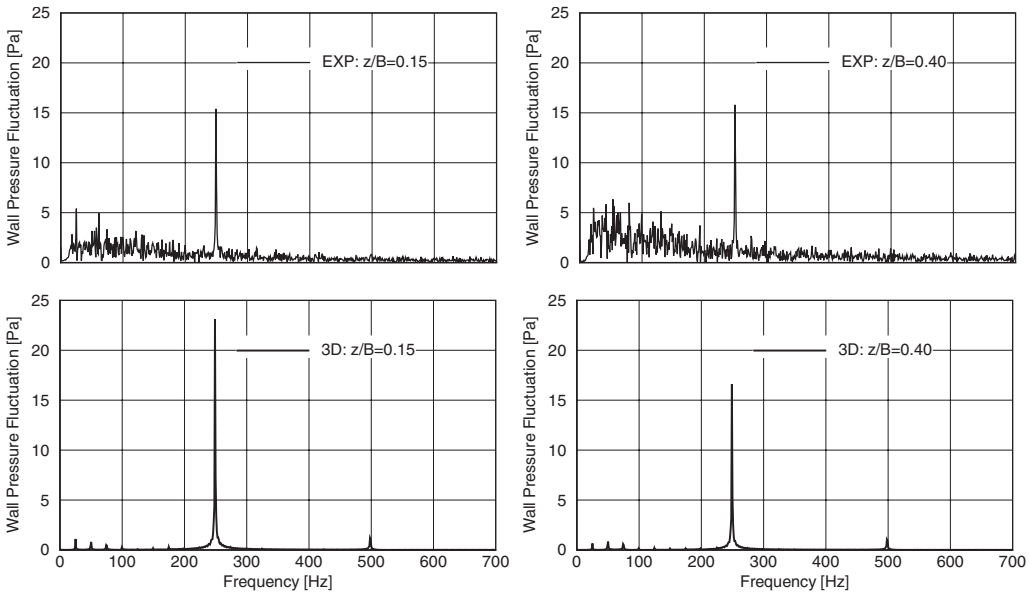

Fig. 13 Power spectra of volute pressure fluctuations in pascals (experimental, upper side; 3D-numerical simulation, bottom side) at the measurement Point P02 (at 2 deg from the tongue, $z/B=0.15$ and $z/B=0.40$), with the fan operating at the BEP

$$\mathbf{M}_i = \frac{1}{c_0}\frac{\partial \mathbf{y}_i}{\partial \tau}, \quad M_r = \mathbf{r}_i \cdot \mathbf{M}_i \tag{10}$$

where $\mathbf{y}_i$ is a position vector to the noise source i.

Aeroacoustic Results. The acoustic pressure $p'(\mathbf{x},t)$ is calculated at the observer time (t) using the described aeroacoustic noise prediction procedure. The sound pressure level (SPL) spectrum is obtained by a fast-Fourier transform (FFT) algorithm. Figure 18 shows a picture of the studied fan and the Cartesian coordinates used. The origin of this coordinate system is placed on the rotation axis at the impeller hub. During the measurements of the SPL around the fan, the exit duct was not used. Thus, a calibrated plate was used to obtain the desired flow rate. These measurements were made for the following flow rates: $1.70\times$BEP and $Q_{\max}$; the latter is the flow rate obtained when neither plate nor duct is connected at the fan exit. Obviously, this flow rate was not reachable when the fan was connected to the normalized test installation.

In order to have a more comprehensive outlook of the results, the algorithm was applied to observer points placed in the following planes: $(x,y,0)$, $(0,y,z)$, and $(x,0,z)$. For instance, in Fig. 19 the total SPL is represented over those planes for the flow rate corresponding to $1.70\times$BEP. In this figure, it can be seen that the directivity pattern of the acoustic source is similar to the dipole source. The figure also shows that the data are symmetric in the

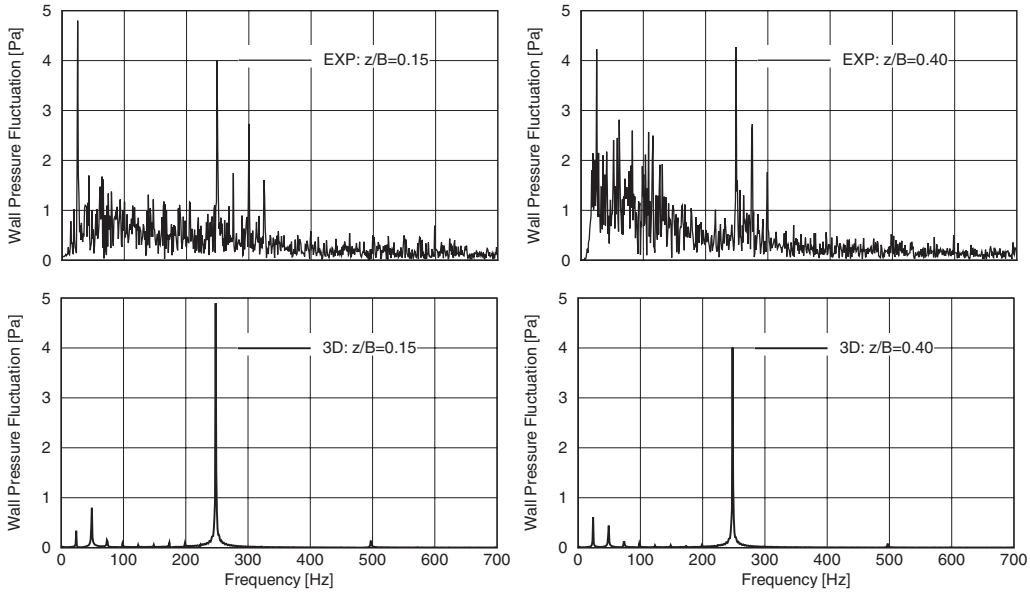

Fig. 14 Power spectra of volute pressure fluctuations in pascals (experimental, upper side; 3D-numerical simulation, bottom side) at the measurement Point P06 (at 60 deg from the tongue, $z/B=0.15$ and $z/B=0.40$), with the fan operating at the BEP

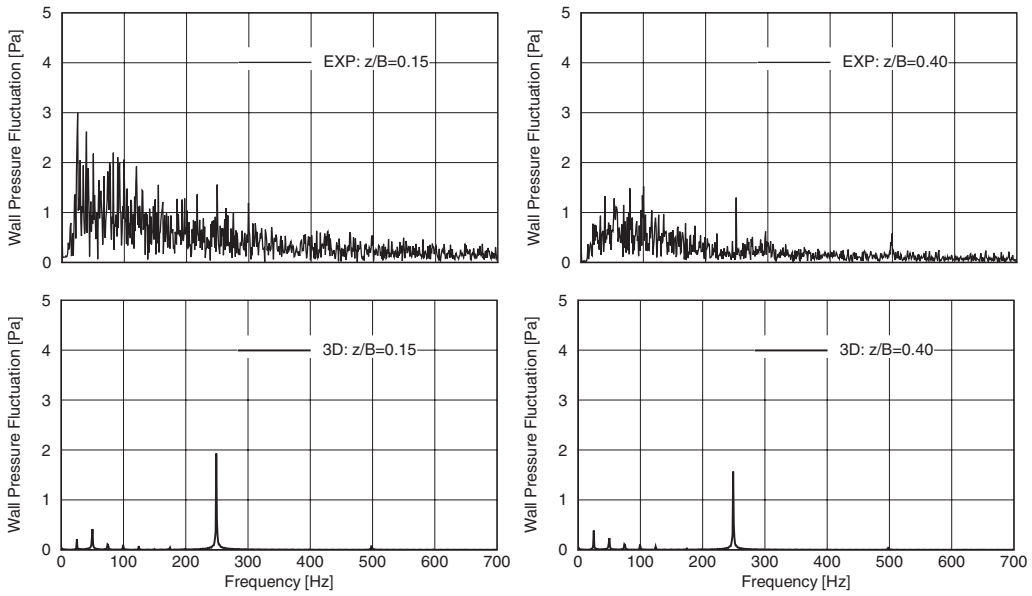

Fig. 15 Power spectra of volute pressure fluctuations in pascals (experimental, upper side; 3D-numerical simulation, bottom side) at the measurement Point P10 (at 180 deg from the tongue, z/B =0.15 and z/B=0.40), with the fan operating at the BEP

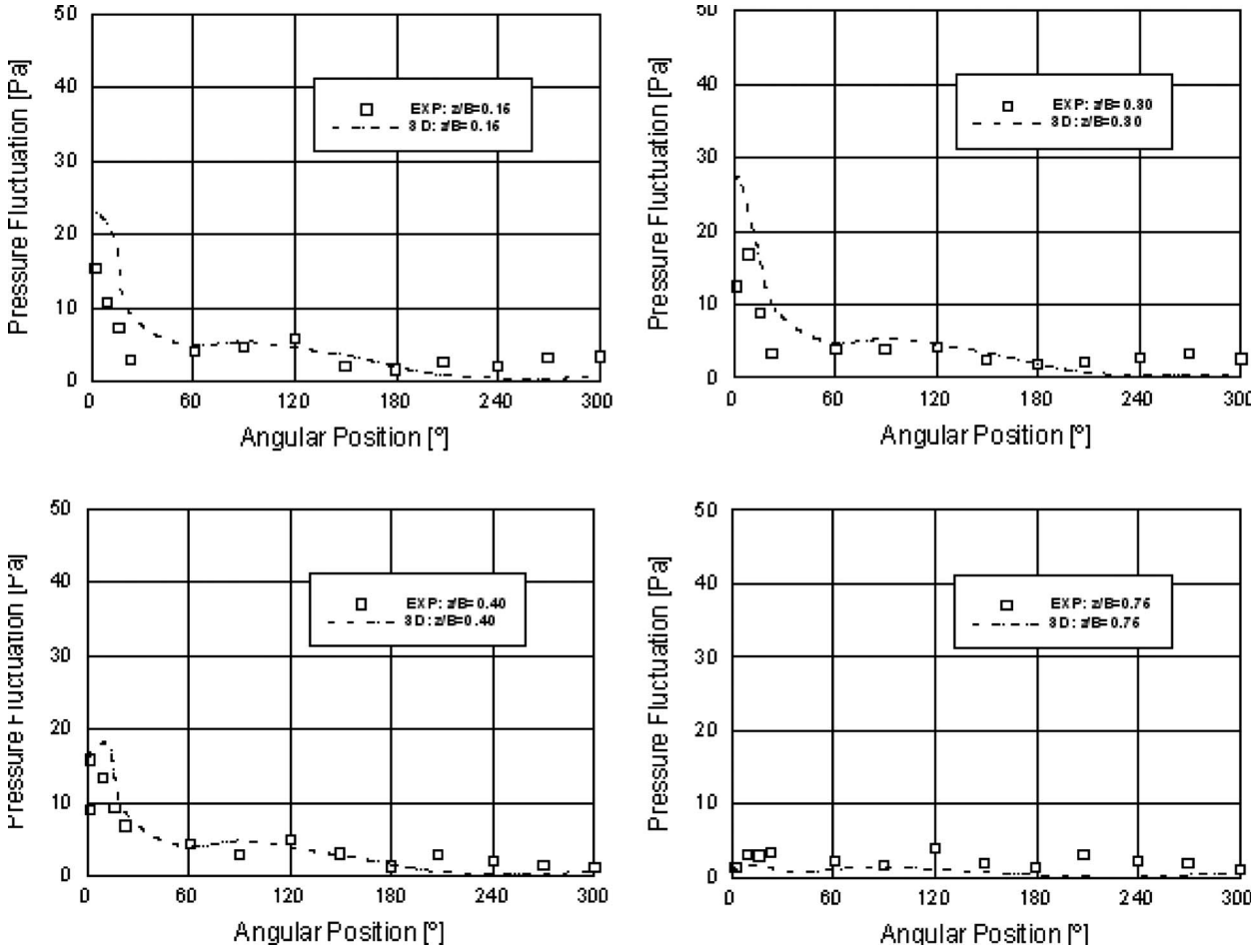

Fig. 16 Amplitude (pascals) of volute pressure fluctuation at the blade passing frequency, 3D-numerical (white squares) and experimental (dotted line), with the fan operating at the BEP

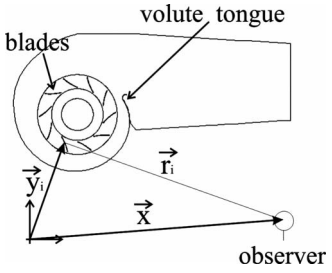

Fig. 17 Geometric parameters used in the Ffowcs Williams–Hawkings equation

$(0,y,z)$ and $(x,0,z)$ planes, but it is not in the $(x,y,0)$ plane, due to the fact that the geometry of the centrifugal fan is not symmetric in the latter plane.

Also, the acoustic field radiated by the centrifugal fan has been measured over the mentioned planes. In order to eliminate the influence of the reflections of the laboratory walls, the fan was placed outside the building. Only the reflection on the pavement floor influenced the experimental measurements, but the background noise was still very high (around 50 dB) and it masked the floor influence for positions further than 2 m from the fan. The acoustic pressure measurements have been made using a B&K 4189 1/2 in. microphone. The uncertainty of the microphone was established by the manufacturer in ± 0.2 dB, with a confidence level of 95%. The signal from the microphone was introduced into a real time frequency analyzer B&K 2133, with a 1/24 octave band resolution, in order to obtain the power spectra of the pressure signals.

Figure 20 shows the comparison between the predicted (*a*) and the measured (*b*) SPL (decibels) at the BPF around the fan in the plane $(x,0,z)$ for the flow rate corresponding to $1.70\times$BEP. Comparison is only made at the BPF because an experimental study on the determination of the noise sources in the same fan [17] showed that the component was predominant in the noise generation of the fan.

The dipolar behavior can be appreciated in the experimental results, particularly in the vicinity of the fan. Given the approximations made, the agreement between the predicted and the measured SPL distributions in the vicinity of the fan is reasonable. In the experimental results, a higher sound pressure level is obtained in further positions of the fan due to the pavement reflection and to the noise background level that is not present in the numerical results. These features also mask the dipolar behavior in the experimental results. The discrepancies in symmetry, peak amplitude, and decay with distance could be related to the overprediction of volute pressure fluctuations and to the neglect of the casing influence in the aeroacoustic computations.

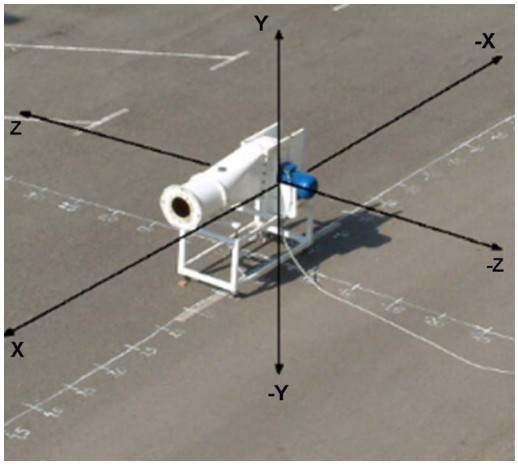

Fig. 18 Picture of the fan during the acoustic measurements

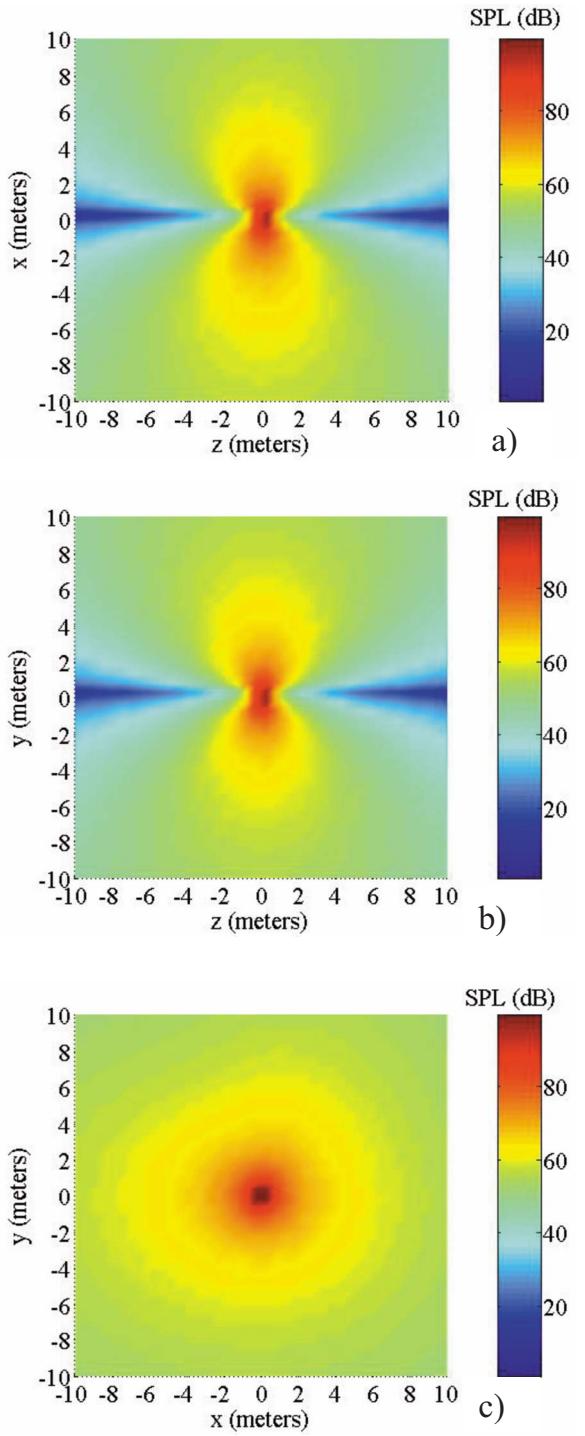

Fig. 19 Predicted SPL (decibels) around the fan: (*a*) plane $(x,0,z)$, (*b*) plane $(x,y,0)$, and (*c*) plane $(0,y,z)$; flow rate: BEP

Also, Fig. 21 shows the measured SPL (decibels) around the fan in the plane $(x,0,z)$ for the flow rate corresponding to Q_{max}. The dipolar behavior can also be appreciated for this flow rate, particularly in the vicinity of the fan. The comparison of Figs. 20(*b*) and 21 shows that the strength of the dipole increases when the flow rate increases.

Figure 22 shows the comparison between the predicted and the measured SPL (decibels) along an *x*-constant line on the plane

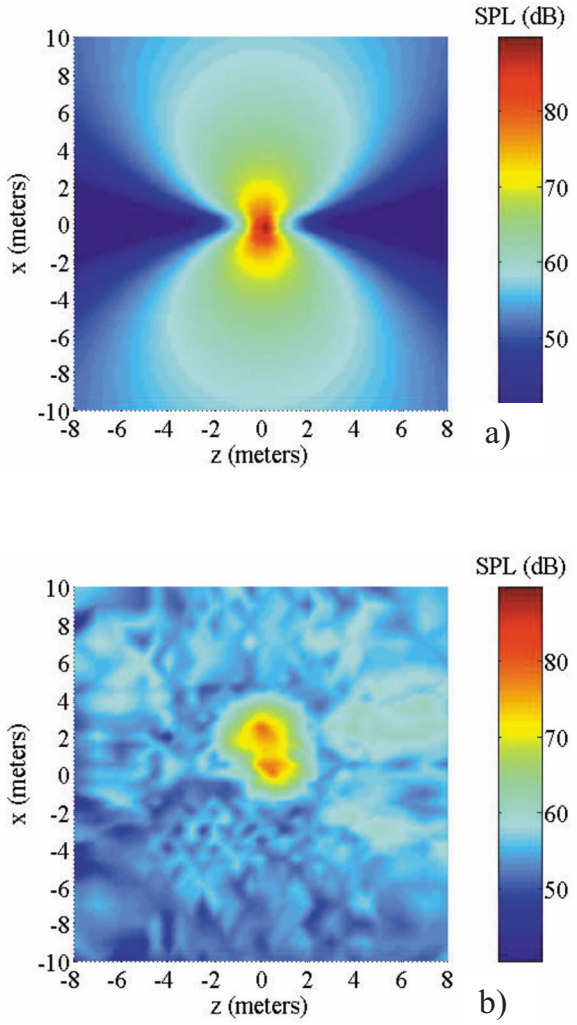

Fig. 20 SPL (decibels) at the blade passing frequency around the fan; plane $(x,0,z)$; flow rate: 1.70×BEP: (*a*) predicted and (*b*) measured

$(x,0,z)$ for the flow rate corresponding to 1.70×BEP. In both lines the results agree in the vicinity of the fan. In further positions from the fan, the effects of the motor casing and the floor reflection, and the background noise significantly affect the experimental results.

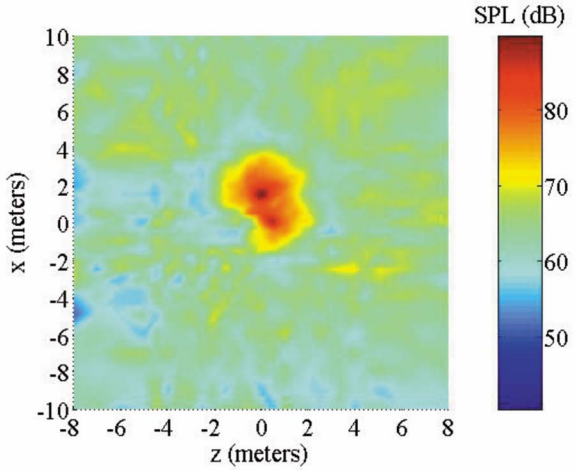

Fig. 21 Measured SPL (decibels) at the blade passing frequency around the fan; plane $(x,0,z)$; flow rate: Q_{max}

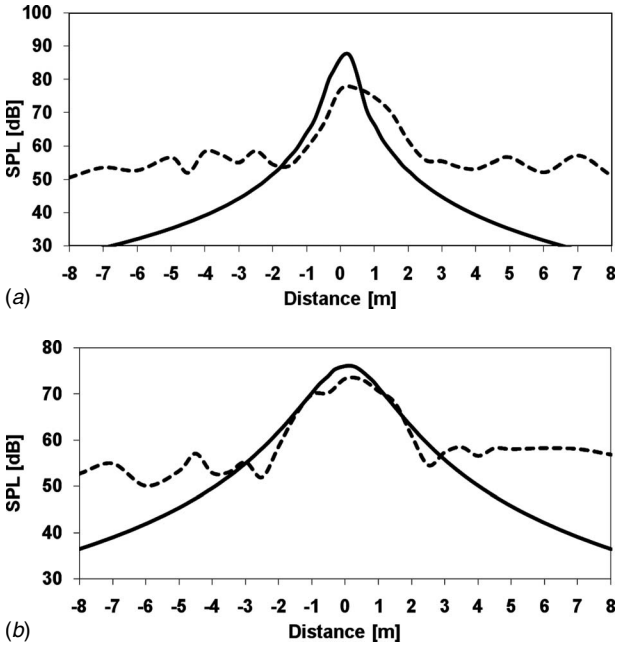

Fig. 22 Predicted (full line) and measured (dotted line) SPLs (decibels) along a line on the plane $(x,0,z)$: (*a*) x=0.5 m and (*b*) x=1.5 m; flow rate: 1.70×BEP

Conclusions

In this study, a previously published aeroacoustic prediction methodology [5] has been extended to three-dimensional turbulent flow in order to predict the noise generated by a centrifugal fan using the Ffowcs Williams and Hawkings model extension of Lighthill's analogy. The forces exerted by the fan blades on the air obtained from an unsteady viscous flow computation are used as input data for the calculation of the acoustic pressure around the fan.

Both the predicted and the measured SPL at the BPF around the fan show a dipolar behavior. The experimental results were influenced by the pavement reflection and the noise background level, which are not present in the numerical results. These features also mask the dipolar behavior in the experimental results. It has also been observed that the strength of the dipole increases when the flow rate increases. Given the approximations made, the agreement between the predicted and the measured SPL distributions in the vicinity of the fan is reasonable.

This methodology could be applied in the design stage in order to optimize the aeroacoustic behavior of centrifugal fans.

Acknowledgment

This work was supported by the Research Projects TRA2007-62708, TRA2004-04269, and DPI2001-2598 (Ministerio de Educación y Ciencia, España).

Nomenclature

B = volute width
$C_{1\varepsilon}, C_{2\varepsilon}, C_{\mu}$ = parameters of the standard k-ε model
D = diameter
c_0 = speed of sound
f = frequency
$\mathbf{f}_i$ = force vector acting onto the fluid

G_k = rate of production of the turbulent kinetic energy, Eq. (6)
k = turbulent kinetic energy
M = Mach number
$\mathbf{M}_i$ = local source Mach number vector
M_r = relative Mach number
p = static pressure
p_0 = reference acoustic pressure (20 μPa)
p' = acoustic pressure
P_T = total pressure
Q = flow rate
$\mathbf{r}_i$ = unit vector from the noise source i to the observer
r_i = modulus of $\mathbf{r}$
SPL = sound pressure level, $\mathrm{SPL}=20\log(p'/p_0)$ (dB, reference 20 μPa)
t = observer time
u_i = velocity component in direction i
V_0 = blade volume
$\mathbf{x}$ = position vector of the observer
$\mathbf{y}_i$ = position vector of the noise source i
x = Cartesian coordinate
y = Cartesian coordinate
z = Cartesian coordinate
ε = dissipation rate of turbulent kinetic energy
φ = flow coefficient $\phi=Q/\omega D^3$
μ_t = turbulent viscosity, Eq. (5)
ρ = density
ρ_0 = density of the undisturbed medium
$\sigma_k, \sigma_\varepsilon$ = parameters of the standard k-ε model
τ = retarded time
τ_{ij} = stress tensor
ψ = total pressure coefficient $\psi=P_T/\rho\omega^2D^2$
ω = angular velocity

Subscripts/superscripts

max = maximum flow rate
th = thickness
ff = far field
fn = near field

References

[1] Neise, W., 1992, "Review of Fan Noise Generation Mechanisms and Control Methods," *Proceedings of FAN NOISE Symposium*, Senlis, France, CETIAT-CETIM.

[2] Jeon, W., Baek, S., and Kim, C., 2003, "Analysis of the Aeroacoustic Characteristics of the Centrifugal Fan in a Vacuum Cleaner," J. Sound Vib., **268**, pp. 1025–1035.

[3] Ffowcs Williams, J. E., and Hawkings, D. L., 1969, "Sound Generation by Turbulence and Surfaces in Arbitrary Motion," Philos. Trans. R. Soc. London, Ser. A, **264**, pp. 321–342.

[4] Jeon, W., Baek, S., and Kim, C., 2003, "A Numerical Study on the Effects of Design Parameters on the Performance and Noise of a Centrifugal fan," J. Sound Vib., **265**, pp. 221–230.

[5] Cho, Y., and Moon, Y. J., 2003, "Discrete Noise Prediction of Variable Pitch Cross-Flow Fans by Unsteady Navier-Stokes Computations," ASME J. Fluids Eng., **125**, pp. 543–550.

[6] Moon, Y. J., Cho, Y., and Nam, H., 2003, "Computation of Unsteady Viscous Flow and Aeroacoustic Noise of Cross Flow Fans," Comput. Fluids, **32**, pp. 995–1015.

[7] Maaloum, A., Kouidri, S., and Rey, R., 2004, "Aeroacoustic Performance Evaluation of Axial Flow Fans Based on the Unsteady Pressure Field on the Blade Surface," Appl. Acoust., **65**, pp. 367–384.

[8] ISO 5136:2003, "Determination of Sound Power Radiated Into a Duct by Fans and Other Air-Moving Devices. In-Duct Method."

[9] Velarde-Suárez, S., Santolaria-Morros, C., and Ballesteros-Tajadura, R., 1999, "Experimental Study on the Aeroacoustic Behavior of a Forward-Curved Centrifugal Fan," ASME J. Fluids Eng., **121**, pp. 276–281.

[10] Velarde-Suárez, S., Ballesteros-Tajadura, R., Hurtado-Cruz, J. P., and Santolaria-Morros, C., 2006, "Experimental Determination of the Tonal Noise Sources in a Centrifugal Fan," J. Sound Vib., **295**, pp. 781–796.

[11] González, J., Fernández, J., Blanco, E., and Santolaria, C., 2002, "Numerical Simulation of the Dynamic Effects Due to Impeller-Volute Interaction in a Centrifugal Pump," ASME J. Fluids Eng., **121**, pp. 348–355.

[12] Ballesteros-Tajadura, R., Velarde-Suárez, S., Hurtado-Cruz, J. P., and Santolaria-Morros, C., 2006, "Numerical Calculation of Pressure Fluctuations in the Volute of a Centrifugal Fan," ASME J. Fluids Eng., **128**, pp. 359–369.

[13] Launder, B. E., and Spalding, D. B., 1972, *Mathematical Models of Turbulence*, Academic, London.

[14] Rodi, W., 1991, "Experience With Two-Layer Models Combining the k-ε Model With a One-Equation Model Near the Wall," AIAA Paper No. 91-0216.

[15] Patankar, S. V., 1980, *Numerical Heat Transfer and Fluid Flow*, Hemisphere, New York.

[16] Farassat, F., 1981, "Linear Acoustic Formulas for Calculation of Rotating Blade Noise," AIAA J., **19**, pp. 1122–1130.

[17] Velarde-Suárez, S., Ballesteros-Tajadura, R., Santolaria-Morros, C., and Hurtado-Cruz, J. P., 2006, "Experimental Determination of the Tonal Noise Sources in a Centrifugal Fan," J. Sound Vib., **295**, pp. 781–796.

Influence of Curvature and Pressure Gradient on Turbulent Wake Development in Curved Channels

M. T. Schobeiri
Turbomachinery Performance and Flow Research Laboratory,
Texas A&M University,
College Station, TX 77843-3123
e-mail: tschobeiri@mengr.tamu.edu

The development of steady wake flow downstream of a cylindrical rod within a curved channel under the influence of positive, negative, and zero streamwise pressure gradients is theoretically and experimentally investigated. The measured asymmetric wake quantities, such as the mean velocity, turbulent fluctuations in longitudinal and lateral directions, and the turbulent shear stress, are transformed from the probe coordinate system into the curvilinear wake coordinate system. For the transformed nondimensionalized velocity defect and the turbulent quantities, affine profiles are observed throughout the flow regime. Based on the experimental observations and using the transformed equations of motion and continuity, a theoretical framework that generally describes a two-dimensional curvilinear steady wake flow is developed. The theory treats the straight wake flow as a special case for which the curvature radius approaches infinity. A comparison of the developed theory with our own experimental results and with the re-evaluated experimental data from the literature establishes the general validity of the theory. [DOI: 10.1115/1.2953225]

1 Introduction

A wake flow constitutes a special case of free turbulent flows with a broad range of general scientific and engineering applications. In the field of turbomachinery, wake development under the influence of curvature and pressure gradient is a common feature found in several components of a gas turbine engine in steady and periodic unsteady forms. The wake flow associated with inherent unsteadiness induced by mutual interaction between stator and rotor influences the boundary layer transition behavior and heat transfer characteristics of the blades positioned downstream of the wake. Because of its significant impact on turbomachinery efficiency and performance, there have been extensive studies on the impact of wake development on aerodynamics and heat transfer with an abundance of publications. However, few studies have been done on the development of wake itself under turbomachinery flow conditions. This situation motivated us to take up a comprehensive experimental study on wake development under the influence of curvature and pressure gradient. Using the results from the extensive experimental study as the basis, we have developed a theoretical framework that adequately describes two-dimensional curved wakes. A brief outline of the literature relevant to our study follows.

The initial efforts to comprehend wake development have been confined to straight wakes. The hypothesis of dynamic similarity has been the basis of all the earlier developed theories on wake flow. Townsend [1], using a square working section, established a fully developed turbulent wake behind a circular cylinder and investigated the validity of dynamic similarity of mean wake properties. The results, in the range of 500–900 cylinder diameters downstream of the cylinder, fell close to the similarity solution. However, he noticed small, but significant, deviations from the similarity at the extreme edges of the wake. In a comprehensive experimental and theoretical study, Eifler [2] dealt with cylinder wake development in a straight channel for a wide range of downstream locations and for different cylinder diameters varying from 0.5 mm to 10.0 mm, the inlet velocity varying from 20 m/s to 40 m/s with the corresponding Reynolds number between 650 and 27,000. He observed symmetric distributions of the mean velocity defect and Reynolds stresses about the wake center. However, the wake under turbomachinery flow conditions undergoes massive distortion due to the curvature and pressure gradient encountered in blade channels, as shown in the studies by Hill et al. [3], Gartshore [4], Raj and Lakshminarayana [5], Savill [6], and Nakayama [7]. Gartshore [4] investigated the effect of adverse pressure gradients on a straight wake, while the study by Savill [6] dealt with highly deflected curved wakes with no imposed streamwise pressure gradient. Although Savill [6] observed a strong asymmetry due to curvature effects, he concluded that the study of the flow is complex owing to the coexistence of stabilized and destabilized regions across the wake and a strong interaction between them. In a later study, Nakayama [7] investigated the wake flow under the influence of both the curvature and pressure gradient. The small-defect wake was subjected to mild curvature and pressure gradients by deflecting it by an airfoil-like thin plate placed at small angles in the external flow. Despite the governing mild curvature and pressure gradient, the measured wake data exhibited strong asymmetry. Although the published studies so far have helped to understand the wake flow better, they are neither complete enough to be transferable to turbomachinery flow situations nor comprehensive enough to develop a theoretical framework.

The theoretical development to be presented is centered on predicting strictly a two-dimensional curved wake. It does not account for extraneous effects such as secondary flows and flow three dimensionality that might be present in otherwise two-dimensional experimental data. These effects could arise due to the geometry of test sections and from flow conditions. The secondary flow effects become dominant if the test section geometry is such that the breadth and depth are of the same order of magnitude. The theory does not take into account such secondary flow effects. Another relevant aspect is the boundary layer growth under the influence of curvature and pressure gradient that can render the flow three dimensional. Several studies (Merony and Brad-

Contributed by the Fluids Engineering Division of ASME for publication in the JOURNAL OF FLUIDS ENGINEERING. Manuscript received October 31, 2006; final manuscript received March 31, 2008; published online August 11, 2008. Assoc. Editor: Phillip M. Ligrani.

shaw [8], Hoffmann and Bradshaw [9], and Muck et al. [10]) have shown how strongly the streamline curvature in the plane of mean shear produces surprisingly large changes in the structure and development of the turbulent boundary layers. The changes are primarily due to a normal pressure gradient that arises to balance the centrifugal force of the curved stream. This normal pressure gradient greatly affects the stability of the flow, resulting in a significant modification of the turbulent structure. If the sense of flow vorticity aids the flow curvature as in a turbulent boundary layer on a convex surface, the stabilizing effect suppresses the turbulence. However, in a turbulent boundary layer developing on a concave surface (Hoffmann et al. [11]), the convective transport becomes very strong due to the destabilizing effect of pressure gradient that enhances the turbulent mixing. Streamwise vortices of the Taylor–Gortler type may develop to make the mean flow three dimensional and to dominate the turbulent transport.

The theoretical framework, including the flow model, the corresponding governing equations, and the detail of solution procedures, are described in Sec. 2 of this paper. The theory presented in Sec. 2 is a generalized theory that predicts wake development under the influence of curvature and pressure gradient. This is an extension of an earlier theory developed by Schobeiri et al. [12], which could predict wake development under zero streamwise pressure gradient. Section 3 provides the necessary information about the research facility and the corresponding instrumentation, data acquisition, and data reduction. Detailed experimental results and their comparison with the theory are presented in Sec. 4. To demonstrate the general validity of the theory, we have applied it to the straight wake as a classical special case, and some results from the literature are re-evaluated and compared with the theory. Conclusions and a selected reference list follow this section. For a detailed literature review, we refer to NASA Reports by Schobeiri and John [13] and Schobeiri and Pappu [14].

2 Theoretical Concept

This section deals with deriving expressions for required wake characteristics that describe the steady wake development under the influence of pressure gradient and curvature. The required wake characteristics include dimensionless mean velocity defect, mean longitudinal and lateral velocities, and total and partial momenta that lead to an expression for Reynolds shear stress. The first step in the development of theory is to transform the coordinate invariant equations of motion and continuity into curvilinear coordinate systems. For the present theoretical considerations, an incompressible turbulent flow through a two-dimensional curved channel is assumed. Further, it has been assumed that the velocity vector has a temporal and spatial dependency and can be decomposed into a time-independent mean and a time-dependent turbulent fluctuation vector. Based on the experimental observations, the flow regime under investigation can be divided into three distinct zones. Firstly, a highly vortical wake zone is characterized by strongly asymmetric mean velocity components (about the wake centerline), turbulent intensities, and shear stress distributions. Secondly, concerning the wake-external zone where the velocity distribution approximately corresponds to that of a potential flow, although it is rotational, the assumption of a potential flow character is, strictly speaking, not correct. The third zone is the boundary layer at the convex and concave channel walls where the viscosity effect is predominant and the boundary layer approximations can be applied. Based on our own experimental results and in accordance with the investigations by several other researchers (Reichardt [15], Pfeil and Eifler [16], Lakshminarayana and Raj [17], and Nakayama [7]), we further assume that the viscosity effect can practically be neglected for free turbulent flows. Under these assumptions, the conservation equations of fluid mechanics in a coordinate invariant form are treated by transforming from a coordinate invariant form into an orthogonal curvilinear coordinate system (represented by ξ_i) by using tensor analytical tools. The following section deals with the transformation procedure.

Schobeiri et al. [18] further enhanced the theoretical framework described in Ref. [12] to predict the periodic unsteady wake flows by transforming the conservation laws into a rotating frame of reference. To compare the theory with experiments, they generated unsteady wakes downstream of the cylinders of a rotating wake generator positioned at the inlet of a curved channel at zero longitudinal pressure gradient. As in a steady case, the introduction of the velocity defect function and the wake width as a length scale resulted in a fully symmetric distribution of the nondimensionalized velocity defect in a relative frame of reference. The experimental results obtained in an absolute and a relative frame of reference have proven that the wake defect can be described by Gaussian related functions. These functions were implemented in the theory to calculate the total momentum, the partial momentum, and the resulting shear stress. A detailed comparison between the measurement and theory showed that the presented theoretical framework was capable of predicting the zero-pressure gradient wake flow in curved channels within absolute and relative frames of reference.

Following the above investigations, Schobeiri and Chakka [19,20] experimentally investigated the effects of periodic unsteady wake flow and pressure gradient on the boundary layer transition and heat transfer along the concave surface of a constant curvature plate. Analyzing the velocity and the turbulence structure of the impinging wakes and their interaction with the boundary layer, they developed an intermittency based unsteady boundary layer transition model. The analysis revealed a universal pattern for the relative intermittency function for all wake frequencies and pressure gradients investigated. Further detailed investigations of the unsteady boundary layer along a high Reynolds number turbine blade of the space shuttle main engine by Schobeiri et al. [21] and its subsequent analysis [22] verified the universal character of the relative intermittency function.

2.1 Transformation of Conservation Laws. Conservation laws are first presented in a coordinate invariant form that we then transform to the orthogonal curvilinear coordinate system (ξ_i), which is under investigation. In the orthogonal curvilinear coordinate system (ξ_i), ξ_1 is the direction along a streamline near the wake center and ξ_2 is the direction normal to it. Starting with the conservation law of mass, the equation of continuity in a coordinate invariant form is

$$\nabla \cdot \vec{V} = 0 \tag{1}$$

Under the assumption that the viscosity effects can be neglected, the equation of motion in a coordinate invariant form is

$$\vec{V} \cdot \nabla \vec{V} = -\frac{1}{\rho} \nabla p \tag{2}$$

Hereafter, Eq. (2) is referred to as version 1 of the equation of motion. Combining Eqs. (1) and (2) results in a modified appropriate version (referred to as version 2) of the equation of motion as

$$\nabla \cdot (\vec{V}\vec{V}) = -\frac{1}{\rho} \nabla p \tag{3}$$

Version 2 of the equation of motion (Eq. (3)) is particularly useful for comparing the order of magnitude of individual terms and their contributions. For further treatment of conservation laws, the velocity vector is decomposed into a time-averaged mean and a time-dependent fluctuation as

$$\vec{V} = \bar{\vec{V}} + \tilde{\vec{V}} \tag{4}$$

Before decomposing Eq. (3) into its components, we introduce Eq. (4) into Eq. (3) and time average the entire expression as

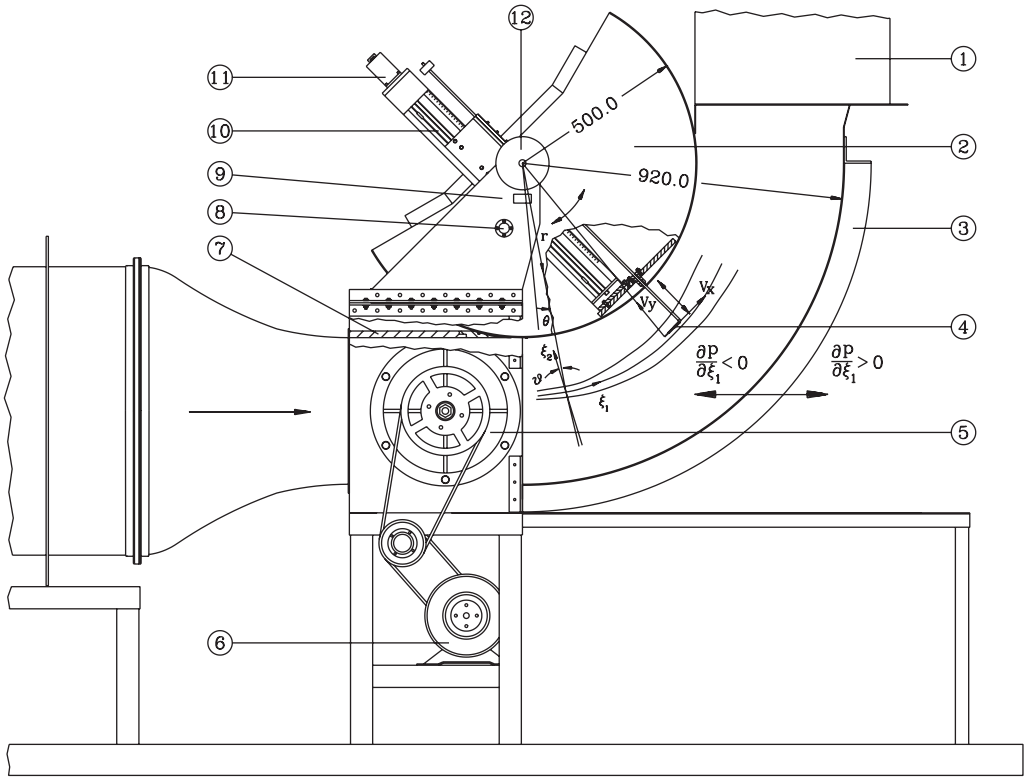

Fig. 1 Curved channel test section: 1, exit duct; 2, convex wall assembly; 3, concave wall; 4, probe; 5, wake generator; 6, motor; 7, top wall; 8, safety pin; 9, rotary vernier; 10, traversing system; 11, stepper motor; 12, locking wheel.

$$\overline{\nabla \cdot (\mathbf{VV})} = \overline{\nabla \cdot [(\bar{\mathbf{V}} + \tilde{\mathbf{V}})(\bar{\mathbf{V}} + \tilde{\mathbf{V}})]} = \nabla \cdot [(\bar{\mathbf{V}}\bar{\mathbf{V}} + \overline{\tilde{\mathbf{V}}\tilde{\mathbf{V}}})] \quad (5)$$

The time-averaged second order tensor $\overline{\mathbf{VV}}$ in Eq. (5) is called the total velocity momentum, the expression $\bar{\mathbf{V}}\bar{\mathbf{V}}$ is termed the partial velocity momentum, and the expression $\overline{\tilde{\mathbf{V}}\tilde{\mathbf{V}}}$ is the Reynolds stress tensor. As seen in Eq. (5), the Reynolds stress tensor is the difference between the total and the partial velocity momenta. In a three-dimensional flow, the above tensors have generally nine components, from which, due to the symmetry, only six are distinct. For the two-dimensional flow assumption of this study, the number of distinct components reduces to 3.

For an analytical treatment, it is appropriate to transform Eqs. (2) and (3) into the wake orthogonal curvilinear coordinate systems ξ_1 and ξ_2 shown in Fig. 1. The metric coefficients and Christoffel symbols of this coordinate system are determined as

$$g_{ij} = \begin{pmatrix} \left(\frac{R+\xi_2}{R}\right)^2 & 0 \\ 0 & 1 \end{pmatrix}, \quad g^{ij} = \begin{pmatrix} \left(\frac{R}{R+\xi_2}\right)^2 & 0 \\ 0 & 1 \end{pmatrix},$$

$$\Gamma^1_{ij} = \begin{pmatrix} 0 & \left(\frac{1}{R+\xi_2}\right) \\ \left(\frac{1}{R+\xi_2}\right) & 0 \end{pmatrix}, \quad \Gamma^2_{ij} = \begin{pmatrix} -\left(\frac{R+\xi_2}{R^2}\right)^2 & 0 \\ 0 & 1 \end{pmatrix} \quad (6)$$

In the above equations, R represents the radius of curvature of the wake centerline at $\xi_2=0$, taken to be positive if convex in the positive ξ_2 direction. Decomposing Eqs. (2) and (3) into the wake curvilinear coordinate system using metric coefficients and Christoffel symbols, the co- and contravariant components are replaced by the physical components. Introducing $\bar{U}$ and $\bar{V}$ for the time-averaged physical velocity components and $\overline{\mathbf{u}}^2$, $\overline{\mathbf{v}}^2$, and $\overline{\mathbf{uv}}$ for the three distinct time-averaged physical components of the Reynolds stress tensor into the transformed versions of Eqs. (1)–(3), the time-averaged version of the continuity equation (Eq. (1)) in the wake curvilinear coordinates is

$$\bar{U}_{,1} + \left[\left(1 + \frac{\xi_2}{R}\right)\bar{V}\right]_{,2} = 0 \quad (7)$$

The subscripts ",1" and ",2" refer to the derivatives in ξ_1 and ξ_2 directions, respectively. Version 1 of the equation of motion (Eq. (2)), when decomposed into the longitudinal direction ξ_1, is

$$\frac{R}{R+\xi_2}\bar{U}\bar{U}_{,1} + \bar{V}\bar{U}_{,2} + \frac{\bar{U}\bar{V}}{R+\xi_2} = -\frac{1}{\rho}\frac{R}{R+\xi_2}\bar{p}_{,1} - \frac{R}{R+\xi_2}(\overline{u^2})_{,1} - (\overline{uv})_{,2} - \frac{2}{R+\xi_2}\overline{uv} \quad (8)$$

and lateral direction ξ_2 is

$$\frac{R}{R+\xi_2}\bar{U}\bar{V}_{,1} + \bar{V}\bar{V}_{,2} - \frac{\bar{U}^2}{R+\xi_2} = -\frac{1}{\rho}\bar{p}_{,2} - \frac{R}{R+\xi_2}(\overline{uv})_{,1} - (\overline{v^2})_{,2} - \frac{\bar{v}^2}{R+\xi_2} + \frac{\bar{u}^2}{R+\xi_2} \quad (9)$$

Similarly, version 2 of the equation of motion (Eq. (3)) decomposed into ξ_1 and ξ_2 components is

$$\frac{R}{R+\xi_2}(\bar{p}/\rho + \bar{U}^2 + \overline{u^2})_{,1} + (\bar{U}\bar{V} + \overline{uv})_{,2} + \frac{2}{R+\xi_2}(\bar{U}\bar{V} + \overline{uv}) = 0 \quad (10)$$

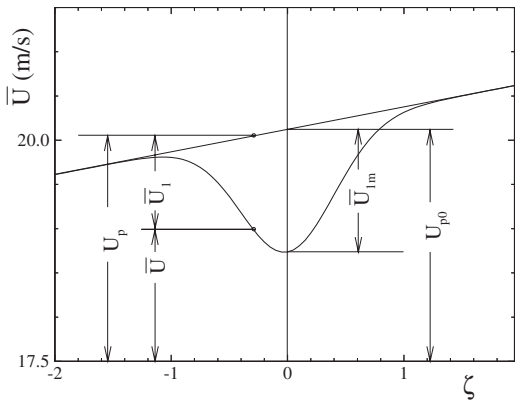

Fig. 2 Schematic velocity distribution, wake defect

$$\frac{R}{R+\xi_2}(\bar{U}\bar{V}+\overline{uv})_{,1}+(\bar{p}/\rho+\bar{V}^2+\bar{v}^2)_{,2}$$
$$-\frac{1}{R+\xi_2}(\bar{U}^2-\bar{V}^2+\bar{u}^2-\bar{v}^2)=0 \tag{11}$$

Equations (10) and (11) are of practical interest for estimating the order of magnitude of each individual term compared with the others. As the experimental results show, the longitudinal fluctuation velocity $|\mathbf{u}|$ is much smaller than the mean velocity $\bar{U}$. The lateral fluctuation velocity $|\mathbf{v}|$, however, has the same order of magnitude as the mean lateral velocity $\bar{V}$, while it is negligible compared with $\bar{U}$. This comparison leads to the conclusion that the contributions of the fluctuation velocity momenta are negligibly small compared to the contribution of the longitudinal mean velocity momentum $\bar{U}^2$. Equations (7) through (11) describe the wake development through a curved channel under the influence of pressure gradients. The next step is to introduce nondimensional parameters aimed at verifying the dynamic similarity assumptions by properly defining the local length and velocity scales.

2.2 Nondimensional Parameters. In order to solve Eqs. (7), (10), and (11) for the required wake characteristics, we assume that from a definite distance ξ_1/d downstream of the wake origin, the velocity and the momentum defect profiles are similar. This distance will have to be experimentally verified, as discussed in the following. The similarity assumption implies that for arbitrary points on the wake center with the longitudinal coordinate ξ_1, a wake width $b=b(\xi_1)$ as a corresponding length scale on the lateral coordinate ξ_2 can be found to generate the dimensionless variable,

$$\zeta=\frac{\xi_2}{b} \tag{12}$$

Furthermore, we define a *wake velocity defect* $\bar{U}_1$ as the difference between the *hypothetical potential* velocity U_p, which would exist without the cylinder and the actual velocity $\bar{U}$, as shown in Fig. 2. Thus, the actual wake velocity can be expressed as

$$\bar{U}=U_p-\bar{U}_1 \tag{13}$$

Correspondingly, we define a *wake momentum defect* $\bar{U}_I^2$, which exhibits the difference between the momentum of the potential velocity U_p^2 and the momentum of the actual velocity $\bar{U}^2$. Thus, the wake velocity momentum can be written as

$$\bar{U}^2=U_p^2-\bar{U}_I^2 \tag{14}$$

In Eq. (13), U_p represents the hypothetical velocity distribution that is an extension of the undisturbed wake-external velocity into the wake. It can be shown by simplifying the equation of motion in the ξ_1 direction (Eq. (8)) for the zero-pressure gradient potential flow case that the velocity U_p can be expressed by a linear variation as

$$U_p=U_{p0}\left(1-\frac{\xi_2}{R}\right) \tag{15}$$

Here, U_{p0} is the hypothetical potential velocity at the wake center, $\xi_2=0$. Thus, the potential velocity U_p outside the wake is a function of ξ_2 only. So and Mellor [23] used the same expression for potential flow velocity while analyzing boundary layer data on curved surfaces. $\bar{U}_1$ and $\bar{U}_I^2$ represent the time-averaged velocity and momentum defects within the wake region.

The similarity assumption stated previously requires the following dimensionless wake velocity, as well as the momentum defect functions,

$$\varphi_1=\frac{\bar{U}_1}{\bar{U}_{1m}},\quad \varphi^2=\frac{\bar{U}_I^2}{\bar{U}_{Im}^2} \tag{16}$$

Here, $\bar{U}_{1m}$ and $\bar{U}_{Im}^2$ represent the maximum wake velocity and momentum defects at the wake center. The above defined dimensionless variables and the linear approximation for U_p will be implemented in Eqs. (7), (10), and (11) to obtain expressions for required wake characteristics.

2.3 Expressions for Wake Characteristics for Nonzero-Pressure Gradients. Introducing the wake velocity defect, Eq. (16) in connection with Eq. (13), into the continuity equation (Eq. (7)) and integrating the resulting equation, we obtain an expression for the mean lateral velocity $\bar{V}$ as

$$\left(1+\frac{\xi_2}{R}\right)\bar{V}=-\int\frac{d}{d\xi_1}\left[U_{p0}\left(1-\frac{\xi_2}{R}\right)-\bar{U}_{1m}\varphi_1\right]bd\zeta+c \tag{17}$$

After a further rearrangement of terms, Eq. (17) leads to

$$\left(1+\frac{\xi_2}{R}\right)\bar{V}=\frac{d(\bar{U}_{1m}b)}{d\xi_1}\int\varphi_1 d\zeta-\frac{db}{d\xi_1}\bar{U}_{1m}\varphi_1\zeta$$
$$-\frac{dU_{p0}}{d\xi_1}b\int\left(1-\frac{\zeta b}{R}\right)d\zeta+c \tag{18}$$

Equation (18) shows that the mean lateral velocity is determined by the turbulent mixing and decay process in the longitudinal direction characterized by the longitudinal changes of the velocity-width product, $\bar{U}_{1m}b$, and by the longitudinal changes of potential velocity at wake center U_{p0}. Note that the longitudinal changes of U_{p0} are closely related to the pressure gradient. Since the lateral velocity component $\bar{V}$ is zero at the wake center, the integration constant c in Eq. (18) must identically vanish. Thus, the general expression for $\bar{V}$ after evaluating the integrals is

$$\left(1+\frac{\xi_2}{R}\right)\bar{V}=\frac{d(\bar{U}_{1m}b)}{d\xi_1}\frac{\sqrt{\pi}}{2}\,\mathrm{erf}(\zeta)-\frac{db}{d\xi_1}\bar{U}_{1m}\varphi_1\zeta$$
$$-\frac{dU_{p0}}{d\xi_1}b\zeta\left(1-\frac{b}{2R}\zeta\right) \tag{19}$$

In the above equation, erf(·) stands for error function, which is the integral of Gaussian distribution. With Eq. (19), the distribution of the mean lateral velocity component can be found provided that the wake velocity defect function φ_1, the distribution of the wake width $b=b(\xi_1)$, as well as the longitudinal distributions of $\bar{U}_{1m}$ and U_{p0} are known. The information regarding the distributions of b, $\bar{U}_{1m}$, and U_{p0} are available from the experimental data, while the procedure for determining the wake velocity defect function

φ_1 is described in the next paragraph.

From the assumption of similarity in wake velocity defect profiles, it follows that for appropriately chosen length and velocity scales, wake width, and maximum wake velocity defects in this case, nondimensional wake velocity defect φ_1 will be a function of ξ_2/b, i.e.,

$$\frac{\bar{U}_1}{\bar{U}_{1m}} = \varphi_1 = f\left(\frac{\xi_2}{b}\right) = f(\zeta) \tag{20}$$

Earlier investigations by Reichardt [15] and Eifler [2] on straight channel wakes with zero longitudinal pressure gradients have shown that the nondimensional wake velocity defect function φ_1 follows the Gaussian distribution. For the curved wake under investigation, a similar solution for φ_1, described in Schobeiri et al. [12], can be obtained by using the equation of motion, Eq. (8), with the earlier specified order of magnitude analysis. The analytical treatment with suitable approximations and use of Eqs. (13) and (19) results in an ordinary second order differential equation in φ_1 that can be solved by numerical integration. It has been found that the numerical solution of the ordinary differential equation follows the Gaussian distribution presented below

$$\varphi_1 = e^{-\zeta^2} \tag{21}$$

Comprehensive experimental measurements in a curved channel with and without a longitudinal pressure gradient was also found to follow the Gaussian distribution given by Eq. (21). Thus, it can be concluded that the effects of curvature and pressure gradient are not significant on dimensionless wake velocity defect distribution. As a result, it can be stated that after transforming the governing equations into an appropriate wake coordinate system, the assumption of similarity in wake velocity defect profiles is valid.

From the time-averaging procedure, it is obvious that Reynolds shear stress is the difference between the total velocity momentum $\overline{UV}$ and partial velocity momentum $\bar{U}\bar{V}$, i.e., $\overline{uv}=\overline{UV}-\bar{U}\bar{V}$. Thus, knowing the expressions for total and partial momenta would lead to an expression for calculating the shear stress. Since the expressions for mean longitudinal and lateral velocities are known from Eqs. (13) and (19), their product leads to the expression for partial velocity momentum,

$$\left(1+\frac{\xi_2}{R}\right)\bar{U}\bar{V} \tag{22}$$

Substituting the approximation for U_p from Eq. (15) and the expressions for $\bar{U},\bar{V}$ from Eqs. (13) and (19) into Eq. (22) and nondimensionalizing the resulting equation with $\bar{U}_{1m}^2$, the expression for nondimensional partial momentum is

$$\begin{aligned}\left(1+\frac{\xi_2}{R}\right)\frac{\bar{U}\bar{V}}{\bar{U}_{1m}^2} =& -\frac{U_{p0}}{\bar{U}_{1m}}\frac{b}{\bar{U}_{1m}}\frac{dU_{p0}}{d\xi_1}\zeta\left[1-\frac{3b}{2R}\zeta+\frac{b^2 2}{R^2}\zeta^2\right]\\ &+\frac{U_{p0}}{\bar{U}_{1m}}\frac{b}{\bar{U}_{1m}}\frac{d\bar{U}_{1m}}{d\xi_1}\left(1-\frac{b}{R}\zeta\right)\frac{\sqrt{\pi}}{2}\,\mathrm{erf}(\zeta)\\ &+\frac{b}{\bar{U}_{1m}}\frac{dU_{p0}}{d\xi_1}\zeta\varphi_1\left(1-\frac{b}{2R}\zeta\right)\\ &-\frac{b}{\bar{U}_{1m}}\frac{d\bar{U}_{1m}}{d\xi_1}\frac{\sqrt{\pi}}{2}\,\mathrm{erf}(\zeta)\varphi_1-\frac{db}{d\xi_1}\left[\zeta\varphi_1-\frac{\sqrt{\pi}}{2}\,\mathrm{erf}(\zeta)\right]\\ &\times\left[\frac{U_{p0}}{\bar{U}_{1m}}\left(1-\frac{b}{R}\zeta\right)-\varphi_1\right]\end{aligned} \tag{23}$$

The expression for total momentum can be obtained by using Eq. (10) in the ξ_1 direction and following the earlier specified order of magnitude analysis as

$$\frac{R}{R+\xi_2}\left(\frac{\bar{p}}{\rho}+\bar{U}^2\right)_{,1}+(\overline{UV})_{,2}+\frac{2}{R+\xi_2}(\overline{UV})=0 \tag{24}$$

Using Eqs. (13) and (14) modifies Eq. (24) to

$$-U_p\frac{\partial U_p}{\partial\xi_1}+\frac{\partial}{\partial\xi_1}(U_p^2-\bar{U}_I^2)=\frac{\partial}{\partial\xi_2}\left[\left(1+\frac{\xi_2}{R}\right)\overline{UV}\right]+\frac{\overline{UV}}{R} \tag{25}$$

Further assuming that $\overline{UV}/R \ll \partial/\partial\xi_2[(1+\xi_2/R)\overline{UV}]$, Eq. (25) can be integrated to obtain an expression for total momentum as

$$\left(1+\frac{\xi_2}{R}\right)\overline{UV}=\int\frac{\partial}{\partial\xi_1}(\bar{U}_I^2)bd\zeta-\int U_p\frac{\partial U_p}{\partial\xi_1}+c \tag{26}$$

In Eq. (26), the linear approximation from Eq. (15) can be substituted for U_p. By differentiating Eq. (15) with respect to ξ_1 and after some simplification through chain rule differentiation, it can be shown that $\partial U_p/\partial\xi_1 = dU_{p0}/d\xi_1$. For $\bar{U}_I^2$ the dimensionless momentum defect function φ^2 from Eq. (16) can be introduced where $\bar{U}_{Im}^2=2U_{p0}\bar{U}_{1m}-\bar{U}_{1m}^2$. The approximate equality of dimensionless wake velocity and momentum defects, i.e., $\varphi^2\cong\varphi_1$, has been experimentally verified for different locations downstream of the wake generating body. It should be pointed out that this approximate equality of the two ratios does not depend on the magnitude of $\bar{U}_1$. Using this approximation and further rearranging the terms will modify Eq. (26) to

$$\begin{aligned}\left(1+\frac{\xi_2}{R}\right)\overline{UV}=& -U_{p0}\frac{dU_{p0}}{d\xi_1}\int\left(1-\frac{2\xi_2}{R}+\frac{\xi_2^2}{R^2}\right)d\xi_2\\ &+\frac{d}{d\xi_1}(2U_{p0}\bar{U}_{1m}-\bar{U}_{1m}^2)\int\varphi_1 bd\zeta\\ &-(2U_{p0}\bar{U}_{1m}-\bar{U}_{1m}^2)\frac{db}{d\xi_1}\int\zeta\frac{d\varphi_1}{d\zeta}d\zeta+c\end{aligned} \tag{27}$$

Evaluating the integrals and finally nondimensionalizing with $\bar{U}_{1m}^2$ will result in an expression for total momentum as

$$\begin{aligned}\left(1+\frac{\xi_2}{R}\right)\frac{\overline{UV}}{\bar{U}_{1m}^2}=& -\frac{U_{p0}}{\bar{U}_{1m}}\frac{b}{\bar{U}_{1m}}\frac{dU_{p0}}{d\xi_1}\zeta\left[1-\frac{b}{R}\zeta+\frac{b^2}{3R^2}\zeta^2\right]\\ &+2\frac{b}{\bar{U}_{1m}}\frac{d\bar{U}_{1m}}{d\xi_1}\frac{\sqrt{\pi}}{2}\,\mathrm{erf}(\zeta)\\ &+2\frac{U_{p0}}{\bar{U}_{1m}}\frac{b}{\bar{U}_{1m}}\frac{d\bar{U}_{1m}}{d\xi_1}\frac{\sqrt{\pi}}{2}\,\mathrm{erf}(\zeta)\\ &-2\frac{b}{\bar{U}_{1m}}\frac{d\bar{U}_{1m}}{d\xi_1}\frac{\sqrt{\pi}}{2}\,\mathrm{erf}(\zeta)-\frac{db}{d\xi_1}\left[\zeta\varphi_1-\frac{\sqrt{\pi}}{2}\,\mathrm{erf}(\zeta)\right]\\ &\times\left[2\frac{U_{p0}}{\bar{U}_{1m}}-1\right]+\frac{c}{\bar{U}_{1m}^2}\end{aligned} \tag{28}$$

The expression for Reynolds shear stress can now be obtained from the difference of total momentum and partial momentum,i.e., Eqs. (23) and (28), as

$$\begin{aligned}\left(1+\frac{\xi_2}{R}\right)\frac{\overline{uv}}{\bar{U}_{1m}^2}=& -\frac{U_{p0}}{\bar{U}_{1m}}\frac{b}{\bar{U}_{1m}}\frac{dU_{p0}}{d\xi_1}\frac{b}{2R}\zeta^2\left[1-\frac{b}{3R}\zeta\right]\\ &+\frac{U_{p0}}{\bar{U}_{1m}}\frac{b}{\bar{U}_{1m}}\frac{d\bar{U}_{1m}}{d\xi_1}\left(1+\frac{b}{R}\zeta\right)\frac{\sqrt{\pi}}{2}\,\mathrm{erf}(\zeta)\\ &+\frac{b}{\bar{U}_{1m}}\frac{dU_{p0}}{d\xi_1}\left[2\frac{\sqrt{\pi}}{2}\,\mathrm{erf}(\zeta)-\zeta\varphi_1\left(1-\frac{b}{2R}\zeta\right)\right]\end{aligned}$$

$$-\frac{b}{\bar{U}_{1m}}\frac{d\bar{U}_{1m}}{d\xi_1}\frac{\sqrt{\pi}}{2}\,\mathrm{erf}(\zeta)[2-\varphi_1]$$
$$-\frac{db}{d\xi_1}\left[\zeta\varphi_1-\frac{\sqrt{\pi}}{2}\,\mathrm{erf}(\zeta)\right]$$
$$\times\left[\frac{U_{p0}}{\bar{U}_{1m}}\left(1+\frac{b}{R}\zeta\right)-(1-\varphi_1)\right]+\frac{c}{\bar{U}_{1m}^2} \tag{29}$$

Thus, Eq. (29) describes the shear stress inside the wake under the influence of both the curvature and pressure gradient. The constant of integration in the above expression is a function of $>_1$ and needs to be evaluated from the experimental results at $\zeta=0$. For the case of the straight channel with no longitudinal pressure gradient, it is known from experimental results that shear stress is zero at the wake center, with the distribution being symmetric about the wake center. In that case, the constant of integration is evaluated to be zero. However, for the curved channel flow, the shear stress distribution is strongly asymmetric, with the value being nonzero at the wake center, thus bringing out the influence of curvature. As a result, the constant of integration is no longer zero and needs to be evaluated from experimental measurements.

Now that the derivation for wake characteristics under the influence of curvature and pressure gradient is complete, we simplify them for the special cases of zero-pressure gradient curved wake and zero-pressure gradient straight wake in the following section.

2.4 Wake Characteristics for Zero Longitudinal Pressure Gradient. Since the longitudinal changes of U_{p0} are related to the governing pressure gradient inside the channel, this term should vanish for zero-pressure gradient cases, which we have verified from our experimental results. Our experimental results for the curved wake, shown in Fig. 3, and the available straight wake data from the literature indicate that for zero-pressure gradient cases, the longitudinal changes of wake velocity-width products are negligibly small, i.e., $(d/d\xi_1)(\bar{U}_{1m}b)\approx 0$. With this observation, and since $\bar{U}_{1m}$ is quite small, it has further been assumed that $(d/d\xi_1)(\bar{U}_{1m}^2 b)\approx 0$. With these findings, the wake characteristics for zero-pressure gradient curved wakes can be summarized in terms of the longitudinal velocity component,

$$\bar{U}=U_{p0}\left(1-\frac{b}{R}\zeta\right)-\bar{U}_{1m}\varphi_1 \tag{30}$$

the lateral velocity component,

$$\left(1+\frac{\xi_2}{R}\right)\bar{V}=-\bar{U}_{1m}\frac{db}{d\xi_1}\zeta\varphi_1 \tag{31}$$

the partial momentum,

$$\left(1+\frac{\xi_2}{R}\right)\frac{\bar{U}\bar{V}}{\bar{U}_{1m}^2}=-\frac{U_{p0}}{\bar{U}_{1m}}\frac{db}{d\xi_1}\left(1-\frac{b}{R}\zeta\right)\zeta\varphi_1+\frac{db}{d\xi_1}\zeta\varphi_1^2 \tag{32}$$

the total momentum,

$$\left(1+\frac{\xi_2}{R}\right)\frac{\overline{UV}}{\bar{U}_{1m}^2}=-2\frac{U_{p0}}{U_{1m}}\frac{db}{d\xi_1}\zeta\varphi_1+\frac{db}{d\xi_1}\zeta\varphi_1+\frac{c}{\bar{U}_{1m}^2} \tag{33}$$

and the shear stress,

$$\left(1+\frac{\xi_2}{R}\right)\frac{\overline{uv}}{\bar{U}_{1m}^2}=-\frac{U_{p0}}{\bar{U}_{1m}}\frac{db}{d\xi_1}\left(1+\frac{b}{R}\zeta\right)\zeta\varphi_1+\frac{db}{d\xi_1}\zeta\varphi_1(1-\varphi_1)+\frac{c}{\bar{U}_{1m}^2} \tag{34}$$

We can further simplify the above expressions for straight wake under zero longitudinal pressure gradient by making the radius of curvature approach infinity, i.e., $R\to\infty$. It is also known from straight wake data that all the wake characteristics exhibit symmetry about the wake center line. Especially, the shear stress value is zero at the wake center, which makes the constant in the total momentum and shear stress expressions identically vanish. Thus, the summary of wake characteristics for straight wakes under zero-pressure gradient is

$$\bar{U}=U_p-\bar{U}_{1m}\varphi_1 \tag{35}$$

$$\bar{V}=-\bar{U}_{1m}\frac{db}{d\xi_1}\zeta\varphi_1 \tag{36}$$

$$\frac{\overline{uv}}{\bar{U}_{1m}^2}=-\frac{U_{p0}}{\bar{U}_{1m}}\frac{db}{d\xi_1}\zeta\varphi_1+\frac{db}{d\xi_1}\zeta\varphi_1(1-\varphi_1) \tag{37}$$

This completes the theoretical formulation for wake development. With the information regarding the longitudinal changes of wake widths, maximum wake velocity defect, potential velocity at the wake center, and radius of curvature, the wake characteristics can be predicted from the above derived expressions.

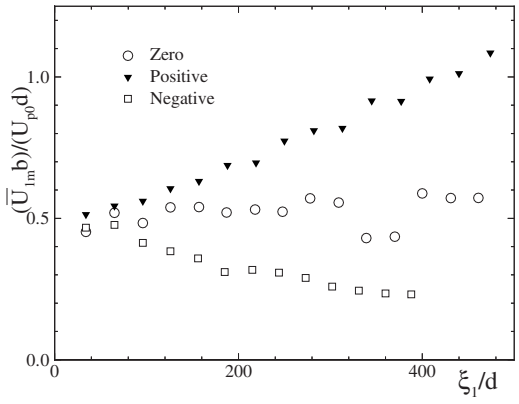

Fig. 3 Nondimensional product of maximum velocity defect and wake width for a curved channel

3 Experimental Setup and Data Measurement Techniques

The test section shown in Fig. 1 is designed to simulate steady and unsteady wake developments in a two-dimensional curved channel at zero, positive, and negative longitudinal pressure gradients. This research facility has been used for several experimental studies. For a detailed information about design description and performance tests, refer to a paper by Schobeiri and Pardivala [24]. The wake is generated by using a cylinder with a diameter of $d=1.984$ mm. The use of a cylinder to simulate a rotor blade wake is appropriate since the turbulence characteristics of the cylinder wake flows, in terms of Reynolds stress components, are similar to those of rotor blade wakes.

For the present investigation, the freestream velocity V_{in} was set to about 20 m/s just upstream of the wake generator. This corresponds to a Reynolds number of 2600 based on the diameter of the wake generator. The freestream turbulence intensity was about 1.2% at the inlet of the test section. For the steady wake development study, a single cylinder is kept stationary at midheight of the channel at a distance 67 mm upstream of the entrance to the curved section. The test section is located downstream of the wake generator and consists of a convex top wall, a concave bottom wall, and two vertical Plexiglass sidewalls. The probe traversing system is mounted within the convex wall assembly. The concave bottom wall is designed to slide horizontally within two T-slots in the bottom wall of the wake generator. This

Table 1 Details of the test section geometry

Test case for steady wake development	Inlet area (mm × mm)	Outlet area (mm × mm)	Area ratio	No. of streamwise traverses
Zero pressure gradient	420 × 593	420 × 593	1.0	15
Positive pressure gradient	420 × 593	547 × 593	0.7	15
Negative pressure gradient	420 × 593	295 × 593	1.3	13

allows the creation of adverse or favorable longitudinal pressure gradients within the test section. The geometry of the test section for the three types of pressure gradient cases investigated in the present study is listed in Table 1. The fourth column of Table 1 gives the area ratio of the inlet to the outlet of the curved test section.

The test facility is instrumented for fully automated digital data acquisition. The data acquisition system is controlled by a personal computer that incorporates a 12 bit analog to digital conversion (A/D) board. The mean velocities and turbulent stress components are obtained by using a three-channel constant temperature anemometer (TSI, IFA 100) system. Based on numerous spectral measurements within the wake, the low pass filter of the signal conditioner is set at 20 kHz. The measurements in the present study are made with TSI 1241 x-film sensors of 25 μm in diameter. A simple and accurate method by John and Schobeiri [25] is used to calibrate the x-film probes. The uncertainties in the measurement of velocity components using an x-film probe are estimated to be about 1.2% for the longitudinal velocity and 3% for the normal velocity. The anemometer outputs are sampled at a rate of 2 kHz, and a total of 32,768 samples per channel are taken. These numbers are chosen on the basis of preliminary tests conducted by varying the sampling rate from 0.5 kHz to 5 kHz, and the total number of samples from 8000 to 64,000. More details on instrumentation, data acquisition system, data reduction, and analysis are available in John [26].

4 Results and Discussion

To demonstrate the general validity of the theory developed in Sec. 2, the wake development under zero, positive, and negative longitudinal pressure gradients within a curved channel is experimentally investigated and compared to the theory. To validate the theory further, straight wake data from Eifler [2] and mild curvature and pressure gradient data from Nakayama [7] are reevaluated and compared to the theory. To compare experimental results to the developed theory directly, it is preferable to present the experimental results in curvilinear coordinates (ξ_1, ξ_2). This requires transformation of experimental results obtained in the probe coordinate (x,y) system (refer to Fig. 1) to the curvilinear coordinate system (ξ_1, ξ_2). The details of the transformation procedure and determining the inclination between the two coordinate systems are available in Schobeiri and John [13]. To obtain the theoretical wake characteristic distributions from the expressions derived in Sec. 2, information regarding the longitudinal variation of wake width, maximum wake velocity defect, hypothetical potential flow velocity at the wake center, and wake curvature radius are needed from the experimental measurements. The comparison of the theory with our own experimental results in a curved channel is presented in Sec. 4.1. Section 4.2 deals with the comparison of the theory to straight channel wake data from Eifler [2], while Sec. 4.3 compares the external experimental data of Nakayama [7] to the theory.

4.1 Curved Channel Wake Flow. Straight wake studies by Reichardt [15] and Eifler [2] have shown that the wake development in the longitudinal direction primarily depends on the ratio x/d (ξ_1/d for curved wake) regardless of the separate variation of the parameters involved in the ratio. Thus, the cylinder diameter was kept constant for this study. The local length scale used to nondimensionalize ξ_2 is the wake width b defined as

$$b = \frac{1}{\bar{U}_{1m}} \int_{-\infty}^{+\infty} \bar{U}_1 d\xi_2 \tag{38}$$

Many researchers have used several definitions for b. Width measured between the edges of the wake and width measured at half-height of the wake velocity defect profile are some commonly used definitions. The wake width b defined in Eq. (38) differs from the b used by Eifler [2] by a constant factor. Maximum velocity defect $\bar{U}_{1m}$ is chosen as the velocity scale to nondimensionalize all the wake properties. These length and velocity scales for the present investigation are represented by power fits as $b/d \sim (\xi_1/d)^{c_1}$ and $\bar{U}_{1m} \sim (\xi_1/d)^{c_2}$ where c_1 and c_2 are constants. A comparison with length scale b of a self-preserving straight wake is now presented. Eifler [2] used $b/d \sim (x/d)^{0.5}$ for a near wake $(x/d < 100)$ and $b/d/(x/d+x_0/d)^{0.5}$ for a far wake $(\mathbf{x}/\mathbf{d} > 100)$, where x_0 is known as the virtual origin of the wake. Some values reported in literature for x_0 are $90d$ by Townsend [1], $100d$ by Eifler [2], and $-40d$ by Nakayama [7], where d is the diameter of the wake generator. In the present investigation, estimating the influence region of the wake generating cylinder, also referred to as near and far wake regions, uses the nondimensional momentum defect ratio $C_w = 2\delta_2/d$ and the wake shape factor $H_{12} = \delta_1/\delta_2$, where the velocity defect function φ_1 is introduced. The expressions for wake momentum thickness δ_2, C_w, and shape factor H_{12} are given by

$$\delta_2 = b \frac{\bar{U}_{1m}}{U_{p0}} \left(1 - \frac{1}{\sqrt{2}} \frac{\bar{U}_{1m}}{U_{p0}} \right) \tag{39}$$

$$C_w = \frac{2\delta_2}{d} = 2\frac{b}{d} \frac{\bar{U}_{1m}}{U_{p0}} \left(1 - \frac{1}{\sqrt{2}} \frac{\bar{U}_{1m}}{U_{p0}} \right) \tag{40}$$

$$H_{12} = \frac{\delta_1}{\delta_2} = \frac{1}{1 - \frac{1}{\sqrt{2}} \frac{\bar{U}_{1m}}{U_{p0}}} \tag{41}$$

Figure 4(*a*) shows the C_w-distribution for zero, positive, and negative longitudinal pressure gradient cases for a wide range of ξ_1/d locations. The momentum thickness ratio increases with ξ_1/d for positive, decreases for negative, and is almost constant for zero-pressure gradient cases. Also, C_w-distribution does not exhibit any major changes that might suggest the existence of a pronounced near wake region similar to that for straight wakes investigated by Reichardt [15] and Pfeil and Eifler [16]. However, considering the wake shape factor H_{12}, shown in Fig. 4(*b*), as an alternative indicator, a transition zone $\lambda_{tr} = \xi_1/d < 40$ may be defined, for which the nondimensional wake velocity defect φ_1 indicates a certain dependency on ξ_1/d. This dependency diminishes for $\lambda_{tr} = \geqslant 40$. Compared to the near wake region of straight wake $(x/d < 100)$, the relatively short transition zone suggested above may be attributed to the asymmetric velocity distribution associated with a lateral pressure gradient, resulting in a stronger longitudinal and lateral mixing. Comparing the H_{12}-distributions for the three pressure gradient cases, it is evident that H_{12} approaches unity in the far wake, and only the rate at which it approaches unity is dependent on the type of pressure gradient.

The path of the wake center represents the ξ_1 direction of the curvilinear coordinate system. The radial distance from the convex wall to the wake center, denoted as $r - r_i$, at various longitudinal positions, is plotted in Fig. 5(*a*) for the three pressure gradient cases. The wake center initially moves toward the convex

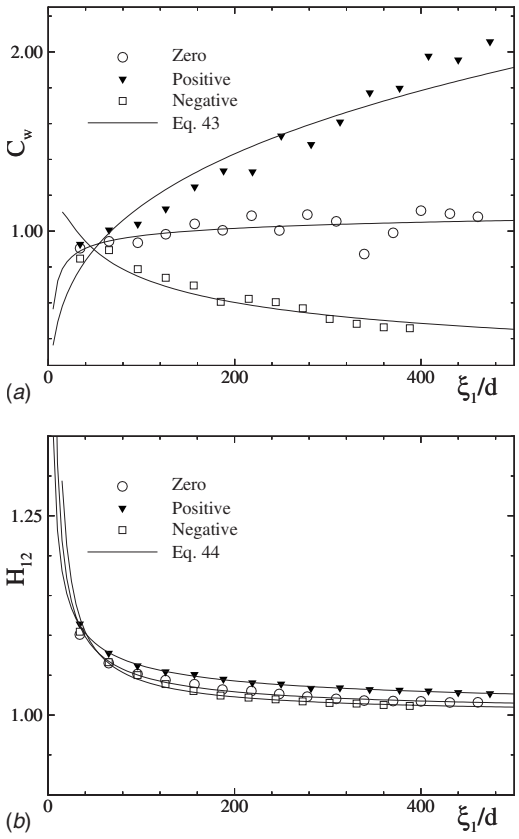

Fig. 4 Nondimensional (*a*) momentum thickness ratio and (*b*) shape factor

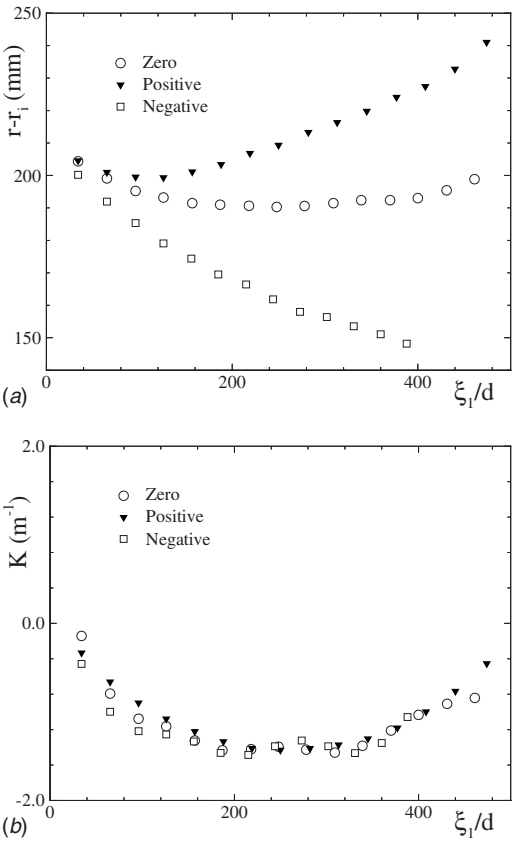

Fig. 5 (*a*) Radial position and (*b*) local curvature of the wake center

wall up to ξ_1/d of 200 for the zero-pressure gradient case and up to ξ_1/d of 100 for the positive pressure gradient case. From there onward, it moves away from the convex wall. However, for the negative pressure gradient case, the wake center moves towards the convex wall for all the longitudinal locations investigated. The local curvature of the wake centerline obtained by double differentiation of the equation to the path of the wake centerline is shown in Fig. 5(*b*). The local curvature of the wake center is almost the same for all three pressure gradient cases investigated. As mentioned earlier, the negative value of K indicates that the curvature of the wake centerline is concave in the positive ξ_2 direction.

The wake decay and growth are generally characterized by the maximum velocity defect $\bar{U}_{1m}$ and the width b that vary only in the longitudinal direction ξ_1/d. Their product $\bar{U}_{1m}b$ reveals specific characteristics of the wake development in the curved channel at different pressure gradients, as shown in Fig. 3 (circle, lower triangle, and square symbols). Unlike the zero-pressure gradient case with an almost constant nondimensionalized value, the positive and negative pressure gradient cases exhibit distinctly different patterns. Considering the positive pressure gradient case, the continuous deceleration of U_{p0} associated with an increase of wake width b results in a pronounced increase in the dimensionless product $\bar{U}_{1m}b$. The opposite pattern is revealed for the negative pressure gradient case due to a continuous acceleration of U_{p0} and a moderate increase in b as a consequence of contraction of the channel.

The distributions of the experimental (symbols) and theoretical (lines) mean longitudinal velocity components are shown in Fig. 6 for the three pressure gradient cases with longitudinal location as the parameter. The choice of longitudinal locations ξ_1/d presented is arbitrary. The velocity is nondimensionalized with respect to the inlet velocity $V_{\text{in}}=20$ m/s. The velocity distribution exhibits a strong asymmetric character with higher velocities on the positive side of ξ_2, corresponding to the locations closer to the convex wall with $\xi_2=0$ as the geometric location of the wake center. The wake velocity defect decreases, resulting in a continuous increase in the wake width with downstream location. The individual velocity profiles are characterized by a highly dissipative vortical core inside the wake region surrounded by an external *hypothetical* potential flow region. A comparison to the theory developed shows a detailed prediction of this behavior over the entire velocity range. The excellent agreement between theory and measurements confirms the validity of assumptions made, including the validity of the derived approximation for potential flow velocity in the vicinity of the wake center.

The distributions of the mean velocity defect function $\varphi_1 = \bar{U}_1/\bar{U}_{1m}=f(\zeta)$ for different longitudinal locations and pressure gradients are shown in Fig. 7. The lateral distance ξ_2 is nondimensionalized by the wake width b. Considering the asymmetric behavior of the velocity distribution, the introduction of the velocity defect has resulted in a fully symmetric defect function, which proves the existence of similarity for the mean velocity defect. In Fig. 7, the experimental results (symbols) are compared with the developed theory (solid line). The solid lines are based on the velocity defect function, $\varphi_1=e^{-\zeta^2}$, which is proven to be a general representation of the wake defect for curved and straight wakes (see also Sec. 4.2). The mean velocity defect profiles are symmetric and almost identical to the straight wake (discussed in Sec. 4.2), except for the fact that they are slightly wider on the inner side (the concave side of the trajectory of the wake centerline) of the wake as they turn. Nakayama [7] observed changes in the width and depth of velocity defect profiles and attributed these changes to pressure gradient. However, such distinct changes are not apparent in the velocity defect profiles plotted in Fig. 7. This

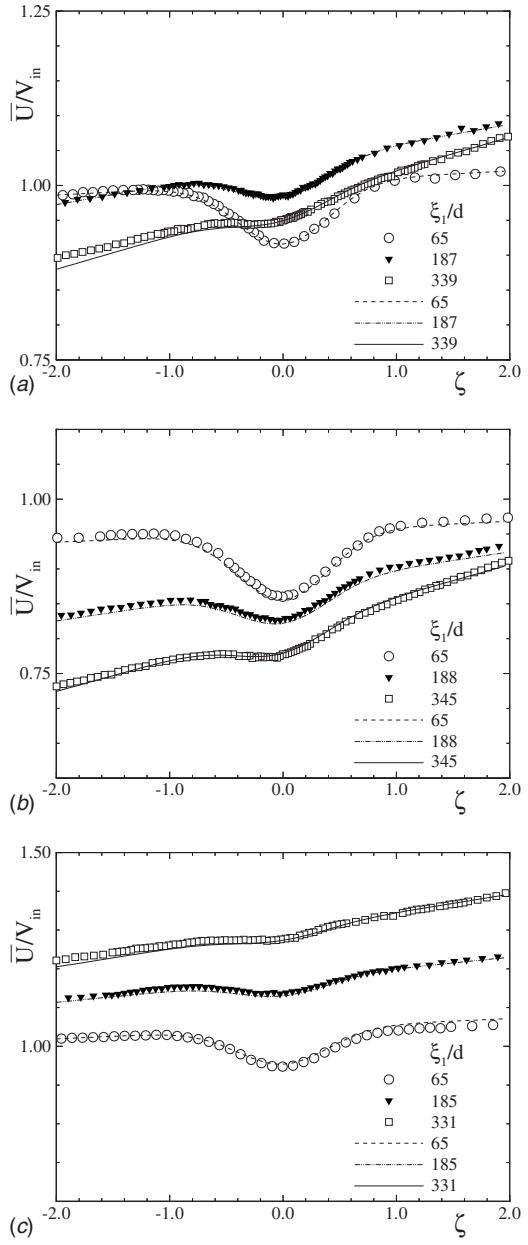

Fig. 6 Mean longitudinal velocity for (*a*) zero, (*b*) positive, and (*c*) negative pressure gradient cases

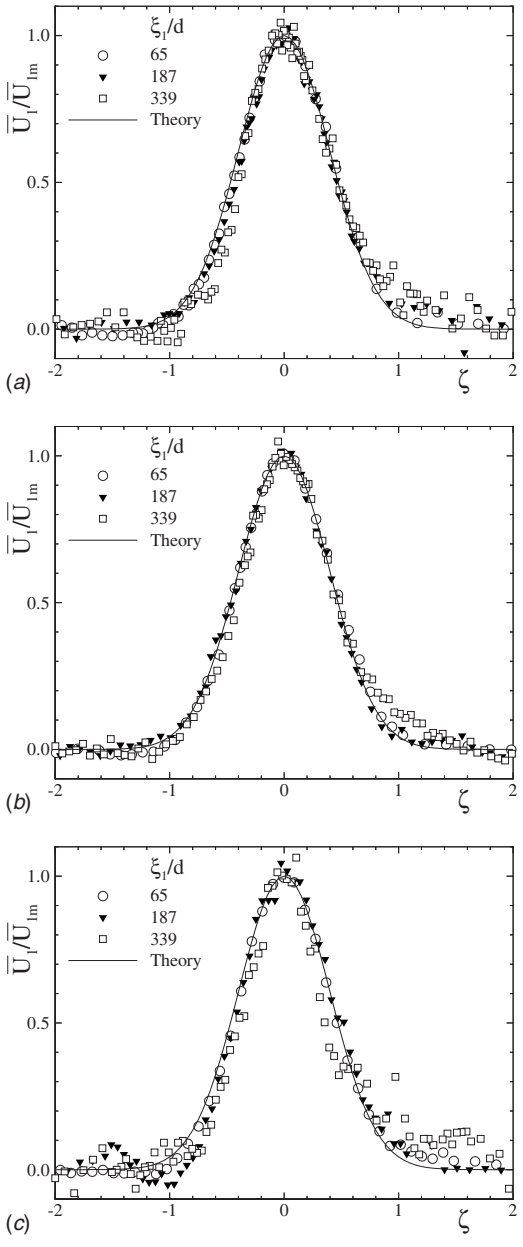

Fig. 7 Nondimensional mean velocity defect for (*a*) zero, (*b*) positive, and (*c*) negative pressure gradient cases

could be due to the difference in the velocity scales used in these investigations. In general, it may be considered that the effect of curvature on mean velocity defect distribution is small.

The distribution of the nondimensionalized lateral velocity component $\bar{V}/\bar{U}_{1m}$ for three representative longitudinal locations and three different pressure gradients is presented in Fig. 8. For the zero-pressure gradient case presented in Fig. 8(*a*), experimental results reveal an asymmetric behavior with a minimum at $\zeta>0$, a maximum at $\zeta<0$, and zero velocity at the center with nonzero values at the edges. Considering the same ξ_1/d locations for the positive pressure gradient case (Fig. 8(*b*)), the lateral velocity component increases continuously starting from the concave side, going through the zero point, and assuming positive values when approaching the convex side. For the negative pressure gradient case shown in Fig. 8(*c*), the trend is opposite to that of the positive pressure gradient case. These three distinctly different patterns can be explained by the continuity requirement. Taking the zero-pressure gradient as the reference case, the steeper slope of the mean longitudinal potential velocity for a negative pressure gradient case has caused the lateral component to assume negative values toward the convex wall to satisfy the continuity requirement. The opposite tendency is observed for a positive pressure gradient case where the slope of mean longitudinal potential velocity is much shallower than the zero-pressure gradient case, which causes the lateral component to assume positive values on the convex side to satisfy the continuity requirement.

The lines in Fig. 8 represent the theoretical results for the lateral velocity distribution obtained from Eq. (19). Although the theoretical results exhibit the same tendency, they deviate slightly from the experimental results. For the zero-pressure gradient case shown in Fig. 8(*a*), the main reason could be due to the lateral velocity component being very small compared to the longitudinal velocity component, and considering the transformation of the velocity components from the probe coordinate system into the curvilinear wake coordinate system, the deviation is within the

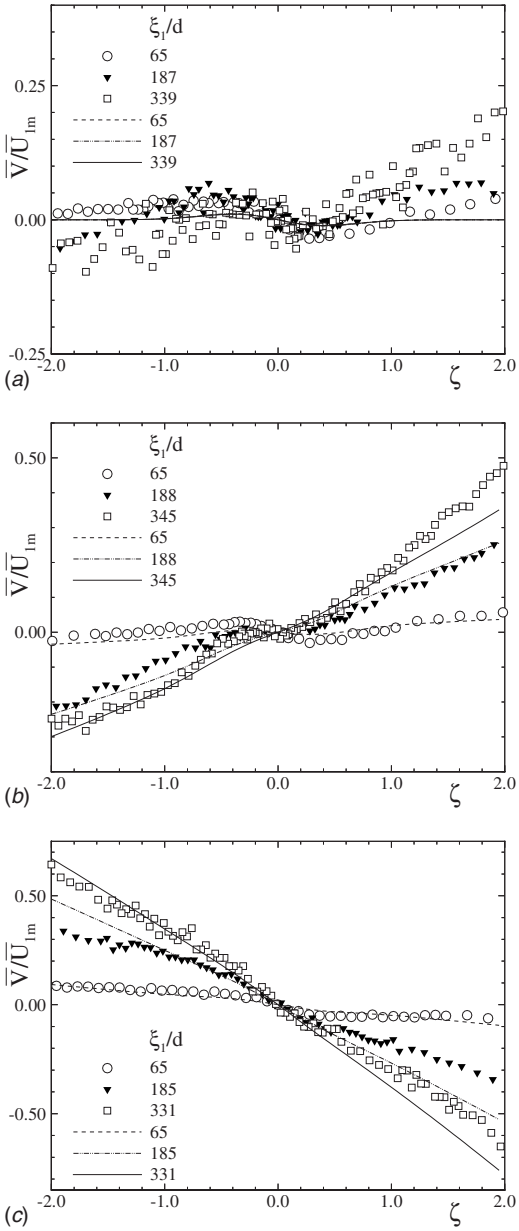

Fig. 8 Mean lateral velocity for (*a*) zero, (*b*) positive, and (*c*) negative pressure gradient cases

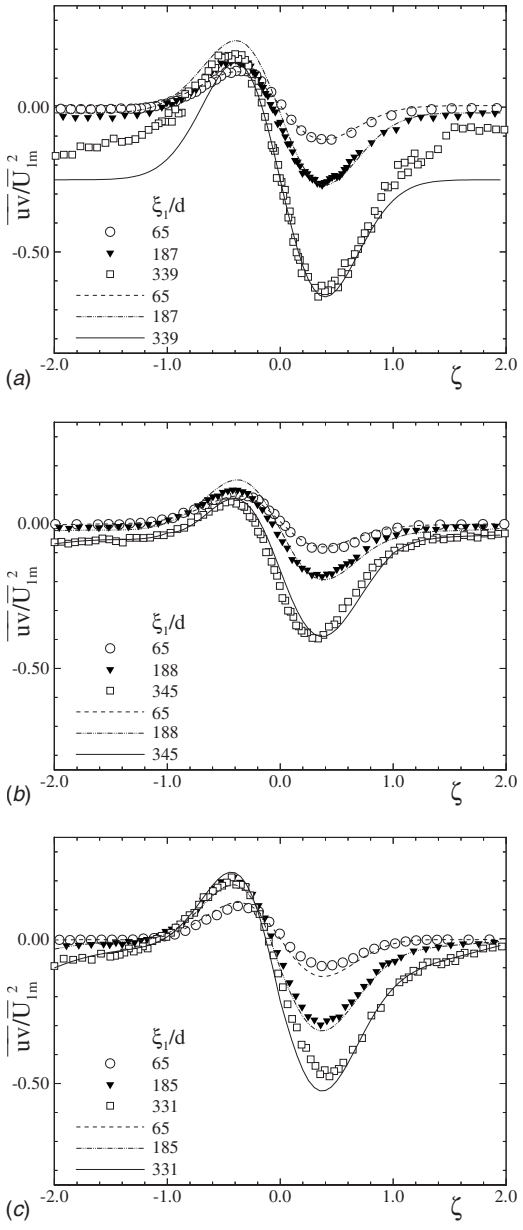

Fig. 9 Reynolds shear stress for (*a*) zero, (*b*) positive, and (*c*) negative pressure gradient cases

accuracy tolerance of the probe associated with inevitable scatter in the measurement. In this connection, it should be noted that many relevant papers on wakes, including the ones dealing with symmetric wakes, have not reported the lateral velocity distribution, probably due to very high scatter in experimental data. However, for positive and negative pressure gradient cases shown in Figs. 8(*b*) and 8(*c*), the magnitude of $\bar{V}$ is in the same order of magnitude as $\bar{U}_1$. In addition, for the present experimental investigation in a curved channel, the secondary flow effects combined with boundary layer growth on the top and bottom walls under the effect of curvature and pressure gradient could have rendered the flow three dimensional. The theory based on two-dimensional continuity is expected to deviate from experimental results under such conditions. So the theory is modified by a ratio to account for the three-dimensional nature of the flow. The $\bar{V}$ reported by Nakayama [7] exhibited an almost linear behavior, but the current investigation shows a nonlinear behavior, which could be due to more severe curvature and pressure gradient effects.

The experimental results (symbols) for Reynolds shear stress distribution at the three longitudinal locations, and for the three different pressure gradients, are presented in Fig. 9 and compared to the theory (lines) developed in Sec. 2. The Reynolds shear stress is nondimensionalized by squaring the maximum velocity defect. As shown in Fig. 9, the shear stress is nonzero at the wake center because of the curvature effect that causes a pressure gradient in the lateral direction, resulting in a highly asymmetric distribution of shear stress profiles. Raj and Lakshminarayana [5] also observed a nonzero value of Reynolds shear stress at the wake center. In their investigation, Raj and Lakshminarayana [5] found that at the point where $\partial\bar{U}/\partial y=0$, the wake center need not be the same where the Reynolds stress is zero. They concluded that the mixing length hypothesis is not valid for predicting the mean and turbulent quantities in such a region.

The Reynolds shear stress in the hypothetical potential flow outside the wake is not exactly equal to zero due to the turbulence existing in that region. Also the $\overline{uv}$ outside the wake has a higher

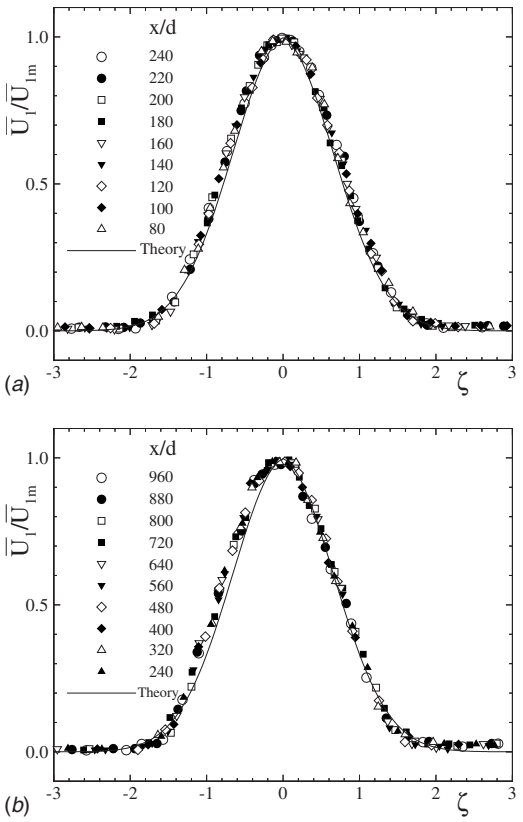

Fig. 10 Nondimensional mean velocity defect for (*a*) *d*=2 mm and (*b*) *d*=0.5 mm; comparison with data from Eifler [2]

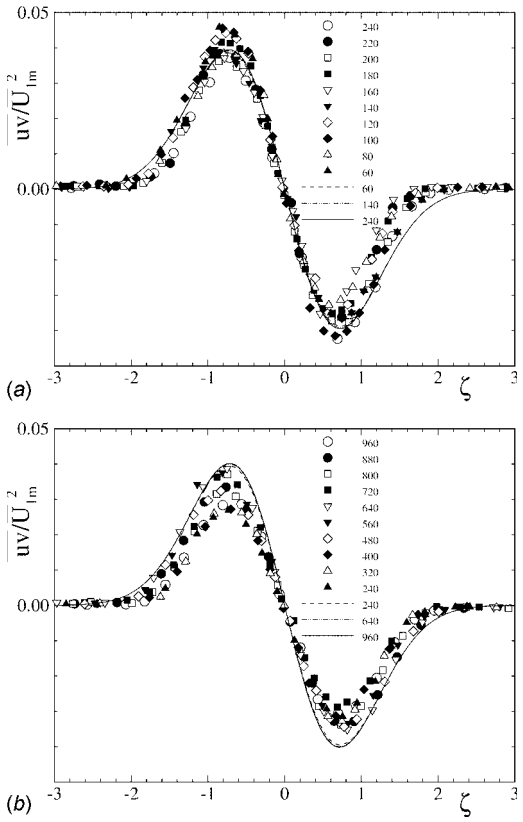

Fig. 11 Reynolds shear stress for (*a*) *d*=2 mm and (*b*) *d*=0.5 mm; comparison with data from Eifler [2]

absolute value near the concave side of the wall ($\xi_2 < 2$). Measurements at selected longitudinal locations without the wake showed a lateral gradient of $\overline{uv}$ with a negative value near the concave wall and a positive value near the convex wall. The radial position, where $\overline{uv}=0$, was located between the convex wall and mean radius of the channel. A similar distribution of Reynolds shear stress has been observed in turbulent flows in curved channels, as reported by Wattendorf [27] and Eskinazi and Yeh [28]

As shown in Fig. 9, the shear stress distribution is strongly asymmetric, which can be attributed to the asymmetry of the mean longitudinal velocity component. Generally, in a curved shear flow, the positive velocity gradient in a positive radial direction suppresses turbulence (stabilizing effect), while a negative velocity gradient in a positive radial direction promotes turbulence (destabilizing effect). From the mean longitudinal velocity distributions, it is apparent that the velocity gradient is negative in the positive radial direction on the inner half of the wake (the concave side of the trajectory of the wake centerline). Thus, higher values of Reynolds shear stress are expected on the inner half of the wake. The opposite trend is true for the outer half of the wake, which results in lower values of Reynolds shear stress. The shear stress values on the outer half of the wake decrease under positive pressure gradient and increase under the influence of negative pressure gradient. However, on the inner side of the wake, the shear stress values increase continuously with downstream location for all three types of pressure gradient cases. It is also apparent that the degree of asymmetry is more pronounced for the positive pressure gradient case than the negative pressure gradient case.

The experimentally determined shear stress distributions (symbols) shown in Fig. 9 are compared with the developed theory (lines). As shown in Sec. 2, the shear stress was calculated as the difference of the total and partial momenta $\overline{uv}=UV-\bar{U}\bar{V}$ by integrating the conservation equations. The integration constants in the corresponding expressions were evaluated from experimental measurements corresponding to the values at the wake center. As can be seen in Fig. 9, the excellent agreement between the theory and the measurement over the entire range, particularly the precise prediction of the asymmetric pattern, proves the validity of necessary assumptions made in developing the theoretical framework.

4.2 Straight Channel Wake Flow. The straight channel wake flow has been treated by theory as a special case where the radius of the curvature approaches infinity. To demonstrate the general validity of the theoretical framework developed in Sec. 2, it was necessary to compare the theoretical results to the available experimental data from the literature. For this purpose, the experimental work by Eifler [2] was chosen because it is probably the most comprehensive research work in this area and entails all the detailed information necessary for a theoretical evaluation and comparison. Eifler carried out an experimental study of cylinder wake characteristics for a wide range of longitudinal locations and also for different diameters of cylinders in a straight channel.

The comparison of theory (lines) and experiment (symbols) of mean wake velocity defect function for two different cylinder diameters $d=2$ mm and 0.5 mm at different longitudinal locations is presented in Fig. 10. As shown in Fig. 10, the wake development in the longitudinal direction depends primarily on the ratio x/d (ξ_1/d for curved wake) regardless of the separate variation of the parameters involved in this ratio. The excellent agreement of theory verifies the validity of the expression $\varphi_1=e^{-\zeta^2}$. The same expression was found to predict both cases of straight and curved channel wake flows, provided that the wake velocity defect is defined properly.

Reynolds shear stress distributions for two different cylinder diameters $d=2$ mm and 0.5 mm at different longitudinal locations are shown in Fig. 11. The shear stress distribution is symmetric about the wake center with a zero value at the wake center. Thus,

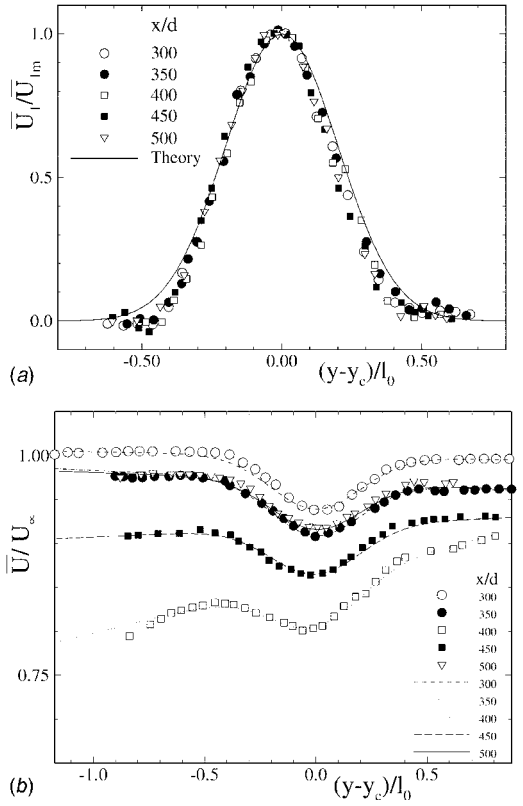

Fig. 12 (*a*) Mean velocity defect and (*b*) mean longitudinal velocity; comparison with data from Nakayama [7]

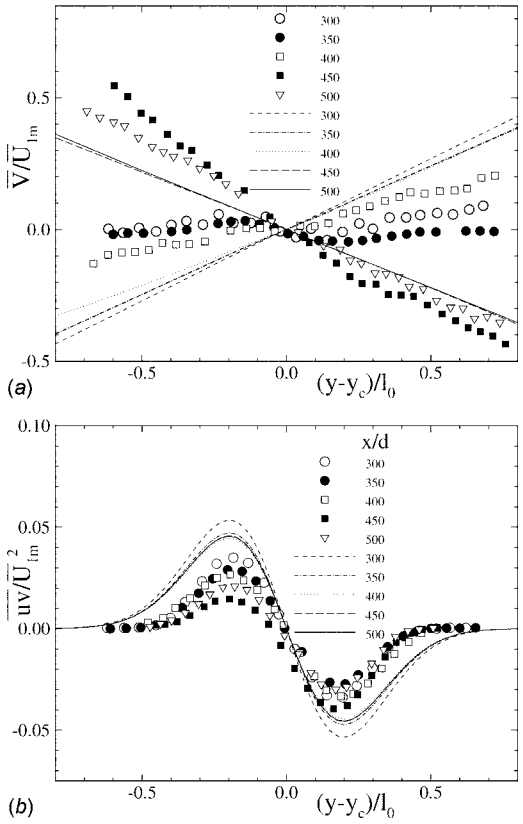

Fig. 13 (*a*) Mean lateral velocity and (*b*) Reynolds shear stress; comparison with data from Nakayama [7]

the integration constant, in the expression for shear stress (Eq. (37)) derived in Sec. 2.4, vanishes. From the comparison, it is obvious that the theory is in reasonable agreement with the measurements.

4.3 External Wake Flow. To conclude the validation procedure, the external experimental data (for flow A) by Nakayama [7] are re-evaluated, compared with the present theory, and the results are summarized below. Nakayama investigated the effect of mild curvature and pressure gradient by deflecting the small-defect wake by an airfoil-like thin plate placed at small angles in the external flow. The flow, when the angle of attack of the deflector plate is +7 deg, is referred to as flow A. It should be pointed out that Nakayama's investigation is of particular interest to external aerodynamics since it deals with the wake development under external flow conditions, which is substantially different from the internal flow discussed in this paper. The theoretical (lines) and experimental (symbols) results are plotted in Figs. 12 and 13. The nondimensional mean velocity defect is shown in Fig. 12(*a*). The velocity scale used in the present investigation, $\bar{U}_{1m}$, is different from that used by Nakayama [7], $u_0=U_\infty(x/d+40)^{-0.5}$. By using u_0 as the velocity scale, Nakayama observed growth in the width and depth of a wake, which has been attributed to the governing pressure gradient. However, such observations are not apparent when we used $\bar{U}_{1m}$ as the velocity scale and re-evaluated Nakayama's data, as all the data collapsed together. The experimental data (symbols) is in good agreement with the theory (solid line) given by $\varphi_1=e^{-\zeta^2}$. The mean longitudinal velocity component, shown in Fig. 12(*b*), reveals strong deceleration up to $x/d=400$. By convecting downstream, this tendency is reversed, resulting in higher values. A comparison to the theory exhibits an excellent agreement over the entire range. The lateral velocity component comparison is presented in Fig. 13(*a*). The lateral velocity profiles appear to be very linear. Although the theory exhibits right tendencies, there are some discrepancies. A comparison between the theory and experimental results for Reynolds shear stress is presented in Fig. 13(*b*). The expression for zero-pressure gradient curved wake (Eq. (34)) is used for the theory. This can be justified on the basis that the longitudinal changes of nondimensional wake velocity-width is almost constant, which is typical for zero longitudinal pressure gradient cases. Small deviations in shear stress appear on the stable and unstable sides for all x/d locations. The deviation could partially be due to the change in pressure gradient from negative to positive over the x/d range investigated. Given the fact that Nakayama's experimental setup and the boundary conditions significantly differ from the present study the presented theory as a whole was able to predict quite adequately the small-defect wake under the influence of mild curvature and pressure gradient.

5 Conclusions

The development of two-dimensional steady wake flows downstream of a cylindrical rod within a curved channel under zero, positive, and negative longitudinal pressure gradients is theoretically and experimentally investigated. The theoretical framework generally describes the wake flow through two-dimensional curvilinear channels. It also describes the wake development through a two-dimensional straight channel as a special case, for which the curvature radius approaches infinity. Detailed experimental results are presented and compared with the theory. The mean and the turbulence quantities were measured and later transformed from the probe coordinate system to the curvilinear wake coordinate system. In contrast to the straight wake flow, the mean quantities of the curved wake, including the longitudinal and lateral velocity components, displayed an asymmetric pattern throughout the flow regime. The introduction of the velocity defect function and the wake width b as a single length scale resulted in a fully symmetric

distribution of the nondimensionalized velocity defect $\varphi_1 = \bar{U}_1/\bar{U}_{1m} = f(\zeta = \xi_2/b)$. The experimental results for both curved and straight wakes have proven that the wake defect can be described by the function $\varphi_1 = e^{-\zeta^2}$. This function was implemented in the theory developed to calculate the total momentum $\overline{UV}$, the partial momentum $\bar{U}\bar{V}$, and the resulting shear stress $\overline{uv} = \overline{UV} - \bar{U}\bar{V}$. The experimental results were compared to the theory developed in Sec. 2 of this study. It was shown that the present theoretical concept is capable of predicting zero, positive, and negative longitudinal pressure gradient curved wake flows. Considering the three pressure gradient situations investigated in this paper, it can be concluded that the pressure gradient significantly influences the wake decay and development processes. The existence of a negative pressure gradient accelerated the wake decay process more significantly when compared to the zero-pressure gradient case. The positive pressure gradient, however, exerted a decelerating influence on the wake decay process.

Acknowledgment

This work was carried out at the Turbomachinery Performance and Flow Research Laboratory, Texas A&M University, College Station and was supported by a National Aeronautics and Space Administration Grant. We would like to express our sincere thanks and appreciation to Dr. R. Simoneau, Chief of Heat Transfer Branch, B. Lucci, and the administration of the NASA Glenn Research Center for their continuous cooperation and support of this project.

Nomenclature

- b = wake width, $b = 1/2\Gamma\int_{-\infty}^{+\infty}(\bar{U}_1/\bar{U}_{1m})d\xi_2$
- c = integration constant
- d = diameter of wake generating cylinder, $d = 1.984$ mm
- C_w = momentum defect ratio, $C_w = 2\delta_2/d$
- erf = error function
- H_{12} = wake shape factor, $H_{12} = \delta_1/\delta_2$
- p = static pressure
- Tu = turbulence intensity, $\mathrm{Tu} = (\sqrt{\bar{u}^2}/\bar{U}_{\mathrm{local}}) \times 100$
- $\bar{U}$ = mean velocity component in the longitudinal (ξ_1) direction of curvilinear coordinates
- U_p = hypothetical potential velocity distribution of longitudinal velocity component
- U_{p0} = hypothetical potential velocity at the wake center, $\xi_2 = 0$
- $\bar{U}_1$ = mean velocity defect, $\bar{U}_1 = U_p - \bar{U}$
- $\bar{U}_{1m}$ = maximum velocity defect at the wake center, $\xi_2 = 0$
- $\bar{U}_I^2$ = wake momentum defect, $\bar{U}_I^2 = 2U_p\bar{U}_1 - \bar{U}_1^2$
- $\bar{U}_{Im}^2$ = maximum wake momentum defect
- $\overline{UV}$ = one of the nine components of the total velocity momentum tensor
- $\bar{U}\bar{V}$ = one of the nine components of the partial velocity momentum tensor
- u = time-dependent physical fluctuation component in the longitudinal direction, ξ_1
- $\bar{u}^2$ = mean longitudinal turbulent fluctuation momentum
- $\overline{uv}$ = Reynolds shear stress
- $\vec{V}$ = velocity vector
- $\bar{\vec{V}}$ = time-averaged mean velocity vector
- $\tilde{\vec{V}}$ = time-dependent fluctuating component of the velocity vector
- $\bar{V}$ = time-averaged physical component in the ξ_2 direction
- V_x = velocity component along the x-direction of the probe coordinate system
- V_y = velocity component along the y-direction of the probe coordinate system
- ∇ = $\vec{g}^i(\partial/\partial\xi_i)$, differential operator in the ξ_i coordinate system
- δ_1 = displacement thickness, $\delta_1 = 1/U_{p0}\int_{-\infty}^{+\infty}(U_p - \bar{U})d\xi_2$
- δ_2 = momentum thickness, $\delta_2 = 1/U_{p0}^2\int_{-\infty}^{+\infty}\bar{U}(U_p - \bar{U})d\xi_2$
- Γ = integral of the Gaussian curve, $\Gamma = \int_{-\infty}^{+\infty}e^{-\zeta^2}d\zeta = \sqrt{\pi}/2$
- Γ_{ij}^k = Christoffel symbols
- ζ = nondimensional coordinate, $\zeta = \xi_2/b$
- ν = kinematic viscosity of air
- $\vec{\xi}$ = absolute spatial vector
- ξ_1 = longitudinal direction of curvilinear coordinates
- ξ_2 = lateral direction of curvilinear coordinates
- ρ = density of air
- φ_1 = nondimensional velocity defect, $\varphi_1 = \bar{U}_1/\bar{U}_{1m} = e^{-\zeta^2}$
- φ^2 = dimensionless wake momentum defect

Superscripts

- — = time-averaged fluctuation
- ~ = periodic value

References

[1] Townsend, A. A., 1949, "The Fully Developed Turbulent Wake of a Circular Cylinder," Aust. J. Sci. Res., Ser. A, **2**, pp. 451–468.

[2] Eifler, J., 1975, "Zur Frage der Freien Turbulenten Strömungen, Insbesondere Hinter Ruhenden und Bewegten Zylindern," Ph.D. thesis, Technische Hochschule Darmstadt, Germany.

[3] Hill, P. G., Schaub, U. W., and Senoo, Y., 1963, "Turbulent Wakes in Pressure Gradients," ASME J. Appl. Mech., **30**, pp. 518–524.

[4] Gartshore, I. S., 1967, "Two-Dimensional Turbulent Wakes," J. Fluid Mech., **30**, pp. 547–560.

[5] Raj, R., and Lakshminarayana, B., 1973, "Characteristics of the Wake Behind a Cascade of Airfoils," J. Fluid Mech., **81**, pp. 707–730.

[6] Savill, A. M., 1983, "The Turbulent Structure of a Highly Curved Two-Dimensional Wake," *IUTAM Symposium on Complex Turbulent Flows*, R. Dumas and F. Fulachier, eds., Springer, Marseille.

[7] Nakayama, A., 1987, "Curvature and Pressure-Gradient Effects on a Small-Defect Wake," J. Fluid Mech., **175**, pp. 215–246.

[8] Merony, R. N., and Bradshaw, P., 1975, "Turbulent Boundary Layer Growth Over Longitudinally Curved Surfaces," AIAA J., **13**, pp. 1448–1453.

[9] Hoffmann, P. H., and Bradshaw, P., 1978, Imperial College Aeronautics, Report No. 78-04.

[10] Muck, K. C., Hoffmann, P. H., and Bradshaw, P., 1985, "Effect of Convex Streamline Curvature on Turbulent Boundary Layers," J. Fluid Mech., **161**, pp. 347–369.

[11] Hoffmann, P. H., Muck, K. C., and Bradshaw, P., 1985, "The Effect of Concave Surface on Turbulent Boundary Layers," J. Fluid Mech., **161**, pp. 371–403.

[12] Schobeiri, T., John, J., and Pappu, K., 1996, "Development of Two-Dimensional Wakes Within Curved Channels: Theoretical Framework and Experimental Investigation," ASME J. Turbomach., **118**, pp. 506–518.

[13] Schobeiri, T., and John, J., 1994, "A Study of the Development of Steady and Periodic Unsteady Turbulent Wakes Through Curved Channels at Positive, Zero, and Negative Streamwise Pressure Gradients," NASA Lewis Research Center, Final Contract Report, Part II, Report No. NAG 3-1256.

[14] Schobeiri, T., and Pappu, K., 1994, "Prediction of Characteristics of Two-Dimensional Turbulent Wakes Under the Influence of Streamline Curvature and Zero, Positive, and Negative Pressure Gradients," NASA Lewis Research Center, Final Contract Report, Part I, Report No. NAG 3-1256.

[15] Reichardt, H., 1950, *Gesetzmässigkeiten der freien Turbulenz*, VDI-Forsch.-Heft 414. 2 Auflage Düsseldorf, VDI-Verlag.

[16] Pfeil, H., and Eifler, J., 1975, "Zur Frage der Schubspannungsverteilung für die Ebenen Freien Turbulenten Strömungen," Forsch. Ingenieurwes., **41**(4), pp. 105–136; 1975, "Messungen im Turbulenten Nachlauf des Einzelzylinders," , **41**(5), pp. 137–145.

[17] Lakshminarayana, B., and Raj, R., 1976, "Three-Dimensional Characteristics of Turbulent Wakes Behind Rotors of Axial Flow Turbomachinery," ASME J.

Eng. Power, **98**, pp. 218–228.
[18] Schobeiri, M. T., Pappu, K., and John, J., 1995, "Theoretical and Experimental Study of Development of Two-Dimensional Steady and Unsteady Wakes Within Curved Channels," ASME Trans. J. Fluids Eng., **117**, pp. 593–598.
[19] Schobeiri, M. T., and Chakka, P., 2002, "Prediction of Turbine Blade Heat Transfer and Aerodynamics Using Unsteady Boundary Layer Transition Model," Int. J. Heat Mass Transfer, **45**, pp. 815–829.
[20] Chakka, P., and Schobeiri, M. T., 1999, "Modeling of Unsteady Boundary Layer Transition on a Curved Plate Under Periodic Unsteady Flow Condition: Aerodynamic and Heat Transfer Investigations," ASME J. Turbomach., **121**, pp. 88–97.
[21] Schobeiri, M. T., Pappu, K., and Wright, L., 1995, "Experimental Study of the Unsteady Boundary Layer Behavior on a Turbine Cascade," *Paper Presented at the International Gas Turbine and Aero-Engine Congress and Exposition*, Houston, TX, Jun. 5–8, ASME Paper No. 95-GT-435.
[22] Schobeiri, M. T., John, J., and Pappu, K., 1997, "Experimental Study on the Effect of Unsteadiness on Boundary Layer Development on a Linear Turbine Cascade," Exp. Fluids, **23**, pp. 303–316.
[23] So, R. M. C., and Mellor, G. L., 1973, "An Experimental Investigation of Turbulent Boundary Layers Along Curved Surfaces," J. Fluid Mech., **60**, pp. 43–62.
[24] Schobeiri, T., and Pardivala, D., 1992, "Development of a Subsonic Flow Research Facility for Simulating the Turbomachinery Flow and Investigating Its Effects on Boundary Layer Transition, Wake Development and Heat Transfer," *Fourth International Symposium on Transport Phenomena and Dynamics of Rotating Machinery*, p. 98.
[25] John, J., and Schobeiri, T., 1993, "A Simple and Accurate Method of Calibrating X-Probes," ASME Trans. J. Fluids Eng., **115**, pp. 148–152.
[26] John, J., 1993, "A Study of the Development of Steady and Periodic Unsteady Turbulent Wakes Through Curved Channels at Positive, Zero, and Negative Longitudinal Pressure Gradients," Ph.D. thesis, Texas A&M University, College Station, USA.
[27] Wattendorf, F. L., 1935, "A Study of the Effect of Curvature on Fully Developed Turbulent Flow," Proc. R. Soc. London, Ser. A, **148**, pp. 565–598.
[28] Eskinazi, S., and Yeh, H., 1956, "An Investigation on Fully Developed Turbulent Flows in a Curved Channel," J. Aeronaut. Sci., **23**, pp. 23–34.

Laminarization of Internal Flows Under the Combined Effect of Strong Curvature and Rotation

K. M. Guleren[1]
Faculty of Engineering,
Mechanical Engineering Department,
Cumhuriyet University,
58140 Sivas, Turkey
e-mail: melihguleren@cumhuriyet.edu.tr

I. Afgan
Institute of Avionics and Aeronautical Engineering,
Air University,
Sector E-9,
Islamabad, Pakistan

A. Turan
School of MACE,
The University of Manchester,
George Begg Building,
Sackville Street,
P.O. Box 88,
Manchester M60 1 QD, UK

The laminarization phenomenon for the flow under the combined effect of strong curvature and rotation is discussed based on numerical predictions of large-eddy simulation (LES). Initially, the laminarization process is presented for the fully developed flow inside a spanwise rotating straight square duct. LES predictions over a wide range of rotation numbers ($Ro=0-5$) show that the turbulent kinetic energy decreases monotonically apart from $0.2<Ro<0.5$. Subsequently, a spanwise rotating U-duct flow is considered with $Ro=\pm 0.2$. The interaction of curvature and Coriolis induced secondary flows enhances the turbulence for the negative rotating case, whereas this interaction ensues strong laminarization for the positive rotating case. Finally, the laminarization is presented in the impeller of a typical centrifugal compressor, rotating at a speed of $\Omega=1862$ rpm ($Ro=0.6$). The resulting LES predictions are observed to be better than those of Reynolds-averaged Navier-Stokes (RANS) in the regions where turbulence is significant. However, for the regions dominated by strong laminarization, RANS results are seen to approach those of LES and experiments. [DOI: 10.1115/1.2953298]

Keywords: centrifugal compressor, curvature, laminarization, LES, rotation, U-duct

1 Introduction

The laminarization phenomenon has been the focus of many studies in the past due to the extremely significant influences on engineering and natural flows. The phenomenon is generally characterized by transitional flow behavior, changing from turbulent to laminar state. The laminarization process is also referred to as "reverse-transition," "inverse-transition," or "relaminarization." The earliest engineering studies regarding laminarization concerned the heat transfer mechanism for the nozzle flow [1]. This study has been superseded by various numerical and experimental investigations for laminarization effects on heat transfer in circular tubes [2–10]. The laminarization is not only a crucial topic in heat transfer but is also an extremely important issue in relation to turbulence modeling [11,12] and various engineering applications, such as magnetohydrodynamic flows [13–15], combustion [16–18], porous media flows [19], and flow control techniques [20].

The effect of curvature on turbulence is strongly related to the specific geometrical characteristics. Turbulence is generally enhanced near the concave surface due to the centrifugal instability associated with the concave curvature. This causes the streamwise-oriented Taylor–Görtler vortices and an adverse pressure gradient [21]. Whereas, the flow displays a suppressed turbulent behavior on the convex surface due to the favorable pressure gradient [22–25]. Rotating flow problems encountered in engineering applications have been the subject of a number of studies with special emphasis on relaminarization effects. Typically, the axis of rotation can be either in the direction of the streamwise flow [26–30] or in the spanwise direction [31–35]. In the former case, the existing Coriolis force in the streamwise direction reduces to zero and hence the laminarization process is dictated primarily by the centrifugal force if the secondary flows are not significantly strong. On the other hand, in the latter case incorporating the consideration of the simple channel flow, the Coriolis force distorts the mean flow by decreasing the mean velocity gradient near the low-pressure side. This causes a reduction in the production of turbulence and leads to the laminarization especially at high rotation rates.

The laminarization process in more complex geometries with strong curvature and rotation, including the rotating *U*-duct and the centrifugal compressor, is little known. In the rotating *U*-duct, the laminarization process is important for the cooling process, whereas in a centrifugal compressor, the resulting laminarization of the flow could be useful for the stability of the wake thus decreasing the wake losses and in consequence increasing the isentropic efficiency of the compressor. The present study discusses the laminarization process in cases where curvature and rotation effects are significantly strong. A detailed investigation for the rotating square duct flow is also carried out along with the verified numerical results for the simple rotating channel flow.

2 Numerical Method

In direct numerical simulation (DNS), all turbulent scales have to be resolved. In LES, on the other hand, only the larger scales are resolved and the smaller ones are modeled via a subgrid-scale (SGS) model. In order to rigorously account for the large scale behavior in the presence of modeled small scales, a filtering operation is performed. For filter type, we adopted the implicit filtering and the filter is assumed to be the grid size, i.e., the scales larger than the grid size are resolved and the scales smaller than the grid size are modeled. The filtered continuity and Navier–Stokes equations read as

$$\frac{\partial \bar{u}_i}{\partial x_i} = 0 \tag{1}$$

and

$$\frac{\partial \bar{u}_i}{\partial t} + \frac{\partial (\bar{u}_i \bar{u}_j)}{\partial x_j} = -\frac{1}{\rho}\frac{\partial \bar{p}}{\partial x_i} + \frac{\partial}{\partial x_j}\left(\nu \frac{\partial \bar{u}_i}{\partial x_j}\right) - \frac{\partial \tau_{ij}^{\mathrm{SGS}}}{\partial x_j} + 2 \in_{ijk} \Omega_j \bar{u}_k \tag{2}$$

respectively. The last term of Eq. (2) is the Coriolis force contribution. As is customary, the centrifugal force is combined with the pressure gradient since it is conservative [31]. The SGS stresses

[1]Corresponding author.

Contributed by the Fluids Engineering Division of ASME for publication in the JOURNAL OF FLUIDS ENGINEERING. Manuscript received September 10, 2007; final manuscript received May 8, 2008; published online August 12, 2008. Assoc. Editor: Paul Durbin.

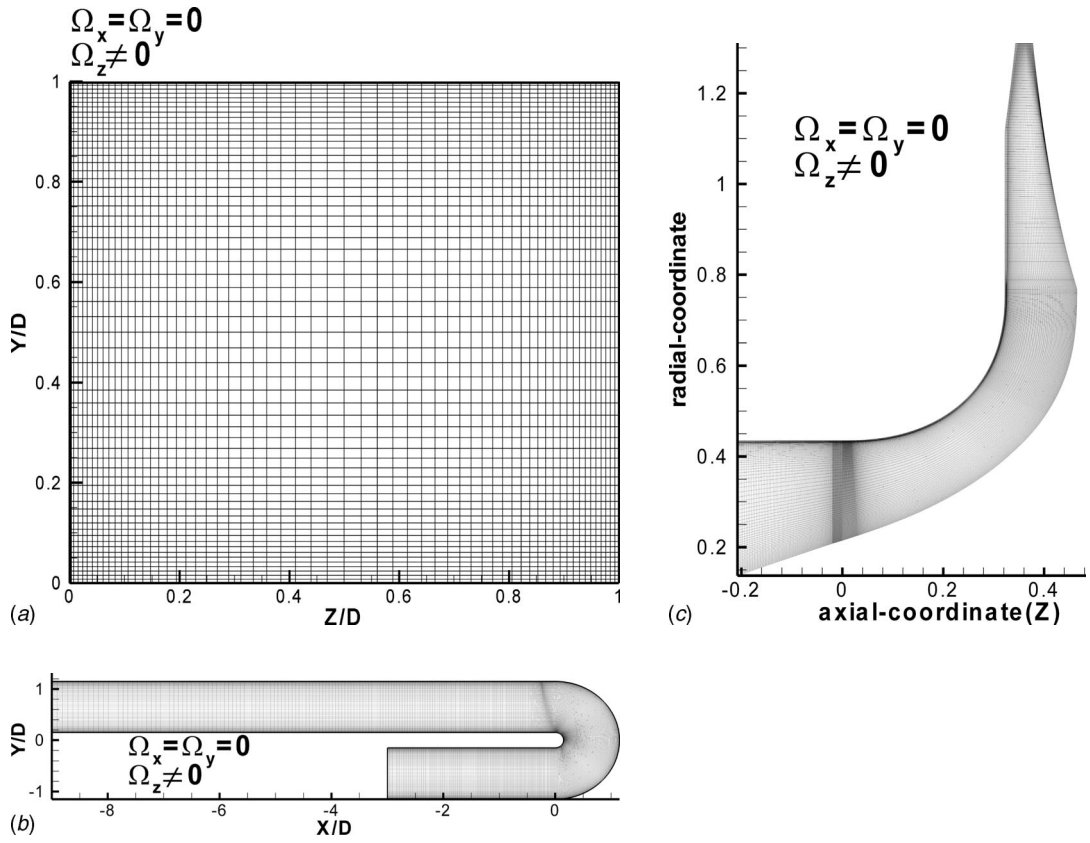

Fig. 1 Cross sections of the computational mesh. (*a*) Rotating straight duct. (*b*) Rotating *U*-duct. (*c*) Centrifugal compressor.

(τ^{SGS}) are modeled using the wall-adapting local eddy-viscosity (WALE) model [36]. In the WALE model, the SGS viscosity is defined as

$$\nu_{SGS} = (C_w\Delta)^2 \frac{(S_{ij}^d S_{ij}^d)^{3/2}}{(\bar{S}_{ij}\bar{S}_{ij})^{5/2} + (S_{ij}^d S_{ij}^d)^{5/4}} \tag{3}$$

where $C_w=0.1$ is the model coefficient, Δ is the filter width, $S_{ij}^d = \frac{1}{2}(\bar{g}_{ij}^2 + \bar{g}_{ji}^2) - \frac{1}{3}\delta_{ij}\bar{g}_{kk}^2$, and $\bar{g}_{ij} = \partial\bar{u}_i/\partial x_j$. Since $S_{ij}^d S_{ij}^d$ behaves like $O(y^{+2})$ near the wall, $(S_{ij}^d S_{ij}^d)^{3/2}$ becomes $O(y^{+3})$. The denominator of Eq. (3) is O(1) since $\bar{S}_{ij}$ is O(1). In order to avoid ill conditioning, $(S_{ij}^d S_{ij}^d)^{5/4}$ is added in to the denominator. $(S_{ij}^d S_{ij}^d)^{5/4}$ is $O(y^{+5/2})$ and negligible near the wall. With this form, Eq. (3) becomes $O(y^{+3})$ with any ad hoc manipulation. However, in the Smagorinsky model [37], the SGS viscosity is defined as $\nu_{SGS} = (C_s\Delta)^2|\bar{S}|$ where C_s is the model coefficient and $|\bar{S}| = \sqrt{2\bar{S}_{ij}\bar{S}_{ij}}$. The SGS has the incorrect wall-behavior of O(1) since S_{ij} is O(1).

The governing differential equations for Eqs. (1) and (2) are solved via a finite-volume code, FLUENT [38], based on the projection method of Chorin [39]. For all calculations, a bounded second-order central differencing scheme [40] is used for the convection term in order to eliminate the unphysical wiggles, caused when a pure classical central differencing scheme is employed [41]. A fully second-order implicit scheme is applied for the temporal discretization. The pressure-implicit with splitting of operators (PISO) algorithm [42] and pressure staggering option (PRESTO) scheme [43] are adopted for the pressure-velocity coupling and the pressure interpolation, respectively. The set of linearized equations is solved by the Gauss–Seidel method, which is coupled with an algebraic multigrid method to accelerate convergence.

3 Model Cases

Cross-sectional views of the computational grid for numerically simulated cases are shown in Fig. 1. Three cases are investigated: the fully developed flow in a straight square duct with spanwise rotation (Fig. 1(*a*), Case 1), the flow in a *U*-duct with positive or negative rotation about the *z*-axis (Fig. 1(*b*), Case 2), and the flow in a centrifugal compressor for which only the impeller (between $z=0$ and radial coordinate$(r)=0.78$) rotates (Fig. 1(*c*), Case 3). For Case 1, the Reynolds number ($\mathrm{Re}=U_bD/\upsilon$, U_b is the bulk velocity, D is the width of the duct, and υ is the kinematic viscosity) is 4410 and the rotation number ($\mathrm{Ro}=\Omega D/U_b$, where Ω is the rotation rate) varies between 0 and 5. The straight square duct has dimensions of $6.28D\times D\times D$ and a grid resolution of $64\times 60\times 60$ in streamwise (x), wall-normal (y), and spanwise (z) directions, respectively. A fully structured hexahedral mesh with stretching near walls is used, as shown in Fig. 1(*a*). This geometry is adequate to capture the largest structures in the streamwise direction [44]. A nondimensional time step ($\Delta tU_b/D$) of 0.05 is employed. This corresponds to a Courant-Friedrichs-Lewy (CFL) number ($\Delta tU_b/\Delta x$) of 0.51. Periodic boundary conditions are applied in the streamwise direction to ensure fully developed flow. Constant mass flow rate is adopted to drive the flow in the streamwise direction. No-slip boundary conditions are applied on the enclosed walls (i.e., wall-normal and spanwise directions).

In the *U*-duct case, a developing turbulent flow enters a 180 deg bend of square cross section ($D\times D$) with a curvature ratio of $R_c/D=0.65$, where R_c is the curvature radius of the bend and D is the width of the duct. The upstream bend length is set at $3D$ whereas to avoid any reverse flow at the outlet domain the downstream bend length is taken as $9D$. The Reynolds number ($\mathrm{Re}=U_bD/\nu$) is 10^5. Two rotating cases are investigated similar to

the experimental study [22]: one with a positive rotation (where the rotation axis is the same as the curvature axis, i.e., counterclockwise) and the other with a negative rotation (where the rotation axis is in opposite sense to the curvature axis, i.e., clockwise). The rotation axis is located at $x=-4.5D$. The rotation number ($\mathrm{Ro}=\Omega D/U_b$) is ± 0.2 depending on the rotation mode. The Coriolis and centrifugal forces reinforce each other for the positive rotating case, whereas these forces oppose each other for the negative rotating case. Grid dependency test [45] showed that there is no significant variation between the results for 4.5×10^6 and 9×10^6 computational cells. The fine grid is distributed as $900\times100\times100$ in the streamwise, wall-normal, and spanwise directions. Grid cells are clustered near the walls, so that the first cell next to the wall boundaries falls within the viscous sublayer $y^+<5$. The information of the other grid topologies adopted for this case can be found in Ref. [45]. Structured hexahedral cells are used in the area upstream and downstream of the bend, which is coupled by a conforming interface with unstructured hexahedral cells in the bend section, as seen in Fig. 1(*b*). A nondimensional time step ($\Delta t U_b/D$) of 0.002 is employed based on the temporal dependency test. No-slip boundary conditions are applied at the inner, outer, and lateral walls. At the inlet, mean velocities are interpolated from the experimental study and perturbed with the random vortex method, as explained in Refs. [45,46]. At the exit, outflow boundary conditions are used, resulting in zero-velocity flux for all flow variables and the satisfaction of overall mass balance correction.

The centrifugal compressor chosen for this study is a low-speed compressor with a vanesless diffuser [47]. Considering the Reynolds number and compressibility effects, low-speed centrifugal compressors (LSCCs) are more suitable for LES methodologies than their high-speed counterparts. The LSCC comprises 20 full impeller blades with a 55 deg backsweep angle. The design tip speed is 153 m/s. The inlet and exit diameters of the impeller are 87 cm and 152.4 cm. The corresponding widths of the impeller blades at the inlet and the exit are 21.8 cm and 14.1 cm, respectively. The LSCC flow field had a design mass flow rate of 30 kg/s and a rotating speed of 1862 rpm. This rotational speed corresponds to a rotation number of 0.6 based on the inlet hydraulic diameter and the bulk velocity. Three different grids were initially tested [45]. The final mesh chosen on the basis of grid dependency test consisted of $1111\times136\times150$ grid cells in the streamwise, spanwise, and pitchwise directions, respectively. A fully conforming and structured hexahedral mesh was used, as shown in Fig. 1(*c*). The time step employed for the predictions is 1.6×10^{-5} s. Temporal and spatial resolutions are calculated on the basis of various flow scales, i.e., the Taylor and the Kolmogorov scales [48]. It is seen that both the spatial and temporal resolutions of LES are sufficient to capture scales of the order of Taylor scales. With the current grid resolution, y^+ values on the walls are kept to be less than 5 to be able to resolve the viscous sublayer. The flow inside the impeller is assumed to be rotating at the impeller speed (1862 rpm). Impeller blades and the attached hub surface also rotate at 1862 rpm. No-slip boundary conditions are applied to all nonrotating solid walls, i.e., shroud casing and the hub surface downstream of the impeller section.

4 Verification Cases

LES predictions are verified with the DNS data of Moser et al. [49] (MKM) and Alveluis [50] (AL) for the stationary channel flow. For the spanwise-rotating channel flow, the DNS data of Kristoffersen and Andersson [32] (KA) is utilized for validation of numerical results. For the simulations of stationary and rotating channel flows, in addition to the WALE model, the dynamic Smagorinsky [51] (DYN) and the dynamic kinetic energy [52] (DYNKE) model results are also presented.

Figure 2 shows the results for the mean velocity (Fig. 2(*a*)) and the mean turbulent kinetic energy (Fig. 2(*b*)) for the stationary

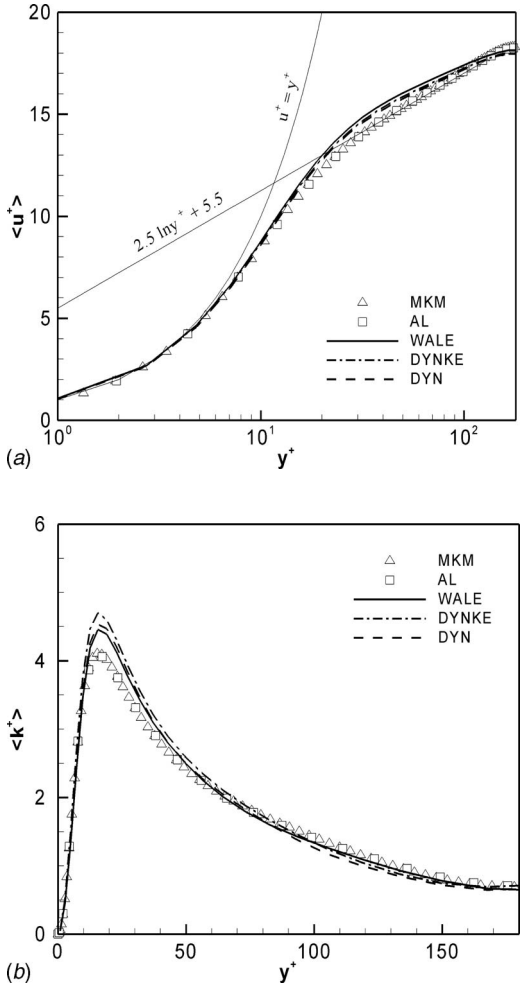

Fig. 2 Stationary channel flow in wall coordinates. (*a*) Mean velocity. (*b*) Mean turbulent kinetic energy. (△) DNS of Moser et al. [49], (□) DNS of Alveluis [50], (—) WALE model, (–·–·–) DYNKE model, and (-----) DYN model

turbulent channel flow at $\mathrm{Re}=5600$. The grid used was 64^3 and the domain taken was $3.2D\times D\times1.6D$. As seen from Fig. 2, the mean velocity predictions are in good agreement with the DNS data. However, all the tested SGS models overpredict the turbulent kinetic energy peak with the WALE model performing slightly better than the DYN and DYNKE models.

Mean velocity and the turbulent kinetic energy predictions for the rotating channel flow are presented in Fig. 3. The Reynolds number is the same as that used for the stationary channel flow. The rotation number is $\mathrm{Ro}=0.5$. It is well known that a region exists in a rotating channel flow (Fig. 3(*a*)) where $\partial U/\partial y=2\Omega$, which represents neutral stability [31,32]. Near the pressure side (PS) ($y/2D=0$), the flow destabilizes due to the enforcing effects of the Coriolis force and the primary shear. Near the suction side (SS) ($y/2D=2$), on the other hand, the Coriolis force and the primary shear oppose each other and thus the flow stabilizes. When the flow stabilizes, the turbulence is suppressed and the laminarization takes place. The SGS model predictions, are in excellent agreement with the DNS data for the mean velocity. On the other hand, for the turbulent kinetic energy predictions, there is a slight discrepancy in the numerical predictions when compared to the experimental results, especially close to the SS, as seen in Fig. 3(*b*). However, the WALE model is seen to perform better than the other SGS models in this case as well. Hence, only the WALE model is adopted for the rest of the simulations in this study.

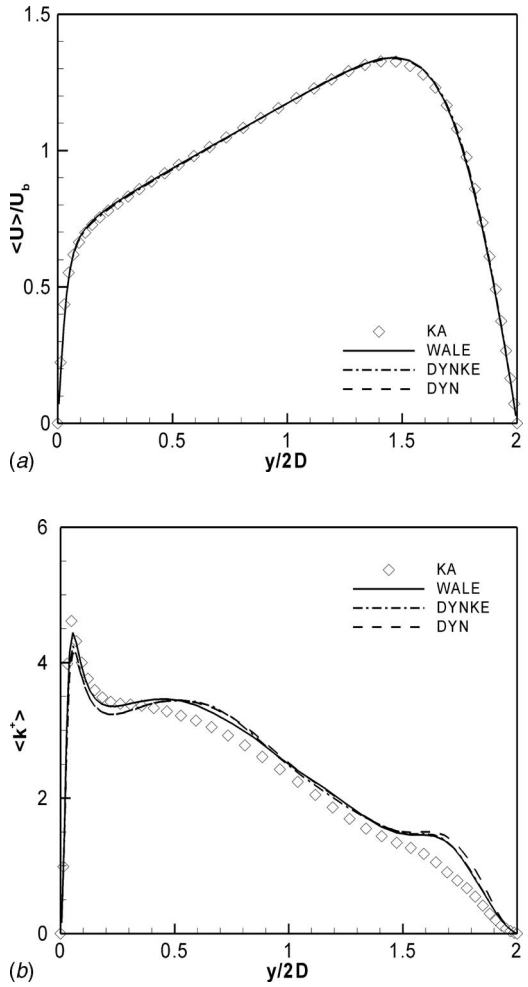

Fig. 3 Rotating channel flow results in global coordinates. (*a*) Mean velocity. (*b*) Mean turbulent kinetic energy. (◇) DNS data of Kristoffersen and Andersson [32], (—) WALE model, (–·–·–) DYNKE model, and (-----) DYN model.

5 Results and Discussion

The laminarization process is discussed initially considering the flow in a rotating square duct. The first known LES study for a rotating square duct conducted by Pallares and Davidson [35] is limited to Ro=0.12. Pallares et al. [53] further performed rotating duct simulations up to Ro=6.6. However, they discussed mostly the effect of rotation on the convection heat transfer. A complete laminarization study for a rotating duct is still not available in literature. Therefore, a part of this study is dedicated to the discussion of the complete laminarization process in the rotating straight square duct.

Figure 4 demonstrates the mean primary (top subfigures) and the mean secondary flow (bottom subfigures) distributions on the cross section of the rotating square duct. Only half of the cross section is shown since the mean flow is symmetric about the wall bisector ($Z/D=0.5$). The bottom and the top walls for each of the subfigures represent the PS and the SS, respectively. Contrary to the channel flow, a low-velocity region is observed near the SS starting from Ro=0.05. Near the SS at Ro=0.2, contour lines of the primary flow tend to be horizontally aligned. This causes $\partial U/\partial z \approx 0$ and is generally referred to as the Taylor–Proudman regime [35]. However, very close to the PS, a low-velocity region is also evident. The distortion of the mean flow resulting in this low-velocity region is attributed to the regeneration of turbulence, which starts when Ro=0.2. The region, where $\partial U/\partial z \approx 0$, enlarges as Ro number increases, ultimately leading to a uniform velocity profile and the disappearance of the primary flow anisotropy near the corners. The rotation not only causes asymmetry of the primary flow, but also leads to a merging of the corner vortices. For the stationary case, the corner vortices are known as the secondary flows of Prandtl's second kind. These secondary flows are a direct result of the imbalance of the turbulence stresses near the corners and can hence only occur in turbulent flows. Following closely from left to right the bottom subfigures of Fig. 4, one observes that as a result of the merging process of the corner vortices in the rotating case, a large vortex is formed near the SS. After the merging process, a small vortex appears near the pressure corner at Ro=0.05. At Ro=0.2, the larger vortex (vortex due to the merging process) moves slightly towards the lateral wall, getting thinner as compared to the vortex of the Ro=0.05 case. The smaller vortex, on the other hand, moves away from the corner while enlarging in size. At Ro=0.2, the bulging of the mean flow from the PS is therefore due to the vortex placed near the PS. This vortex convects the high-momentum flow near the PS towards the center of the duct along the wall bisector ($Z/D=0.5$). The secondary flow distributions at Ro=0.5 and Ro=1 show that this vortex has now moved towards the corner and has substantially decreased in strength and size. Meanwhile, the top (merging process) vortex, which was centered on $Y/D=0.5-0.6$, is further stretched along the lateral wall. Both these vortices eventually disappear at Ro=5. Interestingly, at the same time, with the disappearance of the vortices the contours of the primary flow have aligned themselves perfectly with the pressure and suction surfaces. During this process, the secondary streamlines become aligned with the lateral walls. Therefore, the primary flow contours and the secondary flow streamlines seem to be highly correlated at high rotation numbers.

As reported by many authors [31,32,35,53] as the rotation rate increases, the time-averaged wall shear stress increases on the PS and decreases on the SS. This increase in the wall shear stress near the PS is strongly related to the flow instability, which is triggered by the enhancement of the turbulence. On the other hand, the decrease in wall shear stress is due to the laminarization or flow stability near the SS. As shown logarithmically in Fig. 5, the wall shear stress increases and approaches unity at higher rotations at the SS. At the PS, on the other hand, it increases to Ro=1 and decreases after that, tending to unity analogous to the SS. The increase in the SS and the decrease in the PS can be attributed to changes in the velocity gradients near the walls, which were observed from Fig. 4. Unlike the PS and SS walls, the wall shear stress rises gradually at the lateral wall due to the strong secondary flow and the decrease in the boundary layer thickness. It is observed that the increase after Ro>0.2 is, in fact, linear on the logarithmic plot and can be analytically expressed analytically as

$$\ln(\mathrm{Ro}) = A \ln(\tau/\tau_0) + B \tag{4}$$

where τ and τ_0 represent the wall shear stress at the particular Ro number and the wall shear stress at zero rotation, respectively. In Eq. (3), it is found that $A=2.125$ and $B=-3.227$. This expression could be of use especially for the turbulence model developers and users regarding the development of advanced wall functions in the case of laminarization. Concerning the use of wall functions in a finite-volume calculation like the one considered here, it is of the utmost importance that the wall shear stress be accurately related to the tangential velocity of the nearest cell to the wall.

The volume-averaged turbulent kinetic energy and the contributions of Reynolds normal stresses to the turbulent kinetic energy for a square duct are shown in Fig. 6. At Ro=0, the volume-averaged turbulent kinetic energy is predicted by the DNS of Ref. [44] as 0.97 and by the current LES as 1.05. This corresponds to 8% difference between two numerical studies. Similar to the study of Pallares and Davidson [35], the mean turbulent kinetic energy decreases due to the suppression of $\langle u'^2 \rangle$ (streamwise normal stresses) while $\langle v'^2 \rangle$ and $\langle w'^2 \rangle$ stresses remain fairly constant. The

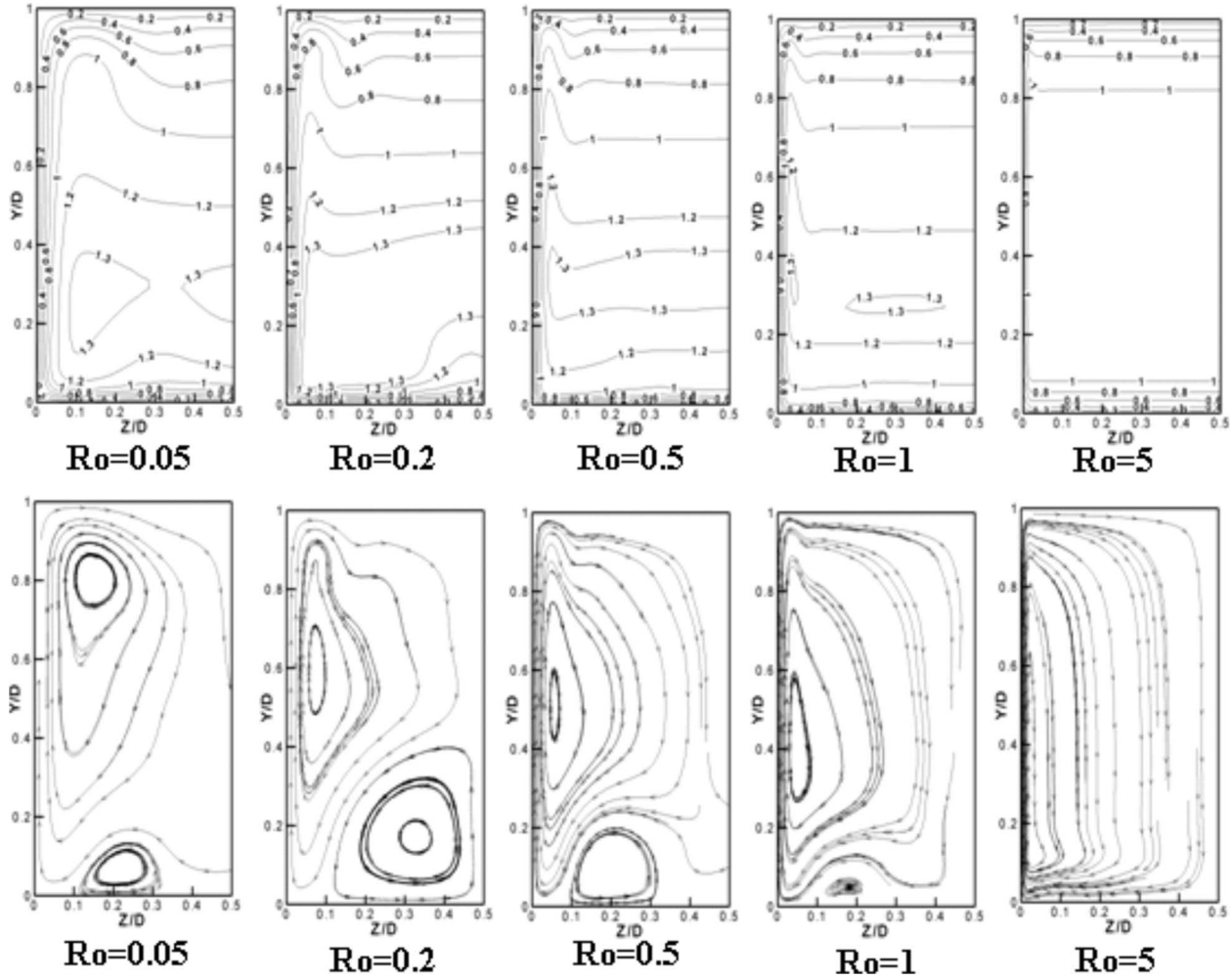

Fig. 4 Mean primary flow contours (top subfigures) and secondary flow distributions (bottom subfigures) for the square duct

maximum rate of decrease in the turbulent kinetic energy takes place as Ro increases from 0.05 to 0.1. The production term for $\langle u'^2 \rangle$ decreases as the flow experiences the Taylor–Proudman regime and thus $\langle u'^2 \rangle$ decreases. The rate of laminarization de-

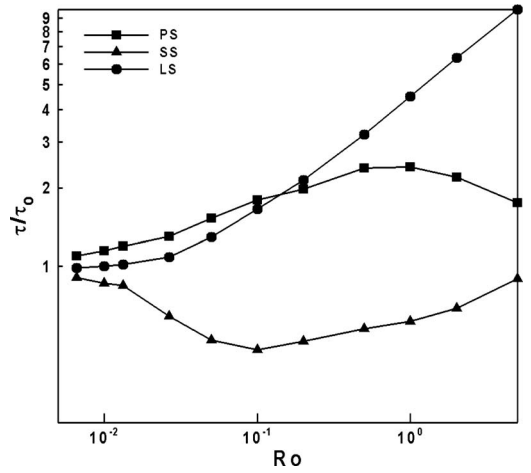

Fig. 5 Plane-averaged wall shear stress on the enclosed walls of the square duct. (PS: pressure side, SS: suction side, and LS: lateral side).

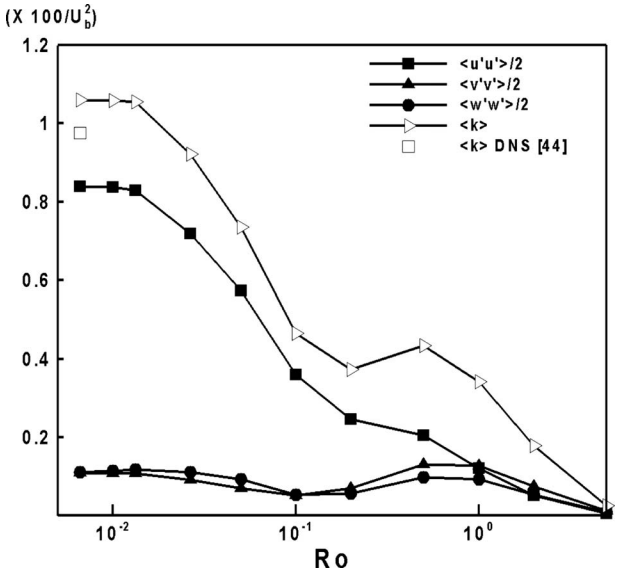

Fig. 6 Volume-averaged mean turbulent kinetic energy and turbulent normal stresses for the square duct

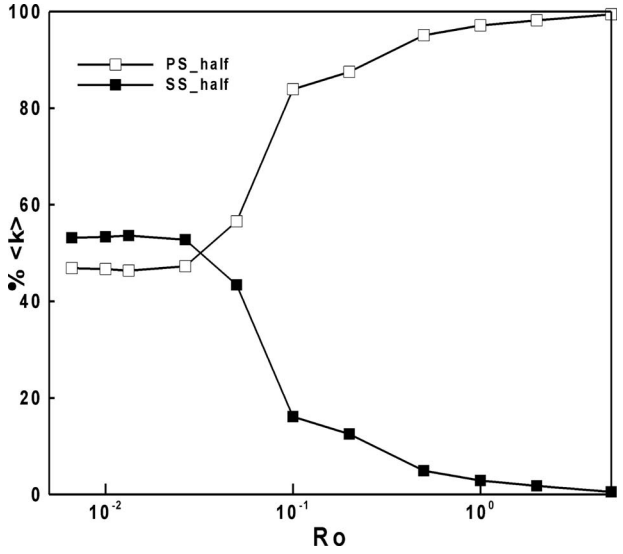

Fig. 7 Distribution of the volume-averaged mean turbulent kinetic energy for the square duct

creases as Ro increases from 0.1 to 0.2. For Ro from 0.2 to 0.5, $\langle u'^2 \rangle$ continues to decrease, while $\langle v'^2 \rangle$ and $\langle w'^2 \rangle$ start to increase again, reintroducing turbulence and thus causing enhancement of turbulent kinetic energy to Ro=0.5. This behavior can be explained by the contribution of volume-averaged Reynolds budget terms of normal stresses, as will be discussed later. The increase in $\langle v'^2 \rangle$ and $\langle w'^2 \rangle$ is stabilized as Ro approaches to 1, after which the behaviors of $\langle v'^2 \rangle$ and $\langle w'^2 \rangle$ become the same as that of $\langle u'^2 \rangle$, i.e., decreasing. All turbulent normal stresses reduce to zero at Ro=5, and hence at this rotation number one could safely assume the flow to be purely laminar.

Figure 7 shows the percentage distribution of the turbulent kinetic energy for the PS ($Y/D<0.5$) and SS ($Y/D>0.5$) halves of the square duct. When Ro is less than 0.025, turbulence balance is distributed approximately as 45% for the PS half and 55% for the SS half of the duct. As Ro number increases from 0.025 to 0.05, the scenario reverses with most of the turbulence being accumulated on the PS half instead of on the SS half. As the Taylor–Proudman regime becomes more significant starting from Ro =0.05 to 0.1, the percentage of the turbulent kinetic energy increases from around 60–80%. With an increase in the rotation rate, this ratio becomes even greater. When the turbulence field develops for the Ro=0.5 case, more than 90% of the turbulence takes place on the PS half. This suggests that the turbulence is globally reduced in a rotating fully developed duct with the laminarization process mostly taking place on the SS.

Figure 8 shows the variations of the volume-averaged Reynolds stress budget terms (production P, dissipation ε, pressure strain ϕ, and production due to rotation G: See Appendix) as a function of the rotation number. Corresponding to the reduction in $\langle u'^2 \rangle$, P_{11} decreases to Ro=0.2. When Ro$\leq$0.2, P_{11} is balanced by ε_{11} and G_{11}. While Ro increases from 0.2 to 0.5, $\langle u'^2 \rangle$ still reduces in spite of a slight increase in turbulent kinetic energy as shown before in Fig. 6. P_{11} increases at Ro=0.5; however, ε_{11} and G_{11} also significantly increase despite the loss. This is the reason for the decrease of $\langle u'^2 \rangle$ at Ro=0.5. At higher rotations, Ro$>$1, $\langle u'^2 \rangle$ is primarily reduced by G_{11} rather than ε_{11}. The reason for the enhancement of $\langle v'^2 \rangle$ and $\langle w'^2 \rangle$ in the reproduction region of the turbulent kinetic energy (Ro=0.2–0.5) is accounted for by the abrupt change in the production due to the rotation term G_{22} and the pressure strain term ϕ_{33}, respectively. It is widely known that $\langle u'^2 \rangle$ extracts energy from mean flow gradient and distributes it to $\langle v'^2 \rangle$ and $\langle w'^2 \rangle$. This relation does not seem to be valid anymore

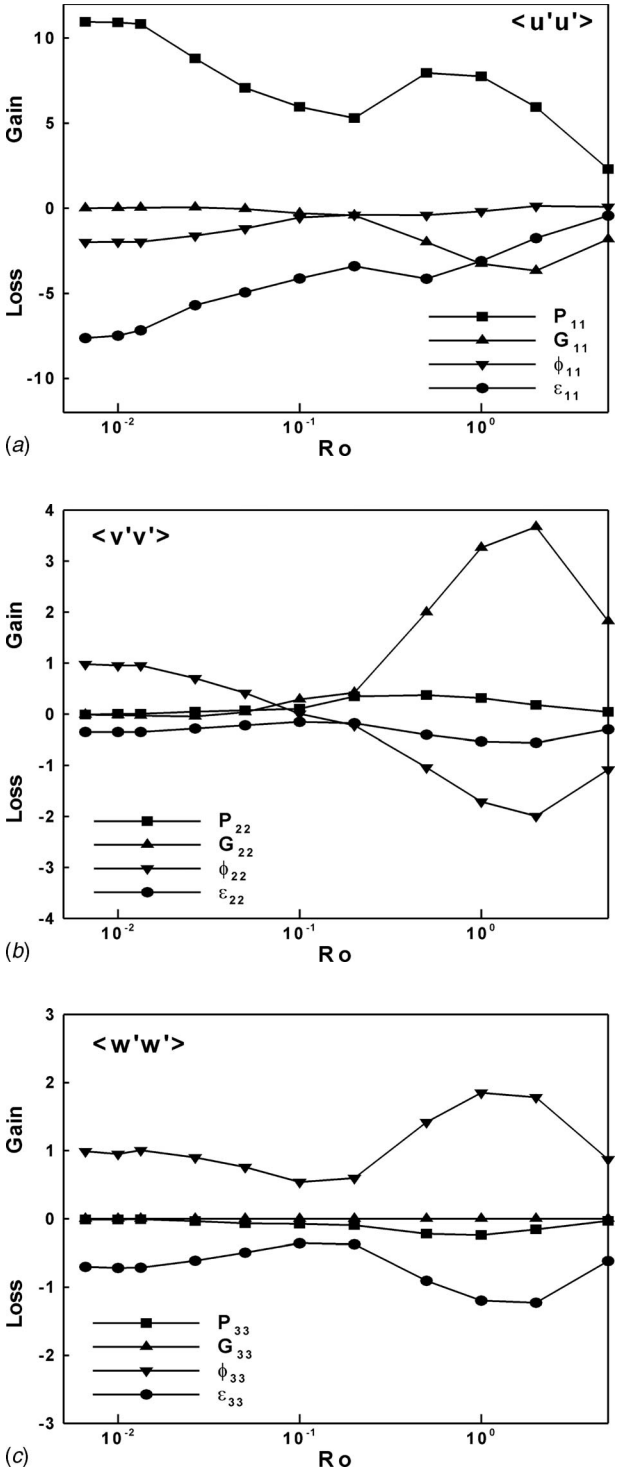

Fig. 8 Volume-averaged Reynolds stress budget terms for the square duct. $\langle u'u' \rangle$ (*a*), $\langle v'v' \rangle$ (*b*), and $\langle w'w' \rangle$ (*c*).

when Ro$>$0.1. $\langle u'^2 \rangle$ still distributes its energy to $\langle w'^2 \rangle$, but not to $\langle v'^2 \rangle$. Since ε_{11} is insufficient to balance G_{22} alone, the pressure strain term for $\langle v'^2 \rangle$ also becomes a loss term.

In RANS models, model coefficients are generally based on the empirical observations. In standard k-ε equation model, the calculation of the coefficient $C\mu$ is based on the equality between the production (P) and the dissipation (ε) of the turbulent kinetic energy. However, this equality generally is not valid for most of the flows. Figure 9 shows the ratio of P/ε for the rotating square

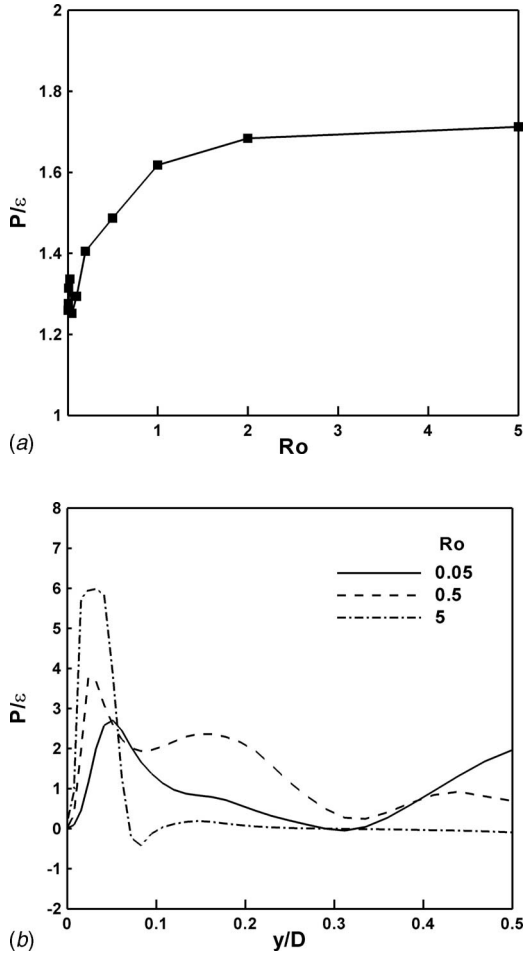

Fig. 9 The ratio of the production to the dissipation for the square duct. Volume-averaged distribution (*a*). Wall-normal distribution on $Z/D=0.5$ (*b*).

duct. In Fig. 9(*a*), the volume average of P/ε is presented as a function of Ro. At low Ro, this ratio varies between 1.2 and 1.4. Starting from Ro=0.2, P/ε increases logarithmically, stabilizing around 1.7 at high Ro where the laminarization is strong. Figure 9(*b*) shows the wall-normal distribution of P/ε along the wall-bisector ($Z/D=0.5$). At Ro=0.05, there is already an asymmetry in P/ε distribution. At the moderate Ro, corresponding to the results in Fig. 9(*a*), P/ε values are substantially higher than those at Ro=0.05. Strong laminarization process can also be deduced form this P/ε distribution at Ro=5. After $y/D=0.1$, P/ε collapses to zero up to the SS. Although the flow is globally laminar, there exists a slightly energetic region ($0<y/D<0.1$) where P/ε suddenly increases to a peak value of 6. This is more than twice the peak value at Ro=0.05. Then, P/ε decreases rapidly and collapses to zero after $y/D>0.1$.

Figure 10 shows the mean streamwise velocity (Fig. 10(*a*)) and the mean turbulent kinetic energy (Fig. 10(*b*)) contours on the midspan plane ($Z/D=0$) of a U-duct for the stationary case. Towards the bend inlet, developing turbulent flow accelerates near the inner wall and decelerates near the outer wall. This is due to the favorable and adverse pressure gradients at the inner and outer walls, respectively. Due to the strong curvature, the flow separates from the inner bend around $\phi\approx 90$ deg (the half bend location). The flow reattaches to the inner wall at around $1.8-2.0D$ downstream of the bend. In contrast to the separation region after the bend exit, the flow accelerates causing a high-velocity region. Further downstream of the bend, the flow near the outer wall

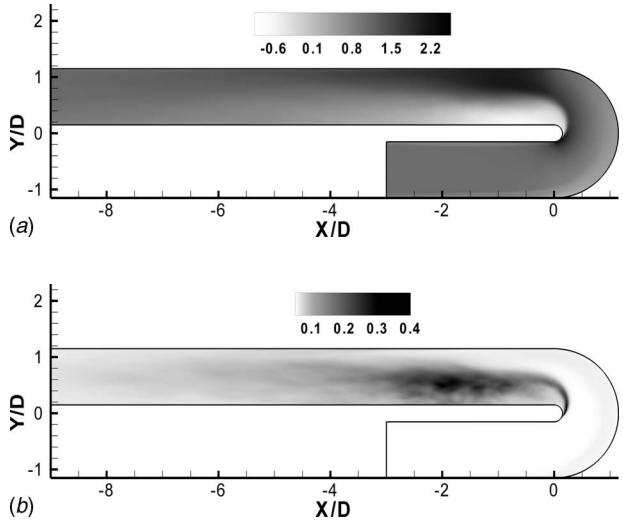

Fig. 10 Contours of mean streamwise velocity $\langle U\rangle/U_b$ (*a*) and mean turbulent kinetic energy $\langle k\rangle/U_b^2$ (*b*)

decelerates corresponding to the recovery of the separation region. The mean turbulent kinetic energy distribution is somewhat akin to the mean velocity distribution. There is a slight increase in mean turbulent kinetic energy near the outer bend corresponding to the flow deceleration. Downstream of the bend exit, near the inner wall, turbulence is noticeably increased due to the separation. However, after the reattachment of the flow, turbulence decreases considerably resulting in a fully developed flow towards the exit of the duct. In contrast to the high levels of turbulence in the separation region, the flow is relatively calm near the outer wall due to the high-momentum flow.

In order to see the laminarization process in the *U*-duct subjected to positive or negative rotations, turbulent kinetic energy results for the rotating cases are normalized by those of the stationary case. This nondimensionalization points to the following predicted behavior:

$$k_{\mathrm{Ro}}/k_0-1>0 \quad \text{for turbulent enhancement}$$

$$k_{\mathrm{Ro}}/k_0-1<0 \quad \text{for turbulent suppression} \tag{5}$$

Here, k_0 and k_{Ro} represent the mean turbulent kinetic energy for the stationary and rotating cases, respectively. Figure 11 demonstrates the contours of k_{Ro}/k_0-1 for the positive (Fig. 11(*a*)) and negative rotating (Fig. 11(*b*)) cases. In these contour plots, light gray regions represent the laminarization trend of the flow whereas the dark regions represent the enhancement of turbulence. As seen from Fig. 11, turbulence is significantly suppressed for the positive rotating case especially after $\phi=90$ deg. On the other hand, turbulence is considerably enhanced in the negative rotating case. In the positive rotating case, turbulence suppression takes place both in the separation region and near the outer wall. In the negative rotating case, the enhancement of the turbulence is observed near the outer wall only. Both the suppression and enhancement processes vanish far downstream of the bend.

A possible explanation for these processes can be offered by the secondary flow behavior, as depicted in Fig. 12. At the bend exit in the stationary case, two pairs of vortices are formed: one close to the inner wall at $Y/D=1$ and the other is close to the lateral wall at around $Z/D=-0.5$. These vortices that develop due to strong curvature effects were observed and successfully analyzed in the aforementioned study of rotating channel flow. Secondary flows presented in this study are responsible for extracting the fluctuating energy from the primary flow (especially around the separation region) and transferring it to the flow close to the outer wall. For the positive rotation, where the primary Coriolis force is

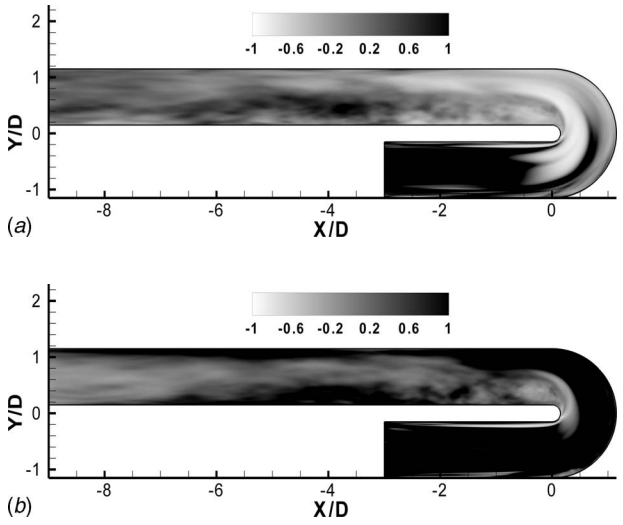

Fig. 11 Contours of k_{Ro}/k_0-1 for positive rotating (*a*) and negative rotating *U*-ducts (*b*)

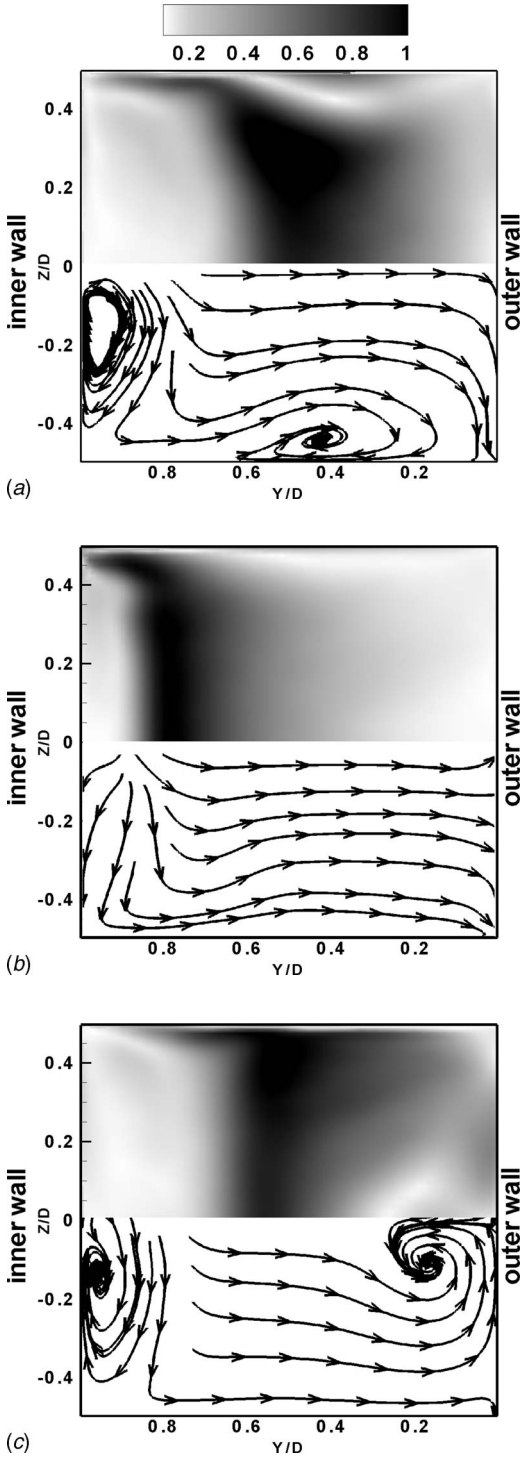

Fig. 12 Secondary velocity contours ($\langle V\rangle^2+\langle W\rangle^2)^{0.5}/U_b$ and streamlines at the bend exit for stationary (*a*) positive rotating (*b*) and negative rotating cases (*c*)

in the same direction of centrifugal force, vortices disappear and the secondary flow becomes less intense while approaching the outer wall. The primary reason for the suppression of the turbulence in the positive rotating case is thus attributed to the disappearance of the secondary vortices due to the interaction of the Coriolis force and the centrifugal forces. For the negative rotating case, secondary flow behaves in stark contrast to the positive rotation case, i.e., extracted fluctuating energy is transferred along the outer walls. This energy is subsequently transferred towards the midregion of the outer wall via the vortex generated due to the opposing effects of the Coriolis and the centrifugal forces. Hence, the negative rotating case depicts higher turbulence levels than the stationary case.

The centrifugal compressor is the final case presented in this paper. This case is simulated according to the given physical rotation rate of $\Omega=1862$ rpm. In order to assess the physics of laminarization, the case is also simulated at $\Omega=0$ rpm (Ro=0) with the same boundary conditions and the discretization procedures. Figure 13 shows the meridional view of the normalized turbulent kinetic energy distribution ($100\sqrt{k}/U_{tip}$, where U_{tip} is 153 m/s) on the midspan plane for the rotating case (Fig. 13(*a*)) and the stationary case (Fig. 13(*b*)). As can be seen, turbulence in the rotating case is significantly suppressed compared to the stationary case. Nevertheless, there is still a high-turbulent region close to the shroud side in the rotating case. Turbulence in this region is due to the tip wake having a direct effect on the efficiency of the compressor, which has been the subject of attention of a number of past studies.

Figure 14 demonstrates the normalized turbulent kinetic energy distribution on cross-sectional planes in the impeller. The results from the rotating case are presented on the left-hand side whereas the stationary case results are shown on the right-hand side of this figure. For the rotating case at $m_i/m=0.149$ (m_i/m is the ratio of the meridional distance from the impeller inlet to the total impeller meridional length), turbulence is seen to originate from the SS (low-pressure) region. In the stationary case, turbulence is significantly enhanced near the PS/shroud surface. The tip jet flow, caused by the pressure difference between the PS and SS, convects the turbulence in the passage. At $m_i/m=0.644$, high-turbulence region is enlarged, but laminarizing effects of the Coriolis force still exist for most of the region. Turbulence near the blade root on the SS is higher in comparison to previous station, which is believed to be due to the interaction of the boundary layer with the tip jet. At $m_i/m=0.99$, turbulence is diffused completely for zero rotation, whereas the turbulence is still low in the hub half side for the rotating case.

In engineering cases, it is important to quantify the quality of LES predictions and assess the possible enhancements/deficiencies compared to RANS predictions. Along with LES, the mixing length [54], k-ε [55], and k-w [56] RANS models were performed for the centrifugal compressor. The meridional velocity $\langle U_m\rangle$ comparisons are made where the flow is laminarized (Fig.

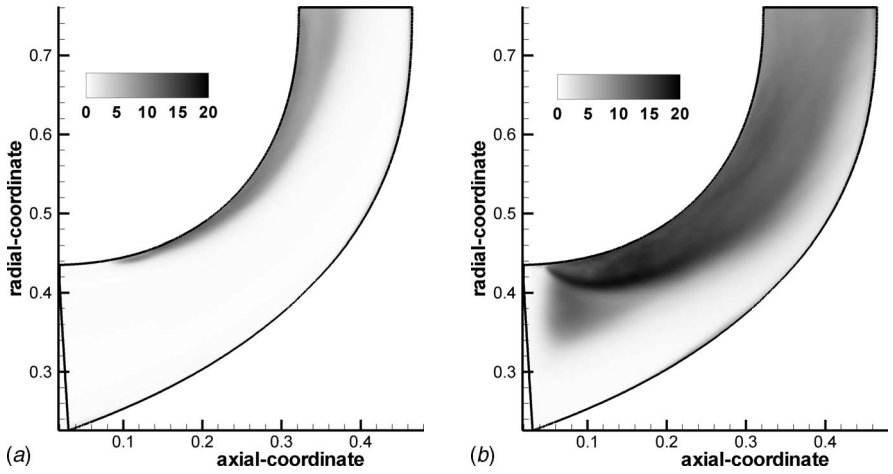

Fig. 13 Normalized turbulent kinetic energy distribution $100\times\sqrt{k}/U_{tip}$ on the midspan plane for the LSCC. First column: Ω=1862 rpm. Second column: Ω=0 rpm.

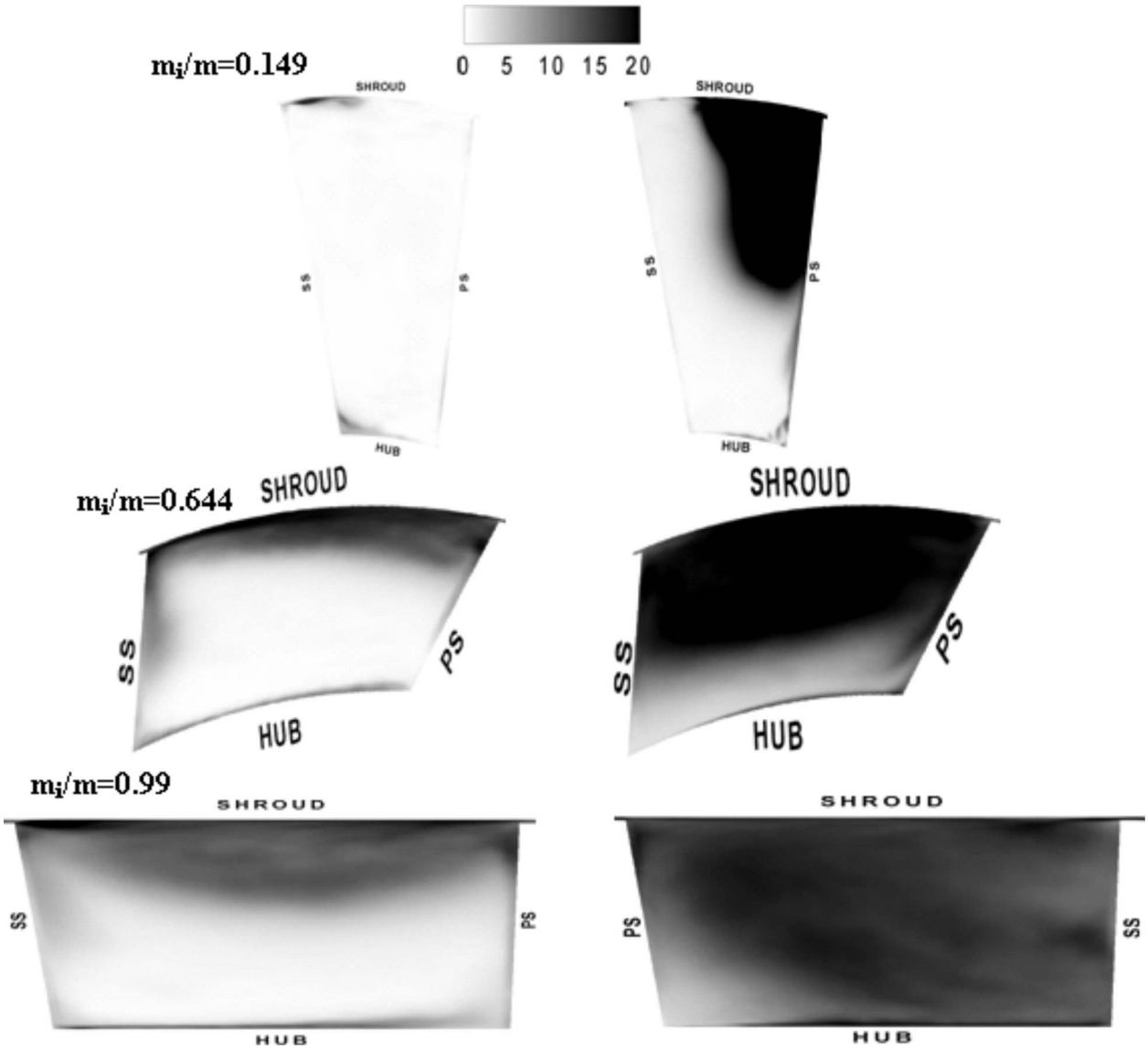

Fig. 14 Normalized turbulent kinetic energy distribution $100\times k/U_{tip}$ at the meridional cross sections for the LSCC. First column: Ω=1862 rpm. Second column: Ω=0 rpm.

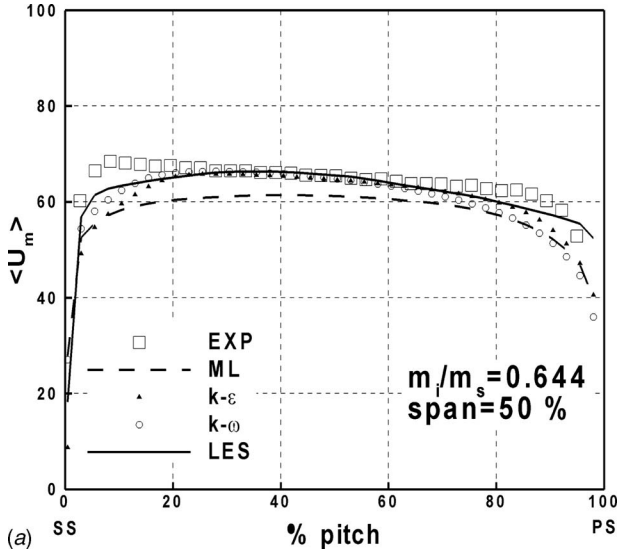

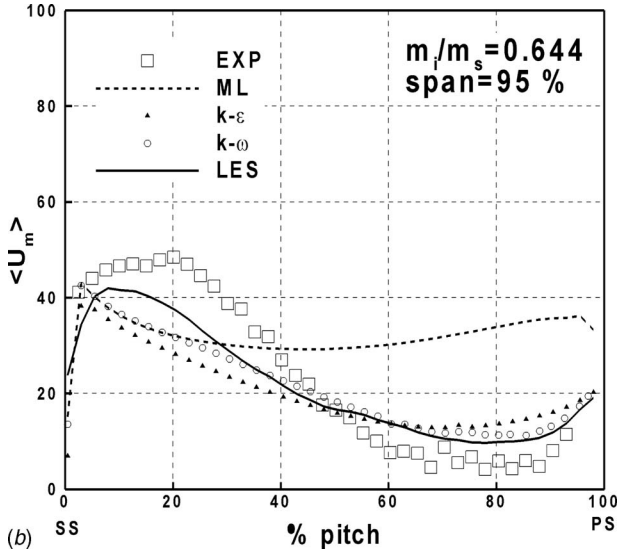

Fig. 15 The pitchwise (blade-to-blade) variation of the meridional velocity near the mid span (*a*) and near the shroud (*b*)

15(*a*)) and relatively turbulent (Fig. 15(*b*)). It is seen that LES predicts the meridional velocity better than the RANS models near the boundary layers. However, outside the boundary layers, LES predictions are almost the same as RANS predictions apart from the mixing-length model. At 95% span, where turbulence is significant, LES predictions are far better than the RANS models, as seen in Fig. 15(*b*).

The ease of applicability, substantially lower computational cost, and comparable predictions of RANS in the laminarized zone for the centrifugal compressor as compared to LES might explain the widespread usage of RANS for turbomachinery cases. However, if the boundary layers and the unsteadiness in the passage are considered, LES can be regarded as the more predictive choice. Furthermore, the current compressor geometry does not have any vanes in the diffuser section. For a vaned centrifugal compressor, unsteadiness and the boundary layer development would be substantially different. Thus, RANS models would not suffice the need for such a complex case.

6 Conclusion

In this paper, a laminarization study of the flow subjected to strong curvature and Coriolis force is presented. Three cases are investigated: the fully developed flow in a straight square duct with spanwise rotation, the turbulent developing flow in a *U*-duct with positive or negative rotation about the spanwise axis, and the flow in a centrifugal compressor.

It is seen that the turbulent kinetic energy does not decrease monotonically as the rotation number increases for the square duct. The diminishing rate of the decay of the turbulent kinetic energy displays a pronounced minimum at around Ro=0.2 where turbulence is reproduced due to the secondary flow being generated near the PS. This behavior is confirmed by an assessment of the Reynolds stress budget terms and is attributed to the vortex generated near the PS. In the *U*-duct case, turbulence is significantly enhanced in the negative rotating case, where the curvature and the Coriolis induced secondary flows oppose each other. On the other hand, for the positive rotating case, significant laminarization is observed near the outer wall where the Coriolis force has a diminishing influence on the existing secondary flow intensity. For the centrifugal compressor, turbulence is significantly suppressed in the entire impeller region apart from the tip leakage flow. LES was henceforth shown to perform better than RANS models in regions of significant turbulence intensity such as near the tip leakage flow region and inside the boundary layers.

Acknowledgment

The authors would like to thank to Professor Helge I. Andersson from Norwegian University of Science and Technology, Professor Arne Johansson from The Royal Institute of Technology in Sweden, and Dr. Michael D. Hathaway from NASA for providing the DNS and experimental data, which are used for comparisons in this paper.

Appendix

Derivation of Reynolds stress budget terms were explained by Daly and Harlow [57]. Briefly, they can be obtained when each momentum transport equation is multiplied by its counterpart velocity component. After the proper construction, this results in

$$\frac{\partial \langle u_i' u_j' \rangle}{\partial t} + U_k \frac{\partial \langle u_i' u_j' \rangle}{\partial x_k} = P_{ij} + G_{ij} + \varphi_{ij} + T_{ij} + PD_{ij} + D_{ij} + \varepsilon_{ij} \quad \text{(A1)}$$

The terms on the right-hand side in this equation represent the following process:

$$P_{ij} = -\langle u_i' u_k' \rangle \frac{\partial U_j}{\partial x_k} + -\langle u_j' u_k' \rangle \frac{\partial U_i}{\partial x_k} \quad \text{(A2)}$$

$$G_{ij} = -2\Omega_k (\langle u_j' u_m' \rangle \in_{ikm} + \langle u_i' u_m' \rangle \in_{jkm}) \quad \text{(A3)}$$

$$\varphi_{ij} = 2\frac{1}{\rho} \overline{p' \left(\frac{\partial u_i'}{\partial x_j} + \frac{\partial u_j'}{\partial x_i} \right)} \quad \text{(A4)}$$

$$T_{ij} = -\frac{\partial \langle u_i' u_j' u_k' \rangle}{\partial x_k} \quad \text{(A5)}$$

$$PD_{ij} = -\frac{1}{\rho} \frac{\partial}{\partial x_k} (\langle p' u_i' \rangle \delta_{jk} + \langle p' u_j' \rangle \delta_{ik}) \quad \text{(A6)}$$

$$D_{ij} = (v + v_{\mathrm{SGS}}) v \frac{\partial^2 \langle u_i' u_j' \rangle}{\partial x_k \partial x_k} \quad \text{(A7)}$$

$$\varepsilon_{ij} = -2(v + v_{\mathrm{SGS}}) \left\langle \frac{\partial u_i'}{\partial x_k} \frac{\partial u_j'}{\partial x_k} \right\rangle \quad \text{(A8)}$$

where P_{ij}, G_{ij}, φ_{ij}, T_{ij}, PD_{ij}, D_{ij}, and ε_{ij} denote production due to mean shear, production due to rotation, pressure strain, turbulent diffusion, pressure diffusion, viscous diffusion, and dissipation rate, respectively. Production due to mean shear arises as a result of the interaction of the mean flow gradient with the turbulent

shear stresses, thus representing energy extraction from the mean flow variation by velocity fluctuations. Similarly, production due to rotation comes about when the turbulent shear stresses are linked with the flow rotation. The main role of the pressure strain is in transferring energy from streamwise turbulent stresses to the spanwise and pitchwise stresses, providing the most important term in the case of the kinetic energy exchange. Turbulence is not only produced or dissipated but also diffused. Diffusion takes place by triple correlation of velocity fluctuations (turbulent diffusion), one-point correlation of pressure and velocity fluctuations (pressure diffusion), and viscous diffusion. Finally, dissipation term represents the kinetic energy dissipated by viscous forces. For LES, the SGS viscosity should be added into the molecular viscosity, as shown in Eqs. (A7) and (A8).

References

[1] Back, L. H., Cuffel, R. F., and Massier, P. F., 1969, "Laminarization of a Turbulent Boundary Layer in Nozzle Flow-Boundary Layer and Heat Transfer Measurements With Wall Cooling," NASA Center, ASME Paper 69-HT-56.

[2] McEligot, D. M., and Bankston, C. A., 1969, "Numerical Predictions for Circular Tube Laminarization by Heating," NASA Center, ASME Paper 69-HT-52.

[3] Kurganov, V. A., and Gladuntsov, A. I., 1977, "Laminarization of Flow and Heat Transfer Crisis in Pipes Under Conditions of Intense Heating of Turbulent-Flow of Gas Dissociating Endothermally at Wall," High Temp., **15**(6), pp. 1052–1062.

[4] Kawamura, M. H., and Takizuka, T., 1982, "Experiment on Laminarization of Strongly Heated Gas-Flow in Vertical Circular Tube," J. Atomic Energy Society of Japan, **24**(1), pp. 60–67.

[5] Fujii, S., Akino, N., Hishida, M., Kawamura, H., and Sanokawa, K., 1991, "Numerical-Studies on Laminarization of Heated Turbulent Gas-Flow in Annular Duct," J. Atomic Energy Society of Japan, **33**(12), pp. 1180–1190.

[6] Torii, S., Shimizu, A., Hasegawa, S., and Higasa, M., 1990, "Laminarization of Strongly Heated Gas-Flows in a Circular Tube (Numerical-Analysis by Means of a Modified Kappa-Epsilon Model)," JSME Int. J., Ser. II, **33**(3), pp. 538–547.

[7] Torii, S., Shimizu, A., Hasegawa, S., and Kusama, N., 1991, "Laminarization of Strongly Heated Annular Gas Flows," JSME Int. J., Ser. II, **34**(2), pp. 157–168.

[8] Torii, S., and Yang, W. J., 1997, "Laminarization of Turbulent Gas Flow Inside a Strongly Heated Tube," Int. J. Heat Mass Transfer, **40**(13), pp. 3105–3117.

[9] Torii, S., and Yang, W. J., 1999, "Swirling Effects on Laminarization of Gas Flow in a Strongly Heated Tube," ASME Trans. J. Heat Transfer, **121**(2), pp. 307–313.

[10] Satake, S., Kunugi, T., Shehata, A. M., and McEligot, D. M., 2000, "Direct Numerical Simulation for Laminarization of Turbulent Forced Gas Flows in Circular Tubes With Strong Heating," Int. J. Heat Fluid Flow, **21**(5), pp. 526–534.

[11] Jones, W. P., and Launder, B. E., 1972, "Prediction of Laminarization With a 2-Equation Model of Turbulence," Int. J. Heat Mass Transfer, **15**(2), pp. 301–314.

[12] Howard, J. H. G., Patankar, S. V., and Bordynuik, R. M., 1980, "Flow Prediction in Rotating Ducts Using Coriolis-Modified Turbulence Models," ASME Trans. J. Fluids Eng., **102**(4), pp. 456–461.

[13] Naot, D., Peled, A., and Tanny, J., 1990, "Response of Shear Flow Turbulence to Diffusional Electromagnetic Fluctuations," Appl. Math. Model., **14**(5), pp. 226–236.

[14] Morley, N. B., Gaizer, A. A., Tillack, M. S., and Abdou, M. A., 1995, "Initial Liquid Metal Magnetohydrodynamic Thin Film Flow Experiments in the Mcga-Loop Facility at UCLA," Fusion Eng. Des., **27**, pp. 725–730.

[15] Kim, E.-J., Hahm, T. S., and Diamond, P. H., 2001, "Eddy Viscosity and Laminarization of Sheared Flow in Three Dimensional Reduced Magnetohydrodynamic Turbulence," Phys. Plasmas, **8**, pp. 3576–3582.

[16] Beér, J. M., Chigier, N. A., Davies, T. W., and Bassindale, K., 1971, "Laminarization of Turbulent Flames in Rotating Environments," Combust. Flame, **16**, pp. 39–45.

[17] Takagi, T., Shin, H.-D., and Ishio, A., 1980, "Local Laminarization in Turbulent Diffusion Flames," Combust. Flame, **37**, pp. 163–170.

[18] Zawadzki, A., and Jarosinski, J., 1983, "Laminarization of Flames in Rotating Flow," Combust. Sci. Technol., **35**, pp. 1–13.

[19] Rodi, W., Pennell, W. T., and Eckert, E. R. G., 1969, "Laminarization of Turbulent Flow in a Circular Porous Tube With Uniform Mass Injection Through Tube Wall," Mech. Eng. (Am. Soc. Mech. Eng.), **91**(11), p. 67.

[20] Arnal, D., and Bulgubure, C., 1996, "Drag Reduction by Boundary Layer Laminarization," Rech. Aerosp., **3**, pp. 157–165.

[21] Moin, R. D., and Moin, P., 1987, "The Effects of Curvature in Wall-Bounded Turbulent Flows," J. Fluid Mech., **175**, pp. 479–510.

[22] Cheah, S. C., Iacovides, H., Jackson, D. C., JI, H., and Launder, B. E., 1996, "LDA Investigation of the Flow Development Through Rotating U-Ducts," ASME J. Turbomach., **118**(3), pp. 590–596.

[23] Lopes, A. S., Piomelli, U., and Palma, J. M. L. M., 2006, "Large-Eddy Simulation of the Flow in an S-Duct," J. Turbul., **7**(11), pp. 1–30.

[24] Sewall, E. A., Tafti, D. K., Graham, A. B., and Thole, K. A., 2006, "Experimental Validation of Large Eddy Simulation of Flow and Heat Transfer in a Stationary Ribbed Duct," Int. J. Heat Fluid Flow, **27**, pp. 243–258.

[25] Laskowski, G. M., and Durbin, P. A., 2007, "Direct Numerical Simulations of Turbulent Flow Through a Stationary and Rotating Finite Serpentine Passage," Phys. Fluids, **19**(1), 015101.

[26] Hirai, S., Takagi, T., and Matsumoto, M., 1986, "Prediction of the Laminarization Phenomena in Turbulent Swirling Flows," Bull. JSME, **29**(258), pp. 4462–4470.

[27] Nishibori, K., Kikuyama, K., and Murakami, M., 1987, "Laminarization of Turbulent-Flow in the Inlet Region of an Axially Rotating Pipe," JSME Int. J., **30**(260), pp. 255–262.

[28] Hirai, S., Takagi, T., and Matsumoto, M., 1988, "Predictions of the Laminarization Phenomena in an Axially Rotating Pipe-Flow," ASME Trans. J. Fluids Eng., **110**(4), pp. 424–430.

[29] Pashtrapanska, M., Jovanović, J., Lienhart, H., and Durst, F., 2006, "Turbulence Measurements in a Swirling Pipe Flow," Exp. Fluids, **41**, pp. 813–827.

[30] Yang, Z., 2000, "Large Eddy Simulation of Fully Developed Turbulent Flow in a Rotating Pipe," Int. J. Numer. Methods Fluids, **33**, pp. 681–694.

[31] Johnston, J. P., Hallen, R. M., and Lezius, R. K., 1972, "Effect of Spanwise Rotation on the Structure of Two-Dimensional Fully Developed Turbulent Channel Flow," J. Fluid Mech., **56**, pp. 533–557.

[32] Kristoffersen, R., and Andersson, H. I., 1993, "Direct Simulations of Low Reynolds-Number Turbulent-Flow in a Rotating Channel," J. Fluid Mech., **256**, pp. 163–197.

[33] Macfarlane, I., Joubert, P. N., and Nickels, T. B., 1998, "Secondary Flows and Developing, Turbulent Boundary Layers in a Rotating Duct," J. Fluid Mech., **373**, pp. 1–32.

[34] Murata, A., and Mochizuki, S., 1999, "Effect of Cross-Sectional Aspect Ratio on Turbulent Heat Transfer in an Orthogonally Rotating Rectangular Smooth Duct," Int. J. Heat Mass Transfer, **42**(20), pp. 3803–3814.

[35] Pallares, J., and Davidson, L., 2000, "Large-Eddy Simulations of Turbulent Flow in a Rotating Square Duct," Phys. Fluids, **12**, pp. 2878–2894.

[36] Nicoud, F., and Ducros, F., 1999, "Subgrid-Scale Stress Modelling Based on the Square of the Velocity Gradient Tensor," Flow, Turbul. Combust., **62**(3), pp. 183–200.

[37] Smagorinsky, J., 1963, "General Circulation Experiments With Primitive Equations. I. The Basic Experiment," Mon. Weather Rev., **91**, pp. 99–164.

[38] 2001, Fluent 6.2 User Guide, Fluent Inc., Lebanon.

[39] Chorin, A. J., 1968, "Numerical Solution of the Navier-Stokes Equations," Math. Comput., **22**(104), pp. 745–762.

[40] Leonard, B. P., 1991, "The Ultimate Conservative Difference Scheme Applied to Unsteady One-Dimensional Advection," Comput. Methods Appl. Mech. Eng., **88**, pp. 17–74.

[41] Ferziger, J. H., and Peric, M., 1996, *Computational Methods for Fluid Dynamics*, Springer, New York.

[42] Issa, R. I., 1986, "Solution of Implicitly Discretized Fluid Flow Equations by Operator Splitting," J. Comput. Phys., **62**, pp. 40–65.

[43] Patankar, S. V., 1980, *Numerical Heat Transfer and Fluid Flows*, Hemisphere, Washington, DC.

[44] Gavralakis, S., 1992, "Numerical-Simulation of Low-Reynolds-Number Turbulent Flow Through a Straight Square Duct," J. Fluid Mech., **244**, pp. 101–129.

[45] Guleren, K. M., 2007, "Large-Eddy Simulation of Wall-Bounded Flows Subjected to Curvature and Rotation," Ph.D. thesis, The University of Manchester, UK 2007, available from http://www.cumhuriyet.edu.tr/~melihguleren/PhDthesis.pdf.

[46] Guleren, K. M., and Turan, A., 2007, "Validation of Large-Eddy Simulation of Strongly Curved Stationary and Rotating U-Duct Flows," Int. J. Heat Fluid Flow, **28**(5), pp. 909–921.

[47] Hathaway, M. S., Chriss, R. M., Wood, J. R., and Strazisar, A., 1993, "Experimental and Computational Investigation of the NASA Low-Speed Centrifugal Compressor Flow Field," ASME J. Turbomach., **115**, pp. 527–542.

[48] Pope, S. B., 2000, *Turbulent Flows*, Cambridge University Press, Cambridge.

[49] Moser, R. D., Kim, J., and Mansour, N. N., 1999, "Direct Numerical Simulation of Turbulent Channel Flow Up to Re_τ=590," Phys. Fluids, **11**, pp. 943–945.

[50] Alvelius, K., 1999, Ph.D. thesis, Department of Mechanics Royal Insititue of Technology, Stockholm, Sweden.

[51] Germano, M., Piomelli, U., Moin, P., and Cabot, W. H., 1991, "A Dynamic Subgrid-Scale Eddy Viscosity Model," Phys. Fluids A, **3**, pp. 1760–1765.

[52] Kim, W. W., and Menon, S., 1995, "A New Dynamic One-Equation Subgrid-Scale Model for Large Eddy Simulations," Paper No. AIAA-95-035.

[53] Pallares, J., Grau, F. X., and Davidson, L., 2005, "Pressure Drop and Heat Transfer Rates in Forced Convection Rotating Square Duct Flows at High Rotation Rates," Phys. Fluids, **17**(7), 075102.

[54] Prandtl, L., 1952, *Essentials of Fluid Dynamics*, Hafner, New York.

[55] Launder, B. E., and Spalding, D. B., 1972, "Lectures in Mathematical Models of Turbulence," Academic, London.

[56] Wilcox, D. C., 1998, *Turbulence Modeling for CFD*, DCW Industries, Inc., La Canada, CA.

[57] Daly, B. J., and Harlow, F. H., 1970, "Transport Equations in Turbulence," Phys. Fluids, **13**, pp. 80.

Buoyancy Dominated He–O_2 Separated Jet Mixing in a Tubular Reactor

Ankur Deep Bordoloi

P. K. Panigrahi

Department of Mechanical Engineering,
Indian Institute of Technology,
Kanpur UP-208016, India

Mixing of two variable-density jets, one of which is essentially a negatively buoyant jet (He) and the other a nonbuoyant jet (O_2) is studied experimentally using digital particle image velocimetry technique for separated nozzle geometry. Two jets are separated from each other, i.e., He jet exit plane is located upstream of the O_2 jet exit plane. Experiments were carried out keeping the nonbuoyant O_2 jet at constant Reynolds number ($Re_2 = 245$) and varying the Richardson number ($Ri_1 = 1.8, 4.7, 16.4$) of the buoyant He jet. The interaction between two jets as a function of buoyancy strength of helium jet is investigated. The flow visualization images clearly demonstrate the growth and shape of buoyant jet as a function of Richardson number. Mean velocity and vorticity field results provide quantitative picture about the mixing and interaction between the two jets. The stream trace results show the flow structures, i.e., recirculation zone and foci of vortex structures as a function of Richardson number. The mixing between two jets takes place at far downstream region for low Richardson number ($Ri_1 = 1.8$). At high Richardson number ($Ri_1 = 16.4$), the buoyant He jet is located near its exit plane without any direct interaction with the O_2 jet. At the intermediate Richardson number ($Ri_1 = 4.7$), the buoyant jet encroaches the nonbuoyant O_2 jet at a favorable penetration distance and a good amount of mixing between the two jets take place. The jet growth results based on the $y_{0.5}$-location development in the streamwise direction clearly demonstrate the interaction between the He and O_2 jets in the interjet region. The entrainment coefficient, vorticity magnitude, and turbulent kinetic energy magnitude are maximum at the intermediate Richardson number ($Ri_1 = 4.7$) demonstrating direct relationship among each other. The mixing between buoyant He jet and nonbuoyant O_2 jet is a function of both shear between the two jets and the strength of buoyant plume. [DOI: 10.1115/1.2953299]

Keywords: buoyant jet, jet mixing, separated jet, PIV, growth rate

1 Introduction

Variable-density jets are present in many industrial applications, i.e., burners, combustion chambers, chemical reactors, manufacturing processes, etc. Two reactive jets are injected inside a bounded domain, i.e., a tubular reactor or a combustion chamber, and allowed to mix with each other. The performance of these devices depends on mixing between the two jets. Therefore, different jet configurations have been investigated in literature to study mixing between the two gases. Among these, coaxial jets have been popular and significant research has been carried out for this geometry. The other important jet configuration is separated jet, where two jets vertically inclined at a specific angle with respect to each other carry two gases. Depending on density difference and momentum content, the two jets can be termed as either buoyant or nonbuoyant jet.

Buoyant jets have extensively been studied by many researchers in the past. For buoyant jet, if the buoyancy is supported by jet inertia, it is called as positively buoyant jet and if the buoyancy is opposed by the jet inertia, it is called as negatively buoyant jet. In case of negatively buoyant jets, the buoyancy and momentum oppose each other, while they assist each other for the positively buoyant jet. The relative magnitude of buoyancy and inertia forces influences the interaction between two jets. Some relevant literature related to jet mixing are reviewed below.

Turner [1] investigated theoretically as well as experimentally the motion near the advancing front of a vertical plume. On reaching the maximum height, the plume takes a caplike structure due to its downward movement. The half spreading angle for such plumes was measured using dye visualization and compared with theoretical estimates. Later, Turner [2] reported the behavior of jets and plumes with negative buoyancy. In a negatively buoyant upward jet, the buoyancy force acts downwards and there should be sufficient momentum of the jet in order to reach a steady height. In plumes, the buoyant force acts upwards until it reaches a particular height from which its density starts to increase due to entrainment of surrounding fluid. Mizushina et al. [3] studied negatively buoyant jet using water at normal temperature (higher density) as the upward jet and water heated to a higher temperature (lower density) as the ambient fluid. Using dye visualization technique, they observed the upward moving jet to spread axially with a constant slope. They reported that the penetration height of a negatively buoyant jet depends only on temperature based discharge Froude number of the jet. Subbarao and Cantwell [4] reported the effect of Richardson number on vertically upward buoyant jets of helium in the presence of coflowing air using Schlieren technique. They observed that at Richardson number above unity, the jet undergoes transition to turbulence exhibiting highly structured and repeatable breakdown while intermixing with the coflowing stream. Dahm et al. [5] investigated mixing in coaxial nonbuoyant homogeneous water jets using vortex dynamics in the near exit region and direct flow visualization technique. They showed that near-field vortex dynamics depend not only on velocity ratio between jets but also on velocity of each individual jet. The instability and rollup of vorticity layers separating each

Contributed by the Fluids Engineering Division of ASME for publication in the JOURNAL OF FLUIDS ENGINEERING. Manuscript received September 25, 2007; final manuscript received May 2, 2008; published online August 12, 2008. Assoc. Editor: Juergen Kompenhans.

stream can result in either wakelike or shear-layer-like near-field vortical structures in the vicinity of the jet. Rajaratnam and Wu [6] studied two intersecting homogeneous air jets of unequal momentum flux using Prandtl type pitot static probe. They reported mean velocity information of individual and mixed jet. Favre-Marinet et al. [7] studied coaxial jets with high density difference using hotwire anemometry. They reported that for coflowing jets with high density difference, density ratio plays a very important role in mixing in addition to the velocity ratio. They demonstrated the existence of global instability regime and consequently a high level of mixing when the density ratio is lower than a critical value. Pantzlaff and Lueptow [8] studied positively and negatively buoyant jets separately in order to understand the transient behavior of buoyancy driven jets using particle image velocimetry (PIV) technique. They suggested that a negatively upward buoyant jet is an optimal mixing strategy in designing systems for jet mixing of different densities. Pham et al. [9] have investigated three-dimensional (3D) behavior of thermal plume and mass entrainment rate of the ambient fluid into the plume using 3D PIV technique.

The present experimental study simulates the flow conditions of a cold wall tubular reactor used in a commercial application. The nozzle geometry has been selected based on preliminary performance studies on the product output. The test gases, i.e., helium and oxygen, have similar kinematic viscosity ratio as the reactive gases used in the prototype tubular reactor. The reactive gases generate heat inside the reactor, which is used during the production process. The interaction between the reactive gases and the nature of mixing is very important for the optimum performance of the system.

A potential advantage of using a separated nozzle over coaxial ones is that of controllability of mixing zones between two jets by controlling the distance between exit planes of the two nozzles. In case of coaxial jets, the primary interaction between the two jets takes place close to the nozzle exit. The exothermic reaction between the reactive gases generates a large amount of heat and there is a possibility of nozzle damage due to high temperature. The reaction zone location can be suitably controlled by allowing the reaction to take place at a distance downstream from the exit plane of the two nozzles in a separated nozzle configuration.

To the best of our knowledge, no work so far has been carried out on mixing of variable-density separated jets. The mixing between variable-density buoyant jets flowing into ambient fluid is not available in literature. The present investigation reports two variable-density (He and O_2) nonreactive separated jets inclined at a small angle (± 3 deg) with the vertical axis. This problem is unique as it essentially deals with mixing of a negatively buoyant jet with a nonbuoyant jet. The digital PIV has been used in this study to facilitate the instantaneous and time-averaged flow field measurements, which provide insight into the mixing phenomenon between the two gases. The role of buoyancy for effective control of mixing between two separated jets is clearly illustrated.

2 Experimental Setup

The schematic of experimental setup and the separated nozzle geometry are shown in Figs. 1(*a*) and 1(*b*), respectively. The helium and oxygen gases are discharged into the tubular reactor through the separated nozzles. The tubular reactor has an octagonal cross section with 1 m length and distance between two parallel faces equal to 21.67 cm. This is essential for eliminating the curvature effect on the PIV measurements. The gas flow through the two separated nozzles takes place via two settling chambers: contraction cones and antiturbulence screens. Two fine brass wire meshes, one at the exit of the settling chambers and another at the inlet to the nozzle assembly, are used in each of the settling chambers to smoothen the flow before entering the nozzle assembly.

All geometrical details of the separated nozzles can be seen in Fig. 1(*b*). The two separated nozzles are mounted to a plate at the top of the tubular reactor. The perforated He nozzle discharges at 100 mm below the top wall of the reactor. The O_2 nozzle exits at 10 mm below the He-nozzle exit. The helium nozzle has a perforated circular plate with 21 randomly distributed perforations of uniform size (diameter=1 mm) at the end of a circular pipe (outer diameter=12.5 mm).

The perforated nozzle configuration helps in achieving smaller turbulence length scale of vortices for better mixing. The special oxygen-nozzle configuration is adopted for increasing the jet mixing. The rapid contraction zone increases the inlet turbulence due to recirculation of flow in the forward facing geometry. The adverse pressure gradient in the diverging section of the nozzle promotes the instability and hence the turbulent mixing. The separation angle between the two nozzles was maintained at ± 3 deg based on two criteria: (a) to enhance the mixing between the two jets by direct interaction and (b) to prevent the reaction in the near wall region of the tubular reactor, so that the wall temperature does not exceed the maximum allowable temperature of the wall material.

Atomized seeding particles are generated using Laskin nozzles. Both the working gases and seeding particles are introduced to their respective settling chambers in a cross flow arrangement. They mix with each other and flow through the nozzle assembly. Dioctyl Sebacate (bis(2-ethylhexyl) sebacate or $C_{26}H_{50}O_4$) was used as seeding particles. The mean diameter of oil particles is estimated to be 2 μm (Kähler et al. [10]). A suction blower at the exit of the reactor is used to purge the reactor before and after each experiment.

Flow in the test section is maintained at a desired flow rate by using two separate flow meters (Scientific Devices, India; Model Nos. ST 5 and ST 6 for oxygen and helium, respectively). The PIV measurements are carried out in the central plane of the jets. The central region of interest is illuminated with a thin light sheet, and the tracer particles in the light sheet are projected on to a recording medium, i.e., charge-coupled device (CCD) in the image plane of the lens. A double pulsed Nd:YAG (yttrium aluminum garnet) laser (New Wave) of wavelength 532 nm and 15 mJ/pulse with maximum repetition rate 15 Hz has been used. The laser sheet has a maximum span area of 10×10 cm^2 and the sheet thickness is about 0.8 mm. A Peltier-cooled 12 bit CCD camera (PCO, Sensicam) and a frame grabber with a frame speed of 8 Hz were used for acquisition of PIV images. The CCD consists of an array of 1280×1024 pixels. A Nikon 50 mm manual lens of $f^{\#}=1.4$ is attached to the CCD camera for imaging the field of interest. Both the camera and laser are synchronized with a synchronizer controlled by a dual processor PC. The field of view employed in the present set of PIV measurements was 40×35 mm^2. A two-dimensional grid, having a grid distance of 1 mm, was placed at the image plane for calibration image and this image was used for mapping the flow domain in millimeter from pixel. The laser light sheet was carefully aligned with the calibration grid to ensure same measurement and calibration locations. The time of separation between two successive pulses is 195 μs for all test cases. The time-averaged velocity field was obtained by averaging a sequence of 200 velocity vector images.

The downward moving helium jet is negatively buoyant and attains a constant penetration when the inertia and the buoyancy forces are balanced. However, when the helium gas accumulates at the top of the reactor, the penetration length of the helium jet is affected due to the change in buoyancy force. We have conducted the PIV experiment during the initial period before the accumulation of helium gas at the top of the reactor. Therefore, the PIV experiments were not conducted continuously for a longer duration. Twenty PIV image pairs were acquired for each experimental run. Hence, ten separate experimental runs were conducted at each Richardson number for acquisition of 200 PIV image pairs.

The unwanted part of a PIV image is annotated before performing PIV cross-correlation calculations. For the present analysis, multipass interrogation technique has been used. In the first evaluation, the images were subdivided into 64×64 pixel interrogation

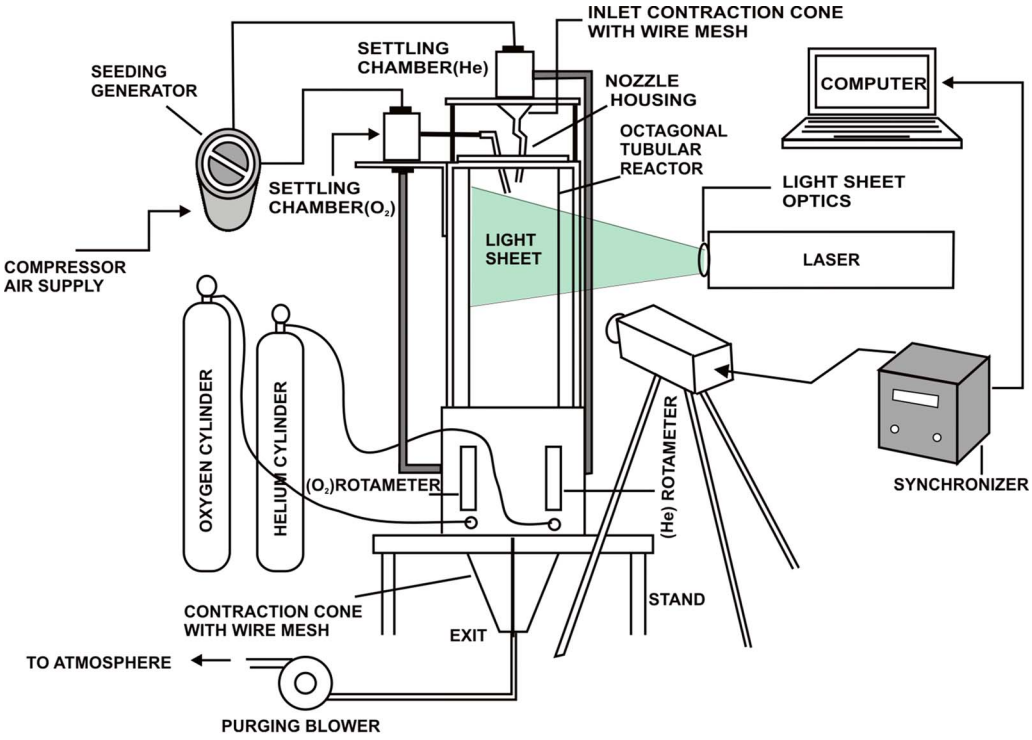

(a)

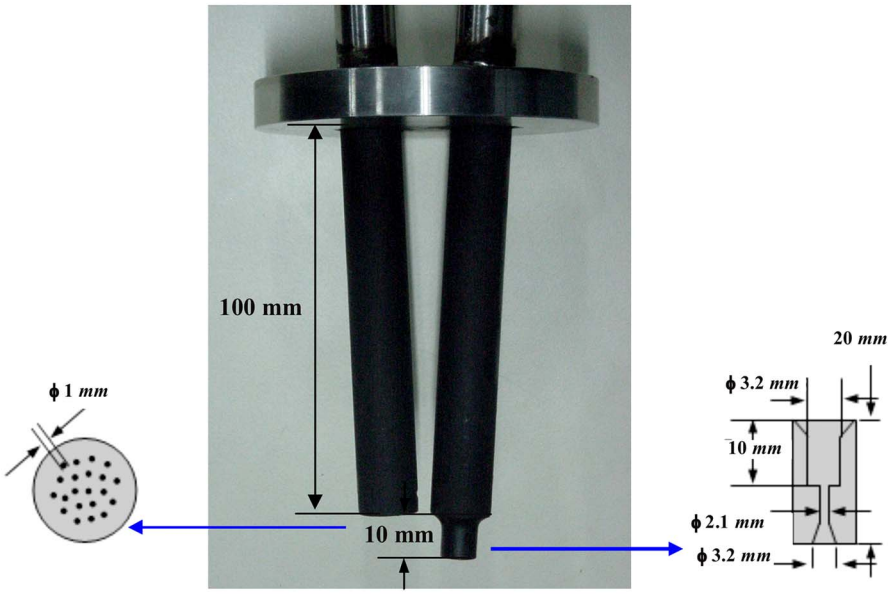

(b)

Fig. 1 (*a*) **Schematic of the experimental setup and** (*b*) **the separated nozzle used in the present study**

zones. The corresponding interrogation zones were analyzed by computing the cross-correlation function. The displacement calculated from this evaluation is used for window offsetting and deformation in subsequent passes. In subsequent passes, interrogation zone sizes were gradually reduced and further analyzed using adaptive cross correlation after performing appropriate window shifting and deformation. The final interrogation zone size was 32×32 pixels. Overlapping (50–75%) between the interrogation zones was used to improve the number of velocity vectors. A total of 2240 velocity vectors were obtained with spatial resolution of 0.65 mm. All measured integer displacements that deviated more than one pixel from the expected displacement were considered as spurious vectors and removed using local filtering. New vectors were obtained by interpolation. The percentages of valid vectors were about 94.5–97%.

The Richardson number (Ri) is calculated individually for two

Table 1 Details on the experimental conditions used in the present study

	Helium jet	Oxygen jet
Nozzle index	1	2
Nozzle pipe diameter (mm)	9.5	9.5
Perforation diameter (mm)	1.0	—
Throat diameter (mm)	—	2.1
Volume flow rates (lpm)	1.27, 0.98, and 0.65	0.358
Reynolds number (Re)	46.6, 28.9, and 15.4	245
Richardson number (Ri)	1.8, 4.7, and 16.4	4.22×10^{-5}

gas jets considering the ambient air to be at rest using the relation $\mathrm{Ri}=|\rho_g-\rho_a|gd/\rho_g U_g^2$ (Favre-Marinet et al. [7]). Here subscript g indicates the dominant gas jet (i.e., helium or oxygen) and a indicates the ambient fluid. The Reynolds number for oxygen jet is calculated on the basis of throat diameter of converging-diverging section and the average velocity of the jet through the throat section. The Reynolds number for helium jet is calculated on the basis of internal diameter of the helium nozzle and the average velocity after the merging of small jets from the perforations. The average velocities are 0.601 m/s, 0.373 m/s, and 0.199 m/s for flow rates of 1.27 lpm, 0.98 lpm, and 0.65 lpm, respectively. The details of experimental conditions, i.e., the volume flow rates, Reynolds number, and Richardson number for both gases, are summarized in Table 1.

We have investigated the behavior of buoyant helium jet as a function of Richardson number, i.e., ratio of buoyancy force to inertia force. For a systematic study, the velocity of the heavier (O_2) gas was kept constant and that of the lighter (He) gas was varied. The experiments were conducted for three different sets of Richardson number (Ri_1) for the helium gas. The interaction between He jet and O_2 jet has been reported.

3 Results and Discussions

Separated jets offer greater controllability for mixing between two jets due to more number of physical parameters. The streamwise separation between the exit planes of two jets is one of the parameters, which can be varied to alter the jet width of upstream jet at the exit plane of the downstream jet. The relative angle between the two jets can also be varied for altering the extent of cross flow between the two jets. The nozzle geometry is another important physical parameter, which determines the nature of jet growth as a single jet. In the present study, all geometric parameters of separated jets are kept constant. The flow conditions, i.e., velocity of buoyant helium jet, are varied to investigate the influence of buoyancy on the interaction between two jets. The flow visualization images, mean velocity, mean vorticity, stream traces, jet growth, entrainment coefficient, turbulent kinetic energy, instantaneous velocity, and vorticity results are presented and discussed in the following sections.

3.1 Visualization. Figure 2 shows instantaneous visualization images for different Richardson numbers of He jet, i.e., $\mathrm{Ri}_1=1.8$, 4.7, and 16.4. At low Richardson number ($\mathrm{Ri}_1=1.8$), the helium jet penetrates the ambient fluid to a larger streamwise distance due to higher strength of jet inertia. In the downstream region, local momentum of the fluid decreases due to entrainment of the ambient fluid and viscous effect. Subsequently, buoyancy effect becomes significant and the flow reversal takes place. The flow reversal leads to formation of recirculation region. The recirculating low density (helium) jet interacts with the higher density (oxygen) jet at the downstream region. At intermediate Richardson number ($\mathrm{Ri}_1=4.7$), the helium jet penetrates the ambient medium to a smaller streamwise distance, compared to that at $\mathrm{Ri}_1=1.8$. The jet reverses its direction and flows upwards as the buoyancy dominates the flow. Figure 2(*b*) shows that helium jet is displaced towards the oxygen jet during reversal motion resulting in strong interaction between the two. The higher velocity of the O_2 jet compared to the surrounding medium leads to formation of low pressure region around the O_2 jet. Therefore, the helium jet is displaced towards this low pressure region between the He and O_2 jets. At $\mathrm{Ri}_1=16.4$, the penetration of the helium jet is the lowest, i.e., it reverses its flow direction before the exit plane of the oxygen nozzle. The He and O_2 jets develop independently without directly influencing each other. The helium jet is symmetric about its axis indicating negligible influence of the oxygen jet. Overall, the visualization images clearly show the relative position and interaction between the two jets.

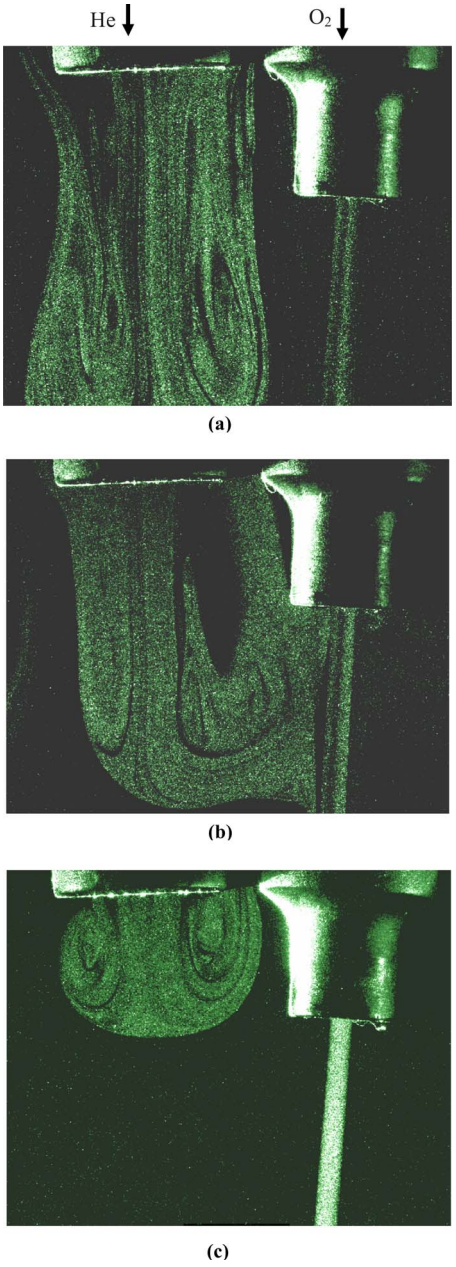

Fig. 2 Instantaneous visualization images at different Richardson numbers: (*a*) $\mathrm{Ri}_1=1.8$, (*b*) $\mathrm{Ri}_1=4.7$, and (*c*) $\mathrm{Ri}_1=16.4$

3.2 Mean Velocity Field. The time-averaged axial velocity ($u/u_{\max}$) field contours and velocity profiles at selected streamwise locations are shown in Fig. 3. Here, $u_{\max}$ is the maximum local u-velocity corresponding to the oxygen jet. At the lowest

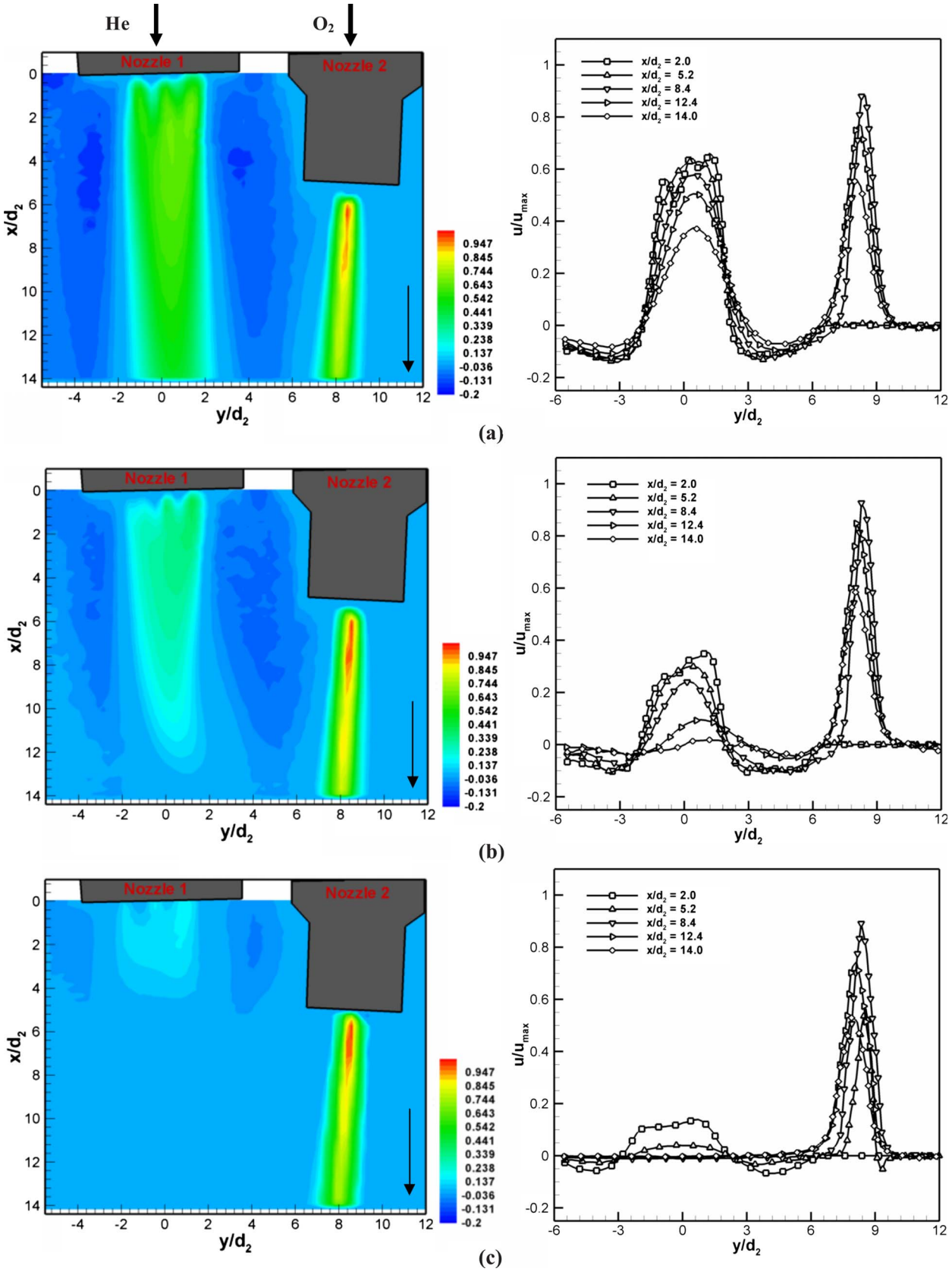

Fig. 3 The time-averaged u-velocity contour normalized by the maximum axial velocity (u_{max}) and the corresponding radial velocity profiles at selected streamwise locations (x/d_2) at different Richardson numbers: (*a*) $Ri_1 = 1.8$, (*b*) $Ri_1 = 4.7$, and (*c*) $Ri_1 = 16.4$

Richardson number ($Ri_1=1.8$), the peak magnitude of u/u_{max} of the helium jet is higher than that at other Richardson numbers. The negative velocity region around the helium jet is due to the flow reversal of buoyant helium gas after the balance between the jet inertia and the viscous shear from the ambient fluid. The negative u-velocity region surrounding helium jet extends further downstream in the region adjacent to the oxygen jet compared to the opposite side due to the presence of low pressure region around the oxygen jet. It also indicates the indirect influence of O_2 jet on the behavior of the He jet. At intermediate Richardson number ($Ri_1=4.7$), the maximum normalized u-velocity of He jet is in the range 0.04–0.4 compared to 0.48–0.64 value at $Ri_1=1.8$. At $Ri_1=16.4$, the maximum normalized u-velocity of He jet is in the range 0.0–0.28. This is due to the difference in bulk velocity of helium jet in these three cases. The helium jet velocity profile is not symmetric at all Richardson numbers. The asymmetry is maximum at $Ri_1=4.7$ indicating greater interaction between helium and oxygen jets. The reverse velocity zone between helium and oxygen jets shows larger streamwise extent and higher magnitude compared to that at the opposite side of the helium jet. This can be attributed to the low pressure zone between the He and O_2 jets leading to stronger buoyant motion compared to that at the opposite side.

The u/u_{max} velocity profile in Fig. 3 shows the nature of interaction between He and O_2 jets. For higher Richardson number ($Ri_1=16.4$), the oxygen jet velocity profile shows symmetric behavior similar to a single jet configuration. However, at other Richardson numbers ($Ri_1=1.8$ and 4.7), the oxygen jet velocity profile at the interjet region of helium jet shows a different slope compared to that in the opposite side. The helium jet profile adjacent to the oxygen jet also shows asymmetric behavior at these Richardson numbers. The y-location for maximum u-velocity of helium jet shifts towards the oxygen jet and is located at the off-centerline for $Ri_1=4.7$ and 16.4. This can be attributed to interaction between these two jets.

The time-averaged transverse velocity (v/u_{max}) contours are shown in Fig. 4 for $Ri_1=1.8$, 4.7, and 16.4. A high magnitude v-velocity region is observed for $Ri_1=4.7$ in the vicinity of the oxygen jet. This is an indication of direct interaction between helium and oxygen jets. For $Ri_1=16.4$, one high v-velocity region is located in the upstream region, i.e., closer to the exit plane of the He nozzle. Another high magnitude v-velocity region is located adjacent to the O_2 jet indicating indirect interaction between O_2 and He jets. At Richardson number $Ri_1=1.8$, the v-velocity magnitude is insignificant at the intermediate region between two jets indicating minimal interaction between them. The v-velocity distribution near the exit plane of helium jet at $Ri_1=1.8$ is different from that at $Ri_1=4.7$ and 16.4. This can be attributed to the difference in nature of recirculation zone around it (see Fig. 5).

Figure 4 also shows the transverse velocity profiles at selected axial locations. The profile remains more or less the same at $Ri_1=1.8$, 4.7, and 16.4 for the oxygen jet. The nature of v-velocity distribution in the interjet region clearly demonstrates the interaction between the two jets. The v-velocity in this region shows maximum variation at intermediate Richardson number ($Ri_1=4.7$). The v-velocity magnitude is insignificant, i.e., closer to zero in this interjet region at lower and higher Richardson numbers ($Ri_1=1.8$ and 16.4). For helium jet, a strong peak in velocity is seen within $y/d_2=0-6$ for $Ri_1=4.7$. At $Ri_1=1.8$, no such peak is observed and the peak is smaller at $Ri_1=16.4$ as compared to that at $Ri_1=4.7$. The overall higher magnitude of v-velocity at $Ri_1=4.7$ indicates greater interaction between the helium and oxygen jets.

3.3 Stream Traces. The separated buoyant jet shows interesting flow structures as a function of the relative strength of buoyancy force with respect to inertia force. The shape, size, and location of these vortex structures indicate the nature of interaction between the two jets. Stream traces are useful in identification of these vortex structures. The time-averaged stream traces superimposed on the nondimensional absolute velocity magnitude are shown in Fig. 5 at different Richardson numbers. The stream trace results show the presence of two recirculation bubbles with regular focilike structures (F^+ and F^-) at both sides of the helium jet. At high Richardson number ($Ri_1=16.4$), the recirculation bubbles are symmetric. The two recirculation bubbles are asymmetric in nature at $Ri_1=1.8$ and 4.7. The recirculation bubble (F^-) forms downstream beyond the test zone at $Ri_1=1.8$. At lower Richardson numbers ($Ri_1=1.8$ and 4.7), the strength of flow inertia is higher leading to larger penetration of the helium jet. The recirculation bubbles appear further downstream at the lowest Richardson number ($Ri_1=1.8$) compared to that at intermediate Richardson number ($Ri_1=4.7$). Therefore, the helium jet interacts with the oxygen jet at the downstream location for $Ri_1=1.8$. This interaction influences the shape and size of the recirculation bubble of the helium jet. The core of helium jet recirculation bubble adjacent to the oxygen jet (F^-) is located at a downstream location compared to that at the other side of He jet (F^+) for $Ri_1=1.8$ and 4.7. This is due to the low pressure region surrounding the oxygen jet. The helium jet is dragged towards this low pressure region resulting in shift of the recirculation bubble. The interaction between helium and oxygen jets also leads to formation of a secondary recirculation bubble (F^+) around the oxygen jet. The nature and location of this recirculation bubble near around the O_2 jet are different between $Ri_1=1.8$ and 4.7. At $Ri_1=16.4$, the buoyant helium jet drags the ambient air upwards indicating indirect interaction between the two jets.

The velocity magnitude contours in Fig. 5 show the spatial location of the high magnitude jet region. The higher velocity region with a larger penetration distance is seen at a lowest Richardson number ($Ri_1=1.8$). The helium jet velocity magnitude shows the discontinuous variation of velocity in the transverse (y) direction due to the flow through pores. The individual helium jet flow through the pores interacts with each other at the downstream region and merges as a single jet flow.

3.4 Mean Vorticity Field. Vorticity in a shear layer is related to the difference in velocity of the fluid elements, i.e., velocity gradient. Figure 6 presents the time-averaged nondimensional spanwise vorticity fields at different Richardson numbers. At $Ri_1=1.8$, due to high velocity of the helium jet, the vorticity level is high. The near exit region of the helium jet shows a small concentrated vorticity region. This is due to the effect of flow through neighboring perforations relative to the measurement plane. At $Ri_1=4.7$ and $Ri_1=16.4$, the average vorticity magnitude is relatively less compared to that at $Ri_1=1.8$. The extent of high velocity gradient region is evident from the axial velocity and transverse velocity fields (refer to Fig. 3 and 4). At $Ri_1=1.8$, the axial velocity contour extends far downstream with more or less the same level giving rise to a larger axial extent of vorticity distribution. At higher Richardson numbers ($Ri_1=4.7$ and 16.4), the axial velocity does not extend far downstream and the extent of high vorticity region is comparatively less. The vorticity distribution of He jet shows an inclination towards the O_2 jet due to the displacement of He jet towards the O_2 jet because of the pressure gradient.

The vorticity profiles at different streamwise locations for three different Richardson numbers are compared in Fig. 6. Both positive and negative peaks are seen inside the shear layers of helium jet. Since helium jet essentially consists of multiple smaller jets, the near exit region ($x/d_2=2.0$) exhibits more than two peaks signifying the presence of more than two shear layers ($Ri_1=1.8$). However, beyond $x/d_2=2.0$, all smaller jets merge to form a bigger single jet and hence, only two peaks with opposite signs are observed. At $Ri_1=1.8$, as we progress axially, the peak vorticity level in the helium jet gradually decreases. At $Ri_1=4.7$, the profile

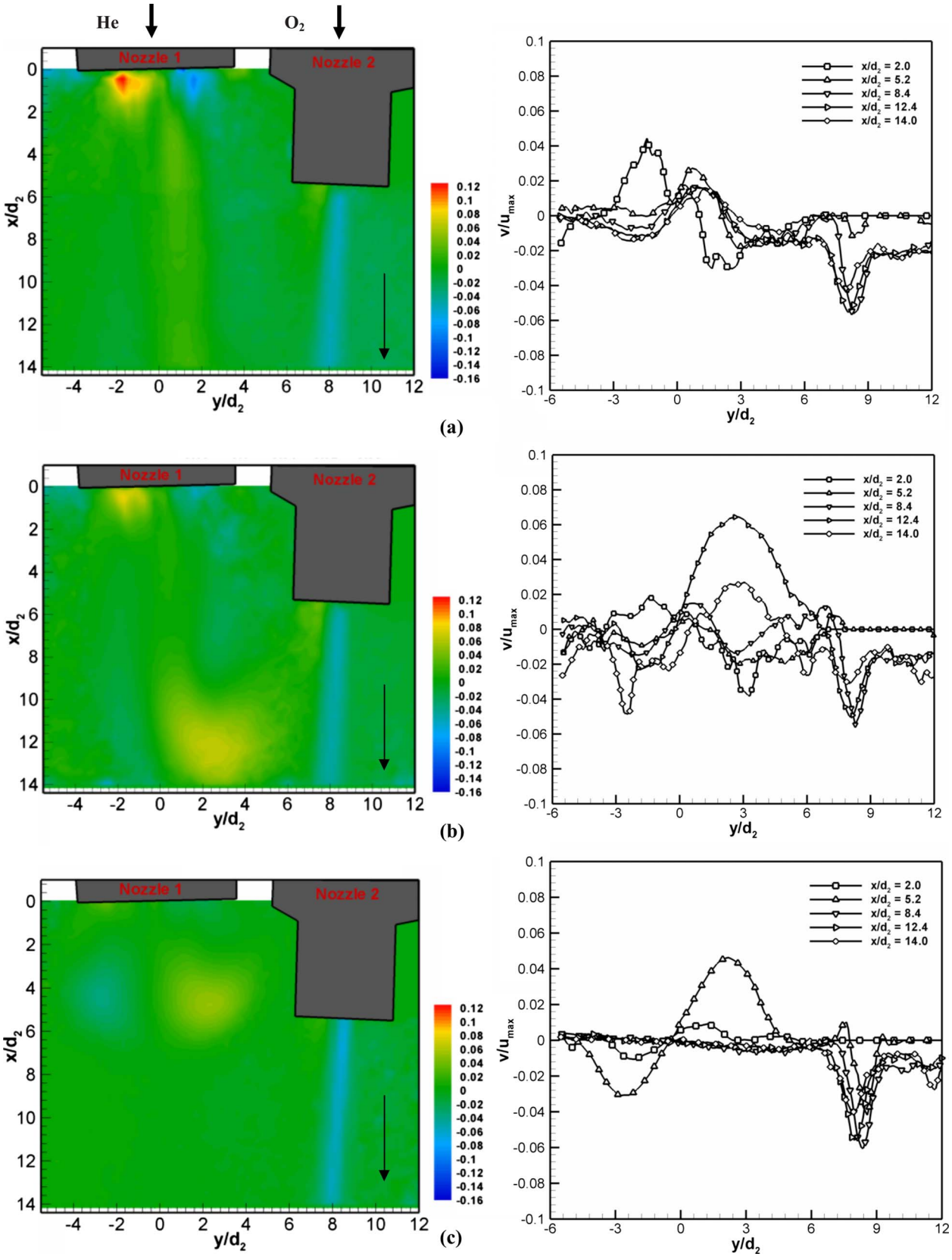

Fig. 4 The time-averaged *v*-velocity contour normalized by the maximum axial velocity (u_{max}) and the corresponding radial velocity profiles at selected streamwise locations (x/d_2) at different Richardson numbers: (*a*) $Ri_1 = 1.8$, (*b*) $Ri_1 = 4.7$, and (*c*) $Ri_1 = 16.4$

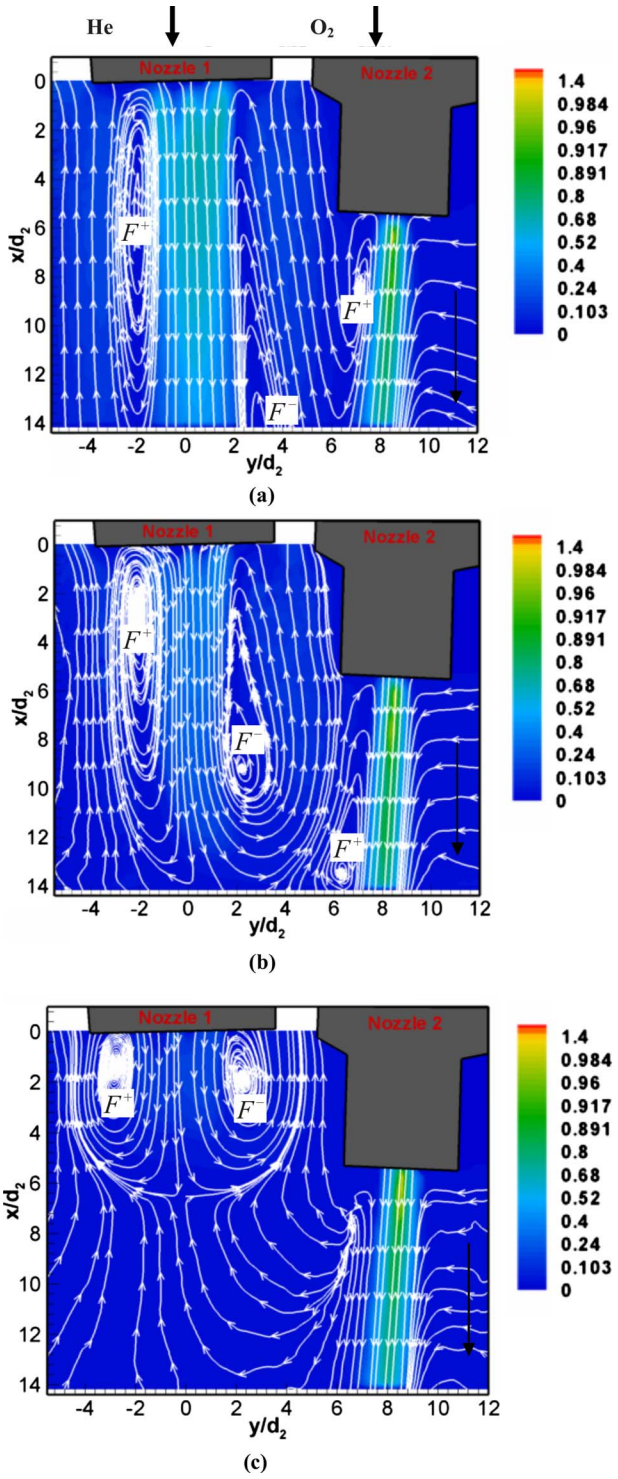

Fig. 5 The time-averaged stream traces superimposed on the nondimensional magnitude of absolute velocity at different Richardson numbers: (*a*) $Ri_1=1.8$, (*b*) $Ri_1=4.7$, and (*c*) $Ri_1=16.4$. The symbol F indicates the core of the focilike structures.

becomes almost flat in the downstream region ($x/d_2=12.4$). Whereas, in the case of $Ri_1=16.4$, the variation of vorticity level almost vanishes rather upstream ($x/d_2=5.2$). The vorticity contours of the helium jet at $Ri_1=4.7$ is displaced towards the oxygen jet, which relates to the u- and v-velocity distribution results in Figs. 3 and 4. The vorticity profile of the O_2 jet shows a larger variation in the streamwise direction at the adjacent region of the He jet compared to the opposite region. This is an indication of the interaction between the two jets. Overall, vorticity distribution clearly demonstrates the interaction between the flow through the perforations, strength of shear content of the jet flow, and interaction between and O_2 jets.

3.5 Instantaneous Velocity and Vorticity Field. The instantaneous vorticity and velocity fields are useful for observation of dynamic features of the flow. The instantaneous vorticity and velocity vector fields at two different time instants for $Ri_1=1.8$, 4.7, and 16.4 are presented in Fig. 7. The helium jet shows two types of vorticity distribution: one concentrated in the near-exit region of the jet for a smaller axial distance and the other which extends further downstream till a larger downstream location. These small vorticity regions can be attributed to the flow of helium jet through the off-center pores, i.e., pores located offset to the measurement plane. The high vorticity regions correspond to the pores aligned along the central measurement plane. Overall, the vorticity distribution of helium jet extends till the largest streamwise location for $Ri_1=1.8$ and the smallest streamwise location for $Ri_1=16.4$. The vorticity distribution of helium jet shows the presence of small scale vorticity patterns presumably due to three dimensionality and interaction between the flows through different pores. This is an indication of small scale mixing of helium jet flow indicating greater efficacy of molecular mixing for reacting flow. In contrast, the flow through oxygen jet shows regular vorticity distribution presumably due to primary contribution of velocity shear on vorticity calculation.

The instantaneous velocity vectors shown in Fig. 7 confirm the nature of recirculating patterns shown in Fig. 5. In addition, it clearly shows the upward flow of buoyant helium jet between the helium jet and oxygen jet regions and the resulting shear between the two leading to effective mixing. The attraction of He jet towards the O_2 jet is also clearly visible from the velocity vector distribution.

3.6 Turbulence Kinetic Energy. The fluctuation of velocity field can be represented in terms of turbulence kinetic energy. This can provide meaningful insight about effective mixing and interaction between two jets. The radial distributions of turbulent kinetic energy at three different axial positions ($x/d_2=5.2$, 8.4, and 14.0) for $Ri_1=1.8$, 4.7, and 16.4 are shown in Fig. 8. The normalized turbulent kinetic energy is calculated as

$$e_K=\frac{1}{2}\left(\frac{\langle u'u'\rangle+\langle v'v'\rangle}{U^2}\right)$$

where u' and v' are the fluctuating velocity in streamwise and transverse directions, respectively. At $Ri_1=1.8$, turbulent kinetic energy of the helium jet shows two peaks at $x/d_2=5.2$ and 8.4 (Figs. 4(*a*) and 4(*b*)), which transforms to a single peak at the downstream location ($x/d_2=14.0$) (Fig. 4(*c*)). The dual peak is due to the mixing layers of the helium jet as a whole and could be correlated to the vorticity in these mixing layers. The single peak in turbulent kinetic energy is due to merging of the two opposite shear layers. A similar behavior is observed at $Ri_1=4.7$ as well. However, the turbulent kinetic energy peak magnitude at $Ri_1=4.7$ is much smaller than that at $Ri_1=1.8$. The higher velocity, i.e., high Reynolds number for $Ri_1=1.8$, leads to higher turbulent energy. At $Ri_1=16.4$, the turbulent kinetic energy is negligible as the helium jet recirculates prior to $x/d_2=5.2$ location. Comparison of Fig. 6 with Fig. 8 indicates a direct relation between the turbulent kinetic energy and vorticity levels, i.e., the vorticity generation contributes towards the fluctuation in the velocity field.

The turbulent kinetic energy of oxygen jet is influenced by both inertia (Reynolds number) and the interaction between the helium and oxygen jets. The turbulent kinetic energy of the oxygen jet is the highest at $Ri_1=4.7$ compared to other Richardson numbers. The highest interaction between the helium and oxygen jets is seen at $Ri_1=4.7$ (see Fig. 2). The highest entrainment of oxygen

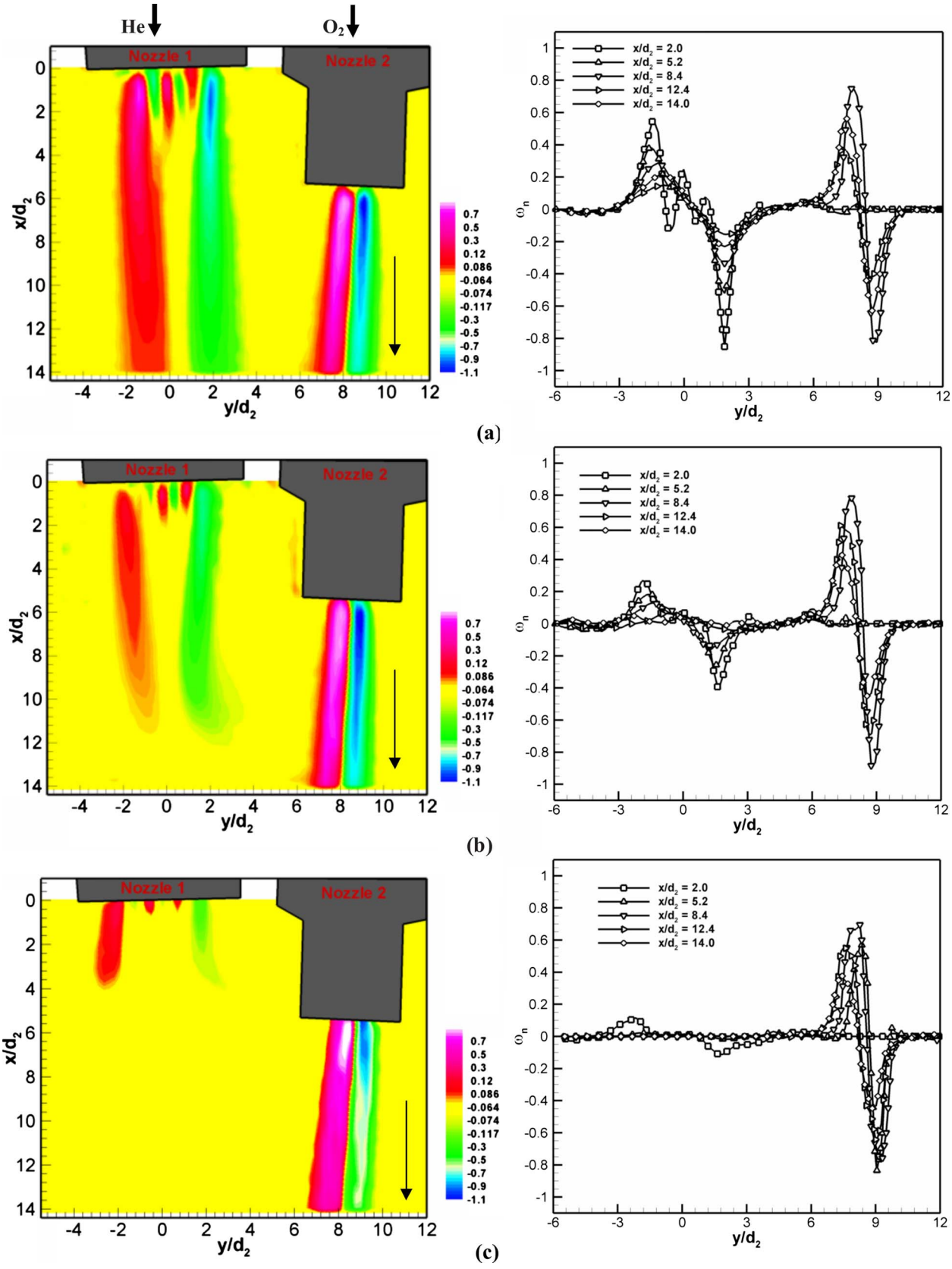

Fig. 6 The time-averaged normalized vorticity (ω_n) contour and the corresponding radial vorticity profiles at selected streamwise locations (x/d_2) at different Richardson numbers: (*a*) $Ri_1=1.8$, (*b*) $Ri_1=4.7$, and (*c*) $Ri_1=16.4$

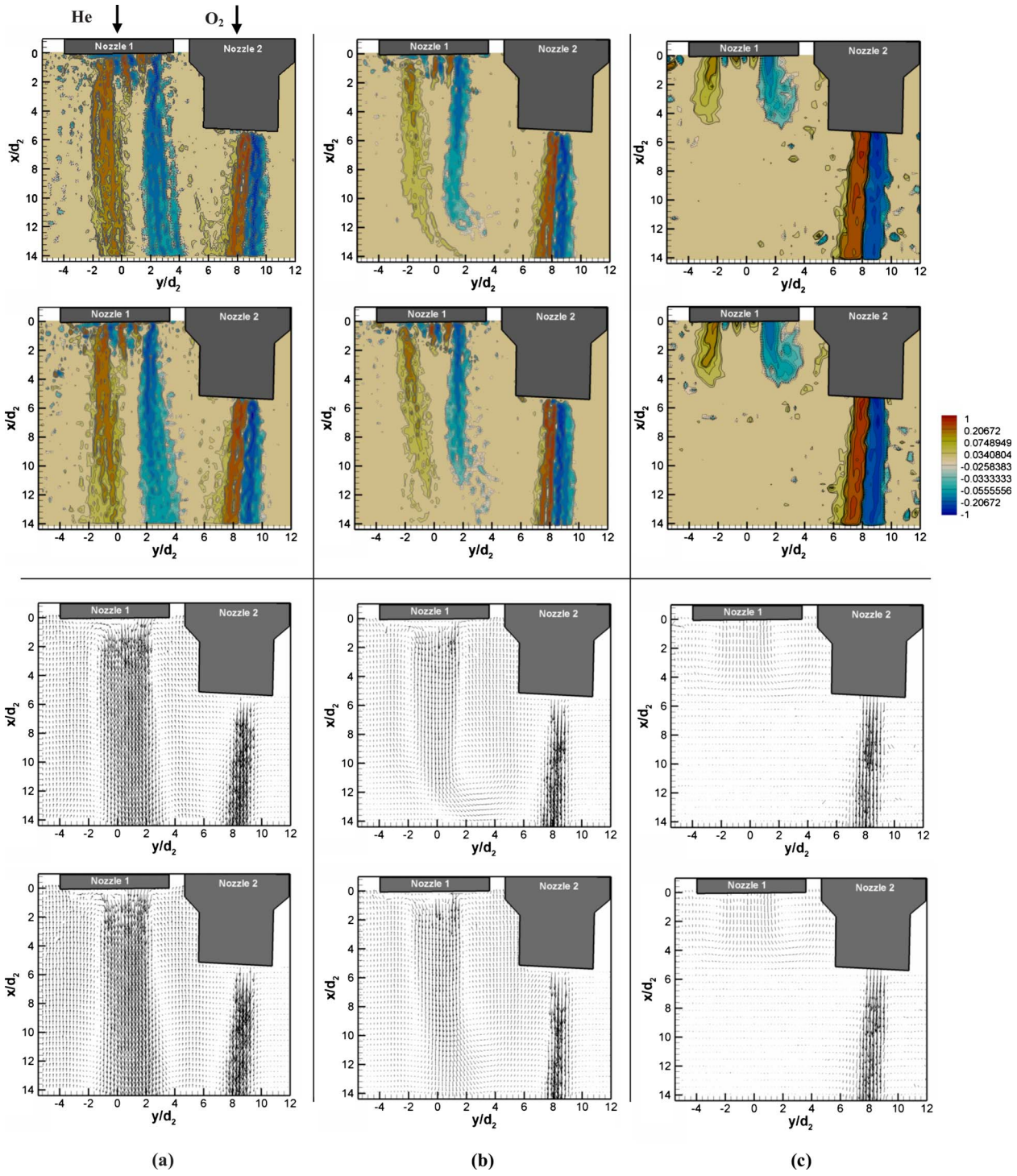

Fig. 7 The normalized instantaneous vorticity contours (top) and corresponding instantaneous velocity vector map (bottom) at two selected time instants for different Richardson numbers: (*a*) $Ri_1=1.8$, (*b*) $Ri_1=4.7$, and (*c*) $Ri_1=16.4$

jet is also observed at $Ri_1=4.7$ (Fig. 10). Hence, the higher turbulence kinetic energy at $Ri_1=4.7$ is attributed to greater mixing and interaction at this intermediate Richardson number ($Ri_1=4.7$). At the highest Richardson number ($Ri_1=16.4$), the turbulence kinetic energy is minimum due to negligible interaction between the helium and oxygen jets as the helium jet penetration ends before the exit plane of the oxygen nozzle.

3.7 Jet Growth and Entrainment. The interaction between He and O_2 jets can be studied based on the comparison of O_2-jet growth at different Richardson numbers. The jet width is calculated based on the y-location ($y_{0.5}$) at which the local velocity is 50% of the maximum u-velocity at that axial location. Normalized $y_{0.5}$-location evolution of O_2 jet at both left (adjacent to the He jet) and right (opposite to the He jet) sides is shown in Fig. 9 at different Richardson numbers. The overall increase of the $y_{0.5}$-location in streamwise direction indicates the nature of jet growth.

Figure 9 shows that the jet growth is not influenced signifi-

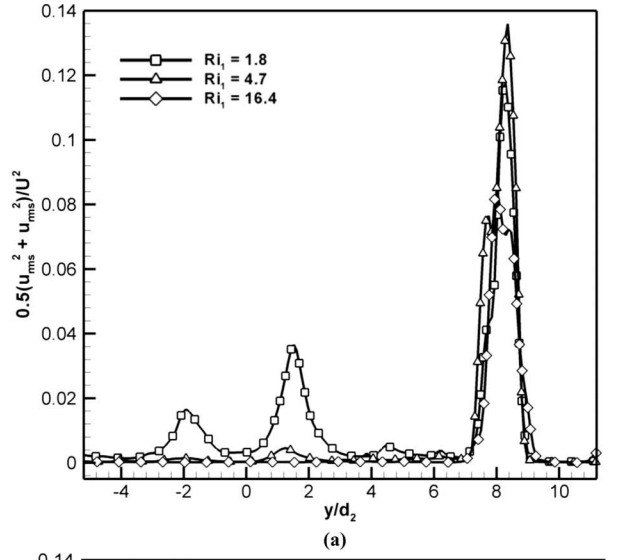

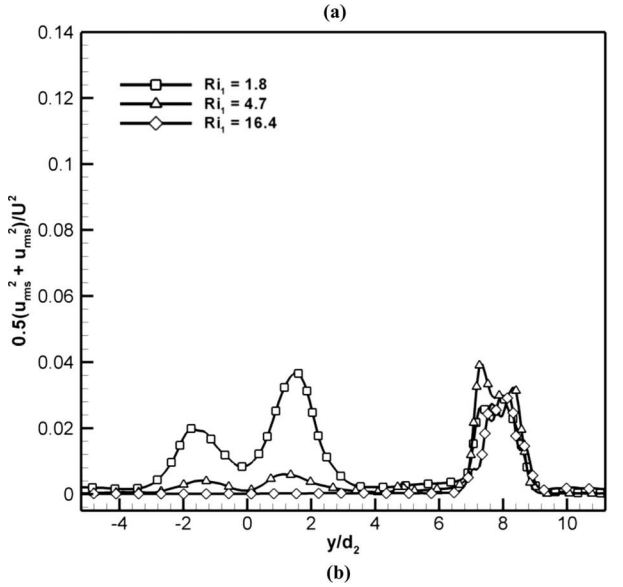

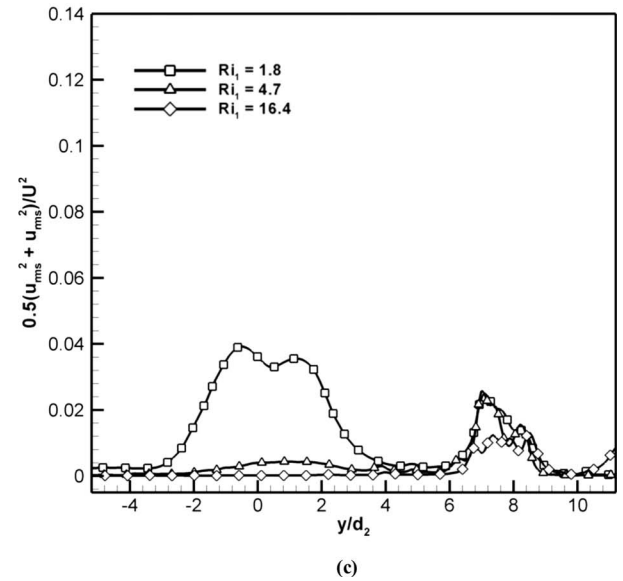

Fig. 8 Radial profiles of turbulence kinetic energy $e_k = 1/2(\langle u'u' \rangle + \langle v'v' \rangle)/U^2$ for $Ri_1 = 1.8$, 4.7, and 16.4, at streamwise locations (*a*) $x/d_2 = 5.2$, (*b*) $x/d_2 = 8.4$, and (*c*) $x/d_2 = 14.0$

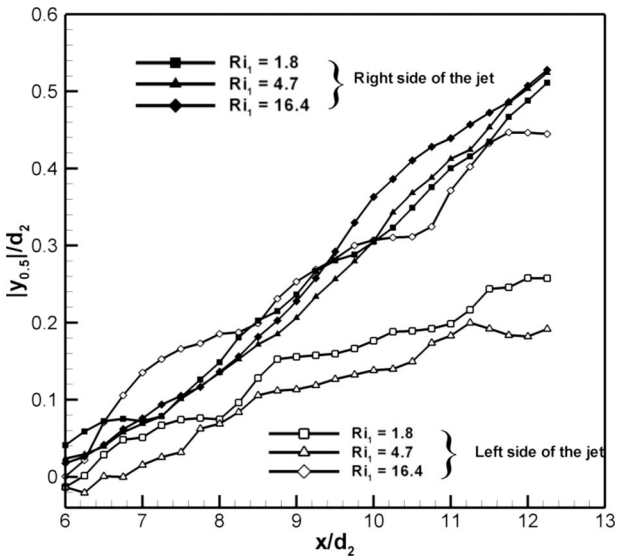

Fig. 9 The axial variation of half jet width of O_2 jet for $Ri_1 = 1.8$, 4.7, and 16.4 at the left hand side, i.e., adjacent to the He jet, and the opposite right hand side

cantly with respect to Richardson number at the right hand side of the O_2 jet, i.e., opposite side of the He jet in comparison to the left hand side. This can be attributed to greater interaction between the two jets at the interjet region of He and O_2 jets. However, the growth rate of O_2 jet in the left hand side, i.e., interjet region at $Ri_1 = 16.4$, is comparable to that at the right hand side. This indicates lesser interaction between separated jets at the highest Richardson number, $Ri_1 = 16.4$. This is due to lesser penetration of the He jet, i.e., it extends to a streamwise distance before the exit plane of the O_2 jet for $Ri_1 = 16.4$. There is no direct interaction between He and O_2 jets at this Richardson number ($Ri_1 = 16.4$) (see Fig. 2(*c*)). The $y_{0.5}$-location of the O_2 jet is the smallest at $Ri_1 = 4.7$. At this Richardson number, direct interaction between the two jets is observed (Fig. 2(*b*)).

Overall, the $y_{0.5}$ development results in Fig. 9 show greater He and O_2 interaction in the interjet region compared to the opposite side. The $y_{0.5}$ location at the left side of O_2 jet is a stronger function of Richardson number compared to that at the right side. The smaller $y_{0.5}$ value at $Ri_1 = 4.7$ is attributed to the direct interaction between the He and O_2 jets (Fig. 2(*b*)). Comparing Fig. 8 with Fig. 9, it is observed that the lower $y_{0.5}$ value, i.e., the jet growth at intermediate Richardson number ($Ri_1 = 4.7$), corresponds to higher turbulent mixing. Kwon and Seo [11] also observed a lower value of jet half width at higher Reynolds number for nonbuoyant jet. They attributed the decreasing spreading rate to higher turbulent mixing. The entrainment coefficient results are presented below to relate the above observations to jet growth.

Pham et al. [9] have calculated the entrainment coefficient as the ratio between the lateral velocity at the jet interface and the mean flow velocity. In similar line, we have calculated the entrainment coefficient, $\alpha = u_{n,0.1}/U$, where $u_{n,0.1}$ is the normal velocity (normal to the axis of the O_2 jet) at the jet interface. The jet interface is the radial location where the local velocity is 0.1 times the maximum velocity. The exact interface location has been obtained by linear curve fitting of data in the neighborhood. The normal velocity is calculated using coordinate transformation, i.e., $u_{n,0.1} = v \cos\theta + u \sin\theta$, where θ is the angle between the interface and the centerline of the O_2 jet.

The entrainment (α) along the streamwise direction at different Richardson numbers has been shown in Fig. 10. The entrainment coefficient reduces till a small value along the streamwise direction. This trend is similar to that observed by Pham et al. [9] for a

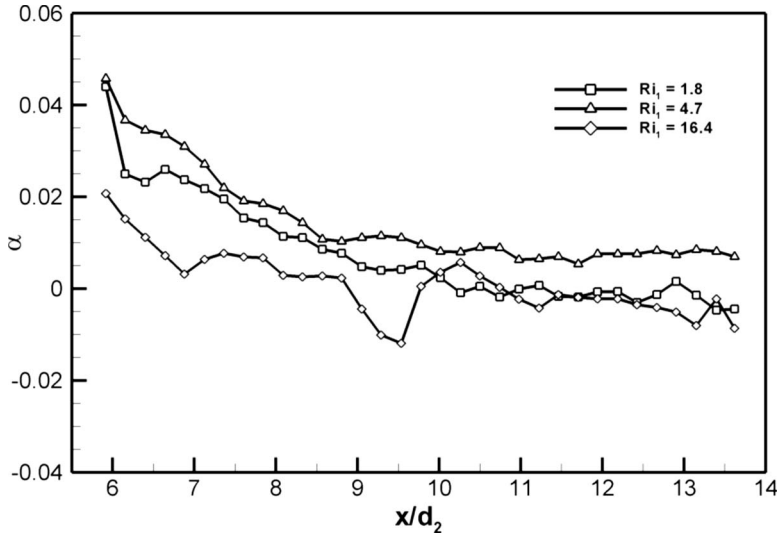

Fig. 10 The entrainment coefficient (α) along the streamwise direction of the O_2 jet for Ri_1=1.8, 4.7, and 16.4

thermal plume. The overall entrainment is the highest at the intermediate Richardson number (Ri_1=4.7) and the lowest at the highest Richardson number (Ri_1=16.4). Hence, higher entrainment of the oxygen jet at Ri_1=4.7 is correlated to the greater interaction between He and O_2 jets (see Fig. 2). The evolution of $y_{0.5}$-location in Fig. 9 and entrainment coefficient in Fig. 10 show similar trend as a function of Richardson number. The higher entrainment at intermediate Richardson number (Ri_1=4.7) is also supported by higher vorticity and turbulent kinetic energy magnitudes (Figs. 6 and 8).

4 Conclusions

The present investigation reports the flow field of helium and oxygen jets through a separated nozzle configuration inside a tubular reactor. PIV measurements were carried out to study the interaction between the two jets as a function of Richardson number of helium jet (Ri_1=1.8, 4.7, and 16.4). The results are discussed using mean velocity, mean and instantaneous vorticity, visualization images, turbulent kinetic energy, stream traces, jet growth, and entrainment. The influence of buoyancy on the interaction between separated jets is demonstrated and explained.

The penetration of helium jet through the ambient medium depends on its Richardson number. The jet penetrates in the mean flow direction till the balance between the buoyancy and inertia force. At the end of the penetration zone, the buoyant helium jet reverses back its flow direction. During its reverse motion, it can directly or indirectly interact with the neighboring oxygen jet. The level of interaction between He and O_2 jets depends on the jet penetration length and the relative streamwise separation between the two jets. The velocity and vorticity field show the influence of Richardson number on the jet penetration length. The flow field is dominated by recirculation zones of different shapes, sizes, and positions, which are functions of interaction between the two jets. The recirculation bubble of the He jet is symmetric at Ri_1=16.4 in contrast to its asymmetric nature at Ri_1=1.8 and 4.7. This is due to greater interaction between He and O_2 jets and the development of low pressure zone at the interjet region between He and O_2 jets at Ri_1=1.8 and 4.7. The jet width ($y_{0.5}$-location) of the O_2 jet is different in the interjet region compared to that at its opposite side. The interaction between He and O_2 jets influences the jet width. The entrainment coefficient, turbulent kinetic energy, and vorticity magnitude increase due to interaction between the He and O_2 jets. The strength of buoyancy to inertia force and the relative axial location of the He and O_2 jets are two critical parameters influencing the interaction between separated jets. Overall, the present study indicates separated jet geometry as a promising tool for reactive flow management.

Acknowledgment

The authors gratefully acknowledge Board of Research in Nuclear Sciences (BRNS) (No. 2003/36/29/BRNS/1986) for the financial support.

Nomenclature

Re = Reynolds number ($\rho U d/\mu$)
Ri = Richardson number ($|\rho_g-\rho_a|gd/\rho_g U_g^2$)
U = average bulk velocity in axial direction
d = internal diameter of the nozzle
g = acceleration due to gravity
u = axial local velocity
v = radial local velocity
x = axial direction
y = radial direction

Greek Symbols

α = entrainment coefficient
β = angle between the central axes of two nozzles
ρ = density of the bulk fluid
ω = local vorticity
ω_n = normalized vorticity ($2\omega/(\omega_{\max}-\omega_{\min})$)
μ = viscosity of fluid

Subscripts

a = ambient fluid property
g = jet fluid under consideration
1 = helium nozzle
2 = oxygen nozzle
max = maximum value
min = minimum value

References

[1] Turner, J. S., 1962, "The Starting Plume in Neutral Surroundings," J. Fluid Mech., **13**, pp. 356–368.
[2] Turner, J. S., 1966, "Jets and Plumes With Negative and Reversing Buoyancy," J. Fluid Mech., **26**, pp. 779–792.
[3] Mizushina, T., Ogino, H., Takeuchi, H., and Ikawa, H., 1982, "An Experimental Study of Vertical Turbulent Jet With Negative Buoyancy," Waerme- Stoffuebertrag., **16**, pp. 15–21.
[4] Subbarao, E. R., and Cantwell, B. J., 1992, "Investigation of a Co-Flowing

Buoyant Jet: Experiments on the Effect of Reynolds Number and Richardson Number," J. Fluid Mech., **245**, pp. 69–90.
[5] Dahm, W. J. A., Frieler, C. E., and Tryggvason, G., 1992, "Vortex Structure and Dynamics in the Near Exit Field of a Coaxial Jet," J. Fluid Mech., **241**, pp. 371–402.
[6] Rajaratnam, N., and Wu, S., 1992, "Intersecting Circular Jets of Unequal Momentum Flux," J. Hydraul. Res., **30**, pp. 755–767.
[7] Favre-Marinet, M., Camano, E. B., and Sarboch, J., 1999, "Near Field of Coaxial Jets With Large Density Differences," Exp. Fluids, **26**, pp. 97–106.
[8] Pantzlaff, L., and Lueptow, R. M., 1999, "Transient Positively and Negatively Buoyant Turbulent Round Jets," Exp. Fluids, **27**, pp. 117–125.
[9] Pham, M. V., Plourde, F., and Kim, S. D., 2005, "Three-Dimensional Characterization of a Pure Thermal Plume," ASME J. Heat Transfer, **127**(6), pp. 624–636.
[10] Kähler, C. J., Sammler, B., and Kompenhans, J., 2002, "Generation and Control of Tracer Particles for Optional Flow Investigation in Air," Exp. Fluids, **33**, pp. 736–742.
[11] Kwon, S. J., and Seo, I. W., 2005, "Reynolds Number Effects on the Behavior of a Non-Buoyant Round Jet," Exp. Fluids, **38**, pp. 801–812.

Hussameddine S. Kabbani
Department of Mechanical Engineering,
University of Nevada Las Vegas,
4505 Maryland Parkway,
Las Vegas, NV 89154-4027

Martin J. Mack
Department of Civil and Environmental Engineering,
University of Nevada Las Vegas,
4505 Maryland Parkway,
Las Vegas, NV 89154-4027

Sang W. Joo
School of Mechanical Engineering,
Yeungnam University,
Gyongson 712-749, Republic of Korea

Shizhi Qian[1]
Department of Aerospace Engineering,
Old Dominion University,
Norfolk, VA 23529-0247
e-mail: sqian@odu.edu

Analytical Prediction of Flow Field in Magnetohydrodynamic-Based Microfluidic Devices

A new approximate solution for the velocity profile of steady incompressible magnetohydrodynamic (MHD) flows in a rectangular microchannel driven by the Lorentz force is proposed. Mean velocity and mass flow rate in a channel, subsequently derived, can be used efficiently for many MHD-based microfluidic applications, including the design of a MHD-based microfluidic network without resorting to costly full-scale computational fluid dynamics. The closed-form solutions, provided for both direct-current (dc) and alternating-current (ac) electric and magnetic fields, are in simple forms, without any series or functions to evaluate, and so can be readily used for inverse or control problems associated with MHD-based lab-on-a-chip (LOC) devices. Extensive comparisons with previous analytical, computational, and experimental results are performed, and summarized in the present study. The proposed solutions are shown to agree better with existing experimental and computational reports than previous approximations and are to be used in a broad range of MHD-based LOC applications with both dc and ac fields with required accuracy. [DOI: 10.1115/1.2953302]

Keywords: magnetohydrodynamic (MHD), microfluidic, lab-on-a-chip (LOC), Lorentz force, micropump

1 Introduction

With the tremendous increase in the need to create minute devices to test samples of blood, DNA, and drugs, studies related to the lab-on-a-chip (LOC) are performed more intensively and extensively than ever before. LOC can be considered as a minute chemical processing plant, where many engineering processes, such as filtration, mixing, separation, and detection, exist within a single microchip. One of the main tasks in a LOC is to pump various fluids with required accuracy, which is not a trivial matter in micro- or nanoscales. At the same time the driving mechanism must be reliable, cheap, efficient, and easily controllable.

The magnetohydrodynamic (MHD) pumping is considered to be a relatively easy and convenient technique that serves the purpose. MHD actuators obviate mechanical stresses and other losses caused by pressure gradients imposed in mechanical pumps. Its advantage over nonmechanical pumps lies in its ability to operate at very low voltages to achieve relatively high flow rates and to allow pumping of weakly conductive liquids, including various buffer solutions. In MHD actuators, fluid flow in a channel is driven by the Lorentz force, generated by the interaction of nonparallel electric and magnetic fields.

Many MHD micropumps have been designed, modeled, constructed, and tested [1–14]. They operate under either direct-current (dc) or alternating-current (ac) electric fields. dc MHD pumps may suffer from the short life of the electrodes placed on opposing walls of a channel and bubble generation due to electrolysis. ac MHD pumps do better with these problems, but can be prone to the induction of eddy currents, which in turn can significantly increase the energy dissipation and thus heat generation. In addition, various MHD-based chaotic stirrers have been developed for various LOC applications [15–19].

The application of MHD-based microfluidics is now ubiquitous, especially in the field of analytical and clinical chemistry [7,20–24]. It is well known that before the design of a LOC device, an analytical method is introduced to predict the flow pattern in the device and subsequently determine control parameters. In order to reduce the computational time or to avoid expensive full-scale computations, a number of researchers have introduced approximate closed-form solutions that can predict the average velocity or mass flow rate in MHD-based microfluidic systems. These approximate solutions are based on the idea of the flow resistance in the pipe [10] or on an approximate closed-form velocity profile in 3D planar microchannels [9].

In the present study, we propose another approximate solution based on a more natural velocity profile corresponding to a steady viscous flow in a three-dimensional channel with a rectangular cross section. The resulting average velocity and flow rate, compared against existing experimental and computational results, show superior accuracy to previous approximations. The proposed solutions for both dc and ac electric fields are listed below, along with the validation of the results for a number of MHD micropumps, with the anticipation that they can be used in designs of MHD-based LOC devices where MHD micropumps are involved.

2 MHD Flow Under dc Electric Field

We consider a microchannel with length L and a rectangular cross section of height H and width W, as shown in Fig. 1. A planar electrode of length L_E and height H is placed on each vertical surface of the channel, with the leading edge located at a distance L_U downstream of the channel inlet. Here a Cartesian coordinate system is used, with the origin positioned at the center of the channel and the coordinates x, y, and z aligned, respectively, along the channel length, width, and height ($-L/2 \leqslant x \leqslant L/2$, $-W/2 \leqslant y \leqslant W/2$, and $-H/2 \leqslant z \leqslant H/2$). The channel surface not coated with the electrodes is made of a dielectric material.

The microchannel is filled with a weakly conductive electrolyte solution. When an electric potential difference is applied across the two planar electrodes facing each other, a current density $\mathbf{J}$ transmits through the electrolyte solution, which becomes $\mathbf{J}=J\mathbf{e}_y$

[1]Corresponding author.

Contributed by the Fluids Engineering Division of ASME for publication in the JOURNAL OF FLUIDS ENGINEERING. Manuscript received January 3, 2008; final manuscript received March 27, 2008; published online August 13, 2008. Assoc. Editor: Ali Beskok.

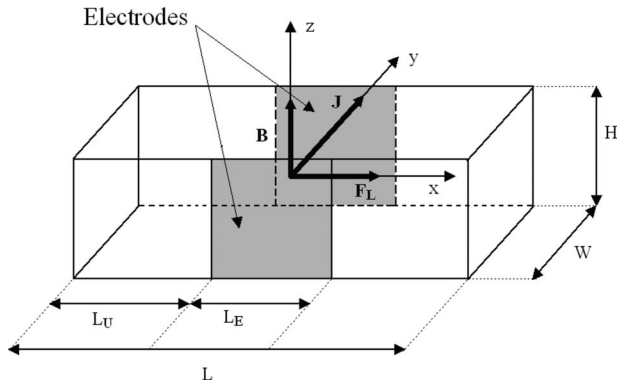

Fig. 1 Schematic diagram of the MHD flow through a microchannel with height *H*, width *W*, and length *L*. An electric current (or a potential difference) is applied to two planar electrodes deposited along the opposing walls of the channel. The length and height of the planar electrodes are, respectively, L_E and *H*. The electric current density J and magnetic field B are act, respectively, in the *y*- and *z*-directions.

in an undisturbed state. Here $\mathbf{e}_i$ ($i=x$, y, and z) represents a unit vector in the x-, y-, and z-directions, respectively. If we then apply a magnetic field with the magnetic flux density $\mathbf{B}$ in the z-direction ($\mathbf{B}=B\mathbf{e}_Z$) by a permanent magnet or an electromagnet, the interaction between the current density $\mathbf{J}$ and the magnetic field $\mathbf{B}$ induces the Lorentz force, $\mathbf{J}\times\mathbf{B}$, which provides the driving force for the fluid transport along the channel.

For an incompressible electrolyte solution of density ρ and viscosity μ in steady state, the conservation laws for mass and momentum are described by

$$\nabla\cdot\mathbf{u}=0 \tag{1}$$

and

$$\rho\mathbf{u}\cdot\nabla\mathbf{u}=-\nabla p+\mu\nabla^2\mathbf{u}+\mathbf{J}\times\mathbf{B} \tag{2}$$

respectively, where $\mathbf{u}$ is the velocity vector and p is the pressure. Here we neglect the natural convection generated by the density variations due to the electrochemical reactions on the surfaces of the electrodes, the paramagnetic forces induced by the concentration gradients of the paramagnetic species, and the magnetic field induction due to small Reynolds numbers of the MHD flows in microchannels. We also assume that the magnetic field is uniform in the z-direction, which is an appropriate approximation when the size of the magnet is much larger than that of the microfluidic device. Equations (1) and (2) are to be solved with the no-slip boundary condition on channel walls and a constant pressure gradient prescribed between the channel inlet ($x=-L/2$) and outlet ($x=L/2$).

Even with a constant electric current imposed, the current density $\mathbf{J}$ varies within the electrolyte solution. In principle it is related to the ionic mass transport and the electrochemical reaction along the surface of the electrodes [9,12]. We will not only exclude such complications here but assume that it is unidirectional, $\mathbf{J}=J\mathbf{e}_y$. Based on the numerical results of MHD flows in 3D microchannels, the velocity field is fully developed and unidirectional ($\mathbf{u}=u\mathbf{e}_x$) in most parts of the channels [9]. The driving force, or the Lorentz force, in the x-component momentum equation (Eq. (2)) is thus known a priori in the present study.

Based on the analytical solution for a fully developed duct flow with a rectangular cross section [25], we seek the solution for the x-component of the velocity vector as

$$u(y,z)=A_1\sum_{i=1,3,5,\ldots}^{\infty}(-1)^{(i-1)/2}\left[1-\frac{\cosh\left(\frac{i\pi z}{2a}\right)}{\cosh\left(\frac{i\pi b}{2a}\right)}\right]\frac{\cos\left(\frac{i\pi y}{2a}\right)}{i^3} \tag{3}$$

with $A_1=A_2\bar{U}$ and

$$A_2=\frac{48}{\pi^3\left[1-\frac{192a}{\pi^5 b}\sum_{j=1,3,5,\ldots}^{\infty}\frac{\tanh(j\pi b/2a)}{j^5}\right]} \tag{4}$$

where $\bar{U}$ is the cross-sectional average velocity, $a=\min(H/2,W/2)$, and $b=\max(H/2,W/2)$.

Noting $\tanh(\pi/2)=0.9172$ and $\tanh(3\pi/2)=0.9998$, we approximate $\tanh(j\pi b/2a)=1$ for $j\geq 3$. Subsequently, the series solution in the coefficient A_2 is approximated by

$$A_2=\frac{48}{\left[\pi^3-\frac{192a}{\pi^2 b}\left(\tanh\left(\frac{\pi b}{2a}\right)+\frac{31}{32}\zeta(5)-1\right)\right]} \tag{5}$$

The Riemann zeta function, $\zeta(x)=\Sigma_{n=1}^{\infty}1/n^x$, available, for example, in the MATLAB symbolic toolbox[2] yields $\zeta(5)=1.0369$. Expression A_2 then is only a function of the aspect ratio, b/a, of the microchannel.

Extracting the x-component from the set of the momentum equation (Eq. (2)) gives

$$-\frac{\partial p}{\partial x}+\mu\left(\frac{\partial^2 u}{\partial y^2}+\frac{\partial^2 u}{\partial z^2}\right)+JB=0 \tag{6}$$

which describes the balance between the pressure gradient, the viscous diffusion, and the Lorentz force. Substituting expression (3) into Eq. (6) and taking the volume integration on the resulting equation for the domain $-L/2\leq x\leq L/2$, $-a\leq y\leq a$, and $-b\leq z\leq b$, we get

$$4\Delta pab-2A_2\bar{U}\mu L\pi\frac{b}{a}\sum_{i=1,3,\ldots}^{\infty}(-1)^{(i-1)/2}\frac{\sin\left(\frac{i\pi}{2}\right)}{i^2}+IBW=0 \tag{7}$$

where I ($=J\times L_E\times H$) is the electric current and the infinite series can be evaluated as

$$\sum_{i=1,3,\ldots}^{\infty}(-1)^{(i-1)/2}\frac{\sin\left(\frac{i\pi}{2}\right)}{i^2}=\sum_{j=1,2,\ldots}^{\infty}(-1)^j\frac{\sin\left((2j+1)\frac{\pi}{2}\right)}{(2j+1)^2}=\frac{\pi^2}{8} \tag{8}$$

A simple arrangement of Eq. (7) thus provides the cross-sectional average velocity as

$$\bar{U}=\frac{16a^2}{\pi^3 A_2\mu}\frac{\Delta p}{L}+\frac{4aWB}{\pi^3 bA_2\mu L}I \tag{9}$$

The volumetric flow rate Q then becomes

$$Q=4\bar{U}ab=\frac{64a^3 b}{\pi^3 A_2\mu}\frac{\Delta p}{L}+\frac{16a^2 WB}{\pi^3 A_2\mu L}I \tag{10}$$

The closed-form expressions for the average velocity and flow rate obtained contain the combined effects of the pressure-driven force and the Lorentz force. In the absence of the pressure gradi-

[2]www.mathworks.com

ent imposed (i.e., $\Delta p=0$), the average velocity becomes

$$\bar{U} = \frac{4aWB}{\pi^3 bA_2 \mu L} I \tag{11}$$

and the volumetric flow rate is simplified as

$$Q = \frac{16a^2 WB}{\pi^3 A_2 \mu L} I \tag{12}$$

One can estimate the performances of dc MHD micropumps and networks by using the simple expressions obtained above without solving the three-dimensional system of Eqs. (1) and (2).

A number of other approximate solutions obtained previously by other researchers are available and need to be discussed here. Based on the idea of the flow resistance in a pipe, Lemoff and Lee [10] gave an approximate solution as

$$Q = \frac{H^2 W^3 B}{16\mu L (W+H)^2} I \tag{13}$$

However, the closed-form solution (Eq. (13)) only considers the Lorentz force and does not incorporate the applied or induced pressure-driven force between the ends of the channel. By approximating the velocity profile (Eq. (3)) with a simple expression, substituting it into Eq. (6), and integrating Eq. (6) for the entire volume of the channel, Kabbani et al. [9] obtained another closed-form solution for the flow rate as

$$Q = \frac{BIWH^2 + \Delta pWH^3}{4\mu L \left[(n+1)\dfrac{H^2}{W^2} + (m+1) \right]} \tag{14}$$

where

$$m = 1.7 + 0.5\left(\frac{H}{W}\right)^{-1.4} \tag{15}$$

and

$$n = \begin{cases} 2 & \text{for } \dfrac{H}{W} \leqslant \dfrac{1}{3} \\ 2 + 0.3\left(\dfrac{H}{W} - \dfrac{1}{3}\right) & \text{for } \dfrac{H}{W} \geqslant \dfrac{1}{3} \end{cases} \tag{16}$$

It will be shown below that the solution presented in this paper can be used more accurately and efficiently for practical applications such as managing inverse problems including the optimization of the channel's dimensions and the determination of the currents needed to achieve the desired flow rates and flow patterns in MHD microfluidic networks [1,4,11,23]. In addition, the previous solution for the flow rate (expression (13)) is applicable only in the absence of the pressure gradient. In many MHD-based microfluidic applications such as MHD networks, pressure gradients are induced across the branch more often than not even in the absence of the externally applied pressure gradient. The present solution can thus be very useful for the design of the device and for the determination of experimental conditions.

3 MHD Flow Under ac Electric Field

When ac electric and magnetic fields are used (ac MHD), the magnetic flux density and the current density are, respectively, $\mathbf{B}\sin(\omega t)$ and $\mathbf{J}\sin(\omega t+\phi)$, where ω is the angular frequency of the fields and ϕ is the phase angle between the electric and magnetic fields. The momentum equation of a fully developed ac MHD flow then is

$$\rho\frac{\partial u}{\partial t} = -\frac{\partial p}{\partial x} + \mu\left(\frac{\partial^2 u}{\partial y^2} + \frac{\partial^2 u}{\partial z^2}\right) + JB\sin(\omega t)\sin(\omega t+\phi) \tag{17}$$

The time-averaged velocity and pressure are, respectively, $\langle u\rangle = \int_0^{2\pi} u\, d\,\omega t$ and $\langle p\rangle = \int_0^{2\pi} p\, d\,\omega t$. Integrating Eq. (17) with respect to ωt from $\omega t=0$ to 2π, we obtain

$$-\frac{\partial\langle p\rangle}{\partial x} + \mu\left(\frac{\partial^2\langle u\rangle}{\partial y^2} + \frac{\partial^2\langle u\rangle}{\partial z^2}\right) + JB\frac{\cos(\phi)}{2} = 0 \tag{18}$$

Equation (18) differs from Eq. (6) by the factor $\cos(\phi)/2$ in the last term of the left hand side.

Considering the solution of Eq. (6), we write the solution of the cross-sectional average velocity in ac MHD as

$$\langle\bar{U}\rangle = \frac{16a^2}{\pi^3 A_2 \mu}\frac{\Delta p}{L} + \frac{2aWB}{\pi^3 bA_2 \mu L} I\cos(\phi) \tag{19}$$

The time-averaged volumetric flow rate $\langle Q\rangle$ then is

$$\langle Q\rangle = \frac{64a^3 b}{\pi^3 A_2 \mu}\frac{\Delta p}{L} + \frac{8a^2 WB}{\pi^3 A_2 \mu L} I\cos(\phi) \tag{20}$$

In the absence of the pressure gradient imposed along the channel, the cross-sectional average velocity and the time-averaged flow rate in ac MHD are written as, respectively,

$$\langle\bar{U}\rangle = \frac{2aWB}{\pi^3 bA_2 \mu L} I\cos(\phi) \tag{21}$$

and

$$\langle Q\rangle = \frac{8a^2 WB}{\pi^3 A_2 \mu L} I\cos(\phi) \tag{22}$$

4 Validation of the Proposed Solutions

In order to validate the present result, rather extensive comparisons with existing analytical and experimental results are made. The integration of systems (1) and (2) is also performed by using a commercial computational fluid dynamics (CFD) package COMSOL (Version 3.3b)[3] and the results are compared with the present solutions.

4.1 dc MHD. In Fig. 2 the volumetric flow rate is plotted against the Lorentz force per unit length (IB) for two different aspect ratios, $H/W=0.475$ (Fig. 2(a)) and 1.5 (Fig. 2(b)), when $\mu=6\times10^{-4}$ Pa s, $L=20$ mm, and $W=800$ μm. The flow rate is linearly proportional to the Lorentz force per unit length. The straight line, triangles, dotted line, and dash-dotted line represent, respectively, the numerical solution of systems (1) and (2), the present approximate solution (Eq. (12)), the approximate solution (Eq. (13)), and Eq. (14) when $\Delta p=0$, respectively. The numerical solution (straight line in Fig. 2) is a fully converged output of COMSOL and serves as a reference for exact solutions. The results clearly show that the present solution mimics the numerical solution better than other approximations. It appears that using the exact series solution obtained for a viscous rectangular channel flow as the basis for the streamwise velocity profile is more favorable than using other profiles that simply satisfy the no-slip condition on channel walls.

Ho [5] experimentally investigated dc MHD pumps in channels with a depth of 7 mm, widths varying from 3 mm to 20 mm, length of 80 mm, and an electrode length of 35 mm. The magnetic field is kept at 0.02 T. The viscosity of the NaCl solution used is 6×10^{-4} Pa s, and the density is 1058 kg/m^3 (Table 1 in Ho [5]). The input current varies from 0.1 A to 1.3 A. The flow rates were measured in channels with various widths. These experimental data reported (▲) are plotted in Fig. 3(a) along with predictions based on the present result (solid line) for an input current of

[3] www.femlab.com

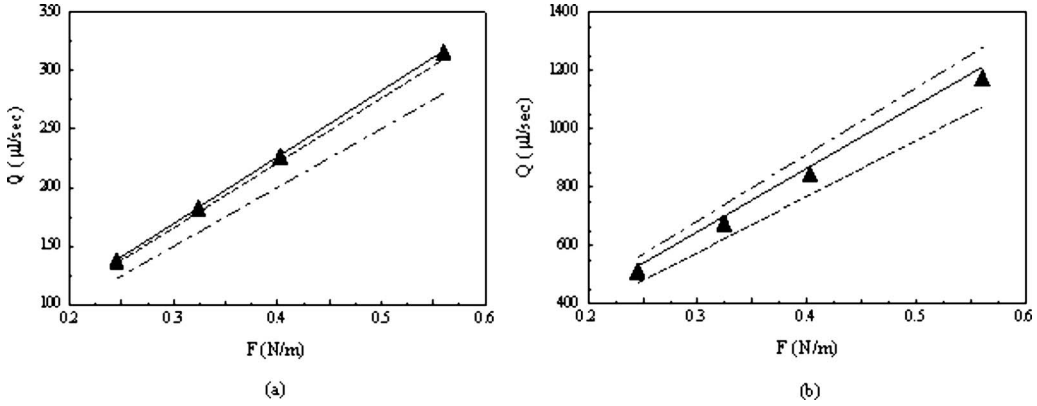

Fig. 2 The volumetric flow rate versus the Lorentz force per unit length ($F=IB$) for aspect ratios (*a*) 0.475 and (*b*) 1.5. The solid line, triangles, dashed line, and dash-dotted line represent, respectively, the results from full numerical simulation, the present closed-form solution, the approximation by Lemoff and Lee [10], and the approximation by Kabbani et al. [9].

0.7 A in the absence of the applied pressure gradient across the channel. It is clear that there is a good match between our closed-form solution and the experimental data obtained from the literature. Figure 3(*b*) depicts the mean velocity as a function of the current applied (0–1.4 A) when the channel width is 3 mm. The match is very good in general. At high current (>1 A), the deviation increases due to bubble formation under high current, which retards the flow in the experiments.

With the validation for a single dc MHD channel favorably established, we next examine the MHD microfluidic network studied experimentally by Bau et al. [4] in order to test the usefulness of the present simplistic solution for more complicated applications. Figure 4 schematically depicts the MHD network of Bau et al. [4]. The lengths of the channels within the network are 77.5 mm, 9.8 mm, 29.4 mm, 10 mm, 22.5 mm, and 22.5 mm for branches 1, 2, 3, 4, 5, and 6, respectively. The height and width of the channels are uniform with values of 1.7 mm and 1.1 mm. It is important to state here that the current density within the channel is not uniform since the planar electrodes only cover part of the sidewalls (i.e., the height of the electrode $<H$), and thus a correction factor k must be multiplied to give the actual value of the current density. Under this condition, the current I in expressions (9)–(12) is replaced by kI. For the network designed, the reported value for k is 0.16 [4]. The current is given as 10.301 mA, 0.967 mA, 0.484 mA, 1.322 mA, 0.745 mA, and 1.491 mA for branches 1, 2, 3, 4, 5, and 6, respectively, and the fluid viscosity is given as 0.001 Pa s. The pressure drop within each branch is negligible since the network is not capped. The achieved experimental flow rates in branches from 1 to 6 are, respectively, 0.75 μl/s, 0.563 μl/s, 0.188 μl/s, 0.75 μl/s, 0.375 μl/s, and 0.375 μl/s. The flow rates obtained from the present solution are, respectively, 0.752 μl/s, 0.558 μl/s, 0.186 μl/s, 0.748 μl/s, 0.375 μl/s, and 0.375 μl/s in the branches from 1 to 6. The predictions from our closed-form solution are shown to agree well with the experimental data available. The present approximation provides reliable predictions of MHD flows in MHD-based microfluidic networks.

Affanni and Chiorboli [1] considered a closed square loop consisting of four branches with a pair of electrodes installed in branch 1, as shown in Fig. 5(*a*). The flow in branch 1 is driven by both the Lorentz force and the induced pressure gradient, and in the rest of the loop the flow is driven by the induced pressure gradient. The viscosity of the fluid is given as 0.0011 Pa s, the magnetic field is 0.07 T, and the electric current is set to 0.2 A. The pressure drop within each branch of the loop is obtained by numerically solving systems (1) and (2) with the commercial software COMSOL, which is to be compared with the predictions based on the present solution here. It is to be noted that the in-phase ac quantities in the reference are treated comparable to dc ones. We

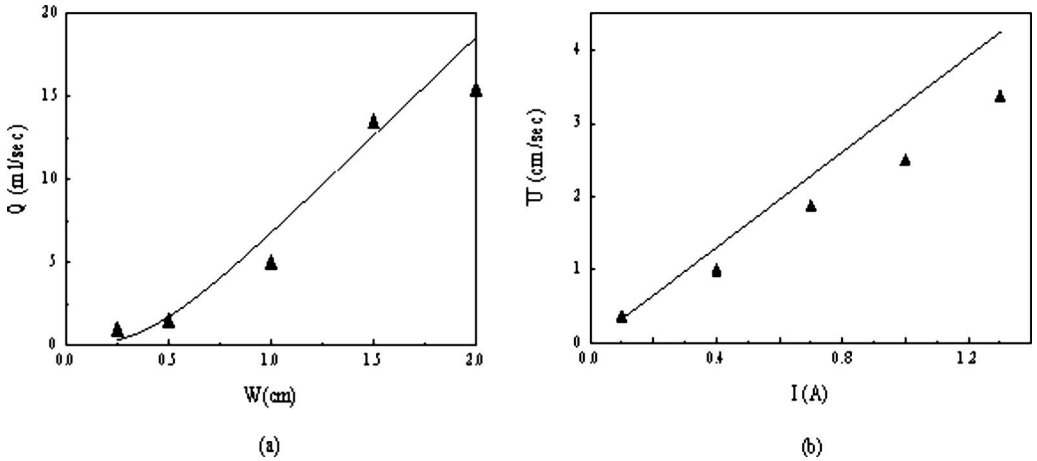

Fig. 3 Comparisons with the experimental data obtained by Ho [5]. (*a*) Flow rate versus channel width; (*b*) average velocity versus current applied. The solid line and the triangles represent, respectively, the results obtained from the present closed-form solution and the experimental data obtained from Ho [5].

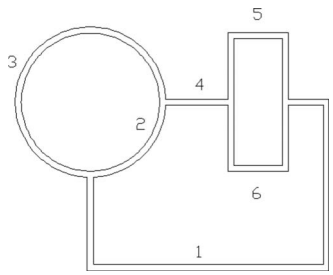

Fig. 4 Schematic diagram of the MHD microfluidic network of Bau et al. [4]

have five unknowns, which are the pressure drops at each branch and the volumetric flow rate flowing through the loop. Using the closed-form solution (Eq. (10)), we have four equations for the branches that relate the volumetric flow rate to other physical quantities and one constraint that sets the summation of all pressure drops in the loop to zero. This system of linear algebraic equations can be easily solved with a Gauss elimination method. Figure 5(*b*) shows the comparisons for the inlet and outlet pressures for each branch, with the origin indicated in Fig. 5(*a*). A counterclockwise fluid motion is induced in the closed loop. In branch 1, the flow is driven by an adverse pressure gradient and a positive Lorentz force in the *x*-direction. A positive pressure gradient is induced in other passive branches. The solid line and symbols in Fig. 5(*b*) represent, respectively, the results obtained

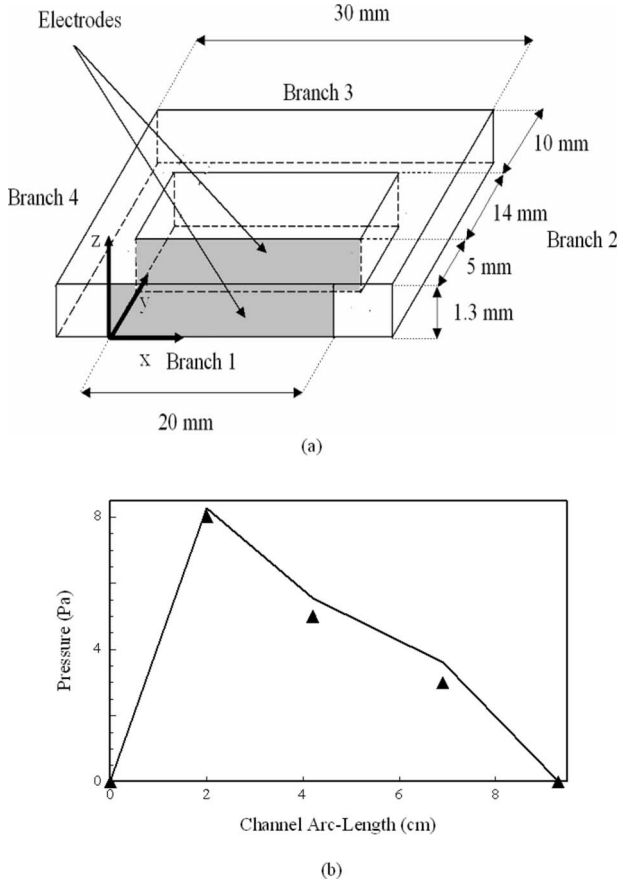

Fig. 5 (*a*) Schematic diagram of the closed microloop of Affanni and Chiorboli [1]. (*b*) Pressure variations along the centerline of the loop. The solid line and triangles represent, respectively, the prediction from the present closed-form solution and numerical solution of full systems (1) and (2).

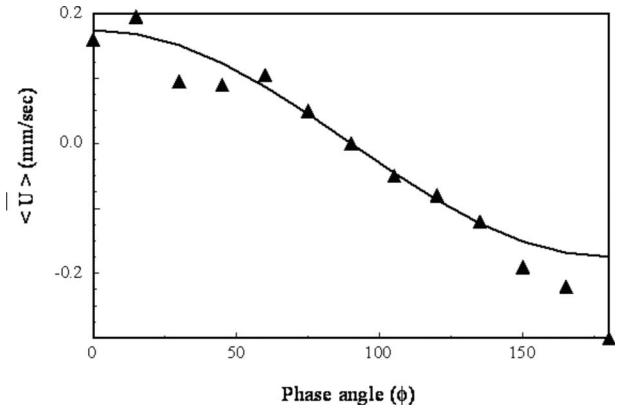

Fig. 6 The time-averaged velocity $\langle \bar{U} \rangle$ as a function of the phase angle. The solid line and the triangles represent, respectively, the result obtained from the present closed-form solution and the experimental data obtained from Lemoff and Lee [10].

from the closed-form solution (Eq. (10)) and the numerical results from systems (1) and (2). It is clear that there is a good match between both results. The reason for the overestimation is that the present solution does not consider the head loss due to the presence of the four bends in the loop. The present approximation nevertheless clearly demonstrates its usefulness for systems with pressure gradients, which is not included in the previous approximate solution (Eq. (13)).

4.2 ac MHD. For ac MHD micropumps, the present closed-form solution is compared with the experimental results of Lemoff and Lee [10], who used a microchannel 20 mm in length, 800 μm in width, and 380 μm in height, with 4 mm-long electrodes. The effective magnetic field used is 13 mT. The solutions used in the experiments are, respectively, 1*M* NaCl with an applied current of 140 mA, 0.1*M* NaCl with 100 mA, 0.01*M* NaCl with 36 mA, 0.01*M* NaOH with 24 mA, phosphate buffered saline (PBS) (*p*H 7.2) with 12 mA, and lambda DNA in 5 mM NaCl with 10 mA. The viscosities of these solutions are deduced from the calculated flow rate for each of the six solutions, listed by Lemoff and Lee [10], and they are 7×10^{-4} Pa s, 14×10^{-4} Pa s, 8×10^{-4} Pa s, 6×10^{-4} Pa s, 5×10^{-4} Pa s, and 6×10^{-4} Pa s, in the order mentioned above. The experimental time-averaged velocities reported for the above solutions are, respectively, 1.51 mm/s, 0.51 mm/s, 0.34 mm/s, 0.30 mm/s, 0.16 mm/s, and 0.11 mm/s. The predictions from the previous approximate solution used are, respectively, 1.0033 mm/s, 0.3344 mm/s, 0.2248 mm/s, 0.1974 mm/s, 0.1042 mm/s, and 0.0713 mm/s [10]. The results from our closed-form solution (Eq. (21)) are, respectively, 1.5392 mm/s, 0.5199 mm/s, 0.3466 mm/s, 0.3058 mm/s, 0.1631 mm/s, and 0.1121 mm/s. The results obtained from the present closed-form solution are consistently in better agreement with the experimental results than the previous approximation. Our results obtained from the closed-form solution are in excellent agreement with the results obtained by Wang et al. [13] by solving the governing system numerically with a finite-difference method. The model derived by Wang et al. [13], however, does not consider the pressure gradient along the channel and is less suitable for the analysis of the MHD network and MHD closed loop where pressure gradients are induced.

Figure 6 depicts the time-averaged velocity as a function of phase angle (ϕ) when the magnetic field is 2.51 mT and the applied current is 75 mA. It is clear that the mean velocity follows a harmonic wave, and the predictions obtained from the closed-form solution (Eq. (21)) agree with the experimental data obtained

from the literature [10]. The agreement in these comparisons shows that the present closed-form solution is reliable also for ac MHD flows in microfluidic devices.

5 Concluding Remarks

We introduce a new approximate solution for MHD flow (both ac and dc) in microchannels. The present solution is shown to be more accurate than previous approximate solutions and is applicable to MHD flows with pressure gradients as well. Comparisons with experimental and computational results indicate that the present solution can be used for MHD micropumps and MHD microfluidic networks under dc or ac fields.

Owing to its simple form and accuracy, the present solution can be efficiently used for design or control problems of MHD-based microfluidic applications. The model also allows one to test quickly and with low cost the effects of all contributing parameters and operating conditions on the performance of MHD-based microfluidic devices for various biomedical, clinical, and environmental applications.

Acknowledgment

This work is supported in part by the National Science Foundation under Grant No. 0447416 and by UNLV NIA and PRA grants. S.W.J. acknowledges the general financial support of Dongil Culture and Scholarship Foundation of Korea.

Nomenclature

a = min $(H/2, W/2)$
b = max $(H/2, W/2)$
B = magnetic flux density (T)
H = height of the channel (m)
I = current (A)
J = current density (A/m^2)
L = length of the channel (m)
L_E = electrode length (m)
ΔP = pressure drop (Pa)
Q = volumetric flow rate (m^3/s)
u = velocity (m/s)
W = width of the channel (m)
x, y, z = rectangular coordinate system

Greek Symbols

μ = viscosity (Pa s)
ω = angular frequency
φ = phase angle
$\langle\ \rangle$ = average quantities

References

[1] Affanni, A., and Chiorboli, G., 2006, "Numerical Modelling and Experimental Study of an ac Magnetohydrodynamic Micropump," *2006 Instrumentation and Measurement Technology Conference*, Sorrento, Italy.

[2] Aguilar, Z. P., Arumugam, P., and Fritsch, I., 2006, "Study of Magnetohydrodynamic Driven Flow Through LTCC Channel With Self-Contained Electrodes," J. Electroanal. Chem., **591**, pp. 201–209.

[3] Arumugam, P. U., Fakunle, E. S., Anderson, E. C., Evans, S. R., King, K. G., Aguilar, Z. P., Carter, C. S., and Fritsch, I., 2006, "Redox Magnetohydrodynamics in a Microfluidic Channel: Characterization and Pumping," J. Electrochem. Soc., **153**, pp. E185–E194.

[4] Bau, H. H., Zhu, J., Qian, S., and Xiang, Y., 2003, "A Magneto-Hydrodynamically Controlled Fluidic Network," Sens. Actuators B, **88**, pp. 205–216.

[5] Ho, J., 2007, "Characteristic Study of MHD Pump With Channel in Rectangular Ducts," J. Mar. Sci. Technol., **15**, pp. 315–321.

[6] Homsy, A., Koster, S., Eijkel, J. C. T., van den Berg, A., Lucklum, F., Verpoorte, E., and de Rooij, N. F., 2005, "A High Current Density DC Magnetohydrodynamic (MHD) Micropump," Lab Chip, **5**, pp. 466–471.

[7] Homsy, A., Linder, V., Lucklum, F., and de Rooij, N. F., 2007, "Magnetohydrodynamic Pumping in Nuclear Magnetic Resonance Environments," Sens. Actuators B, **123**, pp. 636–646.

[8] Jang, J., and Lee, S. S., 2000, "Theoretical and Experimental Study of MHD (Magnetohydrodynamic) Micropump," Sens. Actuators, A, **80**, pp. 84–89.

[9] Kabbani, H., Wang, A., Luo, X., and Qian, S., 2007, "Modeling RedOx-Based Magnetohydrodynamics in Three-Dimensional Microfluidic Channels," Phys. Fluids, **19**, p. 083604.

[10] Lemoff, A. V., and Lee, A. P., 2000, "An AC Magnetohydrodynamic Micropump," Sens. Actuators B, **63**, pp. 178–185.

[11] Mathaba, T., Mpholo, M., Sebitia, S., and Bau, H. H., 2006, "Magneto-Hydrodynamic Fluid Flow Simulation Tool," *2006 International Conference on Micro and Nano Technologies, ICMNT06*, Tizi-Ouzou, Algeria.

[12] Qian, S., and Bau, H. H., 2005, "Magneto-Hydrodynamic Flow of RedOx Electrolyte," Phys. Fluids, **17**, p. 067105.

[13] Wang, P. J., Chang, C. Y., and Chang, M. L., 2004, "Simulation of Two-Dimensional Fully Developed Laminar Flow for a Magneto-Hydrodynamic (MHD) Pump," Biosens. Bioelectron., **20**, pp. 115–121.

[14] Zhong, J., Yi, M., and Bau, H. H., 2000, "Magneto Hydrodynamic (MHD) Pump Fabricated With Ceramic Tapes," Sens. Actuators, A, **96**, pp. 59–66.

[15] Bau, H. H., Zhong, J., and Yi, M., 2001, "A Minute Magneto Hydro Dynamic (MHD) Mixer," Sens. Actuators B, **79**, pp. 207–215.

[16] Qian, S., Zhu, J., and Bau, H. H., 2002, "A Stirrer for Magnetohydrodynamically Controlled Minute Fluidic Networks," Phys. Fluids, **14**, pp. 3584–3592.

[17] Qian, S., and Bau, H. H., 2005, "Magnetohydrodynamic Stirrer for Stationary and Moving Fluids," Sens. Actuators B, **106**, pp. 859–870.

[18] Xiang, Y., and Bau, H. H., 2003, "Complex Magnetohydrodynamic Low-Reynolds-Number Flows," Phys. Rev. E, **68**, p. 016312.

[19] Yi, M., Qian, S., and Bau, H. H., 2002, "A Magnetohydrodynamic Chaotic Stirrer," J. Fluid Mech., **468**, pp. 153–177.

[20] Clark, E. A., and Fritsch, I., 2004, "Anodic Stripping Voltammetry Enhancement by Redox Magnetohydrodynamics," Anal. Chem., **76**, pp. 2415–2418.

[21] Eijkel, J. C. T., Van den Berg, A., and Manz, A., 2004, "Cyclic Electrophoretic and Chromatographic Separation Methods," Electrophoresis, **25**, pp. 243–252.

[22] Gao, Y. P., Wei, W. Z., Gao, X. H., Zhai, X. R., Zeng, J. X., and Yin, J., 2007, "A Novel Sensitive Method for the Determination of Cadmium and Lead Based on Magneto-Voltammetry," Anal. Lett., **40**, pp. 561–572.

[23] Lemoff, A. V., and Lee, A. P., 2003, "An AC Magnetohydrodynamic Microfluidic Switch for Micro Total Analysis Systems," Biomed. Microdevices, **5**, pp. 55–60.

[24] West, J., Karamata, B., Lillis, B., Gleeson, J. P., Alderman, J., Collins, J. K., Lane, W., Mathewson, A., and Berney, H., 2002, "Application of Magnetohydrodynamic Actuation to Continuous Flow Chemistry," Lab Chip, **2**, pp. 224–230.

[25] White, F. M., 2006, *Viscous Fluid Flow*, 3rd ed., McGraw-Hill, New York.

Luo Jing

Li Jian
e-mail: lijian@rimp.com.cn

Wuhan Research Institute of Materials Protection,
126 Bao Feng Er Lu,
Wuhan, Hubei 430030, P.R.C.

Dong Guangneng
Xi'an Jiaotong University,
28 Xian Ning Xi Lu,
Xi'An, Shanxi 710049, P.R.C.

Two-Dimensional Simulation of the Collapse of Vapor Bubbles Near a Wall

In order to investigate the erosion extent and mode of cavitation in different states by the commercial code FLUENT *and evaluate the reliability of the software, the collapse processes of a vapor bubble, which was near or on the wall under the conditions in the stationary water or the high speed water, were simulated by the numerical calculation by using a 2D model. The results are in accordance with results presented by other researchers, so the simulation may testify to the validation of the code. We suppose that a bevel jet, which is generated contrary to the flow direction when the bubble collapses in high speed flow, may cause the ripple and fish-scale pit damage found on the transition parts of many hydraulic systems.* [DOI: 10.1115/1.2953233]

1 Introduction

Hydrodynamic cavitation is one of the major sources of erosion damage in hydraulic systems [1]. To explain the mechanism of cavitation damage, Rayleigh first proposed that cavitation is caused by high pressure. Subsequently, many researchers such as Kornfeld, Benjamin, and Plesset reported that cavitation damage is caused by shock waves or a liquid microjet produced by the collapse of nonspherical bubbles [2–5]. Also, high temperatures and cavitation-inducing electrochemistry and chemical reactions are thought to be factors in cavitation damage of solid materials [3,6].

Visualization technology as a novel verification method has provided direct results on cavitation erosion. The dynamic process of bubbles produced by laser or air injection was captured by high speed video camera [7–10]. Ohl claimed that he had captured the counterjet in the experiment. Shima found that the jet and the shock wave coexist at a very short time [11]. Kimoto observed that stress pulses are caused by both microjet impingement and the residual group of collapsed shock waves [12].

Numerical simulation methods offset some difficulties of experiments. The Rayleigh–Plesset equation modeling the surface tension and the viscous effect has become a basic equation in the numerical studies of cavitation or bubble collapse [1,13]. Strauss supposed the bubbles to be uniform in pressure to study the expansion and collapse of a bubble based on the two-dimensional Rayleigh equation [14]. Shima simulated the collapse processes of a single and also two bubbles, and studied the interaction of the bubbles [11]. Pearson applied the boundary-integral method and assumed an inviscid and incompressible flow to calculate the motion of a single bubble near a rigid boundary [15].

There is no doubt that both the jet and the shock wave are generated when bubbles collapse, but it remains a matter of debate which is the leading cause of damage and the corresponding damage process and appearance [16–18]. Some researchers accept that the material is destroyed by variational stress from shock waves, but others propose that the "water hammer" effect of jets is the direct cause of material damages. Experimental results and simulated results often fail to agree due to limitations in the precision of the apparatus, and also as a result of differing assumptions in modeling cavitation and bubble collapse [19–21].

The purpose of this study is mainly to estimate some cavitation phenomena in experiments being performed. In one experiment of acoustic cavitation, the diameter of the emitter surface is 16 mm and the ultrasound power is 500 W, so the maximum acoustic pressure is about 2 MPa [22], and the bubbles emitted and clustered around the sample surface, which is 10 mm away from the emitter surface, expand to approximately 1 mm observed by the naked eye before collapse. During this experiment, we find that bubbles concentrate at the center of the sample surface, but the damage at the center of the material is much less than at the border. We speculate that the cause may be the bumper effect of bubbles and water. In this paper, we simulate the collapse of a bubble by the software FLUENT, investigate the extent of the erosion and mode of cavitation under different conditions, and verify the reliability of the software code for further study.

2 Physical Model

In this study, we adopt the mixture multiphase flow and cavitation model. Applying the fluid dynamics computation to the Newtonian liquid equation [23–25], the continuity equation is

$$\frac{\partial}{\partial t}((1-a)\rho_l + a\rho_v) + \nabla((1-a)\rho_l \mathbf{v}_l + a\rho_v \mathbf{v}_v) = 0 \tag{1}$$

The mass transfer due to cavitation is

$$\dot{m} = \frac{\partial}{\partial t}(a\rho_v) + \nabla(a\rho_v \mathbf{v}) \tag{2}$$

The momentum equations for vapor bubble and water are

$$\frac{\partial}{\partial t}(a\rho_v \mathbf{v}_v) + \nabla(a\rho_v \mathbf{v}_v \mathbf{v}_v) = -a\nabla p + a\rho_v \mathbf{F}_v + \nabla(a\mu_v(\nabla \mathbf{v}_v + \nabla v_v^T)) + \dot{m}\mathbf{v}_v \tag{3}$$

$$\frac{\partial}{\partial t}((1-a)\rho_l \mathbf{v}_l) + \nabla((1-a)\rho_l \mathbf{v}_l \mathbf{v}_l) = -(1-a)\nabla p + (1-a)\rho_l \mathbf{F}_l + \nabla(a\mu_l(\nabla \mathbf{v}_l + \nabla v_l^T)) + \dot{m}\mathbf{v}_v \tag{4}$$

The energy equation for adiabatic liquid is

Contributed by the Fluids Engineering Division of ASME for publication in the JOURNAL OF FLUIDS ENGINEERING. Manuscript received May 23, 2007; final manuscript received April 28, 2008; published online August 11, 2008. Assoc. Editor: Ian Eames.

$$\frac{\partial}{\partial t}(a(c_v T + v_v{}^2/2 - p/\rho_v) + (1-a)(c_l T + v_l{}^2/2 - p/\rho_l)) + \nabla(a\mathbf{v}_v(c_v T + v_v{}^2/2) + (1-a)\mathbf{v}_l(c_l T + v_l{}^2/2)) = \nabla(k\nabla T) \quad (5)$$

where P is the static pressure, v is the velocity, ρ is the density, μ is the viscosity, T is the temperature, σ is the surface tension coefficient, a is the volume fraction of vapor, c is the specific heat capacity at constant pressure, k is the effective conductivity, and R is the radius of the bubble. The subscripts v and l represent the vapor and water, respectively.

The investigation of Prevenslik indicated that bubble collapse occurs almost isothermally at ambient temperature, and that high bubble temperatures occur not in bubble collapse but by the impact of water [26]. Vapor rapidly transforming into water near the bubble wall because of external high pressure leads to less compression of the vapor inside the bubble. Therefore, the heat exchange between water and vapor can be neglected. Gravity and the incondensible gas are not considered. The compressibility of water is considered to be a constant as its Young's modulus is 2.1×10^9 Pa. The density of vapor is assumed to conform to the ideal gas law. In this study, the parameters assume the physical properties of the water and vapor at 20°C, in which the critical cavitation pressure is 2300 Pa and the surface tension is 0.073 N/m. Other parameters are the default values of FLUENT.

Research [1,27] has reported that cavitation erosion is produced mainly by irregular bubbles adhering to the solid wall. The shape of the bubble can change frequently in the complicated fluid field so that it cannot maintain a perfect sphere or ellipsoid. Generally, it is commonly assumed that the bubble is a hemisphere in simulations. In this simulation, the radius of the bubble is 0.5 mm, and the pressure of the exterior region far away from the bubble is 2 MPa. Three cases are considered: (1) A bubble is 0.25 mm from the solid wall and the initial water flow is stationary; (2) a bubble is on the solid wall and the initial water flow is stationary; (3) a bubble is on the solid wall and the initial mean velocity of the water is 30 m/s. The distance 0.25 mm and the water velocity 30 m/s were chosen to discuss the bumper effect of water and the effect of water flow on the bubbles' collapse, respectively.

In the three simulations, the minimum grid length is 1 μm; the total quadrilateral grids of each model are approximately 4×10^6. The calculation is considered as a semiqualitative and semiquantitative study and the time expense of the simulation is high enough so that we use a two-dimensional semi-infinite plane model as the solver space. The viscous model adopts the Reynolds stress closure. Except for time, density and vapor discretizations are firstorder due to the limitation of the FLUENT code; pressure and pressure velocity coupling discretizations are body force weighted and the pressure-implicit with splitting of operators (PISO) scheme, respectively. Other discretizations adopt third order monotone upstream-centered schemes for conservation laws (MUSCL) scheme. The solid wall is fixed without velocity. In order to capture the details and the maximum pressure and velocity, the time step is set to 0.001 μs. In the initialization, the grid region of the bubble is defined as pure vapor and the pressure is 2300 Pa.

3 Results

3.1 Shape Variety of Bubbles. Figure 1 shows the collapse process of a bubble near the solid wall in the stationary water. The background circles are the original contour lines of the bubbles. The bubble is shrinking into its center and moving toward the wall. The shape of the bubble in the collapse is not completely symmetrical since there is some divergence between the left and right parts. The phenomenon is consistent with the results obtained by the high speed video camera in previous experiments [9,10]. Figure 2 shows the collapse process of a bubble on the wall in stationary water. The shapes of the bubble at different times remain approximately symmetrical. Figure 3 shows the collapse process of a bubble on the wall in a high speed flow from the left to the right. The high speed water causes the bubble contour to tilt in the direction of the flow, and a dent forms on the back where the jet is formed. The bubble contour varies spirally by the effect of the high speed water and dents from the backside where the jet is formed. Finally, the bubble is completely collapsed at a point 0.3 mm from the center of the original bubble.

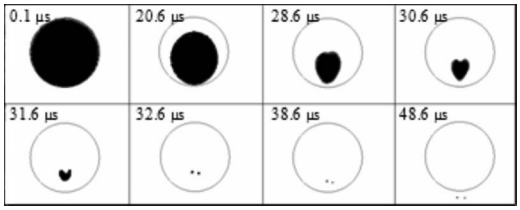

Fig. 1 Collapse process of a bubble near the wall. The initial radius of the bubble is 0.5 mm, the pressure of the exterior region far from the bubble is 2 MPa, and the initial velocity of water is 0.

In the first case, the jet pierces through the collapsing center perpendicular to the solid wall, and then a pair of counter-rotating vortices containing remnants of vapor is formed, as shown in Fig. 4. In three dimensions, it is really a ring bubble with the jet shooting through the center of the ring. The tiny bubble pair moves quickly to the solid wall and separates gradually as the strength and velocity of the jet decreases.

The viscous shear stress of the water above the bubble wall is less than below, so the velocity of the water above the bubble wall increases more rapidly when the bubble is compressed. Therefore, the center of the bubble tends to move toward the solid wall. In the third case, the bottom of the bubble moves slowly because of the effect of the solid wall, but the top of the bubble is pushed by the water flow so the shape of the bubble tilts.

3.2 Collapse Time and Jet. The nearby water penetrates to the interior of the bubble to form the jet and accelerates to the maximum velocity until the bubble is completely collapsed. Figure 5 shows the velocities of the jets' head obtained by the capture function of FLUENT during the collapse of a bubble at three conditions. If we assume that the jet head is accelerated to maximum velocity as the collapse occurs, the complete collapse time of the first case is approximately 32 μs and the corresponding maximum

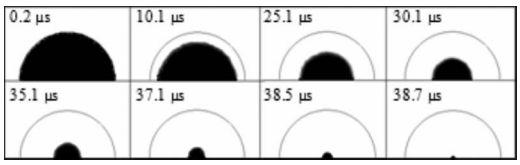

Fig. 2 Collapse process of a bubble on the wall. The initial radius of the bubble is 0.5 mm, the pressure of the exterior region far from the bubble is 2 MPa, and the initial velocity of water is 0.

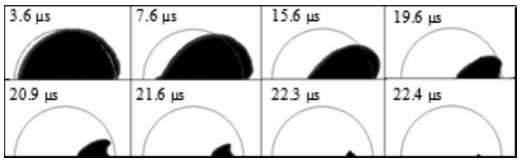

Fig. 3 Collapse process of a bubble on the wall. The initial radius of the bubble is 0.5 mm, the pressure of the exterior region far from the bubble is 2 MPa, and the initial velocity of water is 30 m/s from the left to the right.

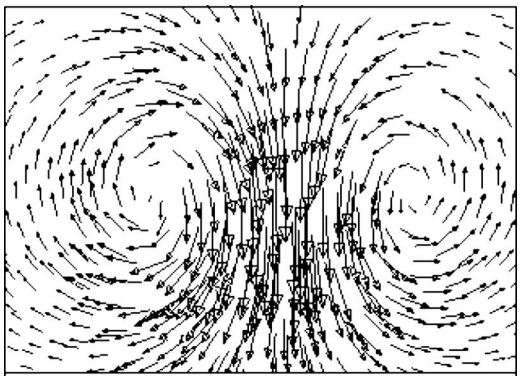

Fig. 4 Counter-rotating vortices

jet velocity is 480 m/s. The other two cases measure 38.7 μs and 1450 m/s, and 22.5 μs and 1360 m/s, respectively.

The amounts of momentum of the bubbles in the three cases are almost equivalent, but the area pierced through by the jet in the first case is larger than the others and the jet velocity of the first case is much lower than the others. As shown in Fig. 5, the collapse time of the bubble in the second case is longer than that of the first case because of heavier viscous shear stress of the water around the solid wall. Furthermore, the high speed flow aggravates the intensity of turbulence and instability of the bubble, such that the collapse time of the third case is approximately half the time of the second.

The direction of the jet formed in the first two cases is almost perpendicular to the solid wall. This is in accordance with the investigation [2]. However, the result is different when a bubble collapses in the high speed flow. Figure 6 shows the jet vector at the moment before the bubble completely collapses in the third case. In this case, the jet shoots to the wall at an angle of about 45 deg and the direction of the jet is contrary to the flow. However, the jet angle is less than 45 deg at the point when the bubble is completely collapsed. We suppose that a local high pressure area is generated by the Karman vortex street to form the jet in the back of the bubble when the water flows around the bubble.

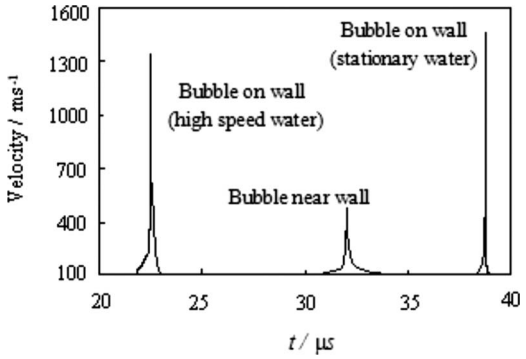

Fig. 5 Jet velocities during bubbles collapse at three conditions

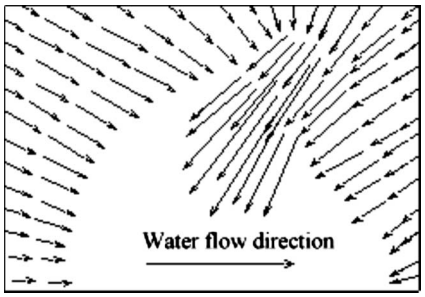

Fig. 6 Jet vector of a bubble on wall before complete collapse (the initial mean velocity of the water is 30 m/s and the time is at 22.4 μs)

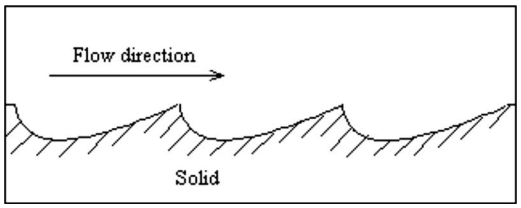

Fig. 7 Sketch of fish-scale pit

When a bevel jet impacts a solid surface, the normal stress and shear stress will occur according to the theories of material mechanics. If the bevel jet is strong enough to penetrate into the interior of the solid at the bevel angle, the kinetic energy of the jet is converted into heat energy and compression energy. When the kinetic energy is exhausted or insufficient to maintain wedging, the potential energy of compression is released to generate a shock wave. If the shock wave is intense enough that cracks occur around the end of the jet trace, then even the solid material is broken to form a pit. Cracks developed by stress fatigue will also generate pits as the material is peeled. The result of these direct or indirect modes of material peeling is fractures, which are deep at the front and shallow at the back along the flow direction. It is noticed that the analysis of material fracture mechanics exceeds the research range of the fluid dynamics; however, our intention is to explain the following case.

As a practical engineering problem, when a hydraulic turbine operates enough time, its smooth surface will present some characteristic damage morphology similar to ripples or fish scales, as shown in Fig. 7. These pits are deep at the front and shallow at the back along the flow direction and large pits comprise many micropits. There is controversy over the cause of the pits in hydraulic engineering [28–30], and there has been no novel explanation until now. Yao presented the view that the pits are the result of bursting and sweeping induced by vortices in the boundary layer [29]. Wu thought the pits are formed by the impact and shear of sands [30]. By the former analysis, we speculate that the microfish-scale pits are possibly generated by the jet.

3.3 Pressure. Figure 8 shows the maximum pressure on the wall obtained by the monitor function of FLUENT during the collapse of the bubble in the three cases. They are 550 MPa, 2200 MPa, and 1860 MPa, respectively.

The shock wave is generated in the center of the collapsing bubble and spreads outwards rapidly. It is weakest in the wave center and strongest on the wave front. Figure 9 shows the state of

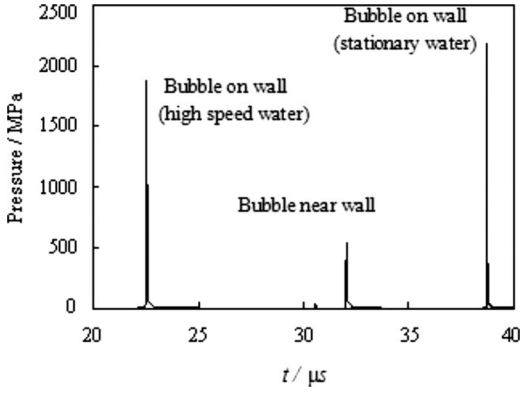

Fig. 8 Maximum pressure on the wall during bubble collapse

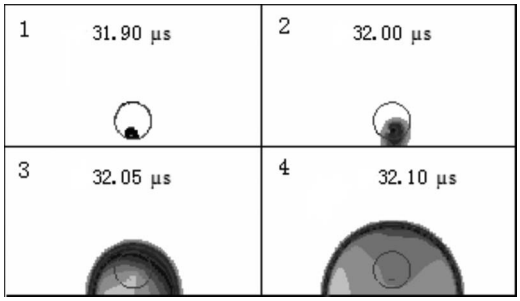

Fig. 9 Shock waves generated when a bubble near the wall has collapsed completely

the shock waves in the first case; the dark boundaries are the shock waves' front and the dark sections are the highest pressure regions. Though the maximum jet velocity of the bubble collapse can reach 480 m/s, the jet impact velocity to the solid wall hardly exceeds 20 m/s. Therefore, it can be concluded that the high pressure on the wall is caused by the shock wave, not the direct impact of the jet. This is due to the bumper effect of the water between the wall and the bubble. The result indicates that the maximum pressure generated in the collapsing center exceeds 1000 MPa, but the maximum pressure on the wall is only 550 MPa. The complete collapse time is approximately 0.1 μs before the maximum pressure reaches the wall; therefore, the attenuation of the shock wave is very rapid.

Figure 10 shows the pressure distribution on the wall after the bubble is completely collapsed in the first case. The pressure around the collapsing center rises abruptly when the shock wave is expanding and declining sharply. Therefore, the intense alternative stress and strain on the material surface are generated by the high pressure and pressure gradient. When the material reaches its yield limit, the damage will appear annularly.

The jet is actually the result of the unbalanced state of the fluid. The shock wave is produced by residual gases, which include undissolved gases or uncoagulated vapor that are condensed to the limit and then expanded, or by the mutual impact of different direction liquids, or by the impact of the jet on the wall. Thus, a jet would not be formed in an ideal fluid without a solid wall, but the shock wave is inevitable in the final collapse stage of a bubble. Because the dimension is very small, the jet produces some severe damage such as pinholes. The shock wave is spherical; therefore, it can produce a large circular area of damage.

4 Conclusions

The simulation shows bubble collapse in three different cases. From these cases, we suppose that the micropits on the wall are produced by the impact of jets directly and the ring damage by the shock waves. Otherwise, we suppose that a bevel jet is maybe the generating cause of the ripple or fish-scale pit in many hydraulic systems. Although these simple cases are based on a 2D model, they are in accordance with results presented in other research.

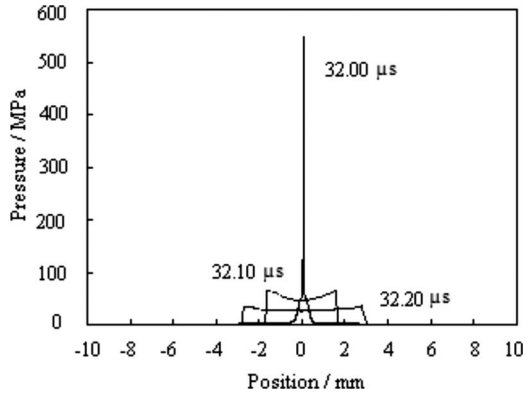

Fig. 10 Pressure distribution on the wall after the bubble near the wall is collapsed completely

Acknowledgment

The authors would like to thank the support provided by National Natural Science Foundation of China (No. 50432020, No. 50675160) and National Scientific and Technical Project of China (No. 2007CB607603).

References

[1] Brennen, C. E., 1995, *Cavitation and Bubble Dynamics*, Oxford University Press, New York.
[2] Popinet, S., and Zaleski, S., 2002, "Bubble Collapse Near A Solid Boundary: A Numerical Study of the Influence of Viscosity," J. Fluid Mech., **464**, pp. 137–163.
[3] Philipp, Lauterborn, 1998, "Cavitation Erosion by Single Laser-Produced Bubbles," J. Fluid Mech., **361**, pp. 75–116.
[4] Hickling, R., and Plesset, M. S., 1964, "Collapse and Rebound of a Spherical Bubble in Water," Phys. Fluids, **7**, pp. 7–14.
[5] Plesset, M. S., and Chapman, R. B., 1971, "Collapse of an Initially Spherical Vapor Cavity in the Neighborhood of a Solid Boundary," J. Fluid Mech., **47**, pp. 283–290.
[6] Lin, H., Brian, D. S., and Andrew, J. S., 2002, "Rayleigh–Taylor Instability of Violently Collapsing Bubbles," Phys. Fluids, **14**, pp. 2925–2928.
[7] Tomita, Y., and Shima, A., 1990, "High-Speed Photographic Observations of Laser Induced Cavitation Bubbles in Water," Acustica, **71**, pp. 161–171.
[8] Lauterborn, W., 1997, "Cavitation Bubble Dynamics," Ultrason. Sonochem., **4**, pp. 65–75.
[9] Ohl, C. D., Lindau, O., and Lauterborn, W., 1998, "Details of Asymmetric Bubble Collapse," *Third International Symposium on Cavitation*, Grenoble, France, Band 1, pp. 39–44.
[10] Lu, F. K., and Zhang, X., 1999, "Visualization of a Confined Accelerated Bubble," Shock Waves, **9**, pp. 333–339.
[11] Shima, A., 1997, "Studies on Bubble Dynamics," Shock Waves, **7**, pp. 33–42.
[12] Ishida, H., Nuntadusit, C., and Kimoto, H., 2001, "Cavitation Bubble Behavior Near Solid Boundaries," *Fourth International Symposium on Cavitation*, Pasadena, CA.
[13] Sunitha, N., Kenneth, J., Lahey, R. T., Jr., and Iskander, A., 2006, "Hydrodynamic Simulation of Air Bubble Implosion Using a Level Set Approach," J. Comput. Phys., **215**, pp. 98–132.
[14] Strauss, M., Friedman, M., Gurewitz, E., Amendt, P., London, R. A., and Glinsky, M. E., 1999, "Two Dimensional Rayleigh Model of Vapor Bubble Evolution," Proc. SPIE, **3601**, pp. 212–224.
[15] Pearson, A., Blake, J. R., and Otto, S. R., 2004, "Jets in Bubbles," J. Eng. Math., **48**, pp. 391–412.
[16] Parag, M. K., Parag, R. G., Aniruddha, B. P., and Anne, M. W., 2003, "Cavity Cluster Approach for Quantification of Cavitational Intensity in Sonochemical Reactors," Ultrason. Sonochem., **10**, pp. 181–189.
[17] Parag, M. K., Parag, R. G., Aniruddha, B. P., and Anne, M. W., 2005, "Dynamics of Cavitational Bubbles and Design of a Hydrodynamic Cavitational Reactors: Cluster Approach," Ultrason. Sonochem., **12**, pp. 441–452.
[18] Iga, Y., Nonmi, N., Goto, A., Shin, B. R., and Ikohagi, T., 2003, "Numerical Study of Sheet Cavitation Breakoff Phenomenon on a Cascade Hydrofoil," J. Fluid Mech., **125**, pp. 643–650.
[19] Bourne, N. K., 2005, "On Stress Wave Interactions in Liquid Impact," Wear, **258**, pp. 588–595.
[20] Chen, X., Xu, R. Q., Shen, Z. H., Lu, J., and Ni, X. W., 2004, "Optical Investigation of Cavitation Erosion by Laser-Induced Bubble Collapse," Opt. Laser Technol., **36**, pp. 197–203.
[21] Kyuichi, Y., 2002, "Segregation of Vapor and Gas in a Sonoluminescing Bubble," Ultrasonics, **40**, pp. 643–647.
[22] Burdin, F., Tsochatzidis, N. A., Guiraud, P., Wilhelm, A. M., and Delmas, H., 1999, "Characterization of the Acoustic Cavitation Cloud by Two Laser Techniques," Ultrason. Sonochem., **6**, pp. 43–51.
[23] Anderson, J. D., Jr., 1995, *Computational Fluid Dynamics: The Basics With Applications*, McGraw-Hill, New York.
[24] Bowen, R. M., 1976, *Theory of Mixtures*, Academic, New York.
[25] Fluent Inc, 2005, FLUENT 6.2 User's Guide.
[26] Prevenslik, T. V., 2003, "The Cavitation Induced Becquerel Effect and the Hot Spot Theory of Sonoluminescence," Ultrasonics, **41**, pp. 313–317.
[27] Yasuhiro, S., and Keiichi, S., 2003, "Cavitation Bubble Collapse and Impact in the Wake of a Circular Cylinder," *Fifth International Symposium on Cavitation*, Osaka, Japan, Paper No. Cav03-GS-11-004.
[28] Wang, L. Y., 1998, "Chat About Fish-Scale Pit," *China Proceedings Abrasion and Cavitation in Hydraulic Machinery*, pp. 106–119, in Chinese.
[29] Yao, Q. P., 1999–2000, "Some Pattern and Law of Hydraulic Turbine Abrasion and Cavitation Viewing From Boundary Layer Theory," *China Proceedings Abrasion and Cavitation in Hydraulic Machinery*, pp. 45–50, in Chinese.
[30] Wu, P. H., 2002–2003, "Probe Into the Nature and Cause of the Formation of Ripple and Fish-Scale Pit Damages," *China Proceedings Abrasion and Cavitation in Hydraulic Machinery*, pp. 51–58, in Chinese.

Distributions of Pressure, Velocity, and Void Fraction for One-Dimensional Gas-Liquid Bubbly Flow in Horizontal Pipes

Phu D. Tran
Maunsell Australia,
Level 11, 44 Market Street,
Sydney, 2000, Australia
e-mail: phu.tran@maunsell.com

A homogeneous model for prediction of the longitudinal distributions of pressure, velocity, and void fraction for two-phase bubbly flow in horizontal pipes is presented. The mixture flow is described by a system of two nondimensional ordinary differential equations that can be integrated numerically to yield the distributions of the flow variables along the pipe. The viscosity of the two-phase mixture is assumed to vary with the void fraction according to a polynomial form. Experimental data were obtained for a range of air-water bubbly flow in a horizontal pipe. Prediction of pressure distributions along the pipe compares favorably with experimental data, while prediction of void fraction distributions can be achieved with moderate accuracy. [DOI: 10.1115/1.2953226]

Keywords: bubbly flow, homogeneous model, void fraction, pressure distribution, mixture viscosity

1 Introduction

Initial steady-state distributions of pressure, velocity, and void fraction along the pipe are normally required, together with boundary conditions, in any transient flow analysis such as prediction of wave speed and pressure transients following valve closure in a two-phase pipe flow. Griffith [1] pointed out that when the contribution of gravity to the total pressure drop is unimportant, the homogeneous model can be used to calculate void fraction with reasonable accuracy. Griffith recommended the homogeneous model when the pressure drop, rather than the void fraction, is the primary concern, and the gravity contribution to the pressure drop is small such as in horizontal pipe flow. Several researchers found that the homogeneous model was adequate for solving certain two-phase flow problems.

Martin and co-workers [2–4] and Chaudhry et al. [5] successfully predicted pressure pulse propagation in bubbly and slug flows using a one-dimensional homogeneous model, and Davis and Wang [6] developed a flow meter for measuring mass flow rates in bubbly flow based on a one-dimensional nonslip homogeneous flow model.

Wallis [7] and Govier and Aziz [8] recommended a very simple approach using a Reynolds number based on liquid viscosity together with a single-phase correlation to calculate the friction factor. Huey and Bryant [9], Kopalinsky and Bryant [10], and Davis [11] developed explicit analytical expressions for the flow variables using a homogeneous model, treating the bubbly mixture as a pseudogas with average properties. Although Huey and Bryant found that the local friction coefficient would vary considerably along the pipe, they assumed a constant average friction factor for the entire length of the pipe in order to derive an expression for the pressure distribution. Their flow model requires an empirical correlation for the average friction coefficient. Both Kopalinsky and Bryant and Davis correlated the average friction factor with a Reynolds number based on liquid viscosity, the choice of which was necessary so that the Reynolds number became constant for any particular flow condition. Kopalinsky and Bryant constructed average friction factor charts for 25.4 mm and 50.8 mm diameter horizontal pipes, and Davis for 38.2 mm horizontal and vertical pipes, to be used with their models. Both Kopalinsky and Bryant's model and Davis' model can be used to predict pressure distributions along the pipe with good accuracy, provided the flow parameters are within the bounds of their experimental data.

The purpose of this paper is to formulate a steady flow model for providing the initial values of the flow variables to be used in conjunction with a transient flow model for complete description of pressure wave propagation in two-phase pipe flow.

2 Homogeneous Model

The analysis described in this paper is limited to homogeneous flow in horizontal pipes, which is defined herein as steady-state bubbly flow in the dispersed flow regime, i.e., in which the small gas bubbles are dispersed throughout the liquid and the two phases move at approximately the same velocity. For well mixed bubbly flows, it has been established empirically that the relative motion between the phases is generally small and the slip ratio is almost equal to unity (Herringe and Davis [12]). Govier and Aziz [8] found that dispersed flow would begin at superficial liquid velocity approximately 2.7 m/s. This was confirmed by Weisman et al. [13], who observed that dispersed flow regime would be established when the liquid mass flux exceeds 1×10^7 kg/h m^2, i.e., when superficial liquid velocity exceeds 2.8 m/s in an air-water system. All the data presented in this paper, including the experimental data and the literature data, fall within the dispersed flow regime according to Govier and Aziz [8] and Weisman et al. [13].

The steady flow model presented herein is a homogeneous model, which assumes that the gas and liquid are uniformly distributed over the flow cross section so that the mixture can be regarded as a single-phase fluid with mean values of the properties of the two phases. Pressure drops due to friction when the mixture flows along the pipe, causing the gas to expand according to the ideal gas law. Expansion of the gas phase renders the superficial gas velocity to change continuously along the pipe while the superficial liquid velocity remains constant for any particular flow condition (i.e., with constant input liquid and gas mass flow rates). Since void fraction is defined in the homogeneous flow model as

Contributed by the Fluids Engineering Division of ASME for publication in the JOURNAL OF FLUIDS ENGINEERING. Manuscript received December 3, 2006; final manuscript received May 6, 2008; published online August 12, 2008. Assoc. Editor: Theodore Heindel.

the ratio of superficial gas velocity and mixture velocity, a change of superficial gas velocity along the pipe leads to a change of void fraction in the flow direction.

The flow is assumed isothermal due to large thermal capacity of the liquid phase, and the liquid is assumed incompressible because of a moderate change in fluid pressure along the pipe during steady flow. The amount of gas dissolved in the liquid as the two-phase fluid travels along the pipe is assumed negligible; this condition would generally be satisfied if the extent of the pressure variation along the pipe is not very large.

The homogeneous model presented in this paper is applicable to bubbly flow in dispersed flow regime for different types of gas-liquid mixtures as well as for various pipe sizes. Determination of whether a particular flow condition falls within the dispersed flow regime could be carried out using the flow pattern map of Weisman et al. [13], which allows for the effect of gas and liquid properties such as density and viscosity, as well as the effect of pipe size.

2.1 Governing Differential Equations. Conservation of mass and momentum for steady one-dimensional homogeneous two-phase flow in a horizontal pipe are, respectively,

$$\rho_m dv/dz + v d\rho_m/dz = 0 \tag{1}$$

$$dp/dz + \rho_m v dv/dz + (4C_f/2D)\rho_m v^2 = 0 \tag{2}$$

where z=distance along the pipe, ρ_m=mixture density, v=fluid velocity, p=static pressure, C_f=Fanning friction factor=ratio of wall shear stress τ_w and dynamic pressure of the fluid $=\tau_w/(\rho_m v^2/2)$, and D=pipe diameter. The homogeneous velocity is defined as

$$v = (Q_L + Q_G)/A \tag{3}$$

where Q_L=liquid volume flow rate, Q_G=gas volume flow rate, and A=pipe cross-sectional area. The density and velocity gradients may be expressed in terms of the pressure gradient by making use of the continuity equation, the density relations of the mixture, and the equation of state of the gas phase.

The density relations for the mixture are (Wallis [7])

$$1/\rho_m = x/\rho_G + (1-x)/\rho_L \tag{4}$$

$$\rho_G/\rho_m = x/\alpha \tag{5}$$

$$\rho_L/\rho_m = (1-x)/(1-\alpha) \tag{6}$$

where x=mixture quality, ρ_G=gas density, ρ_L=liquid density, and α=void fraction. The mixture quality is defined as

$$x = G_G/(G_L + G_G) \tag{7}$$

where G_L=liquid mass flux and G_G=gas mass flux. Since the gas is assumed insoluble in the liquid, both the gas mass flux and the liquid mass flux remain constant as the two-phase mixture moves along the pipe; therefore, $dx/dz=0$.

Differentiating Eq. (4) while noting that ρ_L is constant for an incompressible liquid, i.e., $d\rho_L/dz=0$, gives

$$d\rho_m/dz = x(\rho_m/\rho_G)^2 d\rho_G/dz \tag{8}$$

Differentiating the equation of state of the gas phase, p/ρ_G =const, substituting into Eq. (8), and making use of Eq. (5), then substituting into Eq. (1) give

$$dv/dz = -(\alpha v/p)dp/dz \tag{9}$$

After replacing the velocity gradient by its expression in Eq. (9), Eq. (2) becomes

$$(1 - \alpha\rho_m v^2/p)dp/dz + (4C_f/2D)\rho_m v^2 = 0 \tag{10}$$

Having written Eq. (6) in the form $\rho_m/(1-\alpha)=\rho_L/(1-x)$=const, differentiating and substituting into Eq. (1) while making use of Eq. (9), and multiplying by $-(1-\alpha)/(\rho_m v)$, give

$$d\alpha/dz + (\alpha(1-\alpha)/p)dp/dz = 0 \tag{11}$$

Two dimensionless variables r and s are now introduced, where r is pressure ratio defined as the ratio of dynamic pressure q to static pressure p, and s is nondimensional distance along the pipe,

$$r = q/p \tag{12}$$

$$q = \rho_m v^2/2 \tag{13}$$

$$s = z/L \tag{14}$$

where L is the pipe length. Differentiation of Eqs. (12) and (13), making use of Eq. (9), and the continuity equation written in the form $d(\rho_m v)/dz=0$, yield the following transformation equation:

$$dp/dz = -p^2(q(1+\alpha))dr/dz \tag{15}$$

Equations (10) and (11) can now be normalized using Eq. (15). Substituting Eq. (15) into Eq. (10), multiplying through by L/q, and making use of Eqs. (12) and (14) give

$$dr/dz = F_r(\alpha, r) = r^2(1+\alpha)f/((1-2\alpha r)D_n) \tag{16}$$

where f is Darcy–Weisbach friction factor, $f=4C_f$, and D_n is nondimensional pipe diameter, $D_n=D/L$.

Substituting Eq. (15) into Eq. (11) and making use of Eqs. (14) and (16) give

$$d\alpha/ds = F_\alpha(\alpha, r) = \alpha(1-\alpha)rf/((1-2\alpha r)D_n) \tag{17}$$

The flow of a bubbly mixture in a horizontal pipe is thus governed by the system of two ordinary differential equations: Eqs. (16) and (17). It is noted that the original system of equations contains three dependent variables (p, v, and α) while the transformed system contains only two dependent variables (r, α).

2.2 Analysis of Phase Plane. The system of ordinary differential equations (16) and (17) constitutes a phase plane system (Boyce and Diprima [14]) whereby $0<\alpha<1$ and $r>0$, since the cases of all liquid flows ($\alpha=0$), all gas flows ($\alpha=1$), and stationary fluids ($r=0$) are outside the scope of this paper. Since F_α and F_r are independent of s, the system of equations (16) and (17) is an autonomous system, and since there is no value of (α, r) to make both F_α and F_r vanish, the system of equations (16) and (17) has no critical points. When $(1-2\alpha r)$ approaches zero, i.e., when the product of α and r approaches 0.5, both F_α and F_r approach infinity; therefore, the limiting values of void fraction and pressure ratio, $\alpha_{\lim}$ and $r_{\lim}$, are given by

$$\alpha_{\lim} r_{\lim} = 0.5 \tag{18}$$

For gas-liquid mixture flow with $r>0$ and $0<\alpha<1$, elimination of ds from F_α and F_r and integrating, noting that $(1-\alpha)>0$, give

$$r = C\alpha/(1-\alpha)^2 \tag{19}$$

where C is a positive constant. Equation (19) is the equation for the phase paths of the system of ordinary differential equations (16) and (17) in the phase plane with C as the parameter of the phase paths.

The limiting void fraction and pressure ratio may be determined by substitution of Eq. (19) into Eq. (18), which gives

$$(1-2C)\alpha_{\lim}^2 - 2\alpha_{\lim} + 1 = 0 \tag{20}$$

Since the first solution of Eq. (20) corresponding to the plus sign is greater than 1, this solution has no physical meaning. The valid solution corresponding to the minus sign is therefore

$$\alpha_{\lim} = \frac{1-\sqrt{2C}}{1-2C} \tag{21}$$

provided $(1-2C)\neq 0$, that is, $C\neq 0.5$.

Equations (19) and (21) only apply for the cases of $0<C<0.5$ and $C>0.5$. When $C=0.5$, Eqs. (20) and (19) yield, respec-

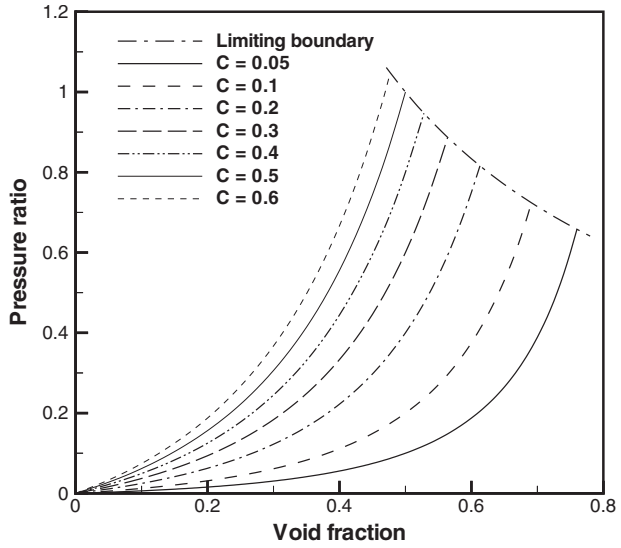

Fig. 1 Phase paths

tively, $\alpha_{\text{lim}}=0.5$ and $r_{\text{lim}}=1$.

The phase paths for various values of the parameter C are shown in Fig. 1. This figure indicates that the phase paths become steeper with increasing value of the parameter C. The limiting values of void fraction and pressure ratio are plotted against parameter C in Fig. 2. It was observed from the experimental data of Kopalinsky [15], Herringe [16], and Phu [17] that for a series of mixture flow conditions with the same quality, the value of parameter C increased as the superficial liquid velocity increased within the series, and for a series of mixture flow conditions with the same superficial liquid velocity, the value of parameter C increased as the quality decreased within the series.

2.3 Viscosity of Gas-Liquid Mixtures. It is well known that the viscosity of pseudohomogeneous suspensions of spherical particles in liquids is determined by the viscosity of the liquid and the concentration of the particles. Einstein in 1905 first analyzed the problem for dilute systems of solid spherical particles, finding that

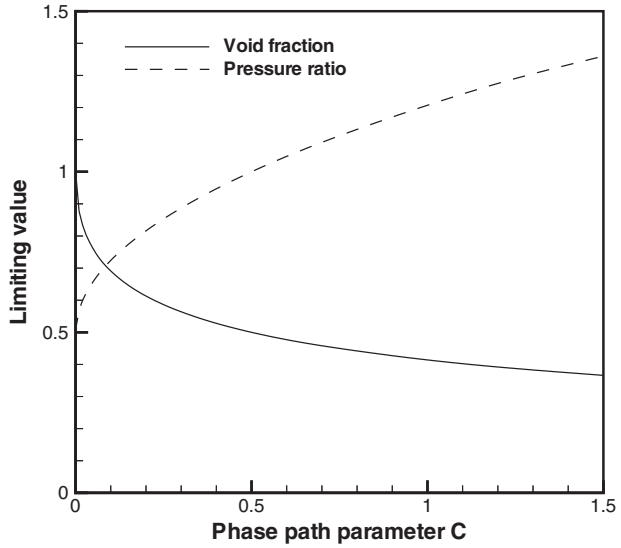

Fig. 2 Limiting values of void fraction and pressure ratio

$$\mu_m = \mu_L(1 + 2.5\alpha_s) \tag{22}$$

where μ_m=mixture viscosity, μ_L=liquid viscosity, and α_s=volume fraction of particles. This equation has been shown to be valid only for concentrations in the order of 2% (Govier and Aziz [8]). Guth and Simha in 1936 extended Einstein's analysis to derive the following expression for the viscosity of liquids containing solid spherical particles, which is applicable to concentrations of approximately 20% (Govier and Aziz [8]).

$$\mu_m = \mu_L(1 + 2.5\alpha_s + 14.1\alpha_s^2) \tag{23}$$

It is noted that Guth and Simha's equation is basically a modified Einstein's equation that contains an additional term in higher power of the volume fraction of particles, and the form of the equation is a second-order polynomial.

Taylor [18,19] extended Einstein's analysis to suspensions of spherical droplets in another liquid, or of gas bubbles in a liquid, obtaining

$$\mu_r = 1 + \alpha(\mu_L + 2.5\mu_G)/(\mu_L + \mu_G) \tag{24}$$

where $\mu_r=\mu_m/\mu_L$=relative viscosity of the mixture. Govier and Aziz [8] suggested that Taylor's equation should only be used to obtain order-of-magnitude viscosity of mixtures containing less than about 3% of the dispersed phase. On the other hand, Wallis [7] recommended using this equation in a simplified form,

$$\mu_r = 1 + \alpha \tag{25}$$

for laminar bubbly flow with gas content less than about 5%.

It is proposed in this paper to modify Taylor's equation in order to obtain an expression for the mixture viscosity that would be applicable for a wider range of void fraction. The proposed viscosity equation will fit the limiting cases in which either the liquid or the gas is flowing alone, that is, at $\alpha=0$, $\mu_m=\mu_L$, or

$$\mu_r = 1 \tag{26}$$

and at $\alpha=1$, $\mu_m=\mu_G$, or

$$\mu_r = \mu_G/\mu_L \tag{27}$$

It is expected that the mixture viscosity in the region of very low gas content is given by Taylor's equation; thus, the viscosity curve, plotted against α, will be tangential to the viscosity line given by Eq. (24), that is, at $\alpha=0$, as follows:

$$d\mu_r/d\alpha = (\mu_L + 2.5\mu_G)/(\mu_L + \mu_G) \tag{28}$$

Equation (24) indicates that the mixture viscosity initially increases from the value of the liquid viscosity as more gas is introduced into the two-phase fluid. Since the mixture viscosity will eventually decrease to the value of the gas viscosity, which is much lower than that of the liquid viscosity, it is expected that the mixture viscosity will reach a maximum at a certain value of the void fraction between 0 and 1.

Liquid viscosity at temperatures below the normal boiling point can be estimated by Thomas' relationship (Govier and Aziz [8]) as follows:

$$\mu_L = 0.1167\rho_L^{0.5}10^{\beta} \tag{29}$$

where β is a function of the fluid temperature. Velocity of sound of the liquid phase is given by (Wallis [7])

$$c_L = (K_L/\rho_L)^{0.5} \tag{30}$$

where K_L is modulus of elasticity of the liquid. Substitution of the expression of ρ_L from Eq. (30) into Eq. (29) gives

$$\mu_L c_L = 0.1167K_L^{0.5}10^{\beta} \tag{31}$$

The right hand side of Eq. (31) is a function of temperature only. It can be written at a certain temperature that $\mu_L c_L$=const. By treating the gas-liquid mixture as a pseudohomogeneous fluid, it may be written at a certain temperature that

$$\mu_m c_m = \text{const} \tag{32}$$

where μ_m and c_m are functions of the void fraction, c_m being velocity of sound of the mixture. Differentiating both sides of Eq. (32) gives

$$d\mu_m/d\alpha = -(\mu_m/c_m)dc_m/d\alpha \tag{33}$$

It is noted that the velocity of sound of a bubbly mixture is a function of the densities and sonic velocities of the individual phases and of the void fraction (Wallis [7]) as follows:

$$c_m = 1 \Bigg/ \sqrt{[(1-\alpha)\rho_L + \alpha\rho_G]\left[\frac{1-\alpha}{\rho_L c_L^2} + \frac{\alpha}{\rho_G c_G^2}\right]} \tag{34}$$

where c_G is the velocity of sound of the gas phase. This equation indicates that as the gas content increases, the sonic velocity of the mixture decreases rapidly to a minimum at $\alpha=0.5$, that is, when the two phases occupy equal volumes. As more gas is introduced into the two-phase mixture, the velocity of sound will increase and finally reach the velocity of sound of the gas phase when the liquid phase is entirely absent. These characteristics may be expressed mathematically as $dc_m/d\alpha<0$ for $0<\alpha<0.5$, and $dc_m/d\alpha>0$ for $0.5<\alpha<1$. Since at $\alpha=0.5$, $dc_m/d\alpha=0$, Eq. (33) gives, at $\alpha=0.5$, $d\mu_m/d\alpha=0$ or

$$d\mu_r/d\alpha = 0 \tag{35}$$

Equation (33) indicates that $d\mu_m/d\alpha>0$ for $0<\alpha<0.5$ (since $dc_m/d\alpha<0$ in this range of void fraction), that is, the mixture viscosity will increase as the velocity of sound decreases with the void fraction. Also, $d\mu_m/d\alpha<0$ for $0.5<\alpha<1$ (since $dc_m/d\alpha>0$ in this range of void fraction), that is, the mixture viscosity will decrease as the velocity of sound increases with the void fraction.

The simplest equation that satisfies the four conditions specified in Eqs. (26)–(28) and (35) is a polynomial equation of the form

$$\mu_r = a_0 + a_1\alpha + a_2\alpha^2 + a_3\alpha^3 \tag{36}$$

where $a_0, \ldots, a_3$ are coefficients. Equation (26) gives $a_0=1$. Differentiating Eq. (36) with respect to α and making use of Eq. (28) give

$$a_1 = (\mu_L + 2.5\mu_G)/(\mu_L + \mu_G) \tag{37}$$

Equations (27) and (35) yield, after simple manipulation,

$$a_2 = 3(1-\mu_G/\mu_L) - (\mu_L + 2.5\mu_G)/(\mu_L + \mu_G) \tag{38}$$

and

$$a_3 = -4(1-\mu_G/\mu_L) \tag{39}$$

The resulting equation is therefore

$$\mu_r = 1 + \left(\frac{\mu_L + 2.5\mu_G}{\mu_L + \mu_G}\right)\alpha + \left[3\left(1 - \frac{\mu_G}{\mu_L}\right) - \frac{\mu_L + 2.5\mu_G}{\mu_L + \mu_G}\right] \times \alpha^2 - 4\left(1 - \frac{\mu_G}{\mu_L}\right)\alpha^3 \tag{40}$$

A graphical comparison of expressions given by Eqs. (24) and (40) for viscosity of air-water mixtures is shown in Fig. 3. It is noted that the viscosity given by Eq. (40) initially increases with the gas content and is slightly greater than Taylor's viscosity in the region of α up to 0.5. Beyond this point, the viscosity reduces sharply as the gas content increases, and it finally reaches the viscosity of the gas phase when the liquid phase is entirely absent.

Since μ_G is normally much less than μ_L, a simplified expression for the mixture viscosity may be written as

$$\mu_r = 1 + \alpha + 2\alpha^2 - 4\alpha^3 \tag{41}$$

In the region of small void fractions, the terms in higher power of α become negligible besides α. Equation (40) then reduces to Taylor's equation (24), and Eq. (41) reduces to the simple form of Eq. (25) as recommended by Wallis [7].

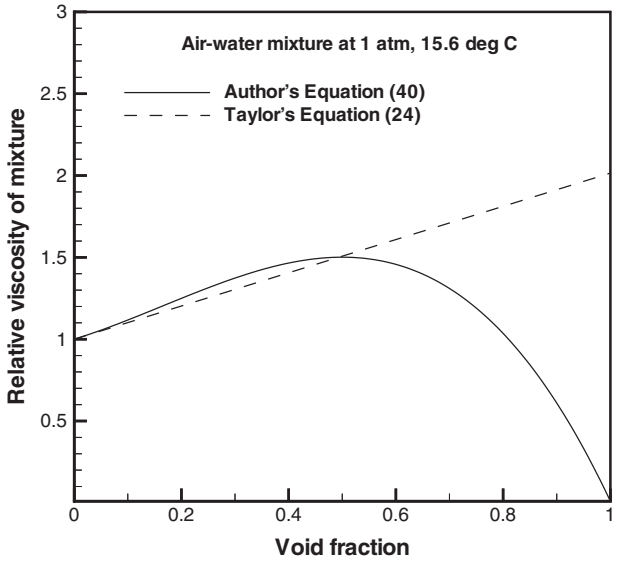

Fig. 3 Variation of mixture viscosity with void fraction

2.4 Computational Procedure. The assumption of homogeneous flow permits the two-phase mixture to be treated as an equivalent single-phase fluid. It is assumed in the homogeneous flow model that the relationship between friction factor and Reynolds number for single-phase flow may also be applied for two-phase flow situations. In this model, Reynolds number for the two-phase fluid is based on mixture density and mixture viscosity, and friction factor is provided by Colebrook's [20] single-phase correlation. This approach is similar to Wallis [7] and Govier and Aziz [8] mentioned previously, with the only difference being in the determination of Reynolds number to be used in Colebrook's equation. This equation expresses friction factor as a function of pipe relative roughness and Reynolds number, and is an implicit one requiring an iterative procedure for its solution. An explicit relationship for friction factor based on Colebrook's equation was developed by Jain [21]. In all subsequent computational work, a two-step procedure for determining the friction factor for any given Reynolds number and pipe roughness is adopted whereby an initial estimate of the friction factor is obtained from Jain's equation then Colebrook's equation is solved iteratively for the final friction factor. Since Jain's friction factor is sufficiently close to the actual friction factor for normal ranges of relative pipe roughness and Reynolds number, the procedure requires only a few iterations to reach convergence.

The system of differential equations (16) and (17), coupled with the viscosity equation (40), the Reynolds number equation, and Colebrook's friction factor correlation, can be integrated numerically for (r, α) as functions of nondimensional distance s. A fourth-order Runge–Kutta method was used for solving this system of differential equations. It was found that sufficient accuracy could be obtained for all flow conditions tested when the number of intervals from the pipe inlet to exit was from 5 to 40, depending on the flow conditions. The mass flow rate of each phase and the static pressure at the pipe inlet are used to determine the initial values of (r, α) before the step-by-step integration can be carried out to the downstream end of the flow. Having obtained the distributions of (r, α) along the pipe, the static pressure and flow velocity can be derived from (r, α) by using the gas equation, $p = \rho_G R_G T$, where R_G=gas constant and T=fluid temperature, in conjunction with Eqs. (5), (6), and (13).

3 Measurement of Pressure Distributions

3.1 Test Apparatus. The experimental setup consisted of water and air supply lines, an air-water mixer, and a test section

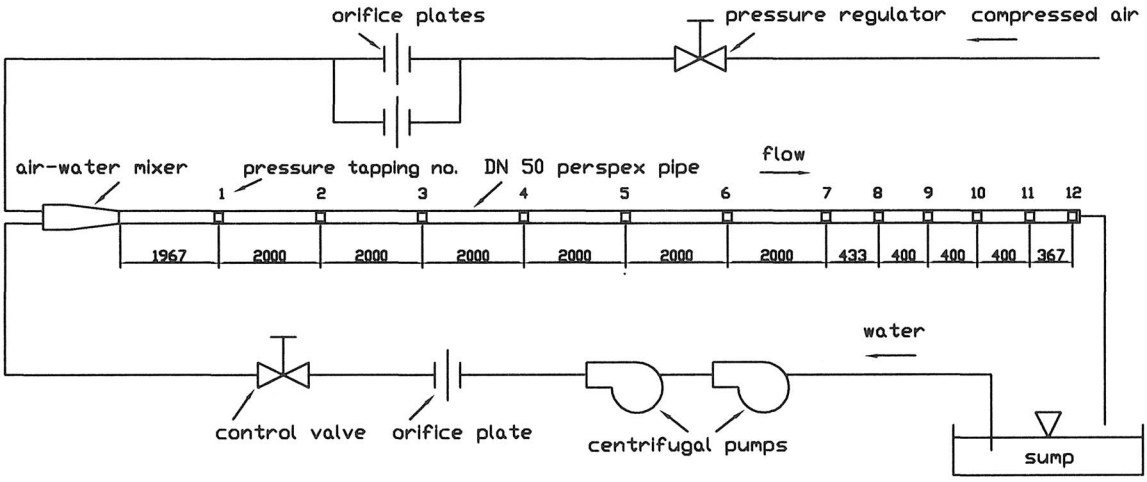

Fig. 4 Schematic diagram of the experimental setup

made up of 50 mm diameter Perspex pipes, as shown in Fig. 4. The air-water mixer comprised a 100 mm diameter cylindrical mixing chamber into which water was injected through eight 12.7 mm diameter tubes evenly spaced around a circle, and air was injected through a 9.5 mm diameter tube at the center. The water flow rate for each flow condition was measured by an orifice plate designed according to BS 1042. The pressure differential across the orifice plate was measured by a mercury manometer. The air flow rate was measured by either one of the two orifice plates mounted in two parallel branches of the supply line. The pressure differential across the orifice plates was measured by a silicone oil manometer. Static pressures were measured at 12 stations, numbered 1–12 along the pipe, at spacing indicated in Fig. 4 (with dimensions shown in millimeters). The first pressure tapping was located at a distance of 39 diameters from the mixer outlet to minimize any effects due to flow irregularity at the pipe entrance. The mixture temperature was measured by a mercury-in-glass thermometer installed in a pocket, which was inserted through the pipe wall at the downstream end of the test section.

3.2 Experimental Results. Four series of tests with a total of 24 flow conditions were carried out. In each series, the water flow rate was maintained constant while the mixture quality was increased by approximately equal increments of 0.0002. The superficial liquid velocities for Series 1, 2, 3, and 4 were 5.43 m/s, 6.08 m/s, 6.83 m/s, and 7.50 m/s, respectively. Series 1 has eight flow conditions, marked 1.1–1.8, with quality ranging from 0.00060 to 0.00207; Series 2 has seven flow conditions, marked 2.1–2.7, with quality ranging from 0.00058 to 0.00185; Series 3 has five flow conditions, marked 3.1–3.5, with quality ranging from 0.00059 to 0.00145; and Series 4 has four flow conditions, marked 4.1–4.4, with quality ranging from 0.00059 to 0.00125. The ranges of mixture quality, superficial liquid velocity, superficial gas velocity, void fraction, and pressure at the inlet section are shown in Table 1, and details of Flow Series 3 are shown in Table 2.

The void fractions at the inlet section indicated in Table 1 were calculated by the homogeneous model. The fluid temperature range was from 17.4°C to 19.5°C with the average of 18.4°C. It was observed that as the mixture quality increased, both the inlet pressure and the pressure drop increased within each series; and for any value of the mixture quality, the higher the water flow rate, the larger the inlet pressure and the pressure drop. The range of flow conditions studied was limited by requirements for bubbly flow and by the capacity of water and air supplies. The air-water mixtures appeared to be frothy, well-mixed bubbly flows for all flow conditions; therefore, it would be reasonable to assume that the flows were homogeneous. The dispersed flow regime observed for all flow conditions is in agreement with the prediction for this range of superficial liquid and gas velocities according to the flow pattern maps by Mandhane et al. [22] and Weisman et al. [13].

The mixture temperature was measured with an error of 0.1°C. Static pressures at the first seven stations were measured with errors varying from 0.15 kPa to 0.35 kPa (larger errors for higher flows) and at Station 12 from 0.05 kPa to 0.15 kPa; pressures at

Table 1 Ranges of experimental data. *N*=number of data points, *=computed void fraction, and **=measured void fraction.

	Author's data (N=24)		Kopalinsky's data (N=106)		Herringe's pressure drop data (N=12)		Herringe's void fraction data (N=9)	
Description	Minimum	Maximum	Minimum	Maximum	Minimum	Maximum	Minimum	Maximum
Mixture quality	0.00058	0.00207	0.00030	0.00328	0.00032	0.00141	0.00033	0.00127
Superficial liquid velocity (m/s)	5.43	7.50	4.21	10.87	4.15	6.18	4.19	6.14
Superficial gas velocity at inlet section (m/s)	1.22	3.39	0.84	5.44	0.80	3.03	0.82	2.73
Pressure at inlet section (kPa abs)	214	349	148	600	144	246	139	199
Void fraction at the inlet section	0.14*	0.38*	0.08*	0.53*	0.16*	0.38*	0.16**	0.33**
Void fraction at the exit section	0.24*	0.57*	0.20*	0.74*	0.18*	0.42*	0.17**	0.41**

Table 2 Experimental data for Flow Series 3

Flow condition	Liquid mass flow rate (kg/s)	Gas mass flow rate (kg/s)	Inlet pressure (kPa abs)	Exit pressure (kPa abs)	Fluid temperature (°C)
3.1	13.39	0.00797	269.4	143.8	19.4
3.2	13.39	0.01060	282.5	147.3	18.8
3.3	13.39	0.01380	295.8	149.7	19.0
3.4	13.39	0.01625	311.8	156.1	18.6
3.5	13.39	0.01945	324.0	158.8	18.6

Stations 8–11 normally had larger fluctuations than pressures at the other stations, particularly for flows at higher mixture qualities, the errors ranging from 0.35 kPa to 0.70 kPa. It was observed that the dominant error in the determination of water flow rate was due to the fluctuation of the pressure differential across the orifice plate. If only this source of error is considered while ignoring other minor sources of error, and noting that the water mass flow rate m_L is proportional to the square root of the pressure differential H, the relative error of m_L is given by

$$\Delta m_L/m_L = \tfrac{1}{2}(\Delta H/H) \tag{42}$$

where ΔH is magnitude of the fluctuation of the pressure differential. Using this equation, it was found that the relative error of the water flow rate was from 0.7% to 1.4% (larger error for lower flow rate); therefore, the range of water flow rate was from 10.67 ± 0.15 kg/s to 14.72 ± 0.10 kg/s. Similarly, the relative error of the air flow rate was from 0.7% to 2.3% for measurements with the smaller orifice plate in flow conditions 1.1–1.4, 2.1–2.4, 3.1–3.3, and 4.1–4.3, and from 0.6% to 1.0% for measurements with the larger orifice plate in flow conditions 1.5–1.8, 2.5–2.7, 3.4–3.5, and 4.4; therefore, the range of air flow rate was from 0.0064 ± 0.00015 kg/s to 0.0222 ± 0.00013 kg/s.

4 Computational Results and Comparison With Experimental Data

Numerical integration was carried forward from the known inlet conditions to the downstream end of the pipe flow. The homogeneous model with the mixture viscosity given by Eq. (40) was used to predict the pressure, velocity, and void fraction distributions along the pipe using the author's experimental data described in the previous section as well as the data from literature. The velocity given by the homogeneous model with the author's data varies from 6.7 m/s to 9.8 m/s at the inlet and from 7.6 m/s to 12.8 m/s at the exit. The predicted void fraction varies from 0.14 to 0.38 at the inlet and from 0.24 to 0.57 at the exit, for all flow conditions.

For each flow series wherein the superficial liquid velocity is maintained constant and the superficial gas velocity is gradually increased, the pressure, velocity, and void fraction at the inlet section increase as the mixture quality increases, as shown in Figs. 5–7 for Flow Series 3. The higher the gas mass flow rate, i.e., more air is introduced into the mixture, the higher the void fraction at the inlet section, as shown in Fig. 7. Since the superficial liquid velocity is constant, the velocity of the liquid phase increases as the liquid has less space in the pipe cross section to flow through. As the gas bubbles are carried along the flow with practically the same velocity as the liquid phase (in a well mixed bubbly flow), the higher the velocity of the liquid phase, the higher the mixture velocity. Higher mixture velocity leads to higher frictional pressure loss along the pipe. Since the mixture discharges to atmosphere for all flow conditions, the higher the pressure loss along the pipe, the higher the inlet pressure as shown in Fig. 5. For each flow condition within the flow series, the pressure decreases along the pipe as a result of frictional pressure loss. As the pressure reduces along the pipe, the gas phase expands to take up more space in the pipe cross section, resulting in higher void fraction along the pipe as shown in Fig. 7. Increased void fraction along the pipe leads to higher velocity of the liquid phase, and of the mixture velocity along the pipe as shown in Fig. 6, since the liquid has less space in the pipe cross section to flow through as previously mentioned.

The accuracy of the predicted pressure distributions is indicated by the percentage error δ of the computed pressure drop relative to the experimental pressure drop,

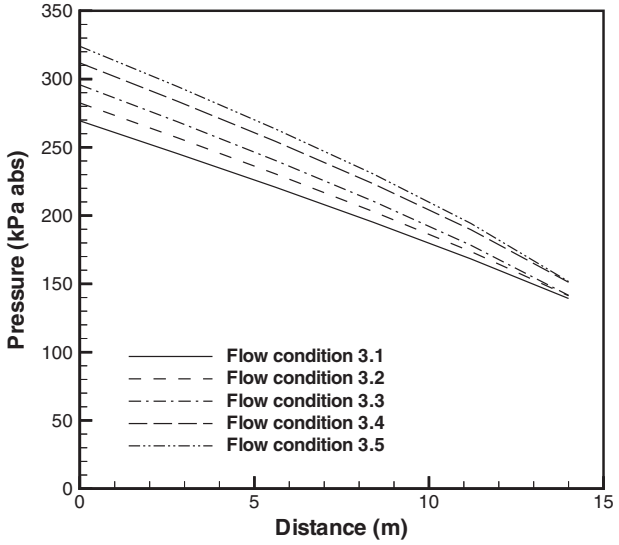

Fig. 5 Computed pressure distributions

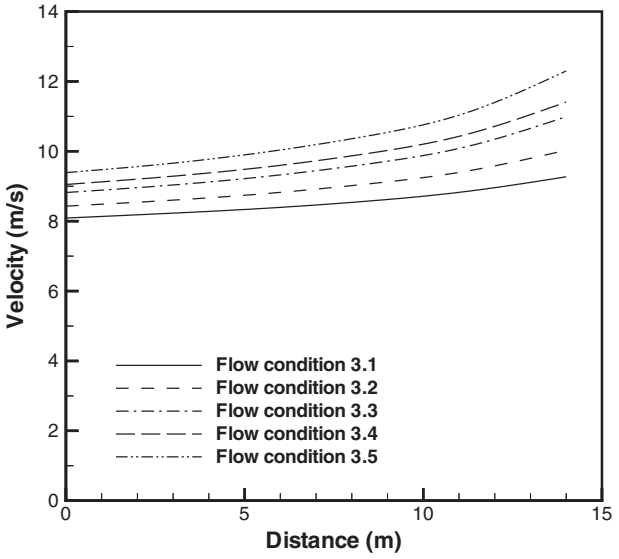

Fig. 6 Computed velocity distributions

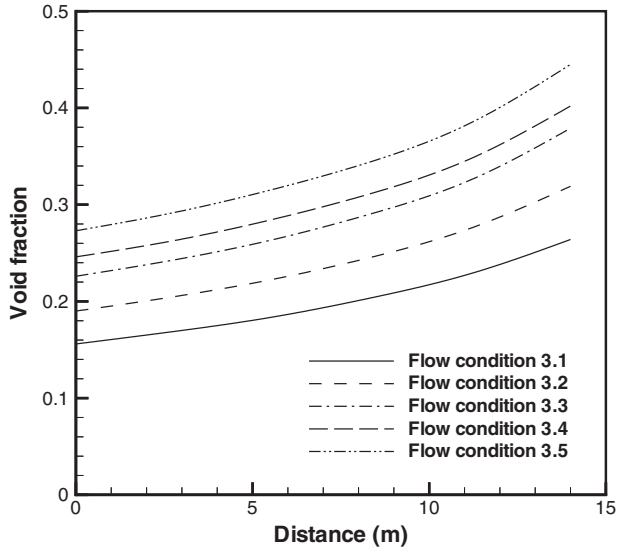

Fig. 7 Computed void fraction distributions

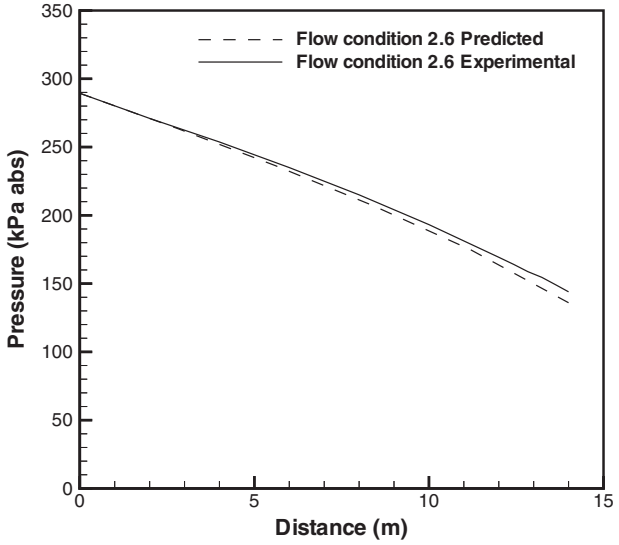

Fig. 9 Comparison of the predicted pressure distribution with author's experimental data

$$\delta = 100(\Delta P_c - \Delta P_e)/\Delta P_e \tag{43}$$

where ΔP_c=computed pressure drop, ΔP_e=experimental pressure drop, with the pressure drop given by $\Delta P = p_i - p_e$, where p_i =static pressure at the inlet section, and p_e=static pressure at the exit section.

Comparison of the computed pressure drops with experimental pressure drops using the author's data is shown in Fig. 8. The error of the predicted pressure drop falls within the range 0.6%–6.1%; the average error for all flow conditions is 3.8% with standard deviation of 1.5%. Comparison of the predicted pressure distribution with experimental data for the flow condition with maximum error is shown in Fig. 9, which shows that the difference between the predicted pressure and experimental pressure increases along the pipe, with the largest deviation occurring at the pipe exit.

This flow model was also used to predict pressure distributions using the data from Kopalinsky [15]. A set of 106 data points was chosen from Kopalinsky's data for air-water mixture flow; this set comprises 73 data points for a horizontal 50.8 mm pipe of length 11.087 m and 33 data points for a horizontal 25.4 mm pipe of length 9.144 m. All data points were generated by nozzle mixers. The data points were selected to have approximately equal increments of the superficial liquid velocity for a certain value of quality. This set of data covers the complete ranges of Kopalinsky's quality and mass flow rate. The ranges of quality, superficial liquid and gas velocities, void fraction, and pressure at the inlet section are shown in Table 1, wherein the void fractions at the inlet section were calculated by the homogeneous model. All flow conditions fall within the dispersed zone according to the flow pattern map of Weisman et al. [13]. Comparison of the predicted pressure drops with experimental data is shown in Fig. 10. The error of the predicted pressure drops falls within the range of −9.8% to 14.9%; the average error for all flow conditions is 1.2% with standard deviation of 5.8%.

The effect of different inlet mixing schemes was analyzed using the data from Herringe [16], who carried out pressure measurements with nozzle, porous, and drilled mixers in a horizontal 50.8 mm pipe of length 5.16 m for four flow conditions, i.e., a

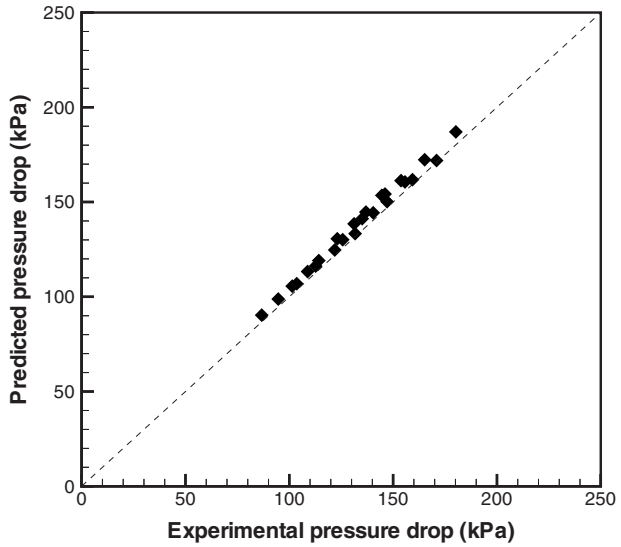

Fig. 8 Comparison of the predicted pressure drops with author's experimental data

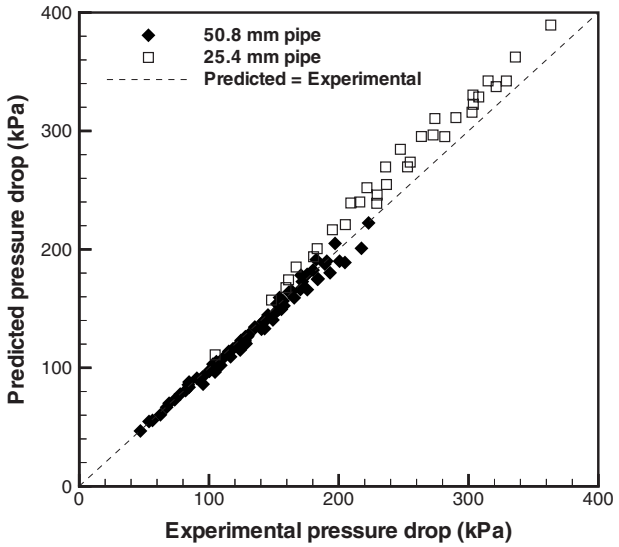

Fig. 10 Comparison of the predicted pressure drops with Kopalinsky's experimental data

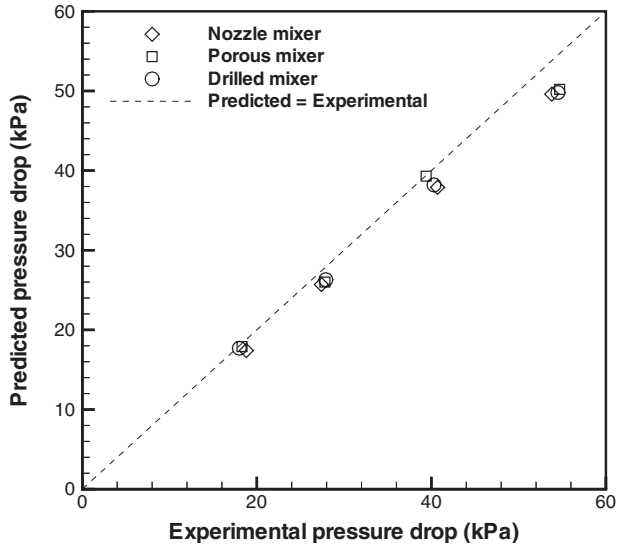

Fig. 11 Comparison of the predicted pressure drops with Herringe's experimental data

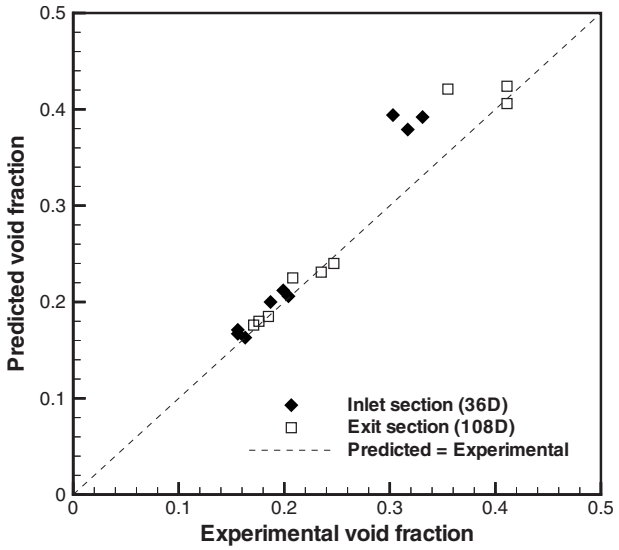

Fig. 12 Comparison of the predicted void fractions with Herringe's experimental data

total of 12 data points. The ranges of quality, superficial liquid and gas velocities, void fraction, and pressure at the inlet section are shown in Table 1, wherein the void fractions at the inlet section were calculated by the homogeneous model. All flow conditions fall within the dispersed zone according to the flow pattern map of Weisman et al. [13]. Comparison of the predicted pressure drops with experimental data is shown in Fig. 11, which indicates that the effect of different inlet mixing schemes is not significant. The error of the predicted pressure drops falls within the range of −8.7% to −0.3%; the average error for all flow conditions is −5.6% with standard deviation of 2.7%. Comparison of the predicted pressure distributions with the author's data, Kopalinsky's data, and Herringe's data demonstrates that the homogeneous flow model presented herein can be used to predict pressure distributions along a horizontal pipe satisfactorily.

The homogeneous flow model was also used to predict void fraction distributions using the data from Herringe [16], who measured void fraction in a horizontal 50.8 mm pipe of length 5.49 m by resistivity probe technique at three sections along the pipe at $z=8D$, $36D$, and $108D$, where z is the distance from the mixer outlet. The sections at $36D$ and $108D$ were selected as the inlet section and the exit section, respectively, in the present work since the measured void fraction at $8D$ was sometimes smaller than the measured void fraction at $36D$ due to flow turbulence in the vicinity of the mixer outlet. Herringe carried out void fraction measurements with nozzle, porous, and drilled mixers for three flow conditions, making a total of nine data points. The ranges of quality, superficial liquid velocity, superficial gas velocity, void fraction, and pressure at the inlet section are also shown in Table 1. The results of void fraction prediction with the homogeneous model are shown in Fig. 12. The error of the predicted void fraction at the inlet section falls within the range 0.0–30.0%; the average error is 11.0% with standard deviation of 9.2%. The error of the predicted void fraction at the exit section falls within the range of −2.8% to 18.6%; the average error is 3.3% with standard deviation of 6.3%. These results indicate that the homogeneous flow model can be used to predict void fraction distributions along a horizontal pipe with moderate accuracy.

5 Conclusions

A method of predicting longitudinal distributions of pressure, velocity, and void fraction in two-phase bubbly flow in horizontal pipes is derived based on a homogeneous model. This model employs a two-phase friction factor relationship provided by Colebrook's equation with a Reynolds number based on a mixture viscosity, which is expressed as a polynomial function of the void fraction. The model is characterized by a system of two nondimensional differential equations with (r, α) as dependent variables, where r is the ratio of dynamic pressure to static pressure and α is the void fraction. Experimental data were obtained for a reasonable range of air-water bubbly flows with superficial liquid velocity up to 7.5 m/s and superficial gas velocity at the inlet section up to 3.4 m/s.

Comparison of the predicted flow variables with experimental data indicates that the flow model can be used to predict pressure distribution along a horizontal pipe satisfactorily, and it can be used to predict void fraction distribution with moderate accuracy. The steady flow model presented herein can be used to predict the initial distributions of pressure, velocity, and void fraction of a two-phase mixture flowing in a horizontal pipe. These initial distributions of the flow variables can be used in conjunction with a transient flow model for simulation of pressure surges.

Acknowledgment

The author wishes to thank Professor Ray A. A. Bryant for his guidance throughout the course of this project, which was carried out at School of Mechanical and Industrial Engineering, University of New South Wales, Kensington (Sydney), Australia. He also wishes to thank Mr. Richard B. Frost and Mr. Jim Beck for their assistance during the construction and setting up of the experimental test apparatus.

Nomenclature

$a_0, \ldots, a_3$ = coefficients in polynomial equation
A = pipe cross-sectional area
c = velocity of sound
C = phase path parameter
C_f = Fanning friction factor
D = pipe diameter
D_n = nondimensional pipe diameter
e = pipe surface roughness
f = Darcy–Weisbach friction factor
G = mass flux
H = pressure differential
K_L = modulus of elasticity of liquid
L = pipe length
m = mass flow rate

p = static pressure
p_e = static pressure at the exit section
p_i = static pressure at the inlet section
q = dynamic pressure
Q = volume flow rate
r = ratio of dynamic pressure to static pressure
Re = Reynolds number
R_G = gas constant
s = nondimensional distance along the pipe
T = fluid temperature
v = fluid velocity
x = quality (mass fraction of gas)
z = distance along the pipe
α = void fraction
α_{lim} = limiting value of void fraction
α_s = volume fraction of particles
β = function of fluid temperature
δ = percentage error
ΔP_c = computed pressure drop
ΔP_e = experimental pressure drop
μ = viscosity
μ_r = relative viscosity of mixture
ρ = density
τ_w = wall shear stress

Subscripts

G = gas
L = liquid
m = mixture

References

[1] Griffith, P., 1984, "Multiphase Flow in Pipes," JPT, J. Pet. Technol., **36**, pp. 361–367.
[2] Martin, C. S., Padmanabhan, M., and Wiggert, D. C., 1976, "Pressure Wave Propagation in Two-Phase Bubbly Air-Water Mixtures," *Second International Conference on Pressure Surges*, BHRA Fluid Engineering, Paper No. C1.
[3] Martin, C. S., and Padmanabhan, M., 1979, "Pressure Pulse Propagation in Two-Component Slug Flow," ASME J. Fluids Eng., **101**, pp. 44–52.
[4] Padmanabhan, M., and Martin, C. S., 1978, "Shock-Wave Formation in Flowing Bubbly Mixtures by Steepening of Compression Waves," Int. J. Multiphase Flow, **4**, pp. 81–88.
[5] Chaudhry, M. H., Bhallamudi, S. M., Martin, C. S., and Naghash, M., 1990, "Analysis of Transient Pressures in Bubbly, Homogeneous, Gas-Liquid Mixtures," ASME J. Fluids Eng., **112**, pp. 225–231.
[6] Davis, M. R., and Wang, D., 1994, "Dual Pressure Drop Metering of Gas-Liquid Mixture Flows," Int. J. Multiphase Flow, **20**, pp. 865–884.
[7] Wallis, G. B., 1969, *One-Dimensional Two-Phase Flow*, McGraw-Hill, New York.
[8] Govier, G. W., and Aziz, K., 1972, *The Flow of Complex Mixtures in Pipes*, Van Nostrand Reinhold, New York.
[9] Huey, C. T., and Bryant, R. A. A., 1967, "Isothermal Homogeneous Two-Phase Flow in Horizontal Pipes," AIChE J., **13**, pp. 70–77.
[10] Kopalinsky, E. M., and Bryant, R. A. A., 1976, "Friction Coefficients for Bubbly Two-Phase Flow in Horizontal Pipes," AIChE J., **22**, pp. 82–86.
[11] Davis, M. R., 1974, "The Determination of Wall Friction for Vertical and Horizontal Two-Phase Bubbly Flows," ASME J. Fluids Eng., **96**, pp. 173–179.
[12] Herringe, R. A., and Davis, M. R., 1978, "Flow Structure and Distribution Effects in Gas-Liquid Mixture Flow," Int. J. Multiphase Flow, **4**, pp. 461–486.
[13] Weisman, J., Duncan, D., Gibson, J., and Crawford, T., 1979, "Effects of Fluid Properties and Pipe Diameter on Two-Phase Flow Patterns in Horizontal Lines," Int. J. Multiphase Flow, **5**, pp. 437–462.
[14] Boyce, W. E., and Diprima, R. C., 1969, *Elementary Differential Equations and Boundary Value Problems*, 2nd ed., Wiley, New York.
[15] Kopalinsky, E. M., 1971, "A Study of Bubbly Two-Phase Flow," Ph.D. thesis, University of New South Wales, Australia.
[16] Herringe, R. A., 1973, "A Study of the Structure of Gas-Liquid Mixture Flows," Ph.D. thesis, University of New South Wales, Australia.
[17] Phu, T. D., 1981, "Water-Hammer Waves in Bubbly Pipe Flows," Ph.D. thesis, University of New South Wales, Australia.
[18] Taylor, G. I., 1932, "The Viscosity of a Fluid Containing Small Drops of Another Fluid," Proc. R. Soc. London, Ser. A, **138**, pp. 41–48.
[19] Taylor, G. I., 1954, "The Two Coefficients of Viscosity for an Incompressible Fluid Containing Air Bubbles," Proc. R. Soc. London, Ser. A, **226**, pp. 34–39.
[20] Colebrook, C. F., 1939, "Turbulent Flow in Pipes, With Particular Reference to the Transition Region Between the Smooth and Rough Pipe Laws," J. Inst. Civil Engrs., London, **11**, pp. 133–156.
[21] Jain, A. K., 1976, "Accurate, Explicit Equation for Friction Factor," J. Hydr. Div., ASCE, **102**, pp. 674–677.
[22] Mandhane, J. M., Gregory, G. A., and Aziz, K., 1974, "A Flow Pattern Map for Gas-Liquid Flow in Horizontal Pipes," Int. J. Multiphase Flow, **1**, pp. 537–553.

Hydrofoil Cavitation Under Strong Thermodynamic Effect

Jonas P. R. Gustavsson
e-mail: jgu@ufl.edu

Kyle C. Denning

Corin Segal

Department of Mechanical and Aerospace Engineering,
University of Florida,
P.O. Box 116250,
Gainesville, FL 32611

Cavitation was studied for a NACA0015 hydrofoil using a material that simulates cryogenic behavior. Several angles of attack and flow speeds up to 8.6 m/s were tested. The material used, 2-trifluoromethyl-1,1,1,2,4,4,5,5,5-nonafluoro-3-pentanone, hereafter referred to as fluoroketone, exhibits a strong thermodynamic effect even under ambient conditions. Static pressures were measured at seven chordwise locations along the centerline of the hydrofoil suction side and on the test section wall immediately upstream of the hydrofoil. Frequency analysis of the test section static pressure showed that the amplitude of the oscillations increased as the tunnel speed increased. A gradual transition corresponding to the Type II-I sheet cavitation transition observed in water was found to occur near $\sigma/2\alpha=5$ with Strouhal numbers based on chord dropping from 0.5 to 0.1 as the cavitation number was reduced. Flash-exposure high-speed imaging showed the cavity covering a larger portion of the chord for a given cavitation number than in cold water. The bubbles appeared significantly smaller in the current study and the pressure data showed increasing rather than constant static pressure in the downstream direction in the cavitating region, in line with observations made in literature for other geometries with fluids exhibiting strong thermodynamic effect.
[DOI: 10.1115/1.2953297]

Introduction

Cavitation in cryogenic turbopumps, primarily in liquid-fuel rocket engine applications, is a long-standing but difficult phenomenon to study due to the combination of highly flammable liquids and extremely low temperatures involved. At the same time, the thermodynamic effect, which causes a localized drop in liquid temperature near the vapor bubble formation due to vaporization, is significantly stronger in cryogenics than in water at moderate temperature and pressure. Water has been by far the most common medium for cavitation investigations. In a study by Ruggeri and Gelder [1], comparing cavitation of water and liquid nitrogen in a venturi, it was found that the temperature drop was an order of magnitude larger and the cavitation was frothier for liquid nitrogen when compared to water. Tani and Nagashima [2] carried out similar tests in a 2D Laval nozzle and found that the static pressure in the cavitating region remained constant and equal to the vapor pressure when water was used. When the test was repeated with liquid nitrogen, pressures below the nitrogen saturation vapor pressure—based on inlet temperature—were found in the cavitating region accompanied by a slight increase in pressure toward the nozzle exit. To quantify the thermodynamic effect, a nominal temperature depression ΔT^* and the ratio between the actual temperature drop and ΔT^*, known as the B-factor, have been introduced as follows [3]:

$$\Delta T^* = \frac{\Delta H_{\text{vap}}}{C_{p,l}} \frac{\rho_v}{\rho_l} \tag{1}$$

$$B = \frac{\Delta T}{\Delta T^*} \tag{2}$$

where ΔH_{vap} is the latent heat of vaporization, $C_{p,l}$ is the liquid heat capacity, ρ_v is the vapor density, and ρ_l is the liquid density. Numerous correlations have been suggested to relate the B-factor to flow geometry and fluid properties, e.g., by Franc et al. [3], Billet et al. [4], and Hord [5]. The large range of correlations suggests that there is still a need to understand which are the dominant parameters. Therefore, extrapolation of the cavitation behavior from one fluid to another with considerably different characteristics, such as water versus cryogenics, is risky. In the present investigation, a perfluorinated ketone, $CF_3CF_2C(O)CF(CF_3)_2$, has been used to simulate the behavior of liquid hydrogen under the conditions present in a low-pressure turbopump rather than ambient water. Water has to be brought to very high temperature to attain a similar ΔT^*, as Table 1 indicates. At ambient conditions, ΔT^* is 20 times higher in fluoroketone than in water. This is due to the liquid/vapor density ratio, which is two orders of magnitude smaller for fluoroketone than for water under ambient conditions. Furthermore, the fluoroketone has low kinematic viscosity, 3.3×10^{-7} m^2/s at ambient conditions, facilitating high-Re testing at low speeds. Other parameters may also need to be considered, potentially using a B-factor model.

The present study allows the cavitation number, angle of attack, and geometry to be matched against water tests in literature, isolating the effect of ΔT^* to provide further insights in cavitation modeling. The cavitation number σ used here is defined as:

$$\sigma \equiv \frac{P_\infty - P_{\text{vap}}(T_\infty)}{\frac{1}{2}\rho_{l,\infty}U_\infty^2} \tag{3}$$

Here, P_∞ is the freestream static pressure, P_{vap} is the vapor pressure, T_∞ is the freestream temperature, $\rho_{l,\infty}$ is the freestream liquid density, and U_∞ is the freestream flow speed.

In the present study, pressure fluctuations and cavitation morphology for sheet and cloud cavitation in fluoroketone at varying angles of attack and cavitation numbers were investigated at speeds up to 8.6 m/s. Several studies with similar goals have been carried out in water, e.g., by Coutier-Delgosha et al. [6] and Cervone et al. [7]. Coutier-Delgosha et al. [6] studied the morphology of cavitation in water on the flat suction side of a hydrofoil with a convex pressure side using an embedded endoscope. This study concluded that the common assumption of spherical bubbles and symmetry in structure between a mostly liquid flow with a few bubbles and a mostly vapor-filled fluid with a few droplets are both invalid in the studied case. Rather, the cavitating region was filled with deformed, interacting bubbles of varying sizes at high liquid volume fractions, and there were no isolated liquid droplets

Contributed by the Fluids Engineering Division of ASME for publication in the JOURNAL OF FLUIDS ENGINEERING. Manuscript received August 29, 2007; final manuscript received May 8, 2008; published online August 12, 2008. Assoc. Editor: Steven Ceccio.

Table 1 Comparison of properties near ambient conditions for fluoroketone and water to liquid hydrogen at cryogenic pump inlet conditions. $Re^{0.2}Pr^{0.7}$ is a *B*-factor scaling suggested by Franc et al. [3]. The Reynolds number is based on the present study geometry with $c=51$ mm, $U_\infty=8.6$ m/s.

	Fluoroketone 25°C	Fluoroketone 49°C	Hydrogen 22.8 K	Water 25°C	Water 75°C	Water 110°C
p_v (MPa)	0.04	0.10	0.20	0.003	0.039	0.152
p_c (MPa)	1.87	1.87	1.3	22.06	22.06	22.06
T_c (K)	442	442	33	647	647	647
$\rho_l/\rho_{v,\mathrm{sat}}$	310	119	27	42842	4031	1104
ΔT^* (K)	0.3	0.7	1.4	0.014	0.137	0.478
Pr	8.2	9.3	1.2	6.1	2.4	1.6
Re	$1.3E+06$	$1.5E+06$	$2.7E+06$	$4.9E+05$	$1.1E+06$	$1.6E+06$
$Re^{0.2}Pr^{0.7}$	73	82	22	49	30	24

in the vapor region under low liquid volume fraction conditions. The maximum void fraction increased rapidly from 0.55 to 0.80 as the cavitation number decreased from 0.7 to 0.6, which also marked the transition to supercavitation on that particular hydrofoil. The dominant measured fluctuation frequency was normalized giving the Strouhal numbers based on cavity and chord length, respectively.

$$\mathrm{St}_{L_{\mathrm{cav}}} = \frac{L_{\mathrm{cav}} f}{U_\infty} \tag{4}$$

$$\mathrm{St}_c = \frac{cf}{U_\infty} \tag{5}$$

where L_{cav} is the cavity streamwise length, c is the chord length, and f is the observed dominant frequency of oscillations. Strouhal numbers based on cavity length of about 0.25 were seen for short, $L_{\mathrm{cav}}/c<0.75$, conditions and $\mathrm{St}_{L_{\mathrm{cav}}}=0.12$ for long cavities, $L_{\mathrm{cav}}/c>0.75$. Cervone et al. [7], who used a NACA0015 hydrofoil in water at varying temperature and angles of attack, α, noted a strengthening of the visible cavitation with increasing temperature when α and σ were kept constant. The surface pressure, however, still showed that increasing temperature had the effect of shortening the cavitation plateau and increasing the $-(C_{\mathrm{Pmin}})$; in fact, at $\alpha=5$ deg, $\sigma=1.5$, pressures similar to those measured under cavitation-free conditions were measured. A fundamental fluctuation Strouhal number was found at $\mathrm{St}_c=0.17$ over a wide range of cavitation numbers, $1.3<\sigma<2.1$ at $\alpha=8$ deg and $25<T_\infty<70$°C. A weaker higher-frequency peak, potentially a higher harmonic, was also observed by Cervone et al. [7] for $1.4<\sigma<2.1$ near $\mathrm{St}_c=0.32$. A somewhat different behavior was observed on a NACA0015 hydrofoil at $\alpha=7$ deg in water by Kjeldsen et al. [9]. For $0.75<\sigma<1$, $\mathrm{St}_c=0.15$ Mode I oscillations dominated, while for $1<\sigma<1.3$, Mode II oscillations at $\mathrm{St}_{L_{\mathrm{cav}}}=0.3$ became more prominent.

Experimental Setup

The hydrofoil used in the present study had a NACA0015 profile, a 102 mm span, and a 51 mm chord. A closed-loop facility was filled with the perfluorinated ketone described above. The facility is driven by a 25 hp pump controlled by a Danfoss VLT 5022 controller that allows the speed of the pump to be controllably varied. A sketch of the facility is shown in Fig. 1. To reduce the tendency of vapor bubbles to circulate and accumulate, as noticed frequently in closed-loop facilities, three fine-meshed screens in series, the finest with 0.074 mm openings, were placed in the stagnation chamber. The facility has a test section cross section of 102×102 mm^2 and is capable of providing flow speeds of up to 10 m/s. The tunnel is connected to an argon-based purge and vacuum systems to reduce the levels of dissolved gases in the fluid, primarily oxygen, which would affect incipient cavitation. Prior to testing, vacuum down to 50 kPa is applied followed by repressurization with argon. This process is repeated for several hours to degas the fluoroketone. The hydrofoil was fitted with seven 1 mm diameter pressure taps along the centerline chord at $x/c=0.000$, 0.056, 0.113, 0.168, 0.212, 0.317, and 0.883, with x being a chordwise coordinate measured from the leading edge. One transducer measured the static pressure at the test section ceiling 25 mm upstream of the hydrofoil leading edge. The taps were connected to 30 psi (absolute) (0.2 MPa) Omega PX303 transducers using 0.2 m long nylon tubings with 1.5 mm inside diameter (i.d). A flush-mounted PCB1502 transducer is placed on the test section wall to ensure fast response. In addition, the tunnel is instrumented with 100 psi (absolute) (0.7 MPa) PX303 transducers connected to the stagnation chamber and the downstream collection box, as well as with RTDs on the stagnation chamber and the pump inlet to monitor fluid temperature, maintained ambient in this study. The 200 mm diameter pump outlet is equipped with a Prandtl probe connected to an Omega PX138 1 psi (differential) (7 kPa) transducer to monitor flow speed. All sensor outputs were recorded at 1 kHz during the tests.

In addition to pressure and temperature measurements, high-speed photography was used to capture the structure and temporal behavior of the cavitation at high speeds. Using a Cooke pco.1200 s camera synchronized with two flash units, a series of 16 sequential images was taken at a frame rate of 1270 fps along the span of the hydrofoil with illumination provided from the top. The flashes were spaced by 5.3 ms and covered a 10 mm wide slice near the centerline of the hydrofoil. Images were acquired with 50 μs exposure time, and corrected for background illumination and variation of light intensity between images caused by the flash light decay over time.

Pressure data at steady conditions, typically the last 10–20 s prior to the next change in tunnel speed, were averaged to obtain hydrofoil C_p curves and frequency spectra. This involved fitting a

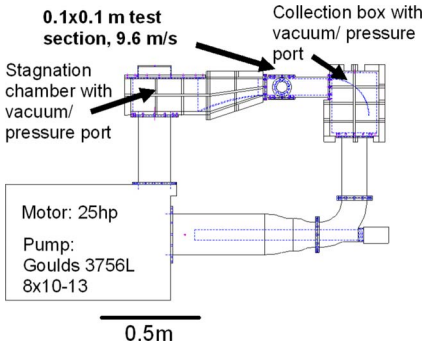

Fig. 1 Water tunnel test facility

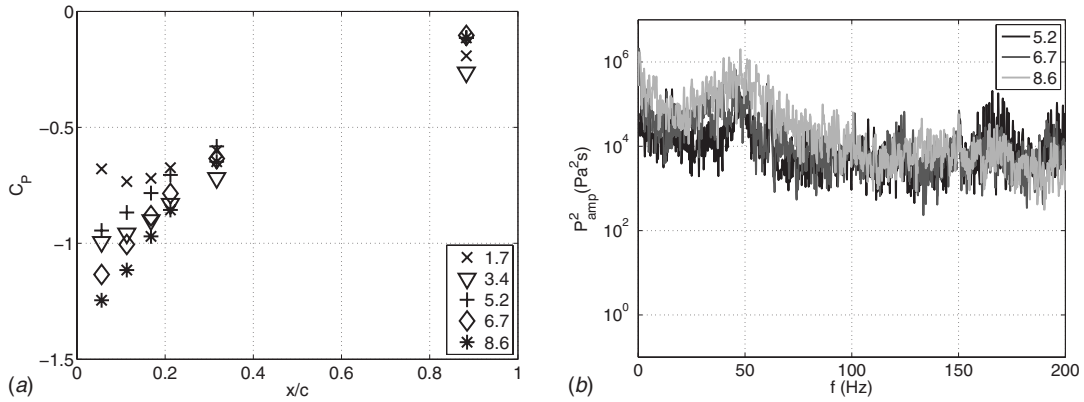

Fig. 2 Suction side pressure coefficient at different freestream speeds (left) and energy spectra at the test section static tap (right) at various freestream flow speeds in m/s; α=4 deg, σ=2.92 at 5.2 m/s, σ=2.14 at 6.7 m/s, and σ=1.67 at 8.6 m/s

linear base line to the selected data, eliminating slow pressure drift seen in the tests, application of a Hanning filter followed by Fourier transformation of the data. The spectra were then low-pass filtered with a 0.1 Hz wide Gaussian filter for clarity before being plotted.

Uncertainties

The Omega PX303 transducer readings have a total uncertainty of 1.2% FS, corresponding to 2.4 kPa. The test section static pressure transducer PCB1502 used in Figs. 2 and 3 has a total uncertainty of 0.7%, corresponding to 1.4 kPa. The tubings used in Fig. 4 have been found in pressure response tests to give a time constant of 20 ms, i.e., $1/e$ damping of oscillations at 50 Hz as well as a pumping pressure shift of 14 kPa during the test. The direct-connect PCB transducer exhibited significantly better response with negligible damping over the frequency region studied as well as negligible pumping effect. Due to the large range of dynamic pressures used in the C_p calculations, from 2.3 kPa at

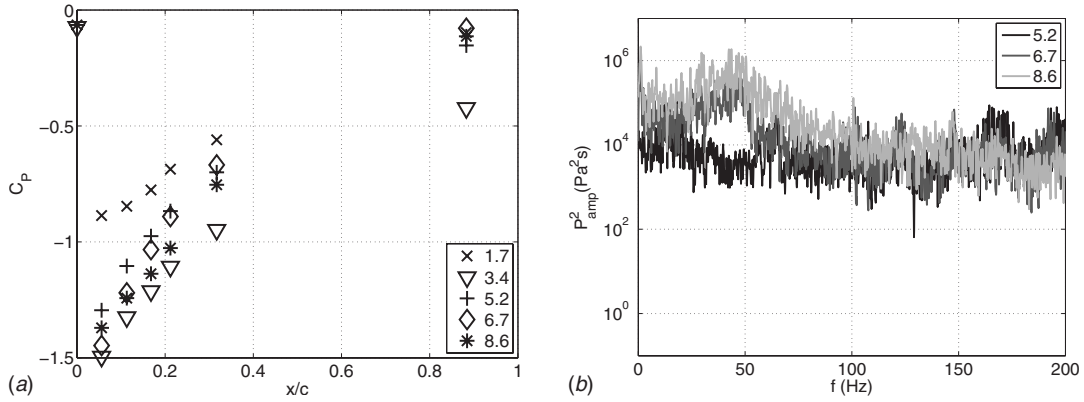

Fig. 3 Suction side pressure coefficient at different freestream speeds (left) and energy spectra at the test section static tap (right) at various freestream flow speeds in m/s; α=6.6 deg, σ=2.80 at 5.2 m/s, σ=2.00 at 6.7 m/s, and σ=1.54 at 8.6 m/s

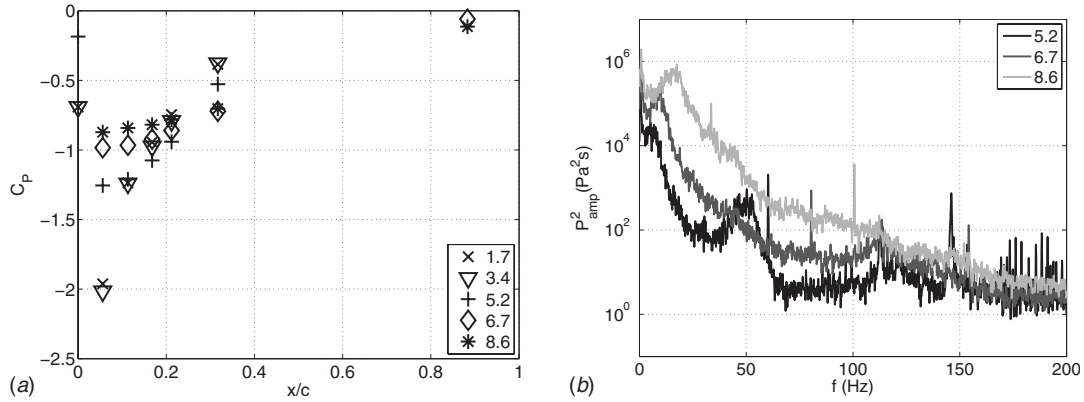

Fig. 4 Suction side pressure coefficient at different freestream speeds (left) and energy spectra at the test section static tap (right) at various freestream flow speeds in m/s; α=8 deg, σ=1.53 at 5.2 m/s, σ=1.21 at 6.7 m/s, and σ=1.06 at 8.6 m/s

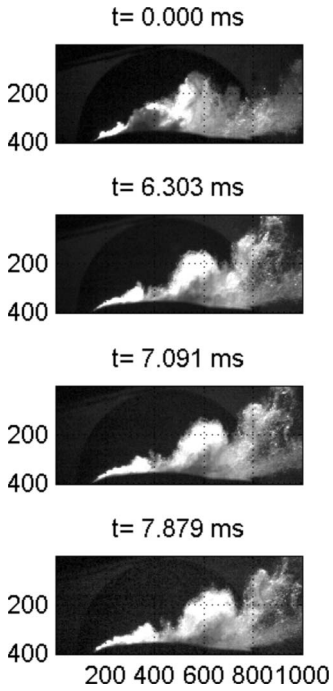

Fig. 5 Vapor formation on suction side of NACA0015 hydrofoil captured at 1270 fps at 5.2 m/s, 8 deg angle of attack at σ =1.53. Flow from left to right, leading edge at horizontal pixel 146, trailing edge at 773, scale: 81 μm/pixel.

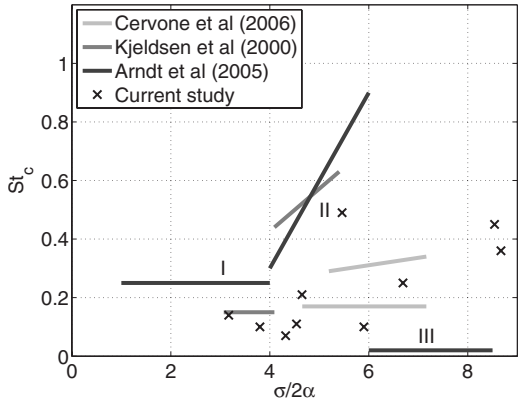

Fig. 6 Strouhal number of dominant frequency based on hydrofoil chord length plotted versus angle of attack-corrected cavitation number for several water studies. The three types of oscillatory behavior suggested by Arndt et al. [11] are indicated by Roman numerals. Conditions for tests where significant oscillations were seen in fluoroketone are indicated by x.

1.7 m/s to 59 kPa at 8.6 m/s, the uncertainty in C_p decreases from 1.2 to 0.05 as the speed increases from 1.7 m/s to 8.6 m/s.

Results

Using the system described above, pressure data were acquired at three different angles of attack and at various tunnel speeds. The time-averaged pressure coefficients and energy spectra at the test section static port are shown in Figs. 2–4. Spectra are only shown for the three highest tunnel speeds for clarity. For the cases shown in Figs. 2 and 3, the spectra had the same $\sim 10^4$ Pa^2 s base line as the higher-speed tests, but with a weaker or missing broad 50 Hz peak. In the α=8 deg case, the oscillations were at the 1 Pa^2 s base line at 50 Hz and below 10^4 Pa^2 s at 10 Hz.

At the two smaller angles of attack, displayed in Figs. 2 and 3, the suction peak is not flattened as the speed is increased, and no significant oscillations are seen in the spectra. In contrast, at the α=8 deg case, shown in Fig. 4, cavitation is indicated by the decrease in the suction peak as speed is increased and the development of peaks in the frequency spectra near 50 Hz at 5.2 m/s and at around 10 Hz primarily for the two higher speeds. Also shown in Fig. 4 are the spikes corresponding to the pump blade passing frequency, e.g., at 100 Hz at 8.6 m/s tunnel speed. Response tests suggested that these oscillations are dampened, an order of magnitude due to the tubing damping in Fig. 4, while the spectra in Figs. 2 and 3 were taken using the flush-mounted PCB transducer, offering improved frequency response.

The sequence of images shown in Fig. 5 illustrates how the region filled with small vapor bubbles exhibits large thickness fluctuations but generally grows in the downstream direction. Also seen is a periodicity of 7 ms, suggesting a frequency of 140 Hz, corresponding to a peak in the spectrum shown in Fig. 4.

Discussion

Similar to the results obtained by Tani and Nagashima [2] in a 2D nozzle using liquid hydrogen and predicted by CFD modeling using the barotropic model of Rapposelli and d'Agostino [8] on a NACA 66-109 hydrofoil, the C_p curve during cavitation in Fig. 4 shows a slight increase rather than remaining absolutely flat following $-(C_{\mathrm{Pmin}})$ as is seen in tests with negligible thermodynamic effect. While the pressure plateau shortening and increased $-(C_{\mathrm{Pmin}})$ predicted by the Rapposelli and d'Agostino model [9] are also found in NACA0015 tests [7], the streamwise increase in pressure is not. In the present tests, the minimum pressure at the x/c=0.056 tap appears to be about $0.2q$ higher than the freestream vapor pressure. It is possible that, given the spacing between the pressure taps, the suction peak possibly resides between the two upstream-most taps. The pressure increase downstream of the cavity is also gradual, unlike the shocklike rapid pressure rise predicted by the Rapposelli and d'Agostino model [8].

Comparing the present results to those obtained by Kjeldsen et al. [9] using a NACA0015 in ambient temperature degassed water general agreement in the occurrence of a Type I–II transition for $\sigma/2\alpha$=5 rather than 4 is suggested by Fig. 4. Mode II oscillations observed for higher cavitation numbers appear to be increasingly indistinct as the cavitation number increases. At σ=1.53 and α =8 deg, the broad peak is centered at St_c=0.49, close to the 0.60 obtained from the Kjeldsen [9] correlation, but for other runs, the dominant frequency in this range is much lower. Several differences were noted. The difference in spectra between σ=2.80 and σ=2.00 at 6.6 deg, as shown in Fig. 3(*b*), suggests inception in the range $8.6 < \sigma/2\alpha < 12$, close to the inception criterion of $\sigma/2\alpha < 8.5$ based on data of Kjeldsen et al. [9]. In Fig. 3 range, no effect was seen on the C_p suction peak, but the local pressures remained above freestream vapor pressure. The general trend of St_c increasing with σ for Mode II oscillations seen by Kjeldsen et al. [9] was also observed in the present study but with significant scatter, as seen in Fig. 6. The increasing trend was noticed on a flat plate hydrofoil in tests by Sato et al. [10] where St_c increased from 0.3 up to 1.3 as the cavity length was decreased from L_{cav}/c=0.8 to L_{cav}/c=0.15. In that study, it was found that St_c could vary by a factor of 2 for the same L_{cav}/c depending on the test section inlet length, suggesting that this kind of oscillation may be facility dependent. This is also suggested by the data of Cervone et al. [7], which found St_c remaining close to 0.17 for a range of σ, and also observed what could be a second harmonic of this frequency, as shown in Fig. 6.

The appearance of the cavitation is also quite different in the present study with the cavitating region stretching across the entire hydrofoil chord even immediately after transition at 5.2 m/s, rather than covering less than 73% of the chord throughout the Type II regime, when $1.0 < \sigma < 1.3$ at 7 deg, as suggested by

Kjeldsen et al. [9]. In the high-speed photographs obtained by Wang et al. [12] in water on a Clark Y hydrofoil at 8 deg and $\sigma = 0.80$, the vapor phase was completely removed from the hydrofoil as a re-entrant jet washes it away from the surface starting at the trailing edge. In the present study, the vapor layer thickness fluctuates as much as a factor of 3 over time at a given chordwise position, but it was never completely absent, even at a moderate cavitation number of $\sigma = 1.53$ at $\alpha = 8$ deg. At this cavitation number, Wang et al. [12] found transition from incipient cavitation to attached small sheet cavitation. This further supports the conclusion that when matching σ, visually more extensive cavitation is present in fluoroketone than in water. This trend is also supported by the observations of Cervone et al. [7], who found that increasing water temperature while keeping α and σ constant generally expanded the visually cavitating region.

The cavitation observed in the present high-speed photographs in Fig. 5 exhibited a frothy appearance with a much finer structure than in water under ambient conditions, as noted for example, by Cervone et al. [7], who noted a trend toward smaller bubbles at higher water temperature and ΔT^*. It is also in line with the fine bubbles observed in liquid nitrogen by Ruggeri and Gelder [1].

Conclusions

Based on pressure measurements and high-speed photographs of cavitation in fluoroketone on a NACA0015 hydrofoil over a range of angles of attack and flow speeds, the following conclusions were drawn.

- The smaller bubbles and finer structures in cavitation observed in the present study compared to water tests, especially at ambient temperature, are attributed to a thermodynamic effect; the surface tension may also be responsible.
- The visual extent of cavitation is enlarged by increasing the thermodynamic effect while keeping the cavitation number constant.
- A large scatter in the frequency of Type II oscillations was found between different studies, supporting the claim by Sato et al. [10] that these are facility-dependent oscillations.
- A gradual Type I-II transition was found near $\sigma/2\alpha = 5$, which is higher than observed in water.

Acknowledgment

This work has been supported by a NASA grant under the Constellation University Institute Program (CUIP). Ms. Claudia Meyer is the CUIP Manager. The authors would like to thank Dr. Dan Dorney from NASA MFSC for his continuous advice.

References

[1] Ruggeri, R. S., and Gelder, T. F., 1964, "Cavitation and Effective Liquid Tension of Nitrogen in a Tunnel Venturi," NASA Report No. TN D-2088.

[2] Tani, N., and Nagashima, T., 2003, "Cryogenic Cavitating Flow in 2D Laval Nozzle," J. Therm. Sci., **12**(2), pp. 157–161.

[3] Franc, J.-P., Rebattet, C., and Coulon, A., 2003, "An Experimental Investigation of Thermal Effects in a Cavitating Inducer," *Fifth International Symposium on Cavitation (Cav2003)*, Osaka, Japan.

[4] Billet, M. L., Holl, J. W., and Weir, D. S., 1981, "Correlations of Thermodynamic Effects for Developed Cavitation," ASME J. Fluids Eng., **103**(12), pp. 534–542.

[5] Hord, J., 1973, "Cavitation in Liquid Cryogens," NASA Report No. CR-2156.

[6] Coutier-Delgosha, O., Devilliers, J.-F., Pichon, T., Vabre, A., Woo, R., and Legoupil, S., 2006, "Internal Structure and Dynamics of Sheet Cavitation," Phys. Fluids, **18**(1), p. 017103.

[7] Cervone, A., Bramanti, C., Rapposelli, E., and d'Agostino, L., 2006, "Thermal Cavitation Experiments on a NACA 0015 Hydrofoil," ASME J. Fluids Eng., **128**(2), pp. 326–331.

[8] Rapposelli, E., and d'Agostino, L., 2003, "A Barotropic Cavitation Model With Thermodynamic Effects," *Fifth International Symposium on Cavitation (Cav2003)*, Osaka, Japan.

[9] Kjeldsen, M., Arndt, R. E. A., and Effertz, M., 2000, "Spectral Characterization of Sheet/Cloud Cavitation," ASME J. Fluids Eng., **122**(9), pp. 481–487.

[10] Sato, K., Tanada, M., Monden, S., and Ysujimoto, Y., 2001, "Observations of Oscillating Cavitation of a Flat Plate Hydrofoil," *Fourth International Symposium on Cavitation (CAV2001)*, Pasadena, CA.

[11] Arndt, R. E. A., Balas, G. J., and Wosnik, M., 2005, "Control of Cavitating Flows: A Perspective," JSME Int. J., Ser. B, **48**(2), pp. 334–341.

[12] Wang, G., Senocak, I., Shyy, W., Ikohagi, T., and Cao, S., 2001, "Dynamics of Attached Turbulent Cavitating Flows," Prog. Aerosp. Sci., **37**, pp. 551–581.

Assessing Rotation/Curvature Corrections to Eddy-Viscosity Models in the Calculations of Centrifugal-Compressor Flows

G. Dufour[1]
e-mail: gdufour@cerfacs.fr

J.-B. Cazalbou

X. Carbonneau

P. Chassaing[2]

ISAE,
Université de Toulouse,
BP 54032 Toulouse Cedex 4, France

*Rotation and curvature (RC) effects on turbulence are expected to impact losses and flow structure in turbomachines. This paper examines two recent eddy-viscosity-model corrections devised to account for these effects: the Spalart and Shur (1997, "On the Sensitization of Turbulence Models to Rotation and Curvature," Aerosp. Sci. Technol., **1**(5), pp. 297–302) correction to the model of Spalart and Allmaras (1994, "A One-Equation Turbulence Model for Aerodynamic Flows," Rech. Aerosp., **1**, pp. 5–21) and the correction of Cazalbou et al. (2005, "Two-Equation Modeling of Turbulent Rotating Flows," Phys. Fluids., **17**, p. 055110) to the (k,ϵ) model. The method of verification and validation is applied to assess the impact of these corrections on the computation of a centrifugal-compressor test case. First, a review of RC effects on turbulence as they apply to centrifugal compressors is made. The two corrected models are then presented. Second, the Radiver open test case (Ziegler K. U., Gallus, H. E., and Niehuis R., 2003, "A Study on Impeller Diffuser Interaction Part 1: Influence on the Performance," ASME J. Turbomach, **125**, pp. 173–182) is used as a basis for the assessment of the two corrections. After a physical-consistency analysis, the Richardson extrapolation is applied to quantify the numerical errors involved in all the calculations. Finally, experimental data are used to perform validation for both global and local predictions. The consistency analysis shows that both corrections lead to significant changes in the turbulent field, in perfect agreement with the underlying theoretical considerations. The uncertainty analysis shows that the predictions of the global performances are more sensitive to grid refinement than they are to RC turbulence modeling. However, the opposite conclusion is drawn with regard to the prediction of some local flow properties: Improvements are obtained with the RC corrections, the best results being observed for the RC-corrected (k,ϵ) model.* [DOI: 10.1115/1.2953231]

1 Introduction

Flows in turbomachines, and particularly in centrifugal compressors, are recognized as being very complex, due to important viscous and three-dimensional (3D) effects, with a significant contribution of the turbulence properties. As mentioned in reviews by Lakshminarayna [1] and Bradshaw [2], the main challenges with regard to the underlying turbulence physics are the prediction of the effects of compressibility, pressure gradients or transition, and the effects of system rotation and streamline curvature (further referred to as RC effects). In this study, we shall focus on the modeling of the effects of RC in centrifugal compressors.

Our basic knowledge of RC effects on turbulence is quite fair for simple configurations, where they are responsible for strong modifications to the fluctuating field: They can induce either an enhancement ("destabilization") or a reduction ("stabilization") in the turbulent activity [3,4]. In centrifugal impellers, streamline curvature is caused by the geometry and by secondary flows (including tip leakage). Rotation is particularly important in small-size or high-pressure-ratio rotors, which need to be operated at high rotation speed. It is therefore expected that RC effects on turbulence significantly impact losses and flow structure in centrifugal impellers. In particular, Baljé [5] conjectured a significant contribution of rotation effects to the formation of the jet/wake structure at the outlet of a centrifugal rotor. Computational fluid dynamics (CFD) can be used to improve our understanding of these issues. Moore and Moore [6] tackled this problem for the NASA low speed centrifugal compressor: They observed significant changes of the turbulent field but a rather limited impact on the mean-flow characteristics. However, their computations were made with a simple modification of a mixing-length model. Generally speaking, most of the early corrections for RC effects were valid only for mild curvature and rotation and were difficult to implement in the calculation of a complex 3D flow. This motivates further investigations with current advanced turbulence-modeling strategies.

In the present study, we shall examine two recent model corrections devised specifically to account for RC effects: The correction proposed by Spalart and Shur [7] applied to the Spalart and Allmaras (SA) model [8] and the two-equation-model correction of Cazalbou et al. [9], applied here to the (k,ϵ) model of Yang and Shih (YS) [10]. The RC-corrected versions of these two models will further be referred to as SARC and YSRC, respectively.

The primary objectives of the present study are to assess the capability of the SARC and YSRC models to reproduce RC effects on turbulence in a centrifugal compressor and to quantify the global impact of RC modeling through a comprehensive comparison against detailed experimental data. Actually quantitative assessment of the benefit of the corrections can be guaranteed by the use of uncertainty analysis within the verification and validation (V&V) framework. The rest of the paper is organized as follows:

[1]Present address: CERFACS, CFD Team, Toulouse, France.
[2]Also at INPT-ENSEEIHT-Institut de Mécanique des Fluides de Toulouse, UMR 5502 CNRS, France.

Contributed by the Fluids Engineering Division of ASME for publication in the JOURNAL OF FLUIDS ENGINEERING. Manuscript received April 25, 2007; final manuscript received May 22, 2008; published online August 11, 2008. Assoc. Editor: Chunill Hah.

(i) Sec. 2 provides a theoretical analysis of RC effects on turbulence in a radial impeller, together with a brief presentation of the corrections, which are then used to make a consistency analysis of the first computational results; (ii) then, in Sec. 3, the *Radiver* test case is used to quantitatively assess the numerical results obtained with the two corrections.

2 Physical Analysis and Modeling of RC Effects in Centrifugal Impellers

2.1 Theoretical Analysis of RC Effects in Centrifugal Compressors. As described by Bradshaw [4], system rotation and streamline curvature have a common physical nature: A parallel flow in a rotating frame becomes a curved flow in the absolute frame of reference. However, if curvature is to be considered as *mainly* caused by the geometry, and if rotation is to be assimilated to *system* rotation, then the analysis should be made in the rotating frame of reference.

The first way by which rotation modifies the turbulent activity is known as the shear/Coriolis instability [3]. The analogy between the plane-channel flow with spanwise rotation and the outlet of a centrifugal impeller suggests that the pressure side should be destabilized, while the suction side should be stabilized [11]. A second effect of the Coriolis acceleration is the inhibition of the energy cascade to small scales [12]. In a radial impeller, this would simply lead to a slower decay of turbulence, but this effect is most probably negligible compared to the shear-Coriolis instability.

The effects of streamline curvature on turbulence are well known (see the review of Bradshaw [4]). In the meridional plane of an impeller, the analysis of these effects is rather straightforward: Concave hub curvature will increase turbulence intensity, and convex shroud curvature will decrease it. In the blade-to-blade plane, curvature may change along the chord, preventing a general analysis. However, for the specific case of a backswept impeller, curvature will counteract the effect of rotation in the aft part of the blades.

The outcome of this competition can be estimated by a modified Rossby number defined as

$$\mathrm{Ro}_m = \left| \frac{W \sin\sigma \cos\beta}{\Omega R_c} \right| \equiv \frac{\text{curvature}}{\text{rotation}}$$

where W is the magnitude of the relative velocity, σ is the inclination of the flow paths to the radial direction, β is the inclination to the tangential direction, and R_c is the radius of curvature. For the *Radiver* compressor, the following estimates can be made close to the trailing edge: $W \simeq 170\ \mathrm{m\,s^{-1}}$, $\sigma \simeq 85$ deg, $\beta_2^b \simeq -38$ deg, and $|R_c| \simeq 0.07$ m, leading to a value $\mathrm{Ro}_m \simeq 0.6$. Therefore, close to the trailing edge in the blade-to-blade plane, rotation should theoretically slightly dominate.

2.2 First-Order Corrections for RC Effects. The two recent model corrections selected for the present study are sensitized to rotation through objective Bradshaw–Richardson and Rossby numbers. High Bradshaw–Richardson and/or Rossby numbers correspond to strong RC effects. Both corrections are designed so as to handle such extreme states, see Ref. [9]. So far, the assessment of these two corrections for complex turbomachinery flows remains to be done.

2.2.1 Equations of the SARC and YSRC Corrections. When applied to the SA model, the Spalart and Shur correction consists in multiplying the production term $\mathcal{P}_{\mathrm{SA}} = c_{b1}\tilde{\mathcal{S}}\tilde{\nu}$ of the base line model by the rotation function f_{r1}:

$$f_{r1}(r^*, \tilde{r}) = (1 + c_{r1}) \frac{2r^*}{1 + r^*} [1 - c_{r3} \tan^{-1}(c_{r2}\tilde{r})] - c_{r1}$$

The nondimensional terms r^* and $\tilde{r}$ are defined as

$$r^* = \frac{\tilde{S}}{\tilde{\mathcal{W}}} \text{ and } \tilde{r} = \frac{2}{D^4}\mathcal{W}_{ik}S_{jk}\left[\frac{dS_{ij}}{dt} + (\varepsilon_{imn}S_{jn} + \varepsilon_{jmn}S_{in})\Omega_m\right] \quad (1)$$

where S_{ij} and $\mathcal{W}_{ij}$ are the strain-rate and absolute-rotation tensors, respectively:

$$S_{ij} = 0.5\left(\frac{\partial U_i}{\partial x_j} + \frac{\partial U_j}{\partial x_i}\right) \text{ and } \mathcal{W}_{ij} = 0.5\left[\left(\frac{\partial U_i}{\partial x_j} - \frac{\partial U_j}{\partial x_i}\right) + 2\varepsilon_{mji}\Omega_m\right]$$

Objective measures of strain and rotation are then obtained as

$$\tilde{S} = (2S_{ij}S_{ij})^{1/2}, \quad \tilde{\mathcal{W}} = (2\mathcal{W}_{ij}\mathcal{W}_{ij})^{1/2}, \quad \text{and } D^2 = 0.5(\tilde{S}^2 + \tilde{\mathcal{W}}^2)$$

Finally, the model coefficients are $c_{r1} = 1.0$, $c_{r2} = 12.0$, and $c_{r3} = 1.0$.

The correction of Cazalbou et al. consists in sensitizing the model coefficient $C_{\epsilon 2}$ to RC through the relation

$$C_{\epsilon 2} = C_{\epsilon 2}^0 + \frac{C_{\epsilon 2}^0 - 1}{1 + a\widetilde{\mathrm{Ro}}^{3/2}} + C_{\epsilon 2}^0 C_{\mathrm{sc}} \frac{\tilde{S}k}{\epsilon}[\tanh(b\widetilde{\mathrm{B_R}} + c) - d] \quad (2)$$

where $\widetilde{\mathrm{Ro}}$ is an objective Rossby number defined as

$$\widetilde{\mathrm{Ro}} = \frac{\epsilon}{\tilde{\Omega}k} \quad \text{with } \tilde{\Omega} = (\mathcal{W}_{ij}\mathcal{W}_{ij}/2)^{1/2}$$

and $\widetilde{\mathrm{B_R}}$ is the objective Bradshaw–Richardson adapted from the proposition of Spalart and Shur:

$$\widetilde{\mathrm{B_R}} = -\frac{2k}{\tilde{S}^3\epsilon}\mathcal{W}_{ik}S_{jk}\left[\frac{dS_{ij}}{dt} + \Omega_m(\varepsilon_{imn}S_{jn} + \varepsilon_{jmn}S_{in})\right] \quad (3)$$

Finally, the constants of the correction are as follows:

$$C_{\epsilon 2}^0 = 1.83, \quad C_{\mathrm{sc}} = 0.119, \quad a = 4.3, \quad b = 5.13$$

$$c = 0.453, \quad \text{and } d = 0.682$$

2.2.2 Implementation Issues. The two RC corrections have been implemented in the EURANUS solver of the FINE/TURBO package of Numeca. This multiblock solver is thoroughly presented by Hirsch et al. [13]. The Reynolds-averaged Navier–Stokes equations in the rotating frame are solved with a time-marching method. Time integration is ensured by a four-stage Runge–Kutta scheme. Local-time stepping and a three- or two-level multigrid technique are used to accelerate convergence to the steady state. The discretization in space is based on a cell-centered control-volume approach. Convective fluxes are determined by a second-order centered scheme with added artificial dissipation of the Jameson type. Viscous fluxes are centered. Total quantities and the direction of velocity are imposed at the inlet. At the outlet, the mass flow is imposed through a velocity scaling procedure.

Implementing the corrections is rather straightforward since only source terms are involved. First and second derivatives of the velocity field are obtained by successive applications of a finite-volume estimation of the gradients.

To verify the implementation, a specific postprocessing was used, independent of the modifications made to the solver. The calculated values are verified against analytical expressions for three basic flow configurations: (i) initially-isotropic homogeneous rotating turbulence, (ii) homogeneously-sheared rotating turbulence, and (iii) a hypothetical case of increasingly-sheared turbulence with rotation (defined as $W_1 = Kxy$, $W_2 = W_3 = 0$, and $\mathbf{\Omega} = \Omega_0 \mathbf{z}$, where K and Ω_0 are positive constants). The latter case was needed to verify the implementation of second-order derivatives in Eqs. (1) and (3).

As the YSRC model is concerned, it must be mentioned that Eq. (2) can return excessively high or low values for the $C_{\epsilon 2}$ coefficient when practical 3D calculations are performed. This is due to the presence of the ratio of the turbulent to mean-flow time scales ($\tilde{S}k/\epsilon$) at the right-hand side of Eq. (2), which can take

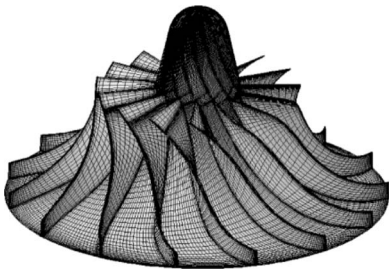

Fig. 1 3D view of the Radiver impeller with the computational grid

unrealistically high values when a (k,ϵ) model is used. A standard fix (see, for instance, Menter [14]) is to limit the possible range of variation of this ratio (or equivalently, of the production-to-dissipation ratio). Here we choose to limit directly the variation of $C_{\epsilon 2}$. A selection of upper and lower bounds consistent with the design method of the corrected model gives at least, $C_{\epsilon 2}^{\max}=3.17$ and $C_{\epsilon 2}^{\min}=1.16$ (see Appendix). On the other hand, Menter [14] suggests to limit the ratio of production to dissipation to 10, which can be shown to limit the value of $C_{\epsilon 2}$ to 3.4 on the basis of Eq. (2). With some margin with respect to these values, the lower and upper bounds retained in the final implementation of the model are $C_{\epsilon 2}^{\min}=1.1$ and $C_{\epsilon 2}^{\max}=5$.

2.3 Qualitative Analysis for the Radiver Compressor

2.3.1 Comparison With Theoretical Considerations. To assess the capability of the corrections to reproduce the expected effects of RC on the turbulent field, preliminary computations for the design point of the Radiver test case are scrutinized. Since the purpose of this part is not the validation of the computations against experimental data, the presentation of the test case and of the numerical setup is left for the next section. The geometry and the computational grid are represented in Fig. 1.

We shall first consider the comparison of the turbulent-viscosity fields obtained with the base line and corrected models. We begin with the meridional mass-averaged fields of normalized turbulent viscosity (μ_t/μ, the turbulent Reynolds number) presented in Fig. 2. For both base line models (Figs. 2(*a*) and 2(*c*)), a highly turbulent region starts just after the leading edge of the blade in the shear layer at the shroud end wall. Turbulence then extends to form a pocket that occupies almost the whole of the meridional section as it enters the vaneless diffuser. There, the maximum turbulence activity occurs at about midspan for both models. It can be noted here that the absolute level of μ_t/μ reaches a higher value with the SA model.

For the SARC model, the impact of curvature can be observed by comparing Figs. 2(*a*) and 2(*b*): (i) at the top of the meridional section, the turbulent-viscosity level is significantly reduced due to the convex shroud curvature; (ii) at the bottom of the meridional section, the concave hub surface induces an important turbulence level at about midpassage, which moves the maximum of turbulent activity closer to the hub. Altogether, these two effects move the maximum turbulence level further into the diffuser.

For the YSRC model, the same impact of convex shroud curvature is observed when comparing Figs. 2(*c*) and 2(*d*). However, there is no additional increase due to hub curvature. As a result, the maximum of turbulent viscosity is confined in the immediate vicinity of the shroud surface. This skewness of the turbulent-viscosity field persists in the vaneless diffuser.

Figure 3 illustrates the behavior of the models with a midspan blade-to-blade view of the turbulent Reynolds number field. For both base line models, the observed turbulent field results from the production in the shroud area mentioned earlier, with no specific contribution of the blade-to-blade flow. For the SARC model, the main impact of the correction can be seen close to the trailing edge, where the intensity of the normal-to-the-blade component of the Coriolis force is maximum. There, the rotation effect triggers an increase in the turbulent activity at the pressure side of the blade (in the area marked D in Fig. 3(*b*)), in agreement with the expected effects of rotation. The stabilizing effect at the suction side is not so obvious. Thus, the computation results indicate that the SARC model fosters the effect of rotation over the effect of curvature for this case, as was predicted from the Rossby number analysis made earlier.

On the other hand, the effect of rotation is not observable for the YSRC correction in Fig. 3(*d*). Figure 4 presents a close-up of the trailing-edge area in a blade-to-blade plane located at 10% of the span. In this case, the destabilization due to rotation can be observed at the pressure side of the blade, and a slight stabilization is present at the suction side.

Altogether, it can be concluded that there is an excellent agreement between elementary considerations on the effects of RC in a centrifugal compressor and the impact of both RC corrections on the prediction of the turbulent field.

3 Verification and Validation for the *Radiver* Test Case

3.1 Test Case Description, Computational Setup, and Postprocessing

3.1.1 Description of the Radiver Test Case. The Radiver test case is a centrifugal-compressor stage, comprising an unshrouded impeller, a wedge-type diffuser, and a downstream collector. The main characteristics of the geometry and the operating point of the compressor are given in Table 1. An extensive experimental study of this compressor was carried out by Ziegler [15] at the RWTH of Aachen and is available as an open test case presented in Refs. [16,17]. The primary goal of this test case is the study of rotor/stator interactions, but a vaneless configuration was also tested. In the present study, we shall only consider the vaneless diffuser cases.

To the authors' knowledge, only three published numerical studies have considered validation for the Radiver test case: Weiß et al. [18] computed the vaneless configuration and Boncinelli et al. [19,20] analyzed the impeller-diffuser interaction.

According to the information given by Ziegler [15], the following experimental uncertainties must be considered: (i) pressure measurements are accurate to 0.2%; (ii) temperature measurements are accurate to 0.3%, combining this with the accuracy of pressure measurement, uncertainty analysis yields an accuracy of 0.8 efficiency points for the isentropic efficiency; and (iii) L2F measurements are accurate to about 2% for velocities and 3 deg for flow angles.

For the geometry modeling, the bulb upstream of the rotor was partially included: Weiß et al. [18] report a negligible influence of the inlet duct, and available experimental results suggest that the corresponding pressure loss is less than measurement accuracy. Although results are only extracted just aft of the rotor, the vaneless diffuser was modeled up to a radius about $R=1.5\times R_2$. The hot-running conditions are solely accounted for by their impact on the clearance height, as described in Refs. [15,18]: The gap size was set to 0.684 mm at the leading edge and was 0.358 mm at the trailing edge. The exact (blunt) shape of the trailing edge is accurately resolved, even on the coarsest mesh.

3.1.2 Computational Setup. All computations were run with the numerical setup detailed in Sec. 2.2.2. Standard iterative-convergence criteria were selected: (i) a reduction in at least three orders of magnitude of the rms residuals; (ii) stabilization of the mass flow, with less than 0.1% difference between inlet and outlet; and (iii) stabilization of the global quantities of interest (pressure ratio and efficiency). The uncertainty associated with iterative convergence was graphically estimated [21] and found to be negligible.

3.1.3 Postprocessing of the Numerical Results. Particular care

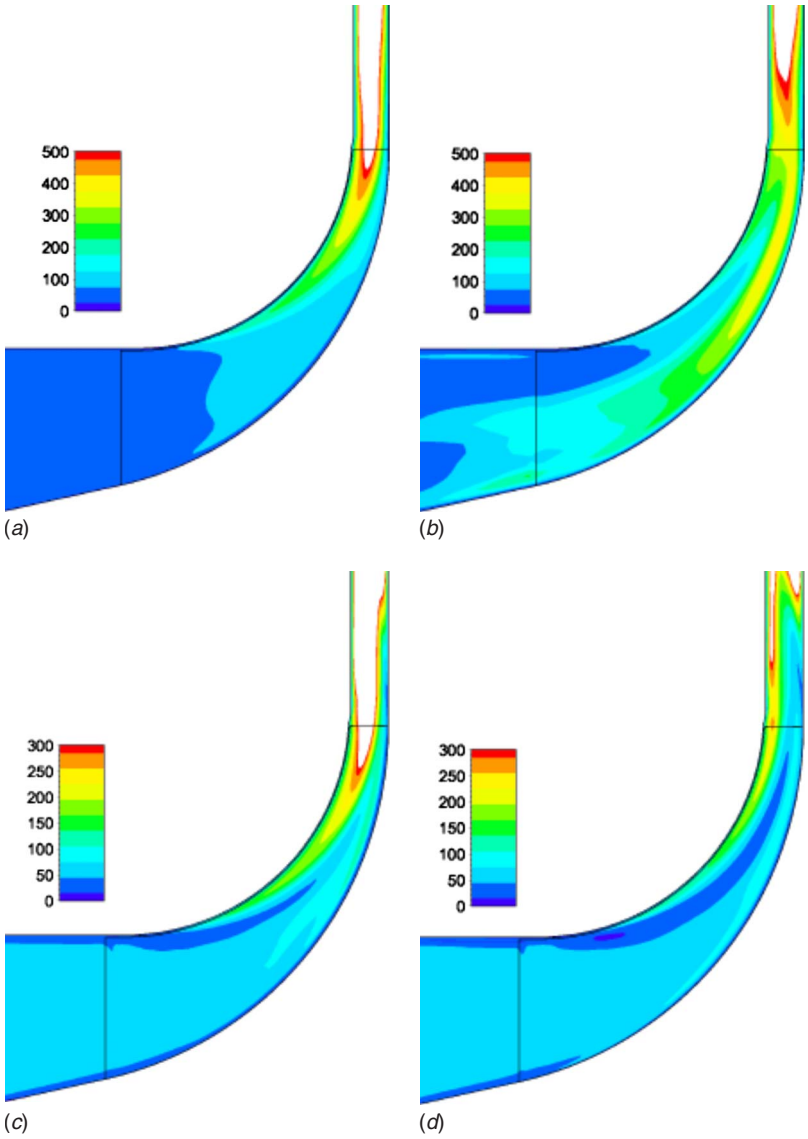

Fig. 2 Meridional view of the mass-averaged field of turbulent viscosity normalized by the dynamic viscosity (μ_t/μ). The two RC corrections reproduce the effect of curvature: Turbulence is increased close to the concave hub surface and reduced near the convex shroud surface. The computational domain is only partially represented, and the color scales are different for the one- and two-equation models. (a) SA; (b) SARC; (c) YS; (d) YSRC.

was devoted to ensure to match the numerical postprocessing with the experimental procedure. The total-total pressure ratio of the rotor was postprocessed using discrete values of total pressure extracted on a constant-radius surface in the channel (R =138.1 mm) after a mass-weighted azimuthal averaging, combined with average static-pressure values extracted at specific locations for the hub and shroud (R=137.5 mm and R=138.8 mm, respectively). The L2F measurement plane was reproduced according to the definition given in Ref. [16]. However, the "Hi-3" experimental procedure for the extraction of total temperature, designed to account for heat fluxes through the shroud end wall, is replaced by a standard mass-averaged extraction in the adiabatic simulations.

3.2 Verification of the Solutions

3.2.1 Mesh Parameters. Before conducting the grid-convergence study, the selection of mesh parameters was made according to Dufour et al. [22]. Based on the fact that different flow characteristics converge at different rates, the study in Ref. [22] uses the design of experiment technique to quantify the influence of different mesh parameters on selected flow quantities. A specific outcome of this study was the demonstration of the determining influence of the tip-gap discretization on the shroud friction coefficient, further quantified in Ref. [23]: For a centrifugal compressor similar to the Radiver, convergence of the shroud friction coefficient within a 5% numerical-error band requires at least 37 grid points between the blade tip and the shroud in the spanwise direction.

Based on these preliminary studies, a reference mesh of 3×10^6 cells was generated. To perform grid-convergence tests, the number of grid points in each direction was halved. However, this is too high a coarsening to ensure an accurate grid-convergence study (a factor r_h=1.3 in each direction is advised by Celik and Li [24]). Therefore, a 1.5×10^6 cell grid was generated, to which a coarsening of r_h=2 was again applied. All grids use an HI four-block topology, which consists of one block in the blade passage,

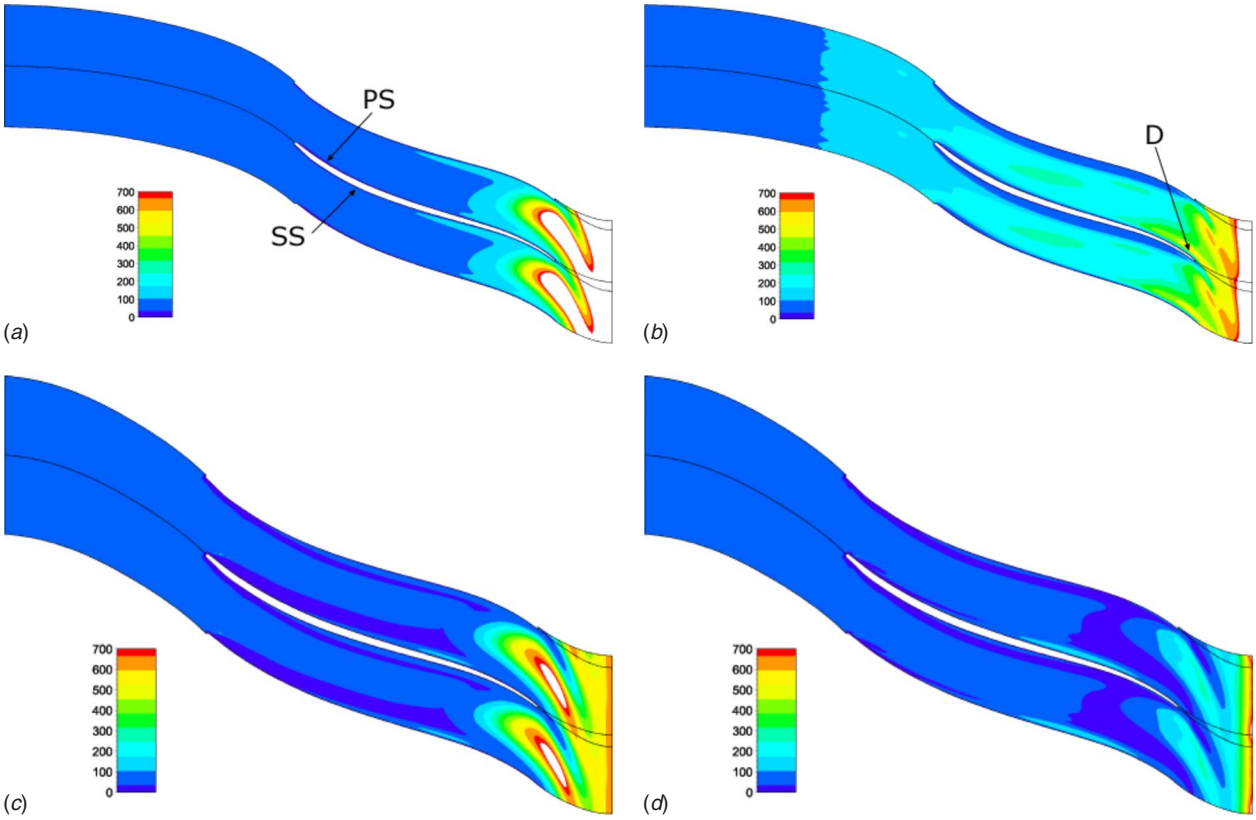

Fig. 3 Midspan blade-to-blade view of the field of normalized turbulent viscosity μ_t/μ. The SARC correction reproduces the effect of rotation: Turbulence is increased close to the pressure side at the trailing edge (area marked by a D) and reduced near the suction side. (a) SA; (b) SARC; (c) YS; (d) YSRC.

two blocks for the butterfly mesh in the tip gap, and one block downstream the blunt trailing edge. Table 2 summarizes all the grids used.

By construction, grid coarsening is uniform between Grids A and C on one hand and Grids B and D on the other hand. However, there is some degree of nonuniformity between Grids A and B (and consequently between C and D). This issue, mentioned in Ref. [21], is not investigated in the present study.

3.2.2 Numerical-Error Estimation. The four models were run on Grids A–D for five operating points (P1, P2, M, S2, and S1 from the lowest to the highest mass flow on the $N=0.8\times N_0$ speed line, see Fig. 6). However, iterative-convergence problems appeared with the (k,ϵ) models on Grid A, for which large oscillations of global quantities (higher than 2%) were observed. The corresponding results are therefore not shown here. This problem may be due to the fact that a very fine grid fosters the appearance of small flow structures, thus questioning the existence of a steady solution.

Figure 5 synthesizes the grid-convergence results for all the models for three operating points (P1, M, and S1). The results

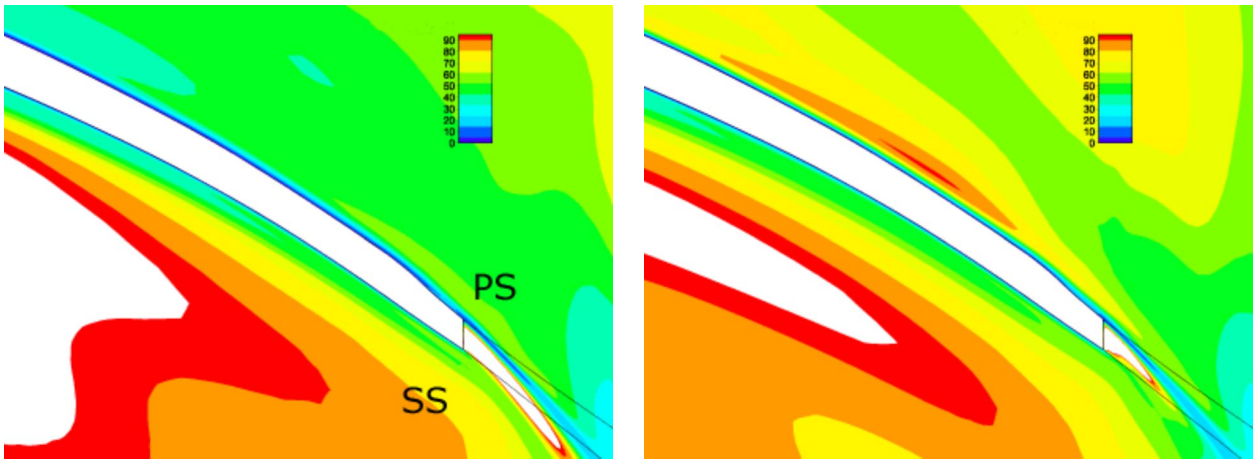

Fig. 4 Trailing-edge close-up of a 10% span blade-to-blade view of the field of the normalized turbulent viscosity μ_t/μ. Contrary to the blade-to-blade midspan of Fig. 3, here the YSRC correction reproduces the effect of rotation: Turbulence is increased close to the pressure side at the trailing edge. (a) YS; (b) YSRC.

Table 1 Radiver test case: geometry and operating point of the compressor

Impeller characteristics			
No. of blades	Z_b	=	15
Outlet radius	R_2	=	135 mm
Outlet backsweep angle	β_2^b	=	−38 deg
Outlet blade height	b_2	=	11.1 mm
Operating point characteristics			
Nominal rotation speed	N_0	=	35,200 rpm
Maximum corrected mass flow	$\dot{m}_{\text{cor}}^{\max}$	=	2.5 kg/s
Nominal specific speed	n_s	=	0.69
Maximum stage pressure ratio	$\pi_{\text{tt}}^{\max}$	=	4.1
Maximum stage isentropic efficiency	$\eta_{\text{is-tt}}^{\max}$	=	0.834

obtained with the three finest grids available for each model are used to apply the extrapolation of Richardson and compute the "estimated (relative) error" (δ_{RE}), as well as the "observed order of accuracy" (p_{obs}), according to the procedures described in Ref. [24], for instance. The results are displayed in log-log scale, with h an average cell size, defined as $h=(\text{total number of points})^{-1/3}$. $h_{\max}$ corresponds to Grid D.

It must first be mentioned that the resolution of the key physics on each grid level was checked. We examined three important features: the 3D meridional separation leading to the formation of the wake, the presence of a tip-leakage vortex, and the development of strong secondary flows. These phenomena were qualitatively observed for all the grids.

For the base line models, the coarsest grid (200,000 points) yields errors of about 2% for the pressure ratio and three points for the efficiency. Beyond 1.5×10^6 points, the pressure ratio reaches grid convergence (at least within 0.1% relative error), while there is still about a one-point error for the efficiency. The errors appear as higher for the one-equation models, which contrasts with results reported elsewhere in other flow configurations [25].

The influence of the RC corrections on the numerical error does not exceed 0.5% for the prediction of the pressure ratio. For the

Table 2 Radiver test case: characteristics of the grids used for mesh-convergence studies. The numbers of points for each block are given in the following form: azimuthal×spanwise×streamwise.

	No. of points				
Grid nomenclature	Total	Blade passage	Tip gap (H)	Tip gap (C)	Downstream blunt
Grid A	2,992,036	81×97×313	25×42×273	17×41×129	41×97×41
Grid B	1,555,620	65×77×249	17×33×273	17×33×129	33×73×33
Grid C	386,708	41×49×157	13×21×137	9×21×65	21×49×21
Grid D	203,052	33×39×125	9×17×137	9×17×65	17×39×17

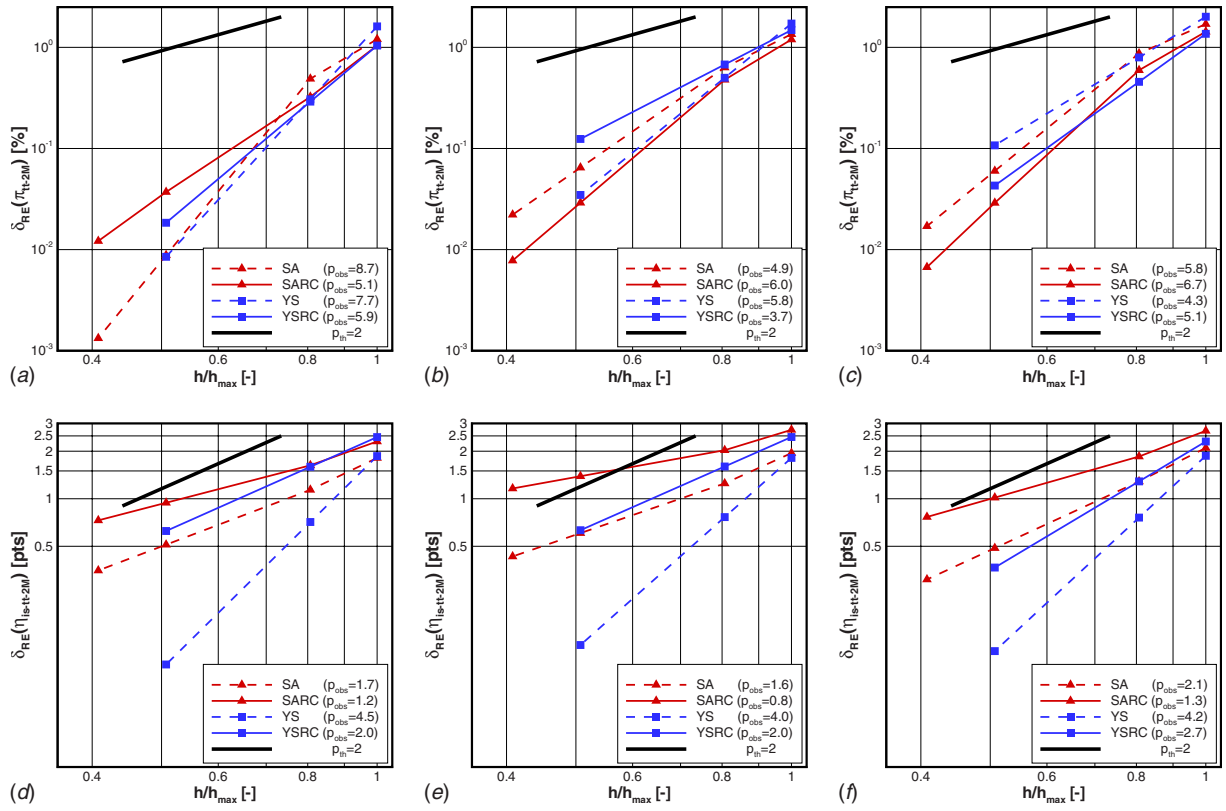

Fig. 5 Numerical errors for the total—total pressure ratio and isentropic efficiency estimated by the Richardson extrapolation. Estimated errors are expressed in percentage of the extrapolated values for the pressure ratio and in efficiency-point decrements with respect to the extrapolated value for the efficiency. The values of the observed order of accuracy are given in the legends. (a) and (d) P1; (b) and (e) M; (c) and (f) S1.

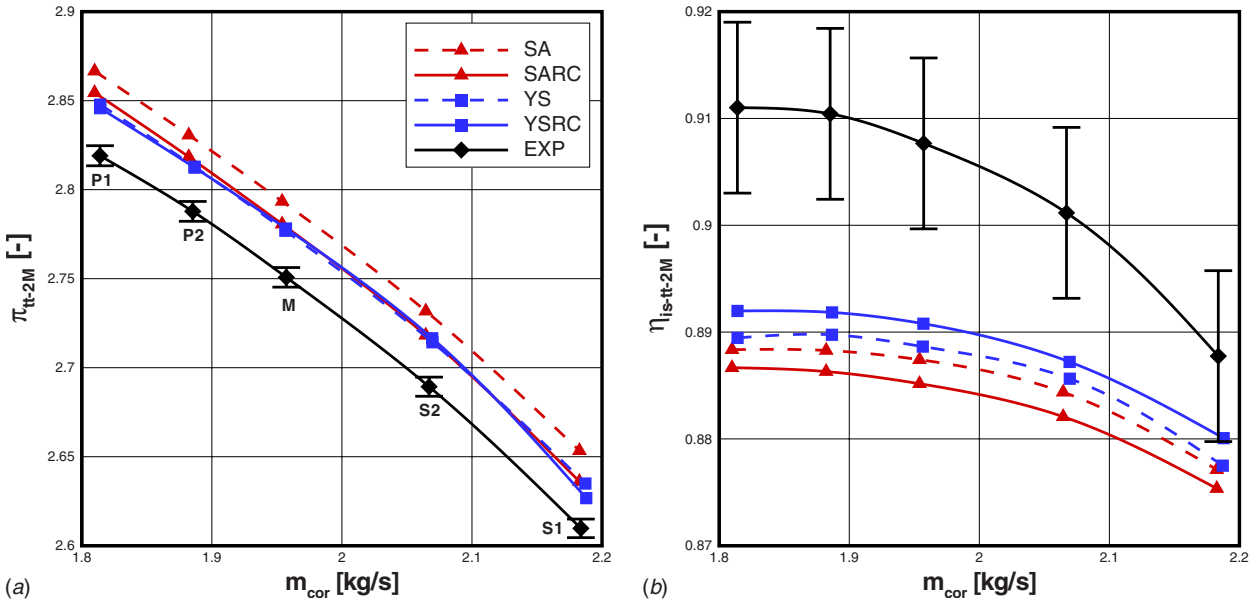

Fig. 6 Comparison of the global performances obtained with the base line and RC-corrected models against experimental values for the Radiver test case. Numerical results obtained on Grid B.

efficiency, the two corrections increase the numerical error of about 0.5 points for all the operating points considered. It can also be noted that the corrections slightly modify the grid-convergence rate: The observed order of accuracy is lower for many of the predictions with the corrected models (see the legends in Fig. 5).

Interestingly, it seems that there is a very weak influence of the operating point on the numerical errors: In other words, it appears that for this specific test case, the classical statement that "tendencies" can be well predicted with relatively coarse grids is substantiated.

3.3 Validation. The results obtained with Grid B are now presented to allow consistent comparisons of the four models on the same mesh. Experimental uncertainties are figured with two-sided error bars.

3.3.1 Global Performances. Figure 6 compares numerical and experimental results for the global performances. For all the models, the pressure ratio is overestimated by 0.7–2%, but with a very good prediction of the trend. Efficiency is underestimated by 0.5–1 point, with a noticeable difference in the trend.

To quantify the impact of the corrections with a minimum bias, we shall use the notion of the "validation uncertainty" proposed by Coleman and Stern [26]. Since then, this notion has been used to form "validation metrics" and has been extended in many publications (see, for instance, [27]). The validation uncertainty, denoted U_{val}, is defined as the root mean square of all the uncertainties that can be estimated. As put by Coleman [28], we shall consider that U_{val} sets the best "level of validation" possible: Any comparison below U_{val} is not significant from an uncertainty point of view. If the comparison E is defined as the difference between the experimental and numerical values, the level of validation L_{val} is finally defined as $L_{val}=\max(|E|, U_{val})$.

In our case, U_{val} involves the numerical (U_{num}) and experimental (U_{exp}) uncertainties, according to $U_{val}=\sqrt{U_{exp}^2+U_{num}^2}$. Assuming that numerical errors and uncertainties are equivalent, validation results are synthesized in Table 3. The uncertainty evaluation is presented only for the nominal operating point (M), but similar results were obtained for the other points of operation.

Regarding the uncertainty analysis in the V&V framework, the significance of the impact of the corrections must be assessed by comparing ΔRC (the variation of a global quantity between the base line and the corrected models) and U_{val} (the best level of validation possible). According to the results given in Table 3, it appears that only the variation of the predicted pressure ratio for the SARC model is above U_{val}. In this case, a very slight improvement of about 0.5% is observed, which is about one-third the difference between the SA model predictions and the experimental data. For all the other cases, the impact of the corrections is negligible, since it is lower than the sum of the experimental and numerical uncertainties.

Therefore, it must be concluded that the RC corrections evaluated here do not have a significant impact on the prediction of global quantities for the Radiver test case. Nevertheless, for all the models tested the validation level achieved is at best 0.95% for the pressure ratio and is 1.69 points for the efficiency.

3.3.2 Azimuthally-Averaged Profiles. A comparison of experimental and numerical results for the azimuthally averaged profiles of total pressure at the rotor outlet is presented in Fig. 7. All the models yield a rather good prediction for all the operating points. The main discrepancies appear at the frontier between the jet and wake structures (roughly at $Z/B=0.5$), where there seems to be too strong a mixing to capture the steep gradients.

Table 3 Radiver test case: validation results for the nominal operating point (*M*). All the differences and uncertainties are expressed as a percentage of the experimental value for the pressure ratio and as efficiency-point decrements for the isentropic efficiency. Comparing U_{val} and ΔRC gives the significance of the impact of the RC corrections.

		SA	SARC	YS	YSRC
$\pi_{tt\text{-}2M}$	E	1.55	1.09	0.95	1.00
	U_{val}	0.21	**0.20**	0.20	**0.24**
	ΔRC	—	**0.46**	—	**–0.05**
	L_{val}	1.55	1.09	0.95	1.00
$\eta_{is\text{-}tt\text{-}2M}$	E	2.02	2.25	1.90	1.69
	U_{val}	1.00	**1.60**	0.81	**1.02**
	ΔRC	—	**–0.22**	—	**0.21**
	L_{val}	2.02	2.25	1.90	1.69

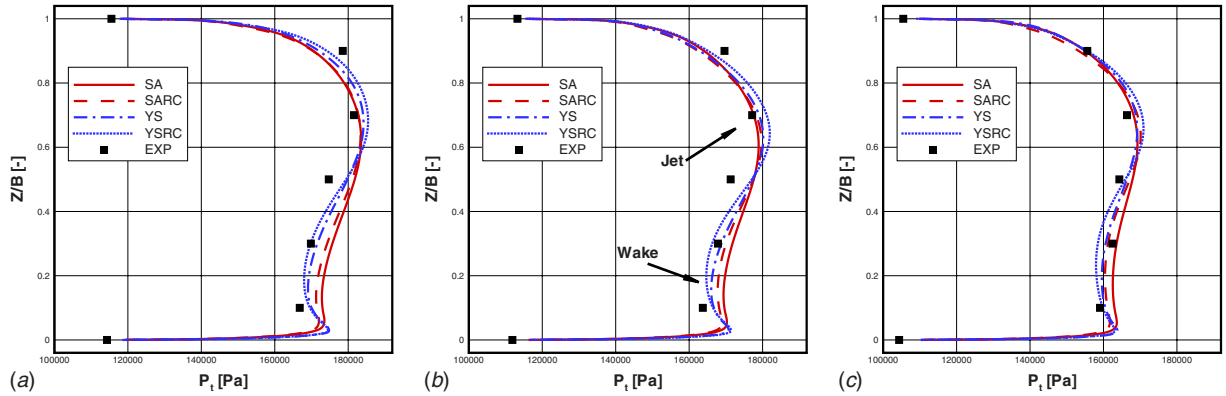

Fig. 7 Comparison of experimental and numerical azimuthally averaged profiles of total pressure. Computational results obtained on Grid B. Experimental- and numerical-uncertainty error bars are smaller than the symbols at the scale of the figure. (a) P1; (b) M; (c) S1.

Again, the notion of validation uncertainty is used to assess the impact of the RC corrections. In this case, both the numerical and the experimental uncertainties are low (as previously mentioned, $U_{\text{exp}} \simeq 0.2\%$, and the numerical uncertainty assessed does not exceed 0.12%). Therefore, the level of validation achieved for the total-pressure profiles is about 0.25% at maximum. Qualitatively, this amounts to an uncertainty band whose size is smaller than that of the symbols in Fig. 7. A mean impact of the corrections can be obtained with the root mean square of the changes between the SA and SARC profiles (defined as $\Delta_{\text{rms}} = \sqrt{1/n \Sigma_{k=1}^{n} (\phi_k^{\text{SARC}} - \phi_k^{\text{SA}})^2}$, where ϕ_k is the considered quantity at the kth spanwise location), which is about 1% (note that there is some compensation between the opposite variations at the hub and shroud). It can thus be concluded here that the impact of the correction is significant for the predictions of the total-pressure profiles. More specifically, the correction gives a better prediction of the *extrema* close to the hub and shroud. The $L2$ norm of the changes between the YS and YSRC profiles is about 0.9%, still higher than the level of validation. Again, the correction yields an improved prediction of the extrema, in better agreement with the experimental results.

Altogether, uncertainty analysis shows that the corrected models improve the comparison with the experimental results, most probably due to a better prediction of the jet/wake composite profiles. This tends to confirm the contribution of turbulence RC effects to the formation of the jet/wake structure as conjectured by Baljé.

Figure 8 compares numerical results with L2F measurements in the form of azimuthally averaged profiles. Only the Operating Point P1 is considered as it is the only one for which L2F data are available. For all the flow quantities considered, it can first be directly observed that the experimental uncertainty alone exceeds the impact of the corrections. Therefore, a first conclusion is that, from an uncertainty point of view, the impact of the corrections is not significant for azimuthally-averaged profiles of kinematic quantities.

For the absolute tangential velocity (a) significant discrepancies are observed between predictions and experiments, with fair agreement only close to the hub and the shroud. At midspan, the differences are consistent with the underestimation of the pressure ratio and efficiency, as it indicates a deficit of work exchange. The prediction of the relative flow angle is only slightly better (b), indicating a rather different flow structure in the predictions. Finally, the comparison of the relative-velocity profiles (c) globally connects these discrepancies with the prediction of the jet/wake structure, which appears to undergo too much mixing.

3.3.3 2D Fields. Figure 9 presents color contours of relative-velocity magnitude at the rotor outlet for the Operating Point P1. The comparison confirms that the slight improvements associated with the RC corrections for the total-pressure profiles are indeed connected to a qualitatively better prediction of the jet/wake structure. It appears that the RC-corrected models predict a larger extension of the wake pocket close to the shroud, together with a more pronounced jet close to the pressure side at the hub. The (k, ϵ) models yield slightly better pressure profiles thanks to a lower mixing, which appears here in the form of a larger differ-

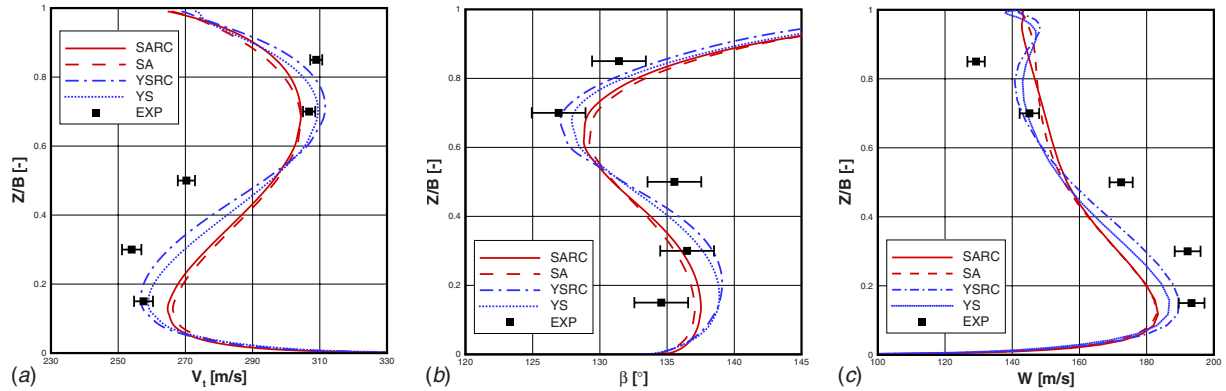

Fig. 8 Comparison of L2F-experimental and numerical azimuthally averaged profiles for the Operating Point P1. Computational results obtained on Grid B.

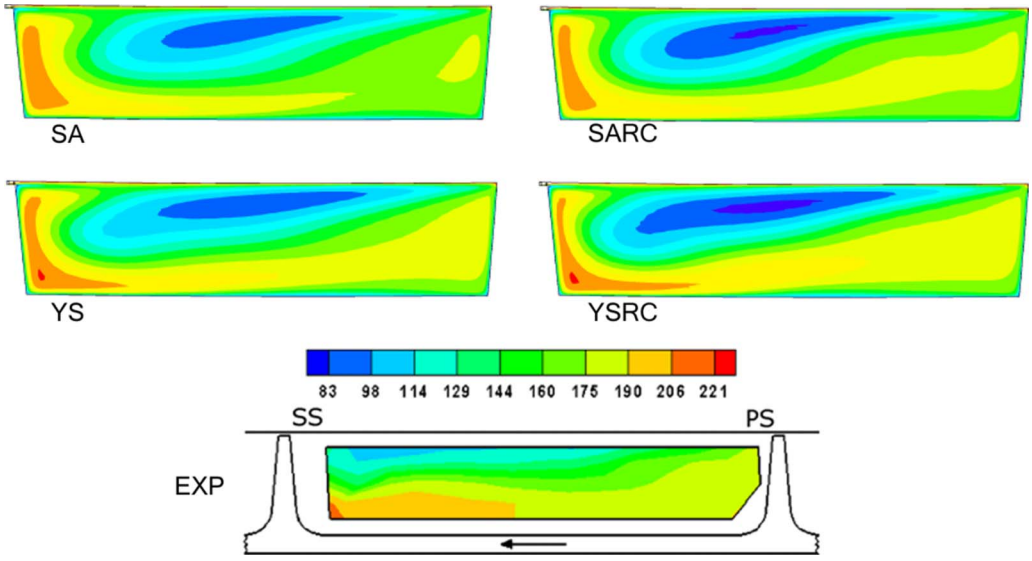

Fig. 9 Comparison of predictions and L2F measurements for the relative velocity at the rotor outlet (Operating Point P1). Computational results obtained on Grid B. Color scale given in m/s.

ence between maximum and minimum velocity levels. This is even more pronounced for the YSRC model, with a significantly larger extension of the wake pocket close to the suction side.

Altogether, these flow fields clearly show that much of the impact of the correction manifests with opposite effects on the pressure and suction sides, which cancels when azimuthally averaged.

4 Synthesis and Conclusions

The present study has examined the physics and the modeling of RC effects on turbulence, and their impact on the flow in a centrifugal compressor. The literature shows that known RC effects in basic configurations motivate a detailed analysis in radial turbomachinery configurations. Given the defects of many existing RC corrections for classical turbulence models, we have implemented two recent corrected models that are sound from both a mathematical and a physical point of view. The assessment of the impact of these two corrections for the prediction of the Radiver test case has been carried out within the verification and validation framework.

The consistency of the two corrections is demonstrated: The numerical predictions are in perfect agreement with the targeted physics. The stabilization and destabilization areas induced by RC are reproduced by the corrections through a significant modification of the turbulent-viscosity field. However, uncertainty analysis shows that the impact of the corrections on global performances is negligible. Locally, slight improvements (about 1%) are observed for azimuthally averaged profiles of total pressure, but flow angles and velocity components are not significantly impacted. Analysis of a 2D field of the relative velocity shows a noticeable impact and confirms the previously hypothesized impact of turbulence RC effects on the formation of the jet/wake structure at the rotor outlet. Taking into account global and local predictions, it appears that all the models studied here yield a fairly good agreement with experiments, although it can be argued that a slightly better prediction of local properties is obtained with the YSRC model.

Our analysis of the rather limited impact of the corrections for this particular test case is the following.

- The dissyminetry (between pressure and suction side on one hand, and hub and shroud on the otherhand) of this impact suggests that averaging may hide some of the effect of the corrections. This prompts the study of a multistage configuration, where the skewness of the flow field at the rotor exit would impact downstream stages.
- As opposed to the rotating plane-channel flow, it appears that in this case, the *direct* impact of RC on global flow characteristics dominates the *indirect* effect via the turbulent field.

Generalization of these conclusions should involve other test cases. The authors have applied the base line and corrected models to an industrial centrifugal compressor of comparable characteristics and obtained similar results. We suspect that a more pronounced impact on global predictions could be obtained for impellers with significantly different specific speed and/or flow coefficients, as these two characteristics are closely related to a rotation number. In such cases, the corrections could trigger a change of the flow regime, and thus entail a more sizable global impact.

Acknowledgment

The authors would like to express their thanks to Liebherr Aerospace Toulouse S.A. for funding the present research project and for authorization to publish the results. The authors would also like to thank the Institute of Jet Propulsion and Turbomachinery of the RWTH Aachen, University of Technology, for providing the Radiver test case.

Appendix: Limiting of $C_{\epsilon 2}$ for the (k,ϵ) RC Correction

The limitation of $C_{\epsilon 2}$ is made so that it does not affect the calibration case of homogeneously sheared rotating turbulence. To this end, we recall here the model problem in that case:

$$\frac{dk}{dt} = C_\mu \frac{k^2}{\epsilon} S^2 - \epsilon$$

$$\frac{d\epsilon}{dt} = C_\mu C_{\epsilon 1} k S^2 - C_{\epsilon 2} \frac{\epsilon^2}{k}$$

which can be combined as

$$\frac{d\alpha}{dt^*} = C_\mu (C_{\epsilon 1} - 1) - (C_{\epsilon 2} - 1)\alpha^2 \equiv \Lambda(\alpha) \qquad \text{(A1)}$$

where $t^* = \mathrm{St}$. With $\alpha(0) = \alpha_0 = \epsilon_0/(Sk_0)$, Eq. (A1) constitutes a fully-defined dynamical system for the state variable α. Its fixed points α_∞ are the solutions to the equation $\Lambda(\alpha) = 0$. Since $C_{\epsilon 2}$ is

the only model coefficient made sensitive to rotation, the following relation holds at the fixed point:

$$C_{\epsilon 2} = 1 + C_\mu \frac{C_{\epsilon 1} - 1}{\alpha_\infty^2} \tag{A2}$$

To preserve the behavior of the model in this situation, the limits of $C_{\epsilon 2}$ must be coherent with the limits of the fixed point. In the fixed-point diagram of the final correction (Fig. 5 of Ref. [9]), these values are as fallows:

- $\alpha_\infty^{\min} = \sqrt{3C_\mu/2} = 0.37$, which is the realizability bound of the model
- $\alpha_\infty^{\max} = 0.5$

Using Eq. (A2), these values give the following upper and lower limits for the corrected model coefficient: $C_{\epsilon 2}^{\max} = 3.17$ and $C_{\epsilon 2}^{\min} = 1.16$.

References

[1] Lakshminarayana, B., 1986, "Turbulence Modeling for Complex Shear Flows," AIAA J., **24**(12), pp. 1900–1917.

[2] Bradshaw, P., 1996, "Turbulence Modeling With Application to Turbomachinery," Prog. Aerosp. Sci., **32**, pp. 575–624.

[3] Tritton, D. J., 1992, "Stabilization and Destabilization of Turbulent Shear Flow in a Rotating Fluid," J. Fluid Mech., **241**, pp. 503–523.

[4] Bradshaw, P., 1973, "Effects of Streamline Curvature on Turbulent Flows," AGARD, Agardograph No. 169.

[5] Baljé, O. E., 1981, *Turbomachines: A Guide to Design, Selection and Theory*, Wiley, New York.

[6] Moore, J., and Moore, J. G., 1990, "Effects of Curvature and Rotation on Turbulence in the NASA Low-Speed Centrifugal Compressor Impeller," *Proceedings of the Fourth Annual Review Meeting of the Center for Turbomachinery and Propulsion Research*, Virginia Polytechnic Institute and State University, Blacksburg, VA.

[7] Spalart, P. R., and Shur, M. L., 1997, "On the Sensitization of Turbulence Models to Rotation and Curvature," Aerosp. Sci. Technol., **1**(5), pp. 297–302.

[8] Spalart, P. R., and Allmaras, S. R., 1994, "A One-Equation Turbulence Model for Aerodynamic Flows," Rech. Aerosp., **1**, pp. 5–21.

[9] Cazalbou, J.-B., Chassaing, P., Dufour, G., and Carbonneau, X., 2005, "Two-Equation Modeling of Turbulent Rotating Flows," Phys. Fluids, **17**, pp. 055110.

[10] Yang, Z., and Shih, T. H., 1993, "A k, ϵ Model for Turbulent and Transitional Boundary Layers," in *Near-Wall Turbulent Flows*, R. M. C. So, C. G. Speziale, and B. E. Launder, eds. Elsevier Science, New York.

[11] Johnston, J. P., 1998, "Effects of System Rotation on Turbulence Structure: A Review Relevant to Turbomachinery Flows," Int. J. Rotating Mach., **4**(2), pp. 97–112.

[12] Rogallo, R. S., 1981, "Numerical Experiment in Homogeneous Turbulence," NASA Technical Report No. TM 81315.

[13] Hirsch, C., Lacor, C., Dener, C., and Vucinic, D., 1991, "An Integrated CFD System for 3D Turbomachinery Applications," AGARD-CP-510.

[14] Menter, F. R., Kuntz, M., and Langtry, R., 2003, "Ten Years of Industrial Experience With the SST Turbulence Model," in *Turbulence, Heat and Mass Transfer*, K. Hanjalić, Y. Nagano, and M. Tummers, Begell House, New York, Vol. 4.

[15] Ziegler, K. U., 2003, "Experimentelle Untersuchung der Laufrad-Diffusor-Interaktion in einem Radialverdichter Variabler Geometrie," Ph.D. thesis, RWTH Aachen, Aachen, Germany, in German.

[16] Ziegler, K. U., Gallus, H. E., and Niehuis, R., 2003, "A Study on Impeller Diffuser Interaction. Part I: Influence on the Performance," ASME J. Turbomach., **125**, pp. 173–182.

[17] Ziegler, K. U., Gallus, H. E., and Niehuis, R., 2003, "A Study on Impeller Diffuser Interaction. Part II: Detailed Flow Analysis," ASME J. Turbomach., **125**, pp. 183–192.

[18] Weiß, C., Grates, D. R., Thermann, H., and Niehuis, R., 2003, "Numerical Investigation of the Influence of the Tip Clearance on the Wake Formation Inside a Radial Impeller," *Proceedings of the ASME Turbo Expo 2003*, Paper No. GT2003-38279.

[19] Boncinelli, P., Ermini, M., Bartolacci, S., and Arnone, A., 2007, "Impeller-Diffuser Interaction in Centrifugal Compressors: Numerical Analysis of the "Radiver" Test Case," J. Propul. Power, **23**(6), pp. 1304–1312.

[20] Boncinelli, P., Ermini, M., Bartolacci, S., and Arnone, A., 2007, "On Effects of Impeller-Diffuser Interaction in the "Radiver" Centrifugal Compressor," *Proceedings of the ASME Turbo Expo 2007*, Canada, Paper No. GT2007-27384.

[21] Stern, F., Wilson, R., Coleman, H. W., and Paterson, E. G., 2001, "Verification and Validation of CFD Simulations: Part 1-Comprehensive Methodology," ASME J. Fluids Eng., **123**(4), pp. 793–802.

[22] Dufour, G., Carbonneau, X., Arbez, P., Cazalbou, J.-B., and Chassaing, P., 2004, "Mesh-Generation Parameters Influence on Centrifugal-Compressor Simulation for Design Optimization," *Proceedings of the 2004 ASME Heat Transfer/Fluids Engineering Summer Conference*, Charlotte, Paper No. HT-FED2004-56314.

[23] Dufour, G., Carbonneau, X., Arbez, P., Cazalbou, J.-B., and Chassaing, P., 2004, "Numerical-Error Evaluation for Tip-Clearance-Flow Calculations in a Centrifugal Compressor," *Proceedings of the XXI ICTAM Conference*, Poland, Paper No. 12510.

[24] Celik, I. B., and Li, J., 2005, "Assessment of Numerical Uncertainty for the Calculations of Turbulent Flow Over a Backward-Facing Step," Int. J. Numer. Methods Fluids, **49**, pp. 1015–1031.

[25] Huang, P. J., 1997, "Validation of Turbulence Models—Uncertainties and Measures to Reduce Them," *Proceedings of the ASME Fluids Engineering Division Summer Meeting*, Vancouver, Canada, Paper No. FEDSM97-3121.

[26] Coleman, H. W., and Stern, F., 1997, "Uncertainties in CFD Code Validation," ASME J. Fluids Eng., **119**, pp. 795–803.

[27] Oberkampf, W. L., and Barone, M. F., 2006, "Measures of Agreement Between Computation and Experiment: Validation Metrics," J. Comput. Phys., **217**, pp. 5–36.

[28] Coleman, H. W., 2003, "Some Observations on Uncertainties and the Verification and Validation of a Simulation," ASME Trans. J. Fluids Eng., **125**, pp. 733–735.

U. Hampel

D. Hoppe

A. Bieberle

Institute of Safety Research,
Forschungszentrum Dresden-Rossendorf e. V.,
P.O. Box 51 01 19,
Dresden 01314, Germany

R. Kernchen

K.-H. Diele

Voith Turbo GmbH,
Voithstrasse 1,
Crailsheim 74564, Germany

E. Schleicher

M. J. da Silva

C. Zippe

Institute of Safety Research,
Forschungszentrum Dresden-Rossendorf e. V.,
P.O. Box 51 01 19,
Dresden 01314, Germany

Measurement of Fluid Distributions in a Rotating Fluid Coupling Using High Resolution Gamma Ray Tomography

Gamma ray tomography has been used to visualize fluid distributions in a rotating fluid coupling in different operation points at a pump speed of 780 rpm and lower turbine speeds. The gamma ray computed tomography system comprises a Cs-137 isotopic source and a high resolution gamma ray detector. An angle synchronized tomographic data acquisition technique was applied to produce sharp slice images from different positions along the coupling axis. The data have been used to assess the hydraulic behavior of the fluid coupling and to help improve our understanding of the flow structure development and its implications on torque transfer in such a device.
[DOI: 10.1115/1.2953295]

Keywords: gamma ray tomography, fluid coupling, two-phase flow measurement

1 Introduction

Fluid couplings are used for power transmission in heavy duty drives, such as in power stations, ship propulsion, band conveyers, mills, and larger transport vehicles. Their hydrodynamic principle enables a low-wear torque conversion from a drive to a load. Depending on their application fluid couplings with constant filling may be of up to 1.3 m diameter and rotate with as much as 3600 rpm for smaller profile diameters. The principal assembly of a fluid coupling with constant filling is shown in Fig. 1. The fluid coupling consists of two bladed wheels, the pump and the turbine, which are attached to shafts on both sides and oppose each other inside a sealed enclosure. Typically, the wheels are made of aluminum alloy casting. For couplings with a very high power range they are made of globular cast iron or steel.

The power transmission in a hydrodynamic coupling is described by the following equations. First, the transmitted power is a product of mass flow and specific energy (energy divided by mass):

$$P = \dot{m}\frac{E}{m} \tag{1}$$

The transmitted torque can be described by the Euler turbine equation, where torque is the product of mass flow and difference in angular momentum

$$M = \dot{m}(R_P c_{u,Po} - R_T c_{u,To}) \tag{2}$$

Here, R_P denotes the output radius of the pump, R_T the output radius of the turbine, $c_{u,Po}$ the circumferential component of the absolute velocity at the pump output side, and $c_{u,To}$ the circumferential component of the absolute velocity at the turbine output side. The momentum is related to some characteristic parameters, namely, fluid density ρ, rotational speed ω_P of the pump, and profile diameter D via the characteristic equation

$$M = \lambda\rho\omega_P^2 D^5 \tag{3}$$

λ is the dimensionless power number, which depends on slip s and filling level v and determines the operational behavior of the coupling. The slip is defined by the ratio of the turbine's and pump's rotational speeds according to

$$s = 1 - \frac{\omega_T}{\omega_P} \tag{4}$$

Moreover, the power number is determined by geometrical parameters (e.g., number, arrangement and shape of blades and chambers, additional fluid reservoirs, runner gap distance, etc.) and to a minor degree by the physical properties of the fluid. The relation $\lambda = f(s)$ is also called secondary characteristics of the coupling.

Today, the two-phase flow phenomena in a fluid coupling seem to be coarsely understood. However, there is still a lack of detailed flow structure knowledge. Typically, it is believed that the circulating flow between the pump and the turbine obtains an ideal flow structure, as shown in Fig. 2 [1]. In accordance with basic fluid mechanics it is assumed that the fluid flows from the pump to the turbine at a speed c_{Po} along the outer radius R_P carrying kinetic energy to the turbine. There, the kinetic energy is transferred to drive the turbine and the fluid crosses back to the pump

Contributed by the Fluids Engineering Division of ASME for publication in the JOURNAL OF FLUIDS ENGINEERING. Manuscript received August 10, 2007; final manuscript received April 29, 2008; published online August 12, 2008. Assoc. Editor: Theodore Heindel.

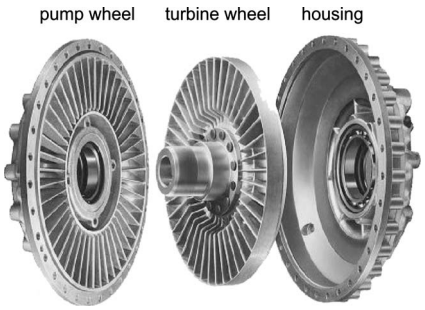

Fig. 1 Construction of a fluid coupling with constant filling

at a lower speed c_{To} and a smaller radius R_T. With increasing load also the slip increases and R_T will become accordingly smaller until eventually the reflux "line" reaches a steep inclination angle that leads to high turbulence and therefore suddenly causes unstable behavior of the power transmission, which may be noted as shocks and vibrations. It is obvious that this unwanted behavior must be avoided or at least be made controllable by proper coupling design.

Figure 3 shows the measured secondary characteristics of the test coupling used in this study for different filling levels. The test coupling is a partially filled coupling that clearly exhibits such a torque transfer discontinuity at intermediate slip values. There, the power number suddenly changes by as much as 30% of its full value within a slip range of 1% (compare the curve for a filling level of 0.8). Also, the characteristics are not symmetric with respect to the direction of slip change. Since such torque leaps in the characteristic curves deteriorate the performance of the power train, it is important to find ways to control or avoid such behavior.

Fluid coupling optimization with respect to the hydraulic behavior is today mainly achieved in an empirical way by changing the geometrical parameters of the coupling design and testing the coupling in a test field in laborious experiments. For the future it is expected that this process can be assisted by computational fluid dynamics (CFD) programs, which must then be able to compute the two-phase flow and the fluid-structure interaction for a fluid coupling computer model [1–3]. However, two-phase flow CFD is challenging and not yet mature. Therefore, there will be a permanent need for experiments with sophisticated measurement techniques to disclose flow structures inside such a device, either for direct use of such measurement data in coupling design or for CFD code validation.

In past experimental work stroboscopic imaging techniques and laser Doppler anemometry were used to elucidate phenomena, such as the discontinuity in the momentum transfer [4]. However, optical methods proved to be inadequate due to the complex two-phase flow structure in such a device. Gamma ray tomography is a potential imaging technique that can provide valuable flow information from machines and vessels that are operated in industrial and thus rough environments. It is comparable to medical computed tomography (CT), which is being used to obtain cross-sectional images of human tissue from X-ray transmission radiographs. However, gamma ray tomography usually employs a radiation source of higher photon energy to be able to penetrate technical objects, which normally consist of metallic structures. Thus, gamma ray tomography has been employed by our group and others for measurements in chemical reactor vessels, axial pumps, and fuel rod bundles [5–14]. Gamma ray tomography uses isotopic sources, which is of some advantage. First, some isotopic sources, such as Cs-137 and Co-60, emit gamma rays of high energy that are able to penetrate a few centimeters of steel or aluminum. This allows measurement in heavy plant components and machines without major intrusion. Second, isotopic sources are mobile and easier to operate than X-ray accelerators, which produce X-ray radiation in a similar energy range above 500 keV. Thus, gamma ray tomography can be used for investigations on industrial objects at their installation site rather than in specially equipped laboratories.

The idea to visualize flow patterns in a fluid coupling has been first pursued by our group a few years ago [15]. At that time we operated a gamma ray tomography scanner with a moderate spatial resolution of about 12 mm. An application of this measurement technique to a fluid coupling produced first indicative results [16]. Recently we made considerable progress by building a high resolution gamma ray CT scanner [17,18], which now allows us to achieve a much higher spatial resolution and thus to disclose the liquid distribution in a running coupling to unprecedented detail.

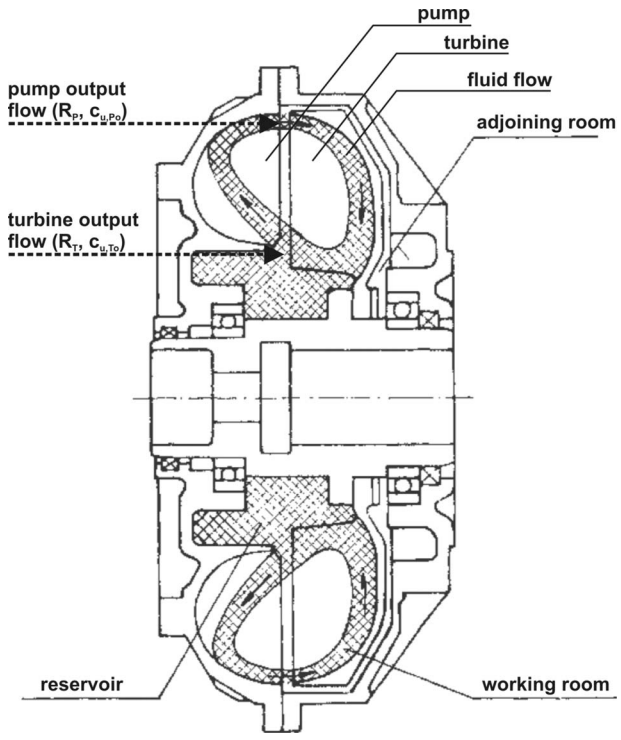

Fig. 2 Idealistic view of the flow structure inside a fluid coupling for nonzero slip (taken and modified from Ref. [4])

2 Test Coupling

The test coupling 422 SVW is a fluid coupling with controlled filling and has some special design features that allow different types of experimental studies on it (Figs. 4 and 5). The coupling has an external diameter of 490 mm and a profile diameter of 422 mm. The pump comprises 48 blades and the turbine, 45 blades. The blade shape is identical for the pump's blades whereas in the turbine two of the three blades are slanted. The runner gap is 4 mm wide. Pump and turbine are driven from the same side, which is achieved by a hollow shaft that drives the pump and a conventional axial shaft for the turbine. This design gives full access to the coupling from one side. Both shafts are driven independently by two speed-controlled electric motors. In this way the rotational speed of the pump and turbine and thereby the slip can be freely adjusted. During experiments the pump was driven at a constant speed of 780 rpm whereas the turbine speed was adjusted as required. Filling level adjustment for the test coupling is achieved by a scoop tube that extracts fluid from the rotating fluid annulus behind the turbine. The radial position of the tube's mouth can be varied to control filling. The extracted liquid is guided through an external heat exchanger for cooling.

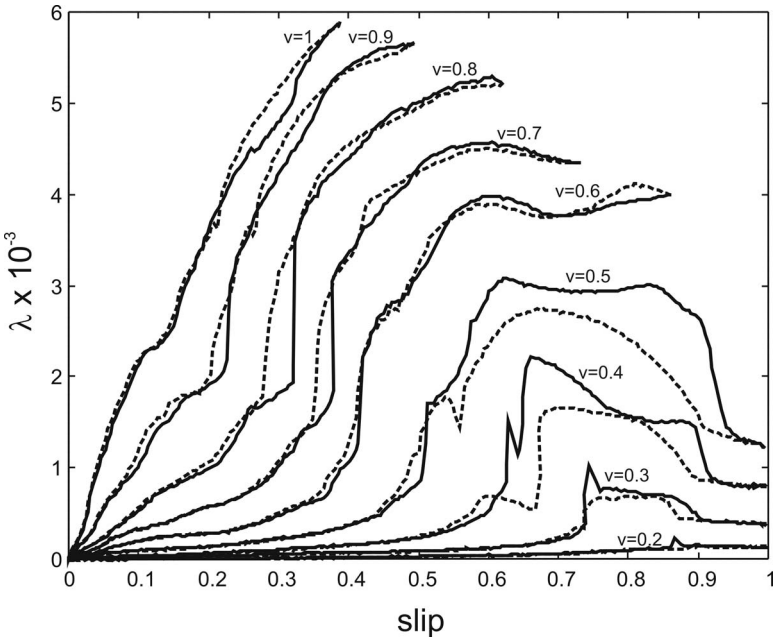

Fig. 3 Secondary characteristic curves of the test coupling 422 SVW with controlled filling for different filling levels *v*. The solid curves represent the characteristics in the direction of the increasing slip and the dotted curves the characteristics for decreasing slip.

3 Gamma Ray CT Setup

The gamma ray CT scanner comprises the isotopic source, detector arc, a gantry, processing electronics, and a measurement PC. Details of the device are given in Ref. [18]. The source isotope is Cs-137 with a gamma emission energy of 662 keV. At the time of the experiments the source had an activity of about 160 GBq. The effective spot diameter of the source pellet is 4 mm. The source pellet resides in a shielding container and can be moved into working position by means of a Bowden cable drive. A special tungsten alloy collimator in front of the shielding container provides fan beam shaping to the gamma radiation cone. The fan beam angle is 46 deg and the fan width is 4 mm. The latter value defines the axial resolution of the tomography system. The gamma ray detector comprises 320 contiguously arranged scintillation detector elements, each with an active element area of 2 mm width and 8 mm height and 75% stopping efficiency for 662 keV gamma rays. The scintillation light is converted by avalanche photodiodes and proper pulse processing electronics connected to the photodiodes enables counting of single gamma photons. Thereby a pulse height discrimination stage excludes scattered photons from counting. A notable feature of the detection system is that the detector can be read out very fast at rates of up to 50 kHz. This is a prerequisite to produce sharp images from rapidly rotating objects. For details we refer to Ref. [19]. Detector and source are mounted on a scanner gantry, which is shown in Fig. 6. In this gantry the detector is placed upright. The coupling rotates in the center between the source and the detector. The whole gantry is mounted on sliders and can be axially traversed by means of an electromechanical drive.

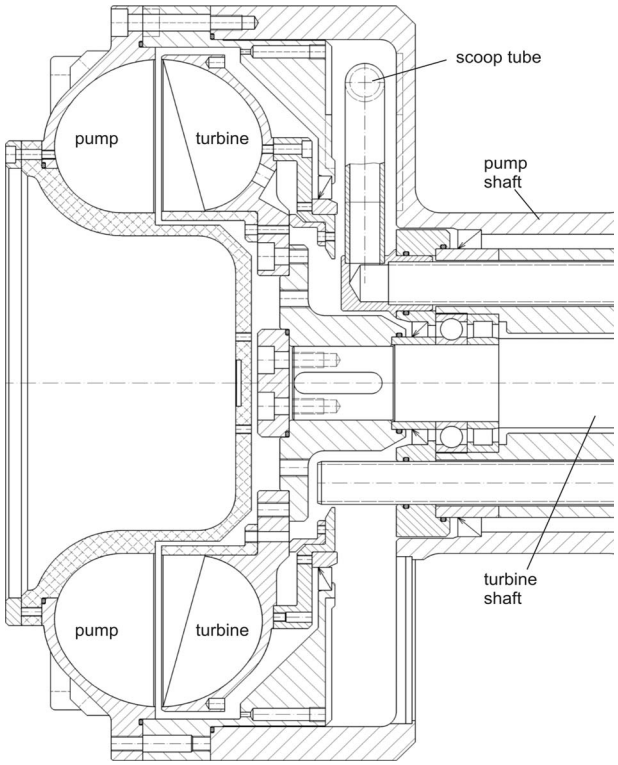

Fig. 4 CAD drawing of the test coupling

4 Data Processing

Data processing and image reconstruction for gamma ray tomography follow the conventional rules of transmission CT as described in many textbooks of computed tomography [20–22]. The only remarkable difference from conventional CT here is that we have to scan an object that rotates itself at a high speed. Figure 7 illustrates the measurement geometry in the scanned plane, which is perpendicular to the coupling axis. The detector receives radiation along 320 discrete rays propagating from the source to each individual detector element. At the moment we assume that the coupling is at a fixed rotation angle φ_k with $\varphi_k = 2\pi k/n_k$ ($k = 0, \ldots, n_k - 1$), where n_k is the number of projection angles that we used for image reconstruction. Further, we denote the detector

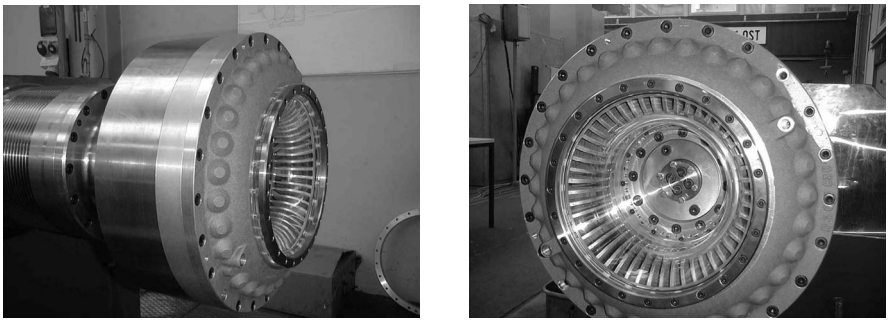

(*a*) (*b*)

Fig. 5 Photographs of the test coupling.

index by l ($l=0,\ldots,319$). Now, for a gamma ray propagating from the source to detector l at rotation angle φ_k, we can measure the integral attenuation

$$E_{k,l} = -\ln \frac{N_{k,l}}{N_{k,l}^{(0)}} = \int_{-\infty}^{+\infty}\int_{-\infty}^{+\infty} L_{k,l}(x,y)\mu(x,y)dxdy \tag{5}$$

where $N_{k,l}^{(0)}$ denotes the number of gamma photons transmitted from the source to the detector with no object in the ray path and $N_{k,l}$ denotes the number of gamma photons when the object is in the ray path. Furthermore, x and y are the spatial coordinates of the scanned plane, $\mu(x,y)$ is the distribution of the linear gamma ray attenuation coefficient that we want to reconstruct from the measurements, and $L_{k,l}(x,y)$ are the spatial ray functions, which are determined by geometrical parameters of the source and detector.

Image reconstruction requires to measure the extinction data from a sufficiently large number of projection angles and then to apply a suitable inverse computation scheme to calculate $\mu(x,y)$ from these data. The most prominent solution algorithm is the filtered backprojection, which is given by

$$\mu(x,y) \approx h(x,y)^* \sum_{l=0}^{n_l-1}\sum_{k=0}^{n_k-1} L_{k,l}(x,y)E_{k,l} \tag{6}$$

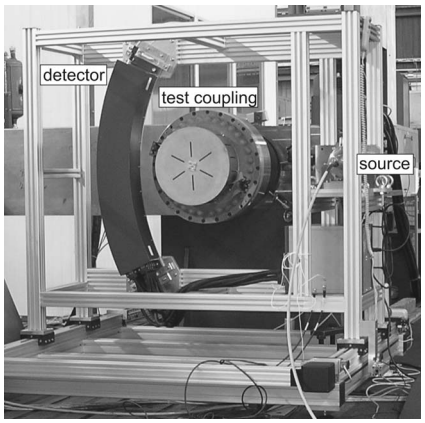

Fig. 6 Gamma ray tomography setup

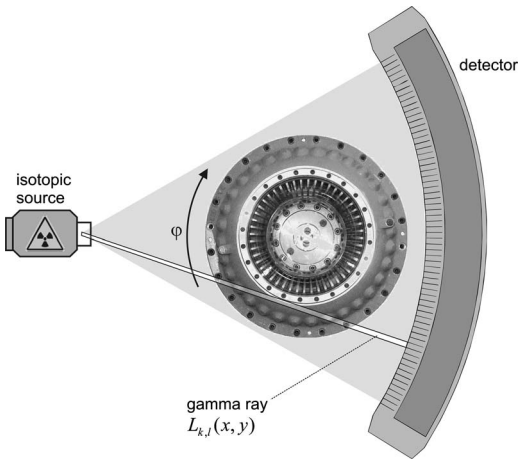

Fig. 7 Geometry and principle of the CT scanning setup

Here, the double sum constitutes the backprojection operation and (*) denotes the (de)convolution of the backprojection image with a restoring filter kernel $h(x,y)$. For further details on tomographic image reconstruction we again refer to Refs. [20–22].

There is, however, still the problem of the high rotational speed of the fluid coupling. Assume that the coupling rotates at 780 rpm. To achieve sufficient spatial resolution we typically need a number of $N_l=500$ projections. Then it follows that one projection has a duration of only 154 μs. On average we register about 12.000 counts per detector and second (the value is lower than the theoretical value for the 160 GBq source activity because of the additional source collimation and the limited detector efficiency). This means that we receive on average two counts per projection interval at the detector for an unattenuated ray, and even less for rays penetrating the coupling. Therefore, it is obvious that we need to acquire data over many rotations of the coupling to achieve sufficient signal-to-noise ratio. This is realized by a so called angle synchronized data acquisition scheme, which is described in detail in Refs. [15,16]. Briefly speaking, we continuously read out the detector at time intervals of 50 μs for a few minutes overall scanning time. In addition to the detector readout we transfer the digital signals of two revolution sensors, which are placed at the pump and the turbine, to the PC. After measurement we are thus able to associate each counter data set of the continuous time series to the actual rotation angle of the respective coupling part by evaluation of the angle sensor signals. In this way we are able to average the data for every projection angle accordingly. Typically, it required up to 5 min measurement time for a full data set with sufficient signal-to-noise ratio for high quality image reconstruction.

To visualize the fluid distribution inside the coupling we use a differential measurement technique. First, two calibration measurements on an empty and a full coupling are performed. If we denote the reconstructed calibration attenuation coefficient distributions by $\mu_0(x,y)$ for the empty coupling and $\mu_1(x,y)$ for the filled coupling, then we may scale an image from a two-phase flow measurement according to

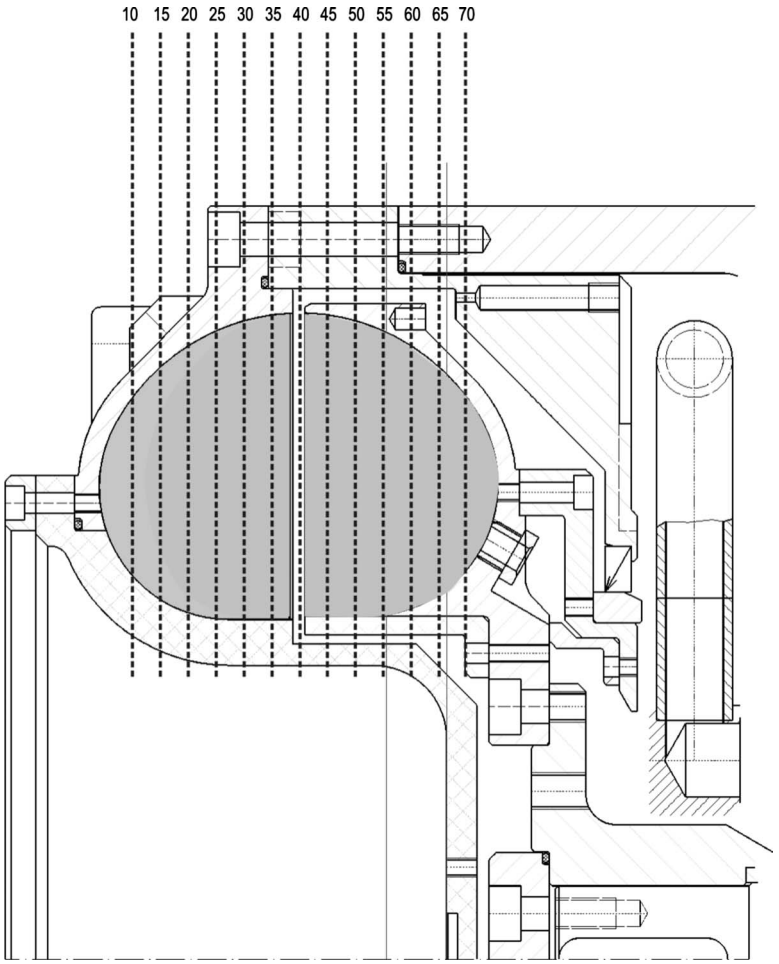

Fig. 8 Axial measurement planes of the coupling

$$\varepsilon(x,y) = \frac{\mu(x,y) - \mu_0(x,y)}{\mu_1(x,y) - \mu_0(x,y)} \tag{7}$$

where $\varepsilon(x,y)$ denotes the liquid holdup distribution in the scanned plane.

5 Results

In a comprehensive experimental campaign we performed measurements on the test coupling at different operating points to study the flow structure for transient coupling operation. Therefore, the coupling was driven into the required operational states by adjusting the turbine speed via one of the electric motors at a constant position of scoop tube. For each operation point we performed tomographic scans along the whole coupling axis in axial steps of 5 mm (Fig. 8). The data were processed according to the procedure described above. All the results discussed hereafter have been obtained with a filling level of $v=0.8$. The corresponding secondary characteristics can be found in Fig. 3.

Figure 9 shows cross-sectional images of the fluid distribution for a slip of $s=0.25$. The images reveal a well separated two-phase flow in the pump and a single-phase flow in the turbine. The turbine acts as a reservoir, which is at this slip value completely filled. The flow from the pump to the turbine at the outer radius is a single-phase flow but changes into a turbulent two-phase flow with decreasing radius. This can be conjectured from the decreasing fluid fraction with radius, which is reflected in the changing color. At the inner radius, where the fluid flows from the turbine back to the pump, the flow is concentrated into a thin liquid film of about 1 mm thickness at the pressure side of pump blade, which keeps its shape along a considerable way of the chamber wall. Note that there is no liquid crossing over to the suction side in this region. Figure 10 shows a three dimensional plot of the time-averaged interfacial area in the pump. It highlights the thin liquid film at the pressure side, which has been found for a wide range of slip values from 0.5 to 0.2 at $v=0.8$. The results of the analysis of the fluid distribution in this working point are shown in Fig. 11. Here, we plotted the phase boundaries at the suction and the pressure side wall, which were taken from gamma ray tomography images into a sectional drawing of the pump and turbine chambers. Pictures of a high speed camera of the region where the flow crosses from the turbine axially into the pump complete and approve the results of gamma ray CT at least in a qualitative sense (Fig. 12). Here, the liquid film could also be seen; however, the complete structure of the liquid distribution in a chamber is not educible.

Figure 13 shows the fluid distribution in a single pump chamber at plane No. 25 (compare Fig. 8) for varying slip and a filling level of $v=0.8$. From the analysis of the fluid structure as a function of slip we found that at low slip ($s<0.1$) the phase interface between the fluid and gas is axially parallel to the axis of rotation. With increasing slip the fluid level in the turbine moves toward a lower radius. Before the torque curve reaches a plateau of higher level at $s>0.2$, the turbine is completely filled. Flow crosses axially from the inner radius of the turbine into the pump and creates the thin fluid film at the pressure side of the pump blade.

As stated earlier, the transmitted torque of a hydrodynamic coupling can be described by the characteristic equation (3) and the torque is directly proportional to the dimensionless power number

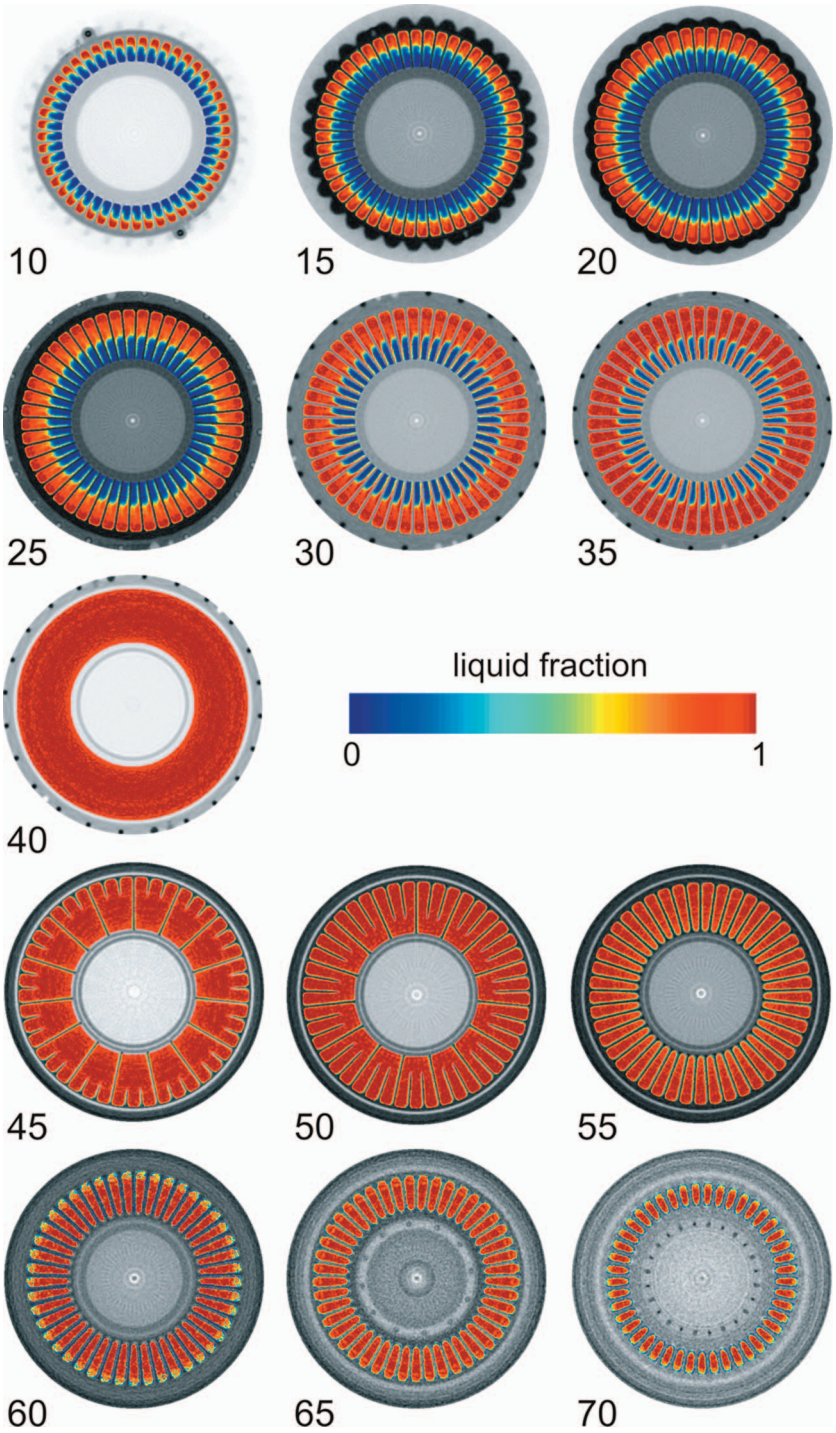

Fig. 9 Fluid distributions in different planes at $s=0.25$ (red: liquid, blue: gas)

λ. The curves (Fig. 3) for partial filling level show an abrupt increase in the transmitted torque with increasing slip. The reason is a change of flow conditions in the coupling and could now be made visible. At nominal small slip, the phase interface is parallel to the axis of rotation. With increasing slip the phase interface becomes more inclined and the turbine is then fully filled. After that, with more increase in slip, the inflow position of the fluid to the pump wheel is changes abruptly. According to the Euler turbine equation (2) in this case, the mass flow and angular momentum difference jump up.

6 Conclusions

We applied high resolution gamma ray tomography to the measurement and visualization of fluid distributions in a running fluid coupling. Gamma ray tomography proved its value to noninvasively disclose flow structures inside such a dense metallic object. With this measurement technique we could reveal the flow structure to yet unprecedented details. New and unexpected flow structures have been found, which will now be analyzed and in the near future compared with results of the two-phase flow CFD

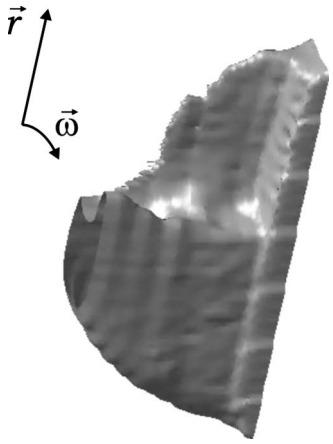

Fig. 10 Three-dimensional view of the fluid-gas interface in a pump chamber

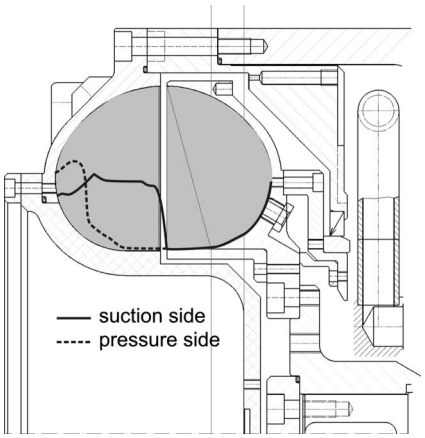

Fig. 11 Position of the phase interface (fluid-air) at v=0.8 and s=0.25 according to gamma ray CT measurements

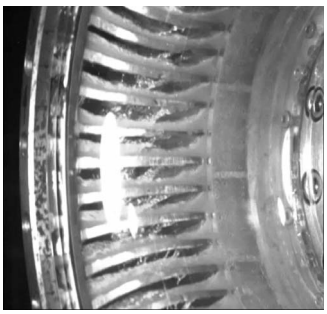

Fig. 12 Camera image of the flow at the inner profile diameter from the turbine to the pump at v=0.8 and s=0.25.

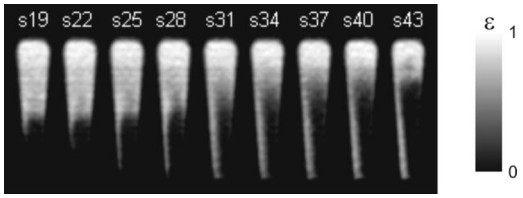

Fig. 13 Fluid distribution in the pump chamber at plane No. 25 at v=0.8 and s=0.25 and slip values denoted in the top row

calculations for such a device. The new understanding of flow inside the coupling helps us largely to find new ways for the active controlling of torque transmission and the optimization of coupling characteristics.

Nomenclature

c = velocity (ms^{-1})
D = profile diameter (m)
E = energy (J), extinction (m^{-1})
h = reconstruction filter (−)
$L(x,y)$ = spatial gamma ray function (−)
$\dot{m}$ = mass flow rate ($kg\ s^{-1}$)
m = mass (kg)
n = number of elements (−)
N = count rate (s^{-1})
M = (hydraulic) angular momentum ($kg\ m^2\ s^{-2}$)
P = power (W)
r = radius (m)
R = profile radius (m)
s = slip (−)
v = filling level (−)
x, y = spatial coordinates (−)

Greek Letters

$\varepsilon(x,y)$ = liquid holdup distribution (−)
λ = dimensionless power number (−)
μ = linear gamma ray attenuation coefficient (m^{-1})
φ = projection angle (−)
ω = angular frequency (s^{-1})

Subscripts

0 = data set for empty coupling
1 = data set for completely filled coupling
k = projection index
l = detector index
P = pump
Po = pump output
T = turbine
To = turbine output
u = circumferential

Superscripts

(0) = initial count rate

References

[1] Höller, H., Hydrodynamische Kupplungen mit konstanter Füllung, Voith Turbo GmbH.
[2] Huitenga, H., and Mitra, N. K., 2000, "Improving Start-Up Behavior of Fluid Couplings Through Modification of Runner Geometry: Part I—Fluid Flow Analysis and Proposed Improvement," ASME J. Fluids Eng., **122**(4), pp. 683–688.
[3] Huitenga, H., and Mitra, N. K., 2000, "Improving Start-Up Behavior of Fluid Couplings Through Modification of Runner Geometry: Part II—Modification of Runner Geometry and Its Effects on the Operation Characteristics," ASME J. Fluids Eng., **122**(4), pp. 689–693.
[4] Christen, M., and Kernchen, R., 2001, "Strömungsgeschwindigkeit in konstantgefüllter Turbokupplung," Messung mittels Laser-Doppler-Velozimetrie, Antriebstechnik, **40**, pp. 71–74.
[5] DeVuono, A. C., Schlosser, P. A., Kulacki, F. A., and Munshi, P., 1980, "Design of an Isotopic CT Scanner for Two-Phase Flow Measurements," IEEE Trans. Nucl. Sci., **27**(1), pp. 814–820.
[6] Kumar, S. B., Moslemian, D., and Dudukovic, M. P., 1995, "A γ-Ray Tomographic Scanner for Imaging Voidage Distribution in Two-Phase Flow Systems," Flow Meas. Instrum., **6**(1), pp. 61–73.
[7] Johansen, G. A., Frøystein, T., Hjertaker, B. T., and Olsen, Ø., 1996, "A Dual Sensor Flow Imaging Tomographic System," Meas. Sci. Technol., **7**(3), pp. 297–307.
[8] Kumar, S. B., Moslemian, D., and Dudukovic, M. P., 1997, "Gas Holdup Measurements in Bubble Columns Using Computed Tomography," AIChE J., **43**(6), pp. 1414–1425.
[9] Shollenberger, K. A., Torczynski, J. R., Adkins, D. R., O'Hern, T. J., and Jackson, N. B., 1997, "Gamma-Densitometry Tomography of Gas Holdup Spatial Distribution in Industrial-Scale Bubble Columns," Chem. Eng. Sci., **52**(13), pp. 2037–2048.

[10] Kemoun, A., Ong, B. C., Gupta, P., Al-Dahhan, M. H., and Dudukovic, M. P., 2001, "Gas Holdup in Bubble Columns at Elevated Pressure Via Computed Tomography," Int. J. Multiphase Flow, **27**(5), pp. 929–946.
[11] Kok, H. V., van der Hagen, T. H. J. J., and Mudde, R. F., 2001, "Subchannel Void-Fraction Measurements in a 6×6 Rod Bundle Using a Simple Gamma-Transmission Method," Int. J. Multiphase Flow, **27**(1), pp. 147–170.
[12] Veera, U. P., 2001, "Gamma Ray Tomography Design for the Measurement of Hold-Up Profiles in Two-Phase Bubble Columns," Chem. Eng. J., **81**(1–3), pp. 251–260.
[13] Khopkar, A. R., Rammohan, A. R., Ranade, W., and Dudukovic, M. P., 2005, "Gas-Liquid Flow Generated by a Rushton Turbine in Stirred Vessel: CARPT/CT Measurements and CFD Simulations," Chem. Eng. Sci., **60**(8–9), pp. 2215–2229.
[14] Bieberle, A., 2006, "Void Fraction Distribution Measurement in Fuel Element Bundles With a New High-Resolution Gamma Tomograph," ATW Int. J. Nucl. Power, **51**(8–9), pp. 539–540.
[15] Prasser, H.-M., Baldauf, D., Fietz, J., Hampel, U., Hoppe, D., Zippe, C., Zschau, J., Christen, M., and Will, G., 2003, "Time Resolving Gamma-Tomography for Periodically Changing Gas Fraction Fields and Its Application to an Axial Pump," Flow Meas. Instrum., **14**(3), pp. 119–125.
[16] Hampel, U., Hoppe, D., Diele, K.-H., Fietz, J., Höller, H., Kernchen, R., Prasser, H.-M., and Zippe, C., 2005, "Application of Gamma Tomography to the Measurement of Fluid Distributions in a Fluid Coupling," Flow Meas. Instrum., **16**(2–3), pp. 85–90.
[17] Bieberle, A., Kronenberg, J., Schleicher, E., and Hampel, U., 2007, "Design of a High-Resolution Gamma-Ray Detector Module for Tomography Applications," Nucl. Instrum. Methods Phys. Res. A, **572**(2), pp. 668–675.
[18] Hampel, U., Bieberle, A., Hoppe, D., Kronenberg, J., Schleicher, E., Sühnel, T., Zimmermann, F., and Zippe, C., 2007, "High Resolution Gamma Ray Tomography Scanner for Flow Measurement and Non-Destructive Testing Applications," Rev. Sci. Instrum., **78**, p. 103704.
[19] Bieberle, A., Schleicher, E., and Hampel, U., 2007, "Data Acquisition System for Angle Synchronized Gamma-ray Tomography of Rapidly Rotating Objects," Meas. Sci. Technol., **18**, pp. 3384–3390.
[20] Herman, G. T., 1980, *Image Reconstruction From Projections: The Fundamentals of Computerized Tomography*, Academic, New York.
[21] Kak, C., and Slaney, M., 1988, *Principles of Computerized Tomographic Imaging*, IEEE, New York.
[22] Natterer, F., and Wübbeling, F., 2001, *Mathematical Methods in Image Reconstruction*, SIAM, Philadelphia.

An Experimental Procedure for Determining Both the Density and Flow Rate From Pressure Drop Measurements in a Cylindrical Pipe

Ghislain Michaux
e-mail: ghislain.michaux@univmed.fr

Olivier Vauquelin

Elsa Gauger

Aix-Marseille Université,
IUSTI, UMR CNRS 6585,
Technopôle de Château-Gombert,
UNIMECA,
60 rue Joliot Curie,
13 453 Marseille, France

An experimental procedure was developed for determining both the density and flow rate of a gas from measurements of pressure drops caused by an abrupt flow area contraction in a cylindrical pipe. Experiments were carried out by varying the density and flow rate of a light gas mixture of air and helium, spanning a Reynolds number range from 0.2×10^4 to 3.4×10^4. From experimental results, a procedure was then proposed for evaluating the density from pressure change measurements in the scope of light gas extraction experiments. [DOI: 10.1115/1.2953294]

1 Introduction

In the case of a fire in an enclosure (e.g., tunnel or building), mechanical ventilation systems can be activated in order to extract the fire-induced smoke through exhaust vents. The efficiency of such systems is defined as the volumetric flow rate ratio between the extracted smoke and the produced smoke [1]. This quantity can be evaluated provided that both the density and volumetric flow rate of the extracted fluid (a mixture of combustion products and fresh air) are known. In general, density and flow rates are simultaneously estimated by combining two flow measurement devices. As an example, a hot wire probe and an oxygen analyzer were used by Vauquelin and Mégret [1] for smoke extraction experiments carried out on a reduced scale tunnel model.

In the scope of small scale smoke extraction investigations (see a typical setup in Fig. 1), a procedure was developed for determining both the density and volumetric flow rate of the fluid extracted through an exhaust pipe with a single flow measurement device. This procedure is presented in this paper.

As shown in Fig. 1, the working fluid used is a light gas mixture of air and helium, which is continuously released through a circular opening located at the floor level in order to simulate the fire-induced smoke. Note that, for flow visualizations, this mixture can be seeded by particles. At the ceiling, an unknown air and helium mixture is mechanically extracted through a cylindrical exhaust pipe where density and flow rate have to be known in order to estimate the extraction efficiency.

In a pipe, the density and the flow rate can be measured using a Coriolis [2] or an ultrasonic flow meter [3]. Unfortunately, these flow measurement devices are not suitable for light gas flows. For air and helium mixtures, Way and Libby [4] have developed a technique based on hot-wire anemometry, which allows determination of the local velocity and mass fraction of helium. Nevertheless, this solution has not been retained since; on the one hand, the mean density and flow rate have to be evaluated by integrating many measured values over the exhaust pipe cross section and, on the other hand, hot-wire probes cannot be used in seeded flows. For flow seeded by particles (in particular, for a smoky atmosphere), McCaffrey and Heskestad [5] have designed a probe, which allows determination of local velocity from static pressure measurements.

In the present paper, a technique that is also based on static pressure measurements, is described. The differential pressure device used, which consisted of a sudden flow area contraction in a cylindrical pipe, is presented in Sec. 2. In Sec. 3, the preliminary experimental results are presented and, then, a procedure is proposed to determine both the mean density and the flow rate from the measurement of static pressure changes. Conclusions are given in Sec. 4.

2 Differential Pressure Device

The differential pressure device used in order to develop the experimental procedure consisted of a sudden reduction in the exhaust pipe diameter. Note that orifice plates, flow nozzles, and Venturi tubes could have been also adopted but, here, the objective was not to investigate the most appropriate pressure device.

Figure 2 presents the experimental test section, which was designed to induce and measure pressure changes. The larger and smaller pipe inner diameters were $d_1=0.094$ m and $d_2=0.034$ m, respectively. The inlet and outlet pipes length were $L_1=L_2=0.5$ m. Two static pressure taps were located at $l_1=l_2=0.25$ m on each side of the contraction location.

Assuming a one-dimensional modeling of the flow in the test section, the generalized Bernoulli equation between the inlet and outlet cross sections yields:

$$p_1+\frac{1}{2}\rho u_1^2=p_2+\frac{1}{2}\rho u_2^2+\zeta\left(\frac{1}{2}\rho u_2^2\right) \tag{1}$$

where u_1 and u_2 are the area-averaged velocities based on the inlet and outlet pipe cross-section areas, ρ is the fluid density, and ζ is the pressure loss coefficient. With the mass flow rate conservation equation, $\rho u_1\pi d_1^2/4=\rho u_2\pi d_2^2/4$, Eq. (1) reduces to

$$\Delta p=p_1-p_2=K\rho u_2^2 \tag{2}$$

where K is the characteristic flow coefficient, which depends on the geometrical parameter $(d_2/d_1)^4$ and the pressure loss coefficient ζ. Here, the test section geometry is fixed $(d_2/d_1=0.36)$, while ζ depends classically on the flow conditions, that is, on the Reynolds number value. The Reynolds number considered in this study is based on the outlet pipe inner diameter, defined as follows:

$$\mathrm{Re}_2=\frac{\rho u_2 d_2}{\mu} \tag{3}$$

where μ is the fluid dynamic viscosity.

According to Eq. (2), the fluid density can be related to the pressure drop and the volumetric flow rate provided that variations in the flow coefficient with the Reynolds number are known. Therefore, in the following section, these variations are experimentally investigated by varying the entering light gas density and volumetric flow rate.

3 Experiments

3.1 Experimental Setup. Experiments were conducted with the test section (Fig. 2) in order to investigate variations in the flow coefficient, K, with both the density and the flow rate of the

Contributed by the Fluids Engineering Division of ASME for publication in the JOURNAL OF FLUIDS ENGINEERING. Manuscript received July 13, 2007; final manuscript received May 14, 2008; published online August 12, 2008. Assoc. Editor: Timothy J. O'Hern.

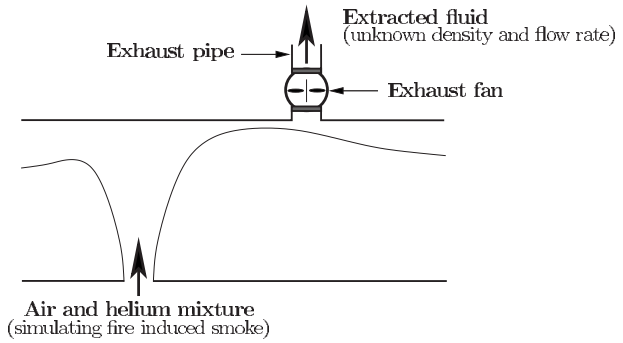

Fig. 1 Schematic of a typical experimental setup used for light gas extraction experiments on scale down models

entering fluid. A schematic of the experimental setup is shown in Fig. 3. The air and helium mixture first entered a Plexiglass plenum and passed through a flow straightener honeycomb. Then, the light gas mixture was turned and entered the test section, constructed from PVC pipes, and, finally, exited to the atmosphere. A second flow straightener honeycomb was also placed upstream of the test section.

Experiments were conducted for different flow conditions by varying both the mixture density, ρ, and the volumetric flow rate, q. Therefore, air and helium flow rates, q_{air} and q_{He}, were adjusted in order to obtain the required flow rate, $q=q_{air}+q_{He}$, volumetric fraction of helium, $\chi_{He}=q_{He}/q$, and mixture density, $\rho=\chi_{He}\rho_{He}+(1-\chi_{He})\rho_{air}$. Standard conditions were assumed (20°C, 10^5 Pa) and air and helium densities were taken equal to $\rho_{air}=1.2$ kg/m^3 and $\rho_{He}=0.166$ kg/m^3, respectively. Air and helium dynamic viscosities being close ($\mu_{air}=1.809\times10^{-5}$ kg/ms and $\mu_{He}=1.955\times10^{-5}$ kg/ms), the Reynolds number was calculated using the averaged value: $\mu\simeq1.88\times10^{-5}$ kg/ms for any mixture.

Air and helium volumetric flow rates, q_{air} and q_{He}, were measured by two independent Bronkhorst High-Tech flow meters with an accuracy better than $\pm1\%$, while the static pressure drop was measured by a Furness Controls, FCO60 manometer. The range of the differential pressure transmitter was 0–1999 Pa, with an accuracy of $\pm1\%$ on the reading scale.

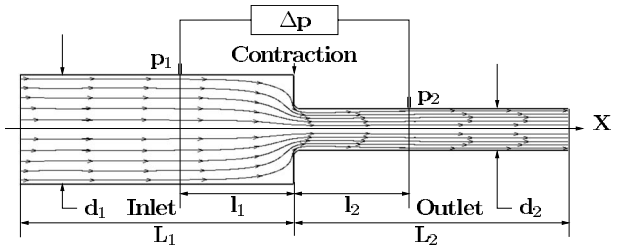

Fig. 2 Schematic of the test section showing the abrupt flow area contraction with main dimensions and pressure tap locations

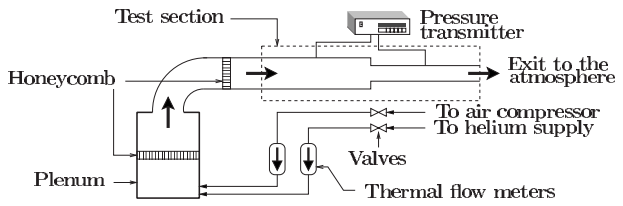

Fig. 3 Schematic of the experimental setup used for experiments on the test section using air and helium mixtures

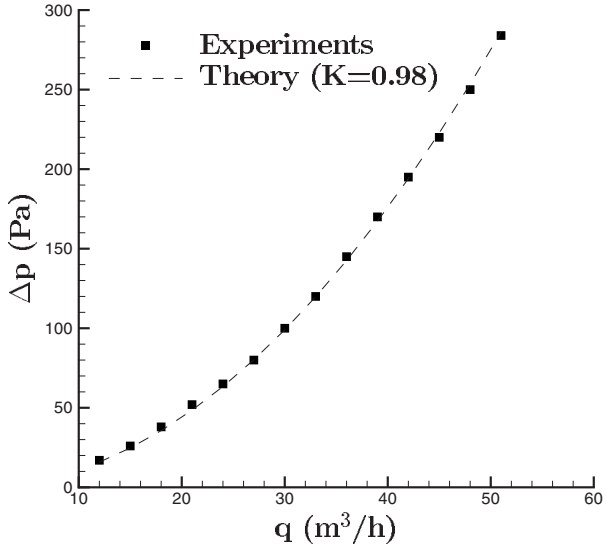

Fig. 4 Comparison between experimental results and theoretical predictions for pure air showing pressure drop variations with the volumetric flow rate

3.2 Experimental Results. First, experiments were conducted for pure air ($\chi_{He}=0\%$) by increasing the volumetric flow rate from 12 m^3/h to 51 m^3/h, by a step of 3 m^3/h. Experimental results are plotted in Fig. 4. These results are in good agreement with the theoretical prediction where, for a given density (air, in this case), the pressure drop is proportional to the volumetric flow rate squared (see Eq. (2)). The flow coefficient K is then estimated to be about 0.98 within the flow rate range investigated.

Next, other values of the volumetric fraction of helium were tested, namely, $\chi_{He}=0\%$, 20%, 40%, 60%, and 80%. For each case, the volumetric flow rate was also increased from 12 m^3/h to 51 m^3/h, by a step of 3 m^3/h, covering a Reynolds number range from roughly $Re_2=0.2\times10^4$ to 3.4×10^4. From pressure drop measurements, the flow coefficient was evaluated and plotted against the Reynolds number, as shown in Fig. 5. One can observe that K is relatively insensitive to Re_2 except for lower Reynolds numbers where K increases as Re_2 decreases. For $Re_2>1.5\times10^4$, K remains constant, estimated close to the value 0.98

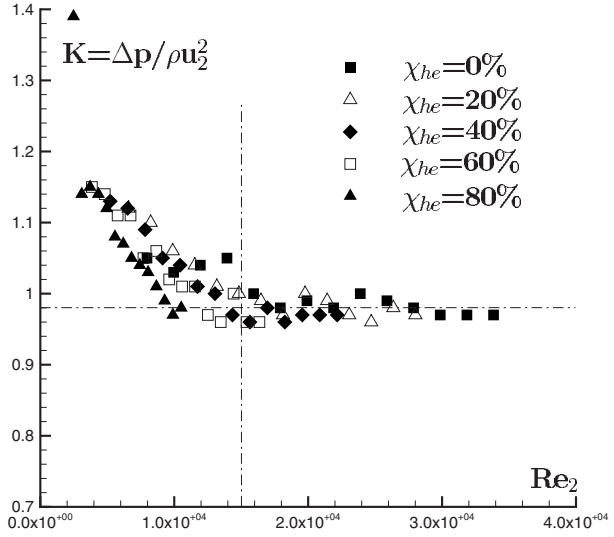

Fig. 5 Flow coefficient variations with the Reynolds number obtained from experiments for several air and helium mixtures

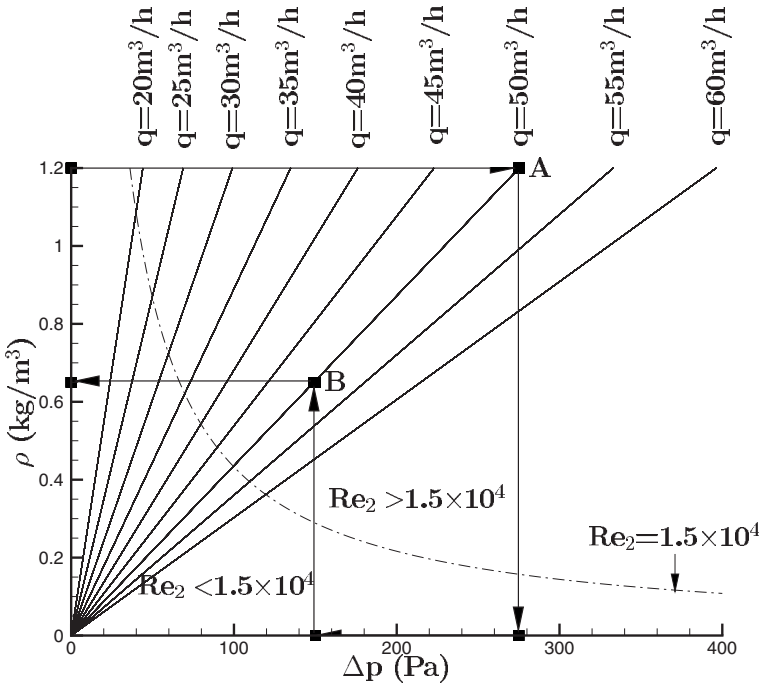

Fig. 6 Curves plotted from experimental results giving the density as a function of the differential pressure for several volumetric flow rate values

with an accuracy of $\pm 3\%$. It can be noted that, for $\chi_{He} \geq 60\%$, the Reynolds number remains smaller than 1.5×10^4. As a consequence, K is not constant for the range of volumetric flow rate tested.

3.3 Application. As an application, a procedure based on the use of this differential pressure device is proposed to evaluate the extraction efficiency. In order to determine both the volumetric flow rate and density of the light gas mixture, which is mechanically extracted (see Fig. 1), the differential pressure device is placed in the continuation of the exhaust pipe.

From Eq. (2) and the experimental result $K=0.98$, the density is plotted as a function of the pressure drop in Fig. 6 for several values of the volumetric flow rate, from 20 m^3/h to 60 m^3/h (this is the range envisaged for our future experiments). Then, assuming that the condition $Re_2 > 1.5 \times 10^4$ is verified, the proposed experimental procedure can be described as follows:

At first, the extracted volumetric flow rate is adjusted when a gas of known density is extracted. Here, pure air is used ($\rho = 1.2$ kg/m^3). In that case, the flow rate can be adjusted from differential pressure measurements using Fig. 6. As an example, let us consider that the required extracted volumetric flow rate is $q=50$ m^3/h. According to Fig. 6, this flow rate value is reached (for pure air) when the measured differential pressure is $\Delta p = 275$ Pa (Point A, in Fig. 6).

Then, when a mixture of air and helium is released in order to simulate a fire induced plume (see Fig. 1), it mixes with ambient air and, as a consequence, a gas of unknown density is extracted through the exhaust pipe. This density can be deduced from the differential pressure decrease using Fig. 6 since the volumetric flow rate remains the same, provided that the fan rotation speed is maintained. As an example, let us assume that, for an unchanged volumetric flow rate ($q=50$ m^3/h), the measured differential pressure falls to $\Delta p = 150$ Pa. In that case, the density can be evaluated from Fig. 6: $\rho \approx 0.65$ kg/m^3 (Point B).

4 Conclusions

An experimental device was developed in order to determine the density and volumetric flow rate from measurements of pressure changes along a simple abrupt flow area contraction. Using pressure taps, this device can be used when the fluid is seeded by particles. Experimental results show that the flow coefficient, which relates the differential pressure, the density, and the volumetric flow rate, was constant for a specific Reynolds number range. From this result, curves were plotted for several flow rate values in order to relate the mixture density to the differential pressure.

For practical conditions, these curves can be used to control the flow rate when pure air is extracted and, then, to deduce the density of any extracted mixture from the pressure decrease. In the near future, such a differential pressure device will be placed in the continuation of exhaust pipes on small scale models in order to investigate experimentally the smoke extraction efficiency.

References

[1] Vauquelin, O., and Mégret, O., 2002, "Smoke Extraction Experiments in Case of Fire in a Tunnel," Fire Saf. J., **37**, pp. 525–533.

[2] Gysling, D. L., 2007, "An Aeroelastic Model of Coriolis Mass and Density Meters Operating on Aerated Mixtures," Flow Meas. Instrum., **18**, pp. 69–77.

[3] Rabalais, R. A., and Sims, L., 2002, "Ultrasonic Flow Measurement: Technology and Applications in Process and Multiple Vent Stream Situations," UR-234, www.gesensing.com/products/resources/whitepapers/ur234.pdf.

[4] Way, J., and Libby, P. A., 1970, "Hot-Wire Probes for Measuring Velocity and Concentration in Helium-Air Mixture," AIAA J., **8**, pp. 976–978.

[5] McCaffrey, B. J., and Heskestad, G., 1976, "A Robust Bidirectional Low-Velocity Probe for Flame and Fire Application (Brief Communications)," Combust. Flame, **26**, pp. 125–127.